HELMHOLTZ ZENTRUM MÜNCHEN
ABTEILUNG FÜR APOPTOSE IN HÄMATOPOIETISCHEN STAMMZELLEN
LEITUNG: PROF. DR. IRMELA JEREMIAS

DISSERTATION ZUR ERLANGUNG DES DOKTORGRADES
DER FAKULTÄT FÜR BIOLOGIE
DER LUDWIG-MAXIMILIANS-UNIVERSITÄT MÜNCHEN

Characterization of treatment resistance in a preclinical *in vivo* model of leukemia

---

ANNA-KATHARINA WIRTH

MÄRZ 2021

Diese Dissertation wurde angefertigt
unter der Leitung von Prof. Dr. Wolfgang Enard
im Bereich für Anthropologie und Humangenetik
an der Ludwig-Maximilians-Universität München

Erstgutachter:	Prof. Dr. Wolfgang Enard
Zweitgutachterin:	Prof. Dr. Irmela Jeremias

Tag der Abgabe:	04.03.2021
Tag der mündlichen Prüfung:	11.10.2021

Eidesstattliche Erklärung

Ich versichere hiermit an Eides statt, dass die vorgelegte Dissertation mit dem Titel

"Characterization of treatment resistance in a preclinical *in vivo* model of leukemia"

von mir selbstständig und ohne unerlaubte Hilfsmittel angefertigt ist.

Hiermit erkläre ich, dass die Dissertation nicht ganz oder in wesentlichen Teilen einer anderen Prüfungskommission vorgelegt worden ist.

Außerdem erkläre ich, dass ich mich nicht anderweitig einer Doktorprüfung ohne Erfolg unterzogen habe.

München, den 04.03.2021

_____

Anna-Katharina Wirth

Table of Contents

Abstract

Over the last decades, cancer therapy has enormously improved the prognosis of patients suffering from many different tumor entities. However, resistance towards therapy remains a major obstacle for the long-term cure rate of cancer patients. Tumors might initially respond to treatment, but develop into a highly resistant disease over time. Likewise, most patients suffering from acute lymphoblastic leukemia (ALL) achieve substantial improvements within the first weeks of chemotherapy treatment. Yet, residual cells surviving treatment might develop resistance, which eventually leads to treatment failure and relapse of the disease, associated with poor prognosis. While understanding of the mechanisms leading to treatment resistance is of enormous clinical relevance, adequate model systems remain scarce.

To overcome this limitation, the present work aimed at modelling and characterizing development of resistance *in vivo*. In a first step, I generated a model of resistance evolution by adapting maintenance chemotherapy protocols for use in the patient-derived xenograft (PDX) mouse model of ALL. Genetic engineering of PDX cells allowed reliable quantification of treatment effects by repetitive *in vivo* imaging. An exemplary standard combination chemotherapy was applied constantly for up to 18 weeks, leading to sequential and reproducible changes in the tumor population. Treatment initially caused strong reduction of tumor burden, proving therapy sensitivity of PDX cells. However, residual leukemic cells persisted at a constant level and ultimately re-grew despite of ongoing therapy. This course of reduction, maintenance and regrowth indicates the acquisition of treatment resistance. Importantly, re-transplantation of resistant PDX cells into next recipient mice and subsequent treatment maintained the phenotype, suggesting that resistance was driven by mechanisms intrinsic to leukemic cells rather than the murine microenvironment.

Eight resistant derivatives originating from the same PDX sample were collected after long-term chemotherapy treatment and characterized individually. Strikingly, genomic and functional analyses revealed substantial heterogeneity between the resistant derivatives. While most derivatives developed an irreversible resistant phenotype, which persisted even after six months without therapeutic pressure, one derivative showed partial response to treatment in this setup. Two derivatives acquired loss of heterozygosity in the tumor suppressor gene *TP53*, which presumably drives the resistant phenotype. In contrast, the other derivatives did not develop alterations in *TP53* but presented a concordant loss of Chr. 1p36, suggesting that different mechanisms of resistance evolved in parallel.

Nevertheless, transcriptome and proteome profiling identified shared differentially expressed genes and proteins associated with the resistant phenotype across all derivatives. A targeted CRISPR/Cas9 *in vivo* dropout screen was performed to study the relevance of these candidates in resistant PDX cells. This approach identified, among others, the anti-apoptotic regulator

Bcl-2 as essential for maintenance of resistance. Blocking of functional Bcl-2 by CRISPR/Cas9-mediated knockout of the *BCL2* gene or by treatment with the Bcl-2 inhibitor Venetoclax sensitized resistant PDX cells to chemotherapy treatment *in vivo*, thus validating their dependency on Bcl-2.

Taken together, I established a clinically relevant *in vivo* model of acquired resistance, which allows following evolution of resistance over time and characterizing underlying mechanisms. Inhibition of Bcl-2 restored treatment sensitivity, thus presenting an attractive approach to tackle treatment resistant disease.

Zusammenfassung

In den letzten Jahrzehnten konnte die Krebstherapie die Prognose von PatientInnen mit verschiedensten Tumorarten erheblich verbessern. Allerdings stellt Resistenz gegen Therapie weiterhin ein großes Hindernis für die Langzeit-Heilung von KrebspatientInnen dar. Obwohl die meisten Tumore in der Regel zunächst auf Therapie ansprechen, können sie sich mit der Zeit in äußerst resistente Erkrankungen entwickeln. So erreichen PatientInnen mit akuter lymphoblastischer Leukämie (ALL) meist eine erhebliche Verbesserung ihres Zustandes innerhalb der ersten Wochen der Behandlung mit Chemotherapie. Trotzdem können verbleibende Tumorzellen, die die Therapie überleben, Resistenz entwickeln. Das führt letztendlich zu Therapieversagen und einer rezidivierenden Erkrankung, einhergehend mit einer schlechten Prognose. Obwohl ein besseres Verständnis der Mechanismen, die zu Therapieresistenz führen, daher klinisch höchst relevant ist, gibt es bisher nur wenige passende Modellsysteme.

Die vorliegende Arbeit hatte zum Ziel, Resistenzentwicklung in einem *in vivo* Modell abzubilden und so die zugrundeliegenden Mechanismen besser zu charakterisieren. Dafür konnte ich zunächst ein Modell etablieren, bei dem Chemotherapie-Protokolle der Erhaltungstherapie für die Anwendung im Xenograft-Mausmodell (engl. „patient derived xenograft model“, PDX) der ALL angepasst wurden. Gentechnische Veränderung der PDX Zellen ermöglichte, die Therapieeffekte verlässlich über *in vivo* Bildgebungsverfahren zu quantifizieren. Eine repräsentative Chemotherapie, bestehend aus einer Kombination etablierter Zytostatika, wurde konstant für bis zu 18 Wochen verabreicht. Das führte zu aufeinanderfolgenden, reproduzierbaren Veränderungen in der Tumorzellpopulation. PDX Zellen waren ursprünglich sensitiv gegenüber der Therapie und die Tumorlast konnte in den ersten Wochen stark verringert werden. Allerdings blieben wenige Tumorzellen auf einem konstanten Niveau erhalten und begannen schließlich trotzdem bestehendem Therapiedruck wieder zu wachsen. Dieser Ablauf von Reduktion, Erhaltung und Wachstum zeigt die Entwicklung von Therapieresistenz. Der resistente Phänotyp blieb auch erhalten, wenn resistente PDX Zellen in neue Empfängermäuse transplantiert wurden. Daraus lässt sich schließen, dass Resistenz von intrinsischen Mechanismen der Leukämiezellen und nicht von der murinen Knochenmarksnische angetrieben wird.

Mit Hilfe des beschriebenen Modells wurden aus einer PDX Probe acht resistente Derivate generiert und einzeln charakterisiert. Genomische und funktionelle Untersuchungen zeigten erstaunlicherweise eine erhebliche Heterogenität zwischen den resistenten Derivaten. Während die meisten Derivate einen irreversiblen, resistenten Phänotyp entwickelt hatten, der auch nach sechs Monaten Therapiepause erhalten blieb, zeigte ein Derivat in dieser Untersuchung ein partielles Ansprechen auf Therapie. Zwei Derivate entwickelten einen Verlust des Tumorsuppressor-Gens *TP53*, der wahrscheinlich den resistenten Phänotyp

verursacht. Im Gegensatz dazu zeigten die anderen Derivate keine Veränderungen im *TP53* Gen, dafür aber einen konsistenten Verlust von Chr. 1p36. Das lässt vermuten, dass sich verschiedene Resistenzmechanismen parallel entwickeln konnten.

Trotzdem zeigten Untersuchungen von Transkriptom und Proteom gemeinsame, differentiell exprimierte Gene und Proteine, die mit dem resistenten Phänotyp unabhängig von einzelnen Derivaten assoziiert waren. Um die Relevanz dieser Kandidaten für die resistenten PDX Zellen zu untersuchen, wurde ein gezielter CRISPR/Cas9 *in vivo* dropout screen durchgeführt. Dieser Ansatz identifizierte unter anderem den anti-apoptotischen Regulator Bcl-2 als essentiell für die Erhaltung der Resistenz. Blockierung der Funktion von Bcl-2 durch Knockout des *BCL2* Gens mittels CRISPR/Cas9 oder durch Behandlung mit dem Bcl-2 Inhibitor Venetoclax stellte die Sensitivität von resistenten PDX Zellen gegenüber Chemotherapie *in vivo* wieder her. Das zeigt die Abhängigkeit dieser Zellen von funktionellem Bcl-2.

Zusammengefasst konnte ich ein klinisch relevantes *in vivo* Modell für Resistenzentwicklung etablieren, das erlaubt, Evolution von Resistenz über die Zeit zu verfolgen und die zugrundeliegenden Mechanismen zu charakterisieren. Inhibierung von Bcl-2 konnte eine Sensitivität für Chemotherapie wiederherstellen. Damit stellt Bcl-2 einen attraktiven Angriffspunkt dar, um therapieresistente Tumorerkrankungen zu behandeln.

List of Abbreviations

ABC	ATP-binding cassette
ALDH	Aldehyde dehydrogenase
ALL	Acute lymphoblastic leukemia
ANOVA	Analysis of variance
APC	Allophycocyanin
BCL2/Bcl-2	B-cell lymphoma 2
BCR	B-cell receptor
BLI	Bioluminescence *in vivo* imaging
BM	Bone marrow
BSA	Bovine serum albumin
CAR	CXCL12-abundant reticular
Cas9	Human codon-optimized Streptococcus pyogenes Cas9
cDNA	Copy DNA
Chr.	Chromosome
CLL	Chronic lymphocytic leukemia
CNA	Copy number alteration
CRISPR	Clustered regularly interspaced short palindromic repeats
CRLF2	Cytokine receptor-like factor 2
CSC	Cancer stem cell
CSNK2A1	Casein kinase II subunit alpha
Cyclo	Cyclophosphamide
DMEM	Dulbecco's modified Eagle's medium
DMSO	Dimethylsulfoxid
DNA	Deoxyribonucleic acid
dNTP	Deoxyribonucleosid triphosphate
EDTA	Ethylenediaminetetraacetic acid
EF1α	Human elongation factor-1 alpha
eFFly	Enhanced Firefly
eGFP	Enhanced green fluorescent protein
EGFR	Epidermal growth factor receptor
ETV6	ETS variant transcription factor 6
f	Female
FACS	Fluorescence-activated cell sorting
FBS	Fetal bovine serum
FDR	False discovery rate
Fig.	Figure
FSC	Forward scatter
g	Relative centrifugal force
gDNA	Genomic DNA
i.p.	Intraperitoneal

i.v.	Intravenous
IKZF1	Ikaros family zinc finger protein 1
InDels	Small insertions or deletions
KDM6B	Lysine demethylase 6B
KMT2A	Histone-lysine N-methyltransferase 2A
LOH	Loss of heterozygosity
MACS	Magnetic cell separation
MAGeCK	Model-based Analysis of Genome-wide CRISPR/Cas9 Knockout
miRNA	Micro RNA
MRD	Minimal residual disease
mRNA	Messenger RNA
MS	Mass spectrometry
mtagBFP	Monomeric blue fluorescent protein
NF-κB	Nuclear factor kappa-light-chain-enhancer of activated B cells
NGS	Next generation sequencing
NOD	Non-obese diabetic
n.s.	Not significant
NSG	NOD.Cg-Prkdc^{scid} Il2rg^{tm1Wjl}/SzJ
NT5C2	Cytosolic 5'-mucleotidase II
Oligo	Oligonucleotide
p.o.	Per os
P/S	Penicillin/Streptomycin
PBS	Phosphate buffered saline
PBX1	Pre-B-cell leukemia transcription factor 1
PCR	Polymerase chain reaction
PDX	Patient-derived xenograft
PE	Phycoerythrin
Ph+	Philadelphia chromosome positive
RNA	Ribonucleic acid
RT	Room temperature
RUNX1	Runt-related transcription factor 1
SCID	Severe combined immunodeficiency
SCN1B	Sodium channel subunit beta-1
SD	Standard deviation
SFFV	Spleen focus-forming virus
sgRNA	Single guide RNA
SNP	Single nucleotide polymorphism
SNV	Single nucleotide variant
SSC	Side scatter
TBX21	T-box transcription factor 21
TCF3	Transcription factor 3
TP53/p53	Cellular tumor antigen p53

VAF	Variant allele frequency
VCR	Vincristine
Ven	Venetoclax
WES	Whole exome sequencing

List of Figures

List of Tables

1 Introduction

1.1 Acute lymphoblastic leukemia

Acute lymphoblastic leukemia (ALL) defines a cancer of the hematopoietic system characterized by malignant transformation of lymphoid progenitor cells, which is mostly caused by chromosomal aberrations. Consequently, transformed cells (lymphoblasts) do not differentiate into mature lymphocytes and proliferate aberrantly, leading to accumulation in bone marrow (BM), peripheral blood and at extramedullary sites. Ultimately, this leads to a block of normal hematopoiesis and to bone marrow failure (Terwilliger and Abdul-Hay, 2017). Resulting symptoms are usually unspecific and include fever, fatigue, weight loss and pale skin (Esparza and Sakamoto, 2005). Involvement of extramedullary sites manifests, among others, in splenomegaly and cranial nerve defects (Terwilliger and Abdul-Hay, 2017).

In 2020, estimations expect 6,150 new cases and 1,520 deaths from ALL in the USA (Siegel et al., 2020). App. 80% of ALL cases are diagnosed in children (Terwilliger and Abdul-Hay, 2017). Thus, ALL accounts for 21% of all cancers in children in the USA between 2012-2016 and represents the most common cancer in children under the age of 14 years (Siegel et al., 2020).

1.1.1 Diagnosis and classification of ALL

Most cases of ALL arise spontaneously in healthy individuals, but predisposing risk factors have been identified in a minority of cases. These include genetic factors, such as inherited gene variants, e.g. mutations in *CDKN2A*, and congenital syndromes, e.g. Trisomy 21, as well as environmental factors, such as childhood infections and ionizing radiation (Malard and Mohty, 2020). Diagnosis relies on identification of lymphoblasts by microscopy, with detection of > 20% lymphoblasts in BM aspirates necessary per definition (Brown et al., 2020). Upon diagnosis, detailed immunophenotyping and cytogenetic analyses are needed for accurate classification and risk stratification (Malard and Mohty, 2020).

Classification of ALL is based on the hematopoietic lineage, which is mainly determined via immunophenotyping of surface markers, and the presence of chromosomal aberrations, which is mainly determined via cytogenetic analysis. Major subtypes comprise T-lymphoblastic leukemia (T-ALL), B-lymphoblastic leukemia (B-ALL) with recurrent genetic abnormalities and B-ALL not otherwise specified (Terwilliger and Abdul-Hay, 2017). B-ALL with recurrent genetic abnormalities can be further distinguished based on its key anomalies, which are either aneuploidy, i.e. gains and losses of whole chromosomes, or chromosomal rearrangements (Roberts and Mullighan, 2015). High hyperdiploidy, i.e. presence of more than 50 chromosomes, represents the most common pediatric B-ALL with 20-30% prevalence, while hypodiploidy, i.e. presence of less than 44 chromosomes, is less frequent. Chromosomal rearrangements result in expression of fusion transcripts or in relocation of an oncogene into

a highly transcribed region. Here, a translocation t(12;21)(p13;q22) resulting in generation of the ETV6-RUNX1 fusion protein represents the most common translocation with up to 25% prevalence. This is followed by t(1;19)(q23;p13) leading to generation of the TCF3-PBX1 fusion protein, t(9;22)(q34;q11.2) resulting in generation of the BCR-ABL1 fusion protein, i.e. Philadelphia chromosome positive (Ph+), and rearrangement of *KMT2A* with diverse fusion partners (Roberts and Mullighan, 2015). Recently, new subgroups of ALL have been identified due to improved detection methods, such as RNA sequencing. These subgroups are based on more complex cytogenetic alterations or gene expression profiles. 10% of childhood B-ALL cases are now classified as Ph-like ALL, since they share similar expression profiles with Ph+ ALL without having the BCR-ABL1 translocation (Malard and Mohty, 2020). Common features of Ph-like ALL include alterations in tyrosine kinase and cytokine receptor signaling, e.g. by *CRLF2* rearrangements, and alterations in B-lymphoid transcription factors, e.g. by deletion of *IKZF1* (Iacobucci and Mullighan, 2017).

Accurate classification upon diagnosis is crucial to evaluate prognosis and determine treatment of patients. While hyperdiploid, ETV6-RUNX1 fusion and TCF3-PBX1 fusion B-ALL shows a favorable outcome, hypodiploid, KMT2A-rearranged, Ph+ and Ph-like B-ALL show a poor prognosis (Roberts and Mullighan, 2015).

1.1.2 Current treatment strategies

Treatment of ALL reflects one of the most complex approaches in cancer therapy. It involves several treatment phases as well as combination of several different drugs, which are adjusted based on classification of the leukemia and risk stratification. First-line treatment typically consists of induction, consolidation and maintenance, covering a total treatment period of 2-3 years. Induction therapy aims at eradicating as many leukemic cells as possible, thus restoring normal hematopoiesis and achieving remission, i.e. < 5% lymphoblasts in BM without extramedullary disease. Consolidation therapy aims at eradicating any residual leukemic cells, followed by maintenance therapy to prevent disease relapse (Brown et al., 2020) (Figure 1).

Common strategy of all treatment stages is the combination of several chemotherapeutic drugs with different modes of action. These typically include mitotic inhibitors, such as vincristine (VCR), alkylating agents, such as cyclophosphamide (Cyclo), antimetabolites, such as methotrexate or 6-mercatopurine, and topoisomerase inhibitors, such as doxorubicin (Bukowski et al., 2020). By combining different approaches, as many leukemic cells should be killed as effectively and fast as possible. Chemotherapy does not specifically target cancer cells, but rather targets fast proliferating cells in general, leading to a wide range of side effects.

Since the first chemotherapeutic applications in the 1940s, treatment protocols have been constantly optimized based on tolerability, response rates and pharmacological aspects, but rarely based on biological characteristics of leukemic cells (Freireich et al., 2014, Inaba and

Mullighan, 2020). Only in recent years, several targeted therapies directed to leukemia-specific surface molecules, fusion transcripts and their downstream effects have been established, allowing individualized therapies based on characteristics of the leukemia. These approaches supplement the existing treatment protocols. As one of the first targeted therapies, implementation of Imatinib, which is a tyrosine kinase inhibitor targeting the BCR-ABL1 fusion protein, has greatly improved outcome of patients with Ph+ ALL since its initial approval in 2001. Other approaches include the recruitment of T-cells to eliminate leukemic cells using bispecific antibodies, such as Blinatumomab, and the use of genetically engineered T-cells, i.e. chimeric antigen receptor-modified (CAR) T-cells. Efforts to reduce side effects of chemotherapy resulted in the development of antibody-drug conjugates, where toxins are bound to monoclonal antibodies, which target B-lineage specific surface molecules. Inotuzumab ozagamicin, for example, binds to the B-lineage marker CD22 to deliver the cytostatic drug calicheamicin specifically to leukemic cells (Carroll and Hunger, 2016, Terwilliger and Abdul-Hay, 2017).

Development of targeted therapies and optimization of existing treatment protocols have led to substantial improvements in prognosis over the last decades, resulting in potential cure rates of at least 80% and a 5-year-survival rate of 91% in patients with pediatric ALL, respectively (Kantarjian et al., 2018, Siegel et al., 2020).

1.1.3 Remaining challenges

Despite the substantial improvements in outcome of patients, 20-25% of patients eventually suffer from relapse (Szczepanek et al., 2011). In this case, 5-year survival rates drop from 91% to only app. 50% (Hunger and Raetz, 2020). Relapse is defined as the reappearance of lymphoblasts following complete remission, can occur both during treatment and after completion of treatment and lacks association with predefined risk factors, such as cytogenetics and immunophenotype (Szczepanek et al., 2011).

Instead, the most relevant prognostic factor was found to be the initial response to treatment. Most patients respond well to induction treatment and achieve complete remission (Fig. 1). However, residual leukemic cells might persist, defined as minimal residual disease (MRD) (Rafei et al., 2019). The initial response to treatment is directly reflected in the level of MRD, which is routinely determined upon treatment, usually by flow cytometry or real-time quantitative polymerase chain reaction (PCR). With these approaches, up to one single leukemic cell within 10^6 healthy cells can be detected (Malard and Mohty, 2020).

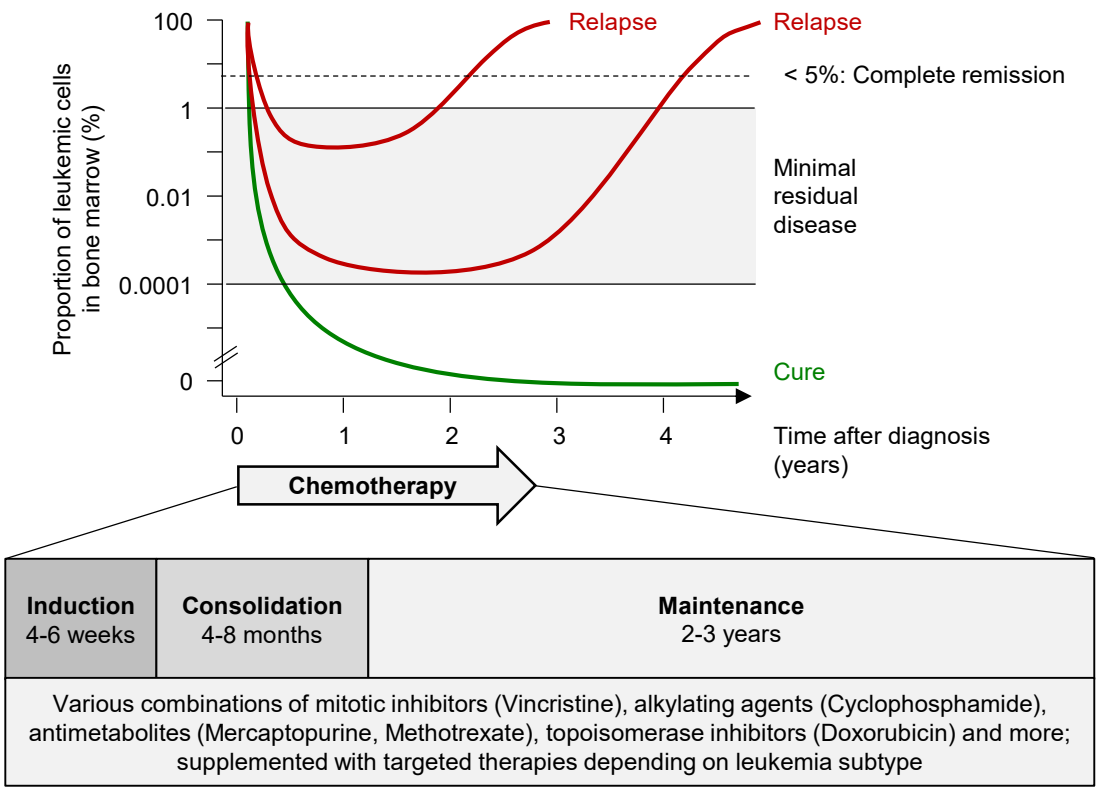

Figure 1: Disease progression upon treatment

Upon diagnosis of ALL, patients harbor a high amount of leukemic cells in the BM. Chemotherapy treatment consists of induction, consolidation and maintenance therapy and covers app. 3 years and various therapy regimens with the aim to cure the patient (green line). In the majority of patients, induction chemotherapy is able to achieve complete remission. However, if residual leukemic cells persist within the BM, patients might eventually suffer from relapse under therapy or at the end of treatment (red lines). The higher the amount of residual cells, the more likely a relapse will happen and the earlier it might occur.

MRD levels have been shown to be an important prognostic factor for overall outcome. 10-year event-free survival in pediatric patients was estimated at 77% in case of negative MRD status in contrast to 32% in case of positive MRD status. Importantly, this was independent from further sub-classifications, e.g. ALL subtype (Berry et al., 2017). In conclusion, the lower the MRD level is, the more susceptible the leukemic population was to treatment initially and the more likely it is that remission will persist and vice versa (Fig. 1).

Approaches to deal with relapse include adaptation of treatment protocols, supplemented with additional treatment options, such as allogeneic hematopoietic stem cell transplantation and CAR T-cell therapy. Long-term benefits of newly developed agents are currently still under investigation, but in general, outcome predictions have not significantly improved within the last decades (Carroll and Hunger, 2016). While initial chemotherapy protocols achieve complete remission in a majority of patients, remission rates upon intensified treatment drop to 30-40% in adults patients with first relapse with even lower rates in following relapses and if relapse occurred during treatment (Gokbuget et al., 2012b).

Because presence of MRD is a major prognostic factor and treatment protocols lack effectivity upon relapse, residual leukemic cells are presumably less responsive to standard chemotherapeutic treatment. Cells inducing a relapse have survived intensive treatment and ultimately re-grown, either during or after completion of treatment (Fig. 1). Although response to secondary treatment approaches is slightly better if relapse happens after treatment, still only 64% of adult patients with late relapses achieve a second complete remission (Gokbuget et al., 2012b). Thus, in both cases, residual cells must harbor or gain alterations, which allow them to survive therapeutic pressure. In line and as mentioned above, MRD levels determine prognosis of patients, independent from other risk stratifications. This suggests that additional factors contribute to relapse, which confer treatment resistance independent from the subtype of ALL.

Taken together, recent advances in treatment strategies have greatly improved the outcome of pediatric ALL patients in the last decades. However, patients still face poor survival rates in case of disease relapse, which is often associated with treatment failure due to resistance. Thus, understanding mechanisms underlying the development of resistance is crucial to improve the outcome of these patients.

1.2 Mechanisms of treatment resistance

Relapse and treatment resistance not only represent major clinical challenges in treatment of ALL, but also in many other types of cancer. Different resistance mechanisms have been described for a variety of therapies and cancer entities, but common features are shared among many of them. In general, resistance might already be present prior to treatment or be acquired due to treatment pressure. In addition, it might involve both tumor-cell intrinsic mechanisms as well as protective mechanisms of the microenvironment. Furthermore, tumor heterogeneity and evolutionary processes influence resistance development.

1.2.1 Resistance to conventional chemotherapy

Treatment resistance to conventional chemotherapeutic drugs is frequently observed across many tumor entities and has been assigned to several mechanisms. In general, on the level of the individual cancer cell, treatment resistance can be achieved by (i) modification of drug uptake and efflux, (ii) prevention of drug activation or increase of inactivation, (iii) alterations in the drug targets, (iv) alterations in the downstream factors of DNA damage and cell death. All of the described options have been observed upon adaptation to various chemotherapeutic drugs (Holohan et al., 2013, Zheng, 2017, Bukowski et al., 2020).

Drug uptake into and efflux from tumor cells is mediated mainly by the ABC transmembrane transporter systems. Upregulation of ABC transporters leads to increased efflux of various chemotherapeutic substrates, but, e.g., does not affect alkylating agents such as Cyclo (Zhang

et al., 2005, Zheng, 2017). While increased drug efflux confers treatment resistance for a broad spectrum of drugs, resistance by inactivation of a drug is highly specific (Holohan et al., 2013). In ALL, specific activating mutations in the nucleotidase NT5C2 result in inactivation of nucleoside analogues, thus causing resistance to 6-mercaptopurine (Tzoneva et al., 2013). Resistance to alkylating agents, such as Cyclo, is associated with upregulation of aldehyde dehydrogenase (ALDH) and components of glutathione metabolism, which both lead to metabolic inactivation. However, this does not seem to affect clinical response, indicating that other mechanisms of resistance are more relevant (Emadi et al., 2009). Alterations in drug targets are observed in resistance to microtubule targeting agents, such as VCR. Here, resistance is associated with changes in expression of individual β-tubulin subtypes, microtubule-associated proteins and the actin cytoskeleton (Verrills et al., 2003, Verrills et al., 2006, Gan and Kavallaris, 2008). Various chemotherapeutic drugs induce DNA damage, which leads to cell cycle arrest and apoptosis. Consequently, major resistance mechanisms induce increased DNA repair capacities or cell cycle progression and evasion of apoptosis despite of persisting DNA damage (Bouwman and Jonkers, 2012, Bukowski et al., 2020). Upregulation of oncogenic signaling pathways, such as pathways activated by EGFR, PI3K/Akt, Erk and NF-kB, and downregulation of pathways activated by p53 are frequently observed upon adaptation to chemotherapy. Concordant downstream effects of these pathways are, among others, blocking of apoptosis by upregulation of anti-apoptotic proteins, e.g. B-cell lymphoma 2 (Bcl-2) (Zheng, 2017). Since the ultimate goal of every chemotherapeutic treatment is cell death, resistance mechanisms against many drugs converge in alterations of p53 and Bcl-2 signaling (Holohan et al., 2013, Bukowski et al., 2020).

Taken together, resistance to some chemotherapeutic drugs with a defined mechanism of action, such as nucleoside analogues, is well understood. In contrast, resistance mechanisms for other drugs with broad mechanisms of action, such as alkylating agents, remain elusive. Even more complex, multidrug resistance mechanisms to combination treatment are often not associated with changes in the individual targets (Pritchard et al., 2013, Bukowski et al., 2020).

Development of chemotherapeutic drugs was achieved app. 50 years ago. Likewise, studies on resistance mechanisms largely have been conducted decades ago (Koelling et al., 1990, Teicher et al., 1990, Hall and Tilby, 1992, Andersson et al., 1996). Since these drugs are still cornerstones of classical ALL treatment, efforts should be made to use recent advances in model systems, multi-omics analyses and genome engineering tools, to gain better understanding of treatment resistance (Gerhards and Rottenberg, 2018). Furthermore, many features of resistance are shared between resistance to cytotoxic therapy and to targeted treatment. Thus, insights on chemotherapy resistance could be of great value for development of more effective targeted treatments (Holohan et al., 2013).

1.2.2 Resistance to targeted therapies

In an effort to individualize treatment strategies and reduce toxicity caused by generalized chemotherapeutic applications, targeted therapies were developed for a broad range of tumor entities and molecular characteristics. Most strategies are based on specific targeting of oncogenic signaling pathways, e.g. by enzymatic inhibitors and antibodies. The success of these approaches is reflected by substantial increase in progression-free survival rates. Strikingly, overall survival rates have not profited and the main reason for this discrepancy is treatment resistance (Groenendijk and Bernards, 2014, Sabnis and Bivona, 2019).

One prominent example for successful establishment of a targeted therapy that was subsequently attenuated by various mechanisms of evolving treatment resistance is Imatinib. It was developed to target the BCR-ABL1 fusion protein, which is characteristic of Ph+ ALL. Expression of BCR-ABL1 leads to constitutive activation of multiple signaling pathways dependent on ABL1 tyrosine kinase activity. Imatinib competitively inhibits the enzymatic activity, thus blocking downstream signaling (Druker et al., 1996). Although initially responding well, the majority of Ph+ ALL patients ultimately suffers from relapse due to resistance (Druker et al., 2001, Lahaye et al., 2005). Resistance is mainly conferred by specific point mutations in the ABL1 kinase domain, which disable binding of Imatinib and consequently restore oncogenic signaling. Furthermore, genomic amplification of BCR-ABL1 was identified (Gorre et al., 2001). To circumvent resistance, variations of Imatinib binding to slightly different residues of the kinase were designed, such as Dasatinib, Nilotinib and Ponatinib. However, specific resistance by a number of different mutations in the binding sites was observed for these treatments as well (Braun et al., 2020).

Resistance mechanisms against Imatinib treatment in Ph+ ALL exemplify the main adaptations of various different cancer types to various different targeted therapies. These include modifications of the drug targets by mutations or alternative splicing, which both inhibit binding of the drug, and upregulation of the drug target by amplification of its genomic locus. In addition, the oncogenic signaling pathway might adapt by downregulation of the drug target, circumvention of the target by activation of parallel signaling pathways, upstream or downstream pathway activation and inactivation of negative regulators (Groenendijk and Bernards, 2014, Sabnis and Bivona, 2019).

In conclusion, development of a single targeted therapy seems to be followed inevitably by multiple different ways of resistance towards this therapy (Braun et al., 2020). Underlying principles are similar to resistance against chemotherapeutic drugs. However, these insights have mostly been obtained retrospectively, while an upfront prediction of the treatment response of a single patient and according adaptation of treatment protocols remains very challenging. Thus, longitudinal studies of individual patients during therapy are needed in

order to gain understanding of resistance development and to ultimately prevent development of resistance (Groenendijk and Bernards, 2014, Sabnis and Bivona, 2019).

1.2.3 Biological characteristics contributing to drug resistance

A number of biological features of cancer cells and their surrounding environment have large impact on drug resistance. The cancer stem cell (CSC) model implies that the majority of cancer cells actively proliferates, while only a subpopulation of CSCs is able to self-renew (Clevers, 2011). These CSCs are characterized by dormancy, i.e. they proliferate very slowly, if at all. Since classical chemotherapy treatment targets proliferating cells, it is believed that therapy often fails because it is not able to target CSCs, which in turn renew the tumor after completion of treatment (Kreso and Dick, 2014). In addition, tumor cells are greatly influenced by their surroundings, i.e. the microenvironment, which for leukemia is the BM niche. The BM niche typically consists of many different cell types of the BM as well as vasculature, immune cells and extracellular matrix. Importantly, in ALL, dormant cancer cells are located mainly in the endosteal niche of the BM and treatment sensitivity is restored when cells are released from the niche (Ebinger et al., 2016). Numerous further studies have shown interaction between tumor cells and the niche, which contributes to treatment resistance (Gilbert and Hemann, 2010, Duan et al., 2014, Bakker et al., 2016, Hawkins et al., 2016, Cahu et al., 2017, Senthebane et al., 2017, Habringer et al., 2018, Witkowski et al., 2020). For example, B-ALL cells alter their immune microenvironment by upregulation of monocytes and recruit mesenchymal cells in response to therapy (Duan et al., 2014, Witkowski et al., 2020).

In summary, stemness features of cancer cells, such as dormancy, and protective factors of the niche contribute to chemotherapy resistance. Stemness defines a small subfraction of the tumor population, indicating that tumors actually consist of heterogeneous populations.

1.2.4 Intratumor heterogeneity and clonal evolution

Presence of CSCs within the tumor population shows that the tumor bulk does not consist of one population of identical tumor cells. In fact, it comprises a dynamic and complex population. Several subpopulations are subject to random mutations, leading to genetic and epigenetic alterations in a heterogeneous manner. These alterations in turn define diverse clones, which undergo evolution and natural selection (Greaves and Maley, 2012). Evolution can not only occur in a linear way with mutations being acquired sequentially, but also in a branched way with multiple mutations being acquired in parallel by different subsets of cells without an order (Ferrando and Lopez-Otin, 2017, Turajlic et al., 2019). Furthermore, epigenetic alterations might be reversible while genetic alterations are most likely irreversible. Clonal evolution leads to intratumor heterogeneity, which in turn provides selective advantages, e.g. in response to treatment pressure. Successful treatment strategies, which

prevent development of resistance, need to account for clonal diversity within the tumor and eliminate all clones (Marusyk et al., 2020).

During leukemia progression and treatment, clonal selection is driven by competition between different leukemic subclones (Ferrando and Lopez-Otin, 2017). Several studies have shown the clinical relevance of clonal diversity for relapse of ALL. Importantly, comparison of matched relapse and diagnosis samples showed that relapse is not simply driven by single mutations but rather by a diversity of alterations (Mullighan et al., 2008). In theory, relapse and resistance can be driven by selection of a pre-existing, resistant subclone (Fig. 2). Alternatively, resistance can evolve due to acquisition of new mutations, either in the major clone of diagnosis, a minor or an ancestor clone. Lastly, different subclones can acquire different mutations, leading to polyclonal evolution of resistance (Dagogo-Jack and Shaw, 2018, Turajlic et al., 2019, Marusyk et al., 2020). All of these possibilities have been described in relapse of ALL (Mullighan et al., 2008, Irving et al., 2005, Choi et al., 2007, Waanders et al., 2020).

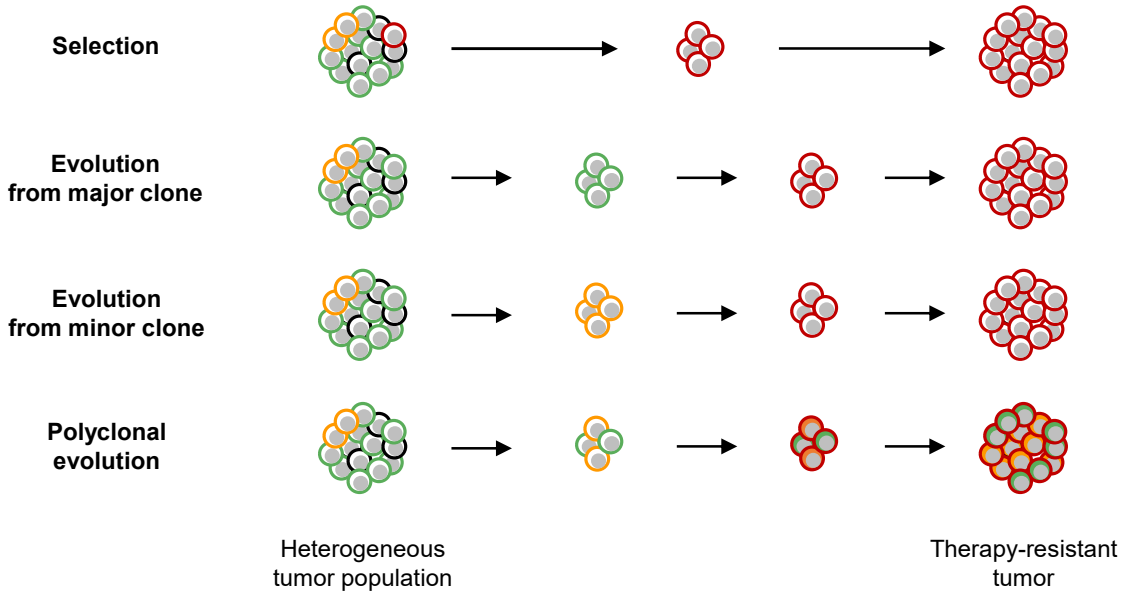

Figure 2: Therapy pressure leads to development of resistance by various mechanisms

In a heterogeneous tumor population, development of resistance can develop via different routes. A minor, pre-existing resistant population might be selected during treatment when all other subpopulations are eradicated. Alternatively, therapy might select an initially sensitive major or minor clone of the tumor population, which then evolves into a therapy resistant population by different mechanisms of adaptation. Lastly, resistance might develop within multiple clones via different routes, leading to polyclonal resistance (Burrell and Swanton, 2014, Dagogo-Jack and Shaw, 2018, Marusyk et al., 2020).

In line with the clonal complexity, no single alteration or mutational signature has been identified, which consistently defines a relapse-fated subclone (Waanders et al., 2020). However, a number of genes have been associated with deletions and mutations, which are increased in relapse, such as *CDNK2A* and *IKZF1* (Maloney et al., 1999, Irving et al., 2005). Likewise, recurrently mutated pathways have been identified, such as lymphoid development, cell cycle regulation, Ras signaling, JAK/STAT signaling, epigenetic modification and

nucleoside metabolism (Ma et al., 2015). Nevertheless, the relevance of these alterations as prognostic markers for relapse remains controversial.

In summary, clonal evolution leads to tumor heterogeneity, which substantially influences development of treatment resistance (Marusyk et al., 2020, Dagogo-Jack and Shaw, 2018). So far, studies have not been able to identify common patterns, which consistently define resistant subclones. While patient cohorts have provided important insight, they are limited in the available time-points during evolution and influenced by inter-patient heterogeneity, which might mask common patterns of treatment resistance. Thus, new investigations rely on the use of accurate tools and model systems for longitudinal studies on evolution of treatment resistance.

1.3 Tools for investigation of drug resistance

In light of the various resistance mechanisms observed in cancer treatment, adequate and innovative tools are needed to improve understanding of treatment resistance and develop new strategies. Current state-of-the-art models include *in vitro* studies in cell lines and analysis of patient material, but studies should also make use of mouse models, recent advances in genome engineering and multi-omics technologies.

1.3.1 Available model systems

Accurate model systems need to mimic the biological characteristics of cancer cells as closely as possible in order to draw reliable conclusions for clinical applications. Routinely, patient material, cell lines and mouse models are used and each model possesses specific advantages and limitations.

Patient samples directly originate from the disease to be analyzed and genomic studies in large patient cohorts have provided important insights into mechanisms of leukemogenesis and generated extensive datasets (Roberts et al., 2012, Anderson et al., 2011, Ma et al., 2018, Downing et al., 2012). Single-nucleotide polymorphism (SNP) arrays and whole exome sequencing have been used to identify copy number alterations (CNA) and mutations between matched diagnosis and relapse samples (Mullighan et al., 2008, Yang et al., 2008, Kawamata et al., 2009, Waanders et al., 2020). A recent study identified several, previously known, relapse-driving mutations along with various mechanisms of clonal evolution in relapsed samples of ALL (Figure 2), but failed to identify a common mutational signature of response to treatment across patients (Waanders et al., 2020). This exemplifies that inter-patient heterogeneity results in a large number of mutations, which hardly allows identifying novel driver alterations in individual patients (Milan et al., 2019). Furthermore, these studies are mainly descriptive and functional investigation of underlying mechanisms is not possible due

to limited cellular material. Thus, functional studies with primary cells remain challenging and better model systems are needed to validate the observations.

Initial data on drug resistance in ALL relapse was obtained from drug tests *in vitro* with patient material (Klumper et al., 1995). However, primary ALL cells hardly survive *in vitro*, which substantially limits the potential of these approaches. Cell lines provide unlimited material, but at the price of additional mutations and reduced heterogeneity, since primarily the most aggressive tumor samples can be used to generate cell lines. Cell lines have contributed to insights about treatment resistance, but major drawbacks need to be considered. Importantly, efficient drug delivery often depends on metabolic activation within the organism. For example, cyclophosphamide requires metabolic activation in the liver, which implies that mechanisms of response and resistance cannot be modeled adequately *in vitro* (Emadi et al., 2009). Furthermore, identical cell lines have shown substantial heterogeneity between different laboratories, as identified by different genetic profiles and different response to identical drug treatment (Ben-David et al., 2018, Liu et al., 2019). In line, drug tests with cell lines are not predictive of treatment response in clinical trials and cell lines do not accurately model the tissue of origin, most likely because of irreversible changes in various characteristics during their establishment (Hidalgo et al., 2014, Gillet et al., 2011). Thus, cell lines are limited in their value for adequate analysis of drug combinations and development of new treatment options and better model systems are needed (Holohan et al., 2013).

To overcome these limitations, preclinical animal models have been established (Hidalgo et al., 2014). Patient-derived xenograft (PDX) models allow implantation and growth of human cancer cells from patients in model organisms *in vivo*. The first PDX model of ALL was described in 1989, when BM samples of ALL patients were engrafted into immunocompromised mice (Kamel-Reid et al., 1989). Since then, the model has been substantially extended and has provided important insights into various aspects of ALL biology.

Current state-of-the-art recipients for the leukemic PDX model are non-obese diabetic (NOD), severe combined immunodeficiency (SCID) Interleukin-2 receptor common γ-chain deficient mice, which lack mature B, T and NK cells, dendritic cells, macrophages and cytokine signaling, hereafter defined as NSG mice (Shultz et al., 2005). Upon intravenous (i.v.) injection of BM aspirates or peripheral blood of patients, human cells home to and proliferate within the murine BM niche, indicating orthotopic growth. Typically, up to 10^7 cells are injected, but few cells are also sufficient and engraftment can also be achieved with cryopreserved samples, providing another technical advantage (Kamel-Reid et al., 1991, Morisot et al., 2010, Meyer and Debatin, 2011, Woiterski et al., 2013, Waanders et al., 2020). Disease progression is accompanied by dissemination of leukemic cells to blood, spleen and peripheral organs, causes clinical signs of disease, such as weight loss, lethargy and rough fur, and ultimately leads to

death of the animals (Kamel-Reid et al., 1989, Kamel-Reid et al., 1991). Leukemic cells can be re-isolated from murine BM and spleen for further analyses and for re-transplantation into next recipient mice, i.e. passaging (Kamel-Reid et al., 1991, Borgmann et al., 2000, Lock et al., 2002).

Numerous studies have shown that the PDX ALL model maintains phenotypic and genotypic characteristics and accurately recapitulates the human disease in various aspects. For example, immunophenotypic surface markers are preserved upon xenotransplantation and subsequent passaging (Baersch et al., 1997, Borgmann et al., 2000, Lock et al., 2002). Furthermore, genomic, transcriptomic and epigenetic profiles are concordant between primary and corresponding xenograft samples (Morisot et al., 2010, Woiterski et al., 2013, Wong et al., 2014, Townsend et al., 2016). Clonal complexity within the tumor population is preserved (Cassidy et al., 2015, Elder et al., 2017), although dominant clones might be selected during passaging (Nijmeijer et al., 2001, Clappier et al., 2011). Importantly, established PDX ALL samples encompass various molecular subtypes, disease stages and risk groups (Townsend et al., 2016). In summary, PDX models represent a suitable tool for investigation of the tumor microenvironment, heterogeneity and treatment response.

Taken together, patient samples are the closest representation of the clinical disease, but are limited in material, while cell lines provide unlimited material but lack the clinical context. The PDX model bridges this gap, since it recapitulates important clinical features and at the same time provides unlimited material for further investigation, thus representing an optimal tool to study mechanisms of drug resistance.

1.3.2 Potential of the genetically engineered PDX model

PDX models bear further unique, technical advantages in preclinical research. A major benefit is the possibility of genetic engineering using lentiviruses, which allows stable expression of transgenes (Fig. 3). Expression of fluorochromes and surface markers, e.g., enables efficient re-isolation from murine tissue and enrichment by fluorescence-activated cell sorting (FACS) and magnetic cell separation (MACS). Specifically, expression of recombinant enhanced firefly luciferase (eFFly) enables bioluminescence imaging (BLI) to reliably monitor tumor burden *in vivo* (Barrett et al., 2011, Terziyska et al., 2012, Bomken et al., 2013, Vick et al., 2015, Jones et al., 2017). BLI is sensitive enough to monitor even minute numbers of residual cells in murine BM (Terziyska et al., 2012, Vick et al., 2015, Ebinger et al., 2016). Furthermore, introduction of knockout, knockdown and overexpression constructs allow specific studies on individual genes and pathways (Liu et al., 2020).

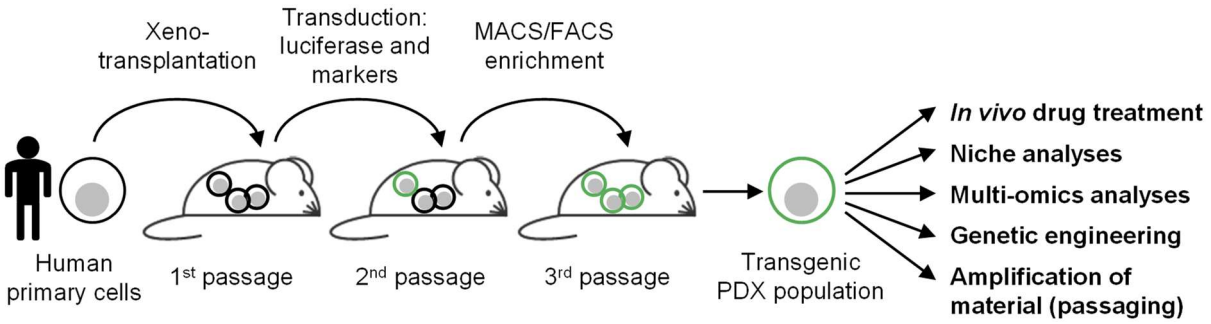

Figure 3: The genetically engineered PDX Model

Xenotransplantation of human primary leukemic cells generates PDX ALL models. Transduction with luciferase and cellular markers and subsequent enrichment generates pure, transgenic PDX populations. These cells enable serial transplantation for drug treatments and analyses of the BM niche *in vivo*, multi-omics analyses, further genetic engineering, e.g. to establish genetic knockouts, and amplification of material by passaging *in vivo*.

In vivo drug treatment of PDX cells allows preclinical testing of novel therapies as well as modelling of established chemotherapy regimens (Lock et al., 2002, Golay et al., 2005, Castro Alves et al., 2012, Samuels et al., 2014, Gao et al., 2015, Ebinger et al., 2016, Yadav et al., 2016, Alruwetei et al., 2020). Here, chemotherapy treatment was mostly applied for a short time period following transplantation of PDX cells (Golay et al., 2005, Gao et al., 2015). Importantly, studies in PDX models of both solid tumors and leukemia have shown concordance between drug response evaluated *in vivo* and observed in the patient (Hidalgo et al., 2014). In contrast to cell lines, PDX treatment studies also accurately resemble effects of metabolism, tumor microenvironment and heterogeneity. For example, they have provided important insights into the relevance of the BM microenvironment and mechanisms of clonal evolution (Duan et al., 2014, Ebinger et al., 2016, Hawkins et al., 2016, Habringer et al., 2018, Dobson et al., 2020, Waanders et al., 2020).

In addition, re-transplantation of PDX cells provides potentially unlimited material for functional studies, genetic engineering and various sequencing approaches, such as genome, transcriptome and proteome analyses. Biological replicates with cells from the same patient allow reliable analysis of individual patients and longitudinal studies of different time points. Taken together, the PDX model holds great potential for reliable studies of mechanisms leading to drug resistance using genetic engineering and *in vivo* treatment.

1.3.3 High-throughput genetic screens

The discovery of the clustered regularly interspaced short palindromic repeats (CRISPR)/ Cas9 system has revolutionized genome engineering and facilitated large-scale, functional genomic screens. CRISPR/Cas9 consists of the two essential components Cas9 enzyme, which is a nuclease, and single-guide RNA (sgRNA), which is complementary to a target region and thus directs Cas9 to its cutting site in the genome. Double-strand breaks induced by Cas9 at the target site lead to activation of cellular repair mechanisms, typically of non-homologous end joining, which is error-prone and frequently generates small insertions or deletions (InDels)

at the cutting sites. Placed in a protein-coding sequence, these InDels often disrupt the reading frame, leading to loss of function, i.e. knockout, of the target gene (Doudna and Charpentier, 2014).

Due to the simplicity and flexibility of the system, genome editing has become widely applicable in cancer biology. Not only does it allow investigation of single genes by targeted knockout, but it also enables high-throughput functional genetic screens. In this setup, libraries comprising different sgRNA sequences are delivered into cell pools in a way that each cell receives one specific sgRNA sequence and thus generates one specific knockout, which can be identified by sequencing of the respective sgRNA (Fig. 4). This has become a powerful tool especially in identification of drug targets and mediators of drug resistance. Selective pressure, e.g. by drug treatment, leads to changes in the abundance of each knockout within the cell pool, which can be identified by amplification and next-generation sequencing (NGS) of the individual sgRNA sequences and comparison of the individual sgRNA read counts to a control group, which does not receive treatment. Knockout of a gene essential for treatment sensitivity would lead to enrichment of this population, while knockout of a gene essential for treatment resistance would lead to depletion of this population upon treatment (Shalem et al., 2015).

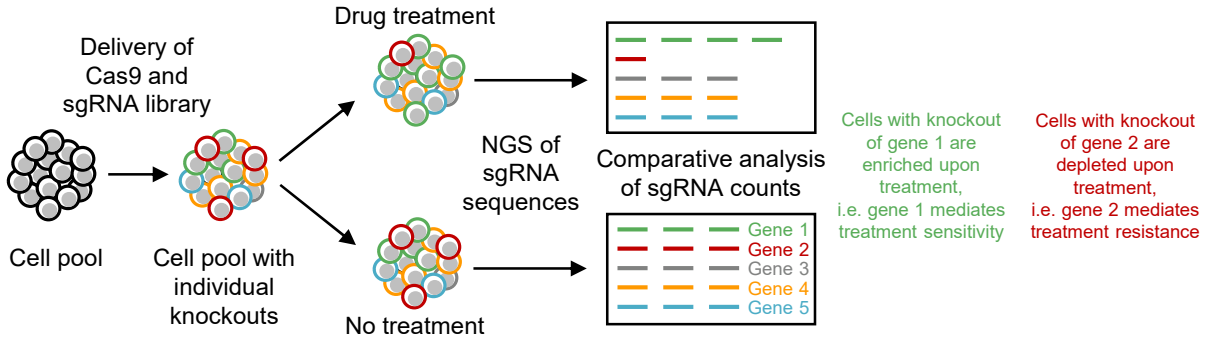

Figure 4: High-throughput CRISPR/Cas9 screening to identify regulators of drug resistance

Cas9 and sgRNA library are delivered into cells to generate cell pools with individual knockouts of target genes. To identify drivers of treatment sensitivity and resistance, cell pools can be equally distributed to two groups, of which one receives treatment. Treatment leads to shifts in the abundance of cells with each knockout, which can be identified by isolation, amplification and NGS of sgRNA sequences. Comparative analysis of sgRNA counts between the two groups allows drawing conclusions about the targeted genes. For example, cells with knockout of gene 1 would be enriched upon treatment, indicating that gene 1 mediates treatment sensitivity, since its knockout leads to advantage upon treatment. Vice versa, cells with knockout of gene 2 would be depleted upon treatment, indicating that gene 2 mediates treatment resistance, since its knockout leads to disadvantage upon treatment.

Already the very first CRISPR/Cas9 genetic screens were designed to identify genes involved in treatment resistance (Shalem et al., 2014, Wang et al., 2014). Since then, screening approaches have been extended to various cell lines and even PDX models. They have provided insight into drug response across a wide range of treatments and cancer entities (Ruiz et al., 2016, Krall et al., 2017, le Sage et al., 2017, Hulton et al., 2020, Lian et al., 2020, Olivieri et al., 2020, Schleicher et al., 2020). However, screening approaches in PDX models *in vivo* remain scarce and technically challenging due to limitation in injected cell numbers (Chow and Chen, 2018). In line, no genetic screens have been carried out to analyze drug resistance in PDX ALL

yet. Still, if technically feasible, they would provide the most clinically relevant insight into mechanisms of drug resistance. In summary, high-throughput genetic screens have become a powerful tool for identification of genes involved in treatment resistance.

1.4 Aim of the project

Treatment resistance determines the prognosis of ALL patients, but the understanding of underlying mechanisms of resistance development remains limited. Thus, gaining deeper insight into those mechanisms in a clinically relevant context is inevitable to improve outcome of patients.

The aim of the present work was to increase understanding of treatment resistance by modelling and characterizing resistance development *in vivo*. To this end, a preclinical model of resistance development was established using long-term *in vivo* chemotherapy treatment in the PDX ALL model. This allowed following resistance acquisition over time, studying cells at different time points during conversion and investigating the underlying mechanisms. At the same time, the *in vivo* model remained close to the clinical context, as PDX cells resemble primary patient cells, while it also allowed determining the relevance of the BM niche on resistance development.

To decipher molecular processes during development of resistance, I investigated transcriptional and genetic profiles of PDX cells and their potential changes under long-term therapy pressure. Differential gene and protein expression analyses can identify targets which could drive the resistant phenotype. Next, these candidates were analyzed in functional validation experiments with the ultimate goal to restore treatment sensitivity. Taken together, the present approach allowed to follow resistance development *in vivo* and to identify underlying mechanisms.

2 Material

2.1 Animals, cell lines and bacterial strains

Table 1: Laboratory animals, cell lines and bacterial strains

Category	Name	Provider
Laboratory animal	NOD.Cg-Prkdc^{scid} Il2rg^{tm1Wjl}/SzJ (NSG) mice	Jackson Laboratory (Bar Harbor, USA)
Cell line	HEK-293T	DSMZ (Braunschweig, Germany)
	NALM-6	DSMZ (Braunschweig, Germany)
Bacterial strain	E.coli DH5α	Thermo Fisher Scientific (Waltham, USA)
	Endura Competent cells	Lucigen (Middleton, USA)

2.2 Plasmids, enzymes and primers

Table 2: Plasmids

Plasmid name	Provider
pCDH-EF1α-eFFly-T2A-eGFP	cloned by Michela Carlet
pCDH-EF1α-eFFly-T2A-mCherry	cloned by Michela Carlet
pCDH-EF1α-NGFR	cloned by Michela Carlet
pCDH-H1-CD19 sgRNA 1-scaffold-EF1α-mtagBFP	cloned by Martin Becker
pCDH-H1-CD19 sgRNA 1-scaffold-EF1α-mtagBFP	cloned by Martin Becker
pCDH-H1-sgRNA-scaffold-EF1α-mtagBFP-H2Kk	cloned by Ehsan Bahrami
pCDH-H1-sgRNAlibrary-scaffold-EF1α-mtagBFP-H2Kk	cloned by Anna-Katharina Wirth
pCDH-SFFV-hSpCas9-T2A-mCherry	cloned by Anna-Katharina Wirth
pMD2.G	Addgene (Cambridge, USA)
pMDLg/pRRE	Addgene (Cambridge, USA)
pRSV-Rev	Addgene (Cambridge, USA)

The oligonucleotide pool containing all sequences for sgRNA library was designed using the pipeline described at www.crispr-clue.de and was ordered from Twist Bioscience (South San Francisco, USA).

Table 3: Enzymes

Enzyme	Manufacturer
BbsI-HF	New England Biolabs (Frankfurt am Main, Germany)
BlpI	Thermo Fisher Scientific (Waltham, USA)
Exonuclease I	Thermo Fisher Scientific (Waltham, USA)
ExTaq Polymerase	Takara Bio Inc. (Kusatsu, Japan)
GoTaq Polymerase	Promega (Madison, USA)
NotI-HF	New England Biolabs (Frankfurt am Main, Germany)
Proteinase K	Thermo Fisher Scientific (Waltham, USA)
SalI-HF	New England Biolabs (Frankfurt am Main, Germany)
T4 DNA Ligase	Thermo Fisher Scientific (Waltham, USA)

Primers were ordered either from Eurofins Genomics (Ebersberg, Germany) or from Sigma Aldrich (St. Louis, USA).

Table 4: Primers

Sequence	Application
TGCGGATCATTCAATACGG	cloning of sgRNA library
CGCCATAACGATGTTTGAG	
GGGGGAAAAGGATCGATT	
CGCATCGTTTACACGTGA	
CTGTATGAGACCACTCTTTCCC	cloning of sgRNA library and amplification of locus for NGS
TGTTTCCAGCATAGCTCTTAAAC	
CGATCTGCAATATTTGCATGTCGC	
ATTCGAATTCGCTAGCTCTAGAGTAGGCGC	
TCCACCATTAGCACCCAAAGC	Finger printing of PDX samples
TCGGATACAGTTCACTTTAGC	
CATAGCGTAAAAGGAGCAACA	Sanger sequencing

Primers for amplification of locus for NGS were extended by individual P5 or P7 Illumina barcode sequences for multiplexing as follows.

Table 5: Illumina barcode sequences

P5 barcode	P5 sequence
N502	CTCTCTAT
N503	TATCCTCT
N510	CGTCTAAT
N511	TCTCTCCG
N513	TCGACTAG
N515	TTCTAGCT
N516	CCTAGAGT
N517	GCGTAAGA
N518	CTATTAAG
N520	AAGGCTAT
N521	GAGCCTTA

P7 barcode	P7 sequence
D705	TTCTGAAT
D706	ACGAATTC
D707	AGCTTCAG
D708	GCGCATTA
D710	TCCGCGAA
D711	TCTCGCGC

2.3 Antibodies

Table 6: Antibodies

Antibody	Manufacturer
anti-human CD19 -APC (HIB19)	eBioscience Inc. (San Diego, USA)
anti-human CD38-PE	BD Biosciences (San Jose, USA)
anti-mouse CD45-APC (30-F11)	BioLegend (San Diego, USA)
anti-mouse H-2Kk-APC	Miltenyi (Bergisch Gladbach, Germany)
anti-mouse IgG1κ-APC isotype control	BD Biosciences (San Jose, USA)
anti-mouse IgG2α-APC isotype control	Miltenyi (Bergisch Gladbach, Germany)

Table 7: MACS beads

MACS beads	Manufacturer
Mouse cell depletion kit	Miltenyi (Bergisch Gladbach, Germany)
MACSelect Kk MicroBeads	Miltenyi (Bergisch Gladbach, Germany)

2.4 Reagents and chemicals

Table 8: Reagents and chemicals

Name	Manufacturer
β-Mercaptoethanol	Sigma Aldrich (St. Louis, USA)
2-propanol	Merck Millipore (Darmstadt, Germany)
Acetic acid	Carl Roth (Karlsruhe, Germany)
Agar-Agar Kobe I	Carl Roth (Karlsruhe, Germany)
Agarose	Invitrogen (Carlsbad, USA)
Ampicillin	Sigma Aldrich (St. Louis, USA)
BSA	Carl Roth (Karlsruhe, Germany)
$CaCl_2$	Carl Roth (Karlsruhe, Germany)
Cut Smart buffer	New England Biolabs (Frankfurt am Main, Germany)
Cyclophosphamide	TEVA GmbH (Ulm, Germany)
D-Luciferin	Biomol GmbH (Hamburg, Germany)
DMEM	Gibco (San Diego, USA)
DMSO	Sigma Aldrich (St. Louis, USA)
DNA ladder	Thermo Fisher Scientific (Waltham, USA)
DNA loading dye	Thermo Fisher Scientific (Waltham, USA)
DNAse I	Thermo Fisher Scientific (Waltham, USA)
dNTPs	Biozym Scientific (Hessisch Oldendorf, Germany)
EDTA (0.5 M)	Lonza (Basel, Switzerland)
Endura recovery medium	Lucigen (Middleton, USA)
Enrofloxacin	Bayer (Leverkusen, Germany)
Ethanol	Carl Roth (Karlsruhe, Germany)
FACS buffer	BD Bioscience (Heidelberg, Germany)
FACS Lysing solution	BD Bioscience (Heidelberg, Germany)
FBS	Gibco (San Diego, USA)
FD buffer	Thermo Fisher Scientific (Waltham, USA)
Ficoll	GE Healthcare (Solingen, Germany)
Glycerin 98%	Carl Roth (Karlsruhe, Germany)
Glycoblue Coprecipitant	Thermo Fisher Scientific (Waltham, USA)
GoTaq reaction buffer	Promega (Madison, USA)
Heparin	Ratiopharm (Ulm, Germany)
Hepes pH 7.4	VWR International (Radnor, USA)
Isoflurane	Sigma Aldrich (St. Louis, USA)
K-Acetate	Sigma Aldrich (St. Louis, USA)

Kanamycin Sulfate	Thermo Fisher Scientific (Waltham, USA)
KCl	Merck Millipore (Darmstadt, Germany)
L-Glutamine	Gibco (San Diego, USA)
Midori Green	Biozym Scientific (Hessisch Oldendorf, Germany)
$MnCl_2$	Sigma Aldrich (St. Louis, USA)
MOPS	Sigma Aldrich (St. Louis, USA)
Na_2HPO_4	Sigma Aldrich (St. Louis, USA)
NaCl	Carl Roth (Karlsruhe, Germany)
Penicillin/Streptavidin (P/S)	Gibco (San Diego, USA)
Polybrene	Sigma Aldrich (St. Louis, USA)
Polyethylenimine	Polysciences (Warrington, USA)
RLT Plus Buffer	Qiagen (Hilde, Germany)
RPMI-1640	Gibco (San Diego, USA)
Selected peptone 140	Gibco (San Diego, USA)
Serum-Free Expansion Medium	Stemcell Technologies (Vancouver, Canada)
T4 DNA Ligase Buffer	Thermo Fisher Scientific (Waltham, USA)
Tris-HCl	Carl Roth (Karlsruhe, Germany)
Trypan blue	Sigma Aldrich (St. Louis, USA)
Trypsine dissociation agent	Gibco (San Diego, USA)
Turbofect	Thermo Fisher Scientific (Waltham, USA)
Venetoclax	Selleck Chemicals Llc (Houston, USA)
Vincristine	Cell Pharm GmbH (Hannover, Germany)
Yeast extract	Carl Roth (Karlsruhe, Germany)

2.5 Buffer and media

Table 9: Buffer

Buffer	**Composition**
Annealing buffer	50 mM Hepes pH 7.4, 100 mM NaCl
LB Medium	1% selected peptone, 0.5% Yeast extract, 1% NaCl
LB Agar	1% selected peptone, 0.5% Yeast extract, 1% NaCl, 1.5% Agar-Agar Kobe I
PBS	140 mM NaCl, 2.7 mM KCl, 10 mM Na_2HPO_4, pH 7.2
SDC buffer	1% SDC, 100 mM Tris pH 8.5, 40 mM CAA, 10 mM TCEP
TAE buffer	40 mM Tris-base, 1 mM EDTA, 20 mM acetic acid
TFB I	100 mM KCl, 10 mM $CaCl_2$, 30 mM K-Acetate, 50 mM $MnCl_2$, 15% Glycerin, pH 5.8
TFB II	10 mM KCl, 75 mM CaCl2, 10 mM MOPS, 15% Glycerin, pH 7.0

Table 10: Cell culture media

Medium	Composition
PDX-ALL culture medium 1	RPMI-1640 supplemented with 20% FCS, 1% P/S, 1% gentamycin and 2 mM glutamine
PDX-ALL culture medium 2	Serum-Free Expansion Medium supplemented with 1% P/S

2.6 Commercial kits

Table 11: Commercial kits

Name	Manufacturer
DNeasy Blood & Tissue Kit	Qiagen (Hilden, Germany)
KAPA HiFi PCR Kit	Roche (Basel, Switzerland)
MinElute PCR purification kit	Qiagen (Hilden, Germany)
NEBuilder HiFi DNA Assembly Master Mix	New England Biolabs (Frankfurt, Germany)
Nextera XT Kit	Illumina (San Diego, USA)
NucleoBond Xtra Maxi Kit	Macherey-Nagel (Düren, Germany)
NucleoBond Xtra Midi Kit	Macherey-Nagel (Düren, Germany)
NucleoSpin Gel and PCR Clean-Up	Macherey-Nagel (Düren, Germany)
NucleoSpin Plasmid Easy Pure	Macherey-Nagel (Düren, Germany)
Phusion High-Fidelity PCR Master Mix	Thermo Fisher Scientific (Waltham, USA)
QIAamp DNA mini kit	Qiagen (Hilden, Germany)
Qubit dsDNA HS Assay	Invitrogen (Carlsbad, USA)
SureSelect Human All Exon V6 Kit	Agilent Technologies (Santa Clara, USA)
Zero Blunt TOPO PCR Cloning Kit	Invitrogen (Carlsbad, USA)

2.7 Consumables

Table 12: Consumables

Consumable	Manufacturer
Amicon-Ultra centrifugal filter units	Merck Millipore (Darmstadt, Germany)
Bacterial tubes	Corning (Corning, USA)
Cell culture EasyFlask T75	Thermo Fisher Scientific (Waltham, USA)
Cell culture flasks (T25, T75)	Greiner bio-one (Kremsmünster, Germany)
Cell strainer	Greiner bio-one (Kremsmünster, Germany)
Centrifuge tubes	Greiner bio-one (Kremsmünster, Germany)
Cryotubes	Thermo Fisher Scientific (Waltham, USA)
Disposable serological pipettes	Greiner bio-one (Kremsmünster, Germany)
Eppendorf reagent tubes	Greiner bio-one (Kremsmünster, Germany)
FACS tubes (with and without filter)	Corning (Corning, USA)
LS columns	Miltenyi (Bergisch Gladbach, Germany)
Microcentrifuge tube, DNA LoBind	Sigma Aldrich (St. Louis, USA)
Microvette	Sarstedt (Nürmbrecht, Germany)

Needles RN G32 PST3 51MM	Hamilton (Reno, USA)
PCR tubes	Sigma Aldrich (St. Louis, USA)
Petri dishes	Greiner bio-one (Kremsmünster, Germany)
Pipette tips (with and without filter)	Starlab (Hamburg, Germany)
Square BioAssay dish	Thermo Fisher Scientific (Waltham, USA)
Well plates for tissue culture	Corning (Corning, USA)

2.8 Equipment

Table 13: Special equipment

Equipment	Manufacturer
Bioanalyzer 2100	Agilent Technologies (Santa Clara, USA)
Cell sorter BD FACS AriaIII	BD Biosciences (San Jose, USA)
Flow cytometer BD LSRFortessa X20	BD Biosciences (San Jose, USA)
Gel documentation station E-box VX5	Peqlab (Erlangen, Germany)
Illumina HiSeq 1500	Illumina (San Diego, USA)
IVIS Lumina II Imaging System	Caliper Life Sciences (Mainz, Germany)
Nanodrop OneC	Thermo Fisher Scientific (Waltham, USA)
Nanoflow EASY-nLC1000 HPLC	Thermo Fisher Scientific (Waltham, USA)
Q Exactive HF-X Hybrid Quadrupole-Orbitrap Mass Spectrometer	Thermo Fisher Scientific (Waltham, USA)
Quietek CO2 Induction Systems	Next Advance (Troy, USA)

2.9 Software

Table 14: Software

Software	Provider
FlowJo 10	FlowJo LLC (Ashley, USA)
Geneious 11	Biomatters Ltd (Auckland, New Zealand)
GraphPad Prism 7	Graphpad Prism (La Jolla, USA)
Integrative Genomics Viewer	Broad Institute (Cambridge, USA)
Living Image Software 4.4	PerkinElmer (Krakow, Poland)
Maxquant 1.5.5.2	MPI Biochemistry (Planegg, Germany)
Microsoft Office 2016	Microsoft Corporation (Tulsa, USA)
MyIMouse	Bioslava (Hagenbach, Germany)
Python	Python Software Foundation (Wilmington, USA)
RStudio (R version 3.6.1)	Rstudio, Inc. (Boston, USA)

3 Methods

3.1 Ethical statements

3.1.1 Patient material

Fresh ALL patient material was obtained from peripheral blood or bone marrow aspirates. For this study, residual material of clinical routine diagnostics at the time of primary or relapse diagnosis before the respective start of treatment was used.

As all patients were minors, written informed consent was obtained from all parents/carers. The study was performed in accordance with the ethical standards of the responsible committee on human experimentation (written approval by Ethikkommission des Klinikums der Ludwig-Maximilians-Universität München, Ethikkommission@med.uni-muenchen.de, April 2008, number 068-08, and September 2010, number 222-10) and with the Helsinki Declaration of 1975, as revised in 2000.

3.1.2 Animal work

NSG mice were maintained in the research animal facility of the Helmholtz Zentrum München (Munich, Germany). Mice were kept under pathogen-free conditions on a 12 h light-dark cycle with constant temperature and food and water *ad libitum*.

All animal trials were performed in accordance with the current ethical standards of the official committee on animal experimentation (written approval by Regierung von Oberbayern, poststelle@reg-ob.bayern.de, 55.2-1-54-2532-7-2016 and 55.2-1-54-2532.0-56-2016).

3.2 Xenograft mouse model of acute lymphoblastic leukemia

Acute lymphoblastic leukemia was studied based on the well-established individualized PDX mouse model (Kamel-Reid et al., 1989, Liem et al., 2004, Lee et al., 2007, Ebinger et al., 2016).

3.2.1 PDX cell engraftment

Up to 1 x 10^7 fresh or thawed PDX ALL cells were re-suspended in 100 µl sterile-filtered PBS and injected into 6 - 8 weeks old NSG mice via tail vein injection. 2.5% Enrofloxacin was added to the drinking water of mice to prevent infection from injection. Engraftment of human cells was monitored by regular flow cytometry measurement of human cells in peripheral blood (see 3.2.2) or by BLI (see 3.2.3).

Mice were left untreated for expansion of transgenic PDX cells or received chemotherapy treatment (see 3.2.4). Mice were sacrificed (see 3.2.5) at defined time-points, at signs of advanced leukemia or at signs of clinical disease and human cells were re-isolated from spleen or bone marrow (see 3.2.6 and 3.2.7).

3.2.2 Quantification of leukemia growth in murine peripheral blood

Leukemic burden of mice which were not included in therapy trials was monitored by flow cytometric analysis of human cells in murine peripheral blood. App. 50 µl blood was collected from the tail vein using a heparin-coated glass capillary and transferred to a reaction tube containing 5 µl Heparin. Cells were incubated for 30 min at room temperature (RT) with 1:100 anti-human CD38 conjugated with phycoerythrin (PE) and 1:100 anti-mouse CD45 conjugated with allophycocyanin (APC). Subsequently, erythrocytes were lysed using 1 ml FACS Lysing solution (15 min, RT). Samples were washed twice using 3 ml FACS buffer (300 g, 5 min, RT) and measured by flow cytometry (see 3.3.7). The amount of human and murine cells was analyzed using FlowJo software.

3.2.3 Bioluminescence *in vivo* imaging

Transgenic PDX ALL cells were generated to express the recombinant codon-optimized form of eFFly. This allowed quantification of leukemic cells by BLI as previously described (Rabinovich et al., 2008, Barrett et al., 2011, Terziyska et al., 2012, Bomken et al., 2013). Mice were routinely monitored weekly or in every other week.

Mice were anesthetized using isoflurane and placed into the imaging chamber of the IVIS Lumina II Imaging System (Caliper Life Sciences, Mainz, Germany). 150 mg/kg D-Luciferin dissolved in sterile PBS was applied by intravenous or intraperitoneal injection. Bioluminescent signal was recorded immediately using a field of view of 12.5 cm, binning 8, f/stop 1 and open filter setting. Quantification of the bioluminescence signal was performed using Living Image Software 4.4.

3.2.4 *In vivo* chemotherapy treatment

Chemotherapeutic drugs of routine clinical regimens were applied in the PDX ALL model to generate and study drug resistant PDX cells. Treatment was started after successful engraftment of PDX ALL cells at a defined leukemic burden or at defined time points, as indicated in the results section. Mice were treated systemically with VCR i.v. once per week and/or with Cyclo i.p. once per week and/or with Venetoclax p.o. five times per week. Drugs were diluted in sterile PBS for efficient application. Animals of the control groups were either treated with PBS in the same route of administration or left untreated.

Drug concentrations were calculated from clinically relevant concentrations converting the human doses to mouse equivalent doses based on body surface area and differences in metabolism as previously described (Sharma and McNeill, 2009, Nair and Jacob, 2016, Ebinger et al., 2016). Drug dosages of VCR and Cyclo were further optimized for each PDX sample individually in order to enable significant treatment response and minimize treatment toxicity:

PDX sample	VCR dosage	Cyclo dosage
ALL-50	0.25 mg/kg	70 mg/kg
ALL-199	0.15 mg/kg	70 mg/kg
ALL-265	0.3 mg/kg	70 mg/kg

In all combination treatment experiments, VCR was applied two days prior to Cyclo. Venetoclax was applied in ALL-199 p.o. with 100 mg/kg. In combination treatment of all three drugs, Venetoclax was applied on days 1-5, VCR on day 3 and Cyclo on day 5. Mice were closely monitored to prevent signs of treatment toxicity and sacrificed as soon as clinical signs of sickness became apparent (weight loss, rough fur, reduced motility, hunchback).

3.2.5 Sacrificing mice by CO_2 exposure

Mice were sacrificed either at pre-defined time points of the experiment or at confirmed stage of advanced leukemia or at first clinical signs of disease. Mice were killed by CO_2 asphyxiation using Quietek CO_2 Induction Systems followed by cervical dislocation. First, mice were anesthetized using a flow rate of 750 ml/min (i.e. 10% of the chamber volume per minute) for one minute, followed by 2,250 ml/min (i.e. 30% of the chamber volume per minute) for four minutes. Clinical death was verified by testing of reflex movements and organs were dissected for further analyses (see 3.2.6 and 3.2.7).

3.2.6 Isolation of PDX cells from spleen

Highly advanced leukemia is accompanied by spleen enlargement due to enrichment of ALL cells. To isolate leukemic cells, the spleen was dissected, homogenized by squashing in a 70 µm cell strainer and the cell suspension was supplemented with PBS. To enable efficient separation of the individual cell types, 10 ml Ficoll was added and a density gradient was created by centrifugation (400 g, 30 min, RT, no brake). The interphase layer of the Ficoll density gradient containing mononuclear cells was carefully aspirated. Cells were washed twice with PBS (400 g, 5 min, RT) and resuspended in the required buffer or cell culture medium depending on the desired application.

3.2.7 Isolation of PDX cells from bone marrow

For isolation of PDX cells from murine bone marrow, femora, tibiae, hip, spine and sternum was dissected and crushed using mortar and pestle. Cells were suspended in PBS and bone remnants were removed by filtering (70 µm cell strainer). After washing (400 g, 5 min, RT), cells were resuspended in the required buffer or cell culture medium depending on the desired application.

3.3 Cell culture methods

3.3.1 Maintenance of PDX *ex vivo*

For *ex vivo* culture, freshly isolated or thawed PDX ALL cells were maintained using PDX ALL culture medium 1 or 2 (see 2.5). Cells were seeded at a density of 1 x 10^7 per ml in 6-well plates and incubated at 37 °C and 5% CO_2. Fresh medium was added every 2-3 days and cells were maintained *ex vivo* for up to 14 days.

3.3.2 Maintenance of cell lines

NALM-6 cell line cells were maintained at a density of 0.5–2 x 10^6 cells/ml in RPMI supplemented with 10% FBS and 1% Glutamin at 37 °C and 5% CO_2 and passaged 1:10 every 2-3 days.

HEK293T cells were cultured at 0.5–2 x 10^6 cells/ml in DMEM supplemented with 10% FBS and 1% Glutamin at 37 °C and 5% CO_2. For passaging, medium was removed, cells were washed with PBS and dissociated using 0.05% trypsin-EDTA. Cells were resuspended in DMEM, diluted 1:10 and seeded into 75 cm^2 flasks.

3.3.3 Cell counting

PDX cell numbers were counted using a Neubauer chamber. An aliquot of cell suspension was diluted 1:10 - 1:1000, stained 1:10 with trypan blue and counted. Cell numbers were calculated as follows:

$$Number\ of\ cells\ per\ ml = mean\ (counted\ cells)\ \times dilution\ factor\ \times\ 10^4$$

3.3.4 Cryopreservation of PDX ALL and cell lines

Cell pellets of freshly isolated cells from spleen or bone marrow or cultivated cell lines were resuspended in one part FBS. Then, one part of freezing medium (80% FBS, 20% DMSO) was carefully added to the cell suspension. Cells were transferred to cryopreservation tubes at aliquots ranging from 10,000 cells up to 1/3 of entire bone marrow per ml. Tubes were placed into a freezing container containing 2-propanol to ensure a slow cooling rate of 1 °C/min for freezing at -80 °C. For long-term storage, cells were transferred to -196 °C.

PDX ALL cells and cell line cells were thawed rapidly at 37 °C to obtain high viability. Cell suspension was immediately washed using 10 ml PBS (400 g, 5 min, RT) and resuspended in culture medium or the required buffer for further use.

3.3.5 Lentivirus production

Third-generation lentiviral particles were produced using HEK293T cells. Cells were seeded at 50-80% confluency into 75 cm² adherent cell culture flasks containing 10 ml DMEM + 10% FCS. Packaging plasmids, transfer plasmids and transfection reagent were mixed as follows:

1 ml	DMEM
24 µl (or 34 µl PEI)	Turbofect (or PEI 1 mg/ml)
2.5 µg	pRSV-Rev
5 µg	pMDLg/pRRE
1.25 µg	pMD2.G
2.5 µg	pCDH transfer plasmid

After 20 min incubation at RT, HEK293T cells were transfected with the plasmid mix and incubated for virus production (3 days, 37 °C, 5% CO_2). Then, supernatant containing viral particles was transferred to a Falcon and cell debris was removed by centrifugation (400 g, 5 min, RT) and filtering (0.45 µm filter). Virus supernatant was concentrated by ultrafiltration using Amicon-Ultra 15 ml and centrifugation (2,000 g, 30 min, RT). Virus concentrate was directly used for transduction or stored at -80 °C until further use.

3.3.6 Lentiviral transduction

Lentiviral particles were used for genetic engineering of PDX cells and testing of virus titer in NALM-6 cell lines.

The functional titer of virus was analyzed by transduction of NALM-6 cells with serial dilutions of virus, followed by analysis of transgene expression by flow cytometry. To this end, NALM-6 cells were seeded at a density of 1 x 10^6 cells/ml in a 24-well cell culture plate, transduced with various amounts of virus together with 8 µg/ml polybrene and incubated overnight (37 °C, 5% CO_2). On the next day, cells were washed three times with PBS (400 g, 5 min, RT). Transgene expression was analyzed three days after transduction by flow cytometry (see 3.3.7).

For transduction of PDX cells, cells were seeded to a 6-well cell culture dish containing 1 ml medium and 8 µg/ml polybrene per well. Subsequently, virus was added and cells were incubated overnight (37 °C and 5% CO_2). On the next day, virus remnant was removed by washing with PBS (400 g, 5 min, RT) and cells were cultivated further in 1.5 ml medium per 1 x 10^7 cells for a maximum time of 14 days.

3.3.7 Flow cytometry

Flow cytometric analysis was performed using a BD LSRFortessa X-20 (BD Bioscience, Hamburg, Germany). Analysis was based on gating for viable lymphocytes (FSC, SSC) and expression of fluorochromes (mCherry, eGFP, mtagBFP) or antibody-conjugated fluorochromes (APC, PE) using the following laser and filter settings:

Table 15: Configuration of LSRFortessa X-20

Laser	Excitation [nm]	Long pass filter	Bandpass filter	Parameter
Violet	405		405/50	mtagBFP
Blue	488	505	530/30	eGFP
			488/10	SSC
Yellowgreen	561	600	610/20	mCherry
		505	586/15	PE
Red	640		670/30	APC

Data analysis was performed using FlowJo software. To quantify the percentage of PDX cells in murine bone marrow, a small aliquot of isolated bone marrow (>10,000 cells) was analyzed by flow cytometry. Gating was performed based on viable lymphocytes and transgene expression (Figure 5).

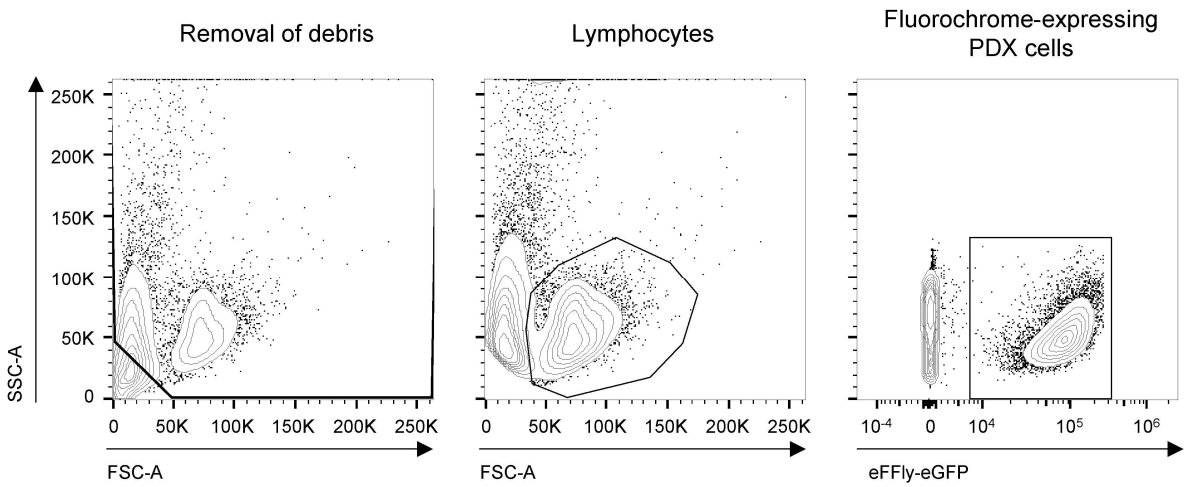

Figure 5: Exemplary gating on fluorochrome-expressing PDX cells

Cell debris was excluded in FSC-A/SSC-A, followed by gating on lymphocytes. Next, cells were gated for the fluorochrome co-expressed with enhanced firefly (eFFly) luciferase (eGFP for ALL-199) to identify the PDX population. Number of events in this gate divided by number of events after removal of debris was used to calculate percentage of PDX in murine bone marrow. The percentage of fluorochrome+ PDX cells was used throughout the study as readout for therapy response of PDX.

Percentage of leukemic cells in bone marrow was calculated as follows:

$$Proportion_{\ PDX\ in\ BM}[\%] = \frac{count_{\ fluorochrome-expressing\ lymphocytes}}{count_{\ all\ events\ excluding\ debris}} \times 100$$

3.3.8 Flow cytometry staining

Expression of human CD19 and transgenes such as H2Kk was analyzed by antibody staining. 0.1–1 x 10^6 cells were resuspended in 100 µl PBS. Antibody was added in the respective dilution (1:25 or 1:50), mixed well and incubated (15 min, 4 °C, dark). Cells were washed twice with PBS (400 g, 5 min, RT) and analyzed by flow cytometry (see 3.3.7).

3.3.9 Enrichment of PDX cells by magnetic cell separation

Magnetic cell separation (MACS) was used for enrichment of small numbers of PDX from the murine bone marrow and for efficient enrichment of transduced PDX cells.

Enrichment of small fractions of PDX cells from murine bone marrow was facilitated using negative selection by mouse cell depletion kit (Miltenyi, Bergisch Gladbach, Germany). Following isolation of murine bone marrow or thawing, cells were resuspended in 3 ml PBS + 0.5% BSA, filtered (70 µm cell strainer) and incubated using 100–400 µl mouse cell depletion beads (15 min, 4 °C, dark). LS columns were placed into a magnet and washed using PBS + 0.5% BSA. 10 ml PBS + 0.5% BSA was added to the cell suspension and the mix was loaded onto the column. Columns were washed twice with PBS + 0.5% BSA and flow-through containing human PDX cells was collected, washed (400 g, 5 min, RT) and re-suspended in buffer depending on the desired application.

Transduced PDX cells positive for H2Kk were enriched by positive selection using MACSelect K^k System (Miltenyi, Bergisch Gladbach, Germany). Cell pellets were resuspended in 480 µl PBS + 0.5% BSA per 1 x 10^7 cells, filtered (70 µm cell strainer) and 20 µl MACSelect K^k beads were added. Mix was incubated (15 min, RT, dark). LS columns were placed into a magnet and washed using PBS + 0.5% BSA. Cell suspension was filtered again (30 µm cell strainer) and loaded onto the column. After washing twice with PBS + 0.5% BSA, the positive fraction was recovered by applying 5 ml PBS + 0.5% BSA onto the column and immediately flushing the cell out using a plunger.

3.3.10 Enrichment of PDX cells by fluorescence-activated cell sorting

PDX cells were enriched based on expression of a fluorochrome marker (mCherry, mtagBFP, eGFP) using a cell sorter BD FACS AriaIII (BD Bioscience, Heidelberg, Germany). Cells were resuspended in PBS and filtered prior to sorting. Gating was performed based on viable lymphocytes and transgene expression (Figure 5).

Table 16: Configuration of FACS AriaIII

Laser	Excitation [nm]	Long pass filter	Bandpass filter	Parameter
Violet	405		450/40	mtagBFP
Blue	488	502	530/30	eGFP
			488/10	SSC
Yellowgreen	561	600	610/20	mCherry

3.4 Microbiology methods

3.4.1 Generation of competent E.coli DH5α

100 ml LB medium was inoculated with 1 ml of E.coli DH5α overnight culture. At an OD_{600} of 0.4-0.5 nm, bacteria suspension was cooled down and pelleted (4,000 g, 5 min, 4 °C). Bacteria pellets were resuspended in 15 ml TFB I buffer, incubated (5 min, 4 °C), centrifuged (4,000 g, 5 min, 4 °C) and resuspended in 4 ml TFB II buffer. Aliquots were stored at -80 °C until further use.

3.4.2 Heat shock transformation

Plasmid DNA was amplified by heat shock transformation and expansion of chemically competent DH5α bacteria. 5 µl ligation product or 50-100 ng of plasmid DNA was gently added to 50 µl DH5α and incubated (30 min, on ice), followed by heat shock (90 s, 42 °C) and incubation (2 min, on ice). 400 µl LB-medium was added and the bacteria suspension was incubated (45 min, 37 °C, shaking). Aliquots were plated onto LB_{Amp} agar plates and incubated overnight at 37 °C to grow bacterial colonies. On the next day, single colonies were picked, transferred into LB_{Amp} medium and incubated for further expansion (overnight, 37 °C, shaking). Subsequently, cell suspension was collected for isolation of plasmid DNA (see 3.5.8).

3.4.3 Transformation by electroporation

sgRNA library plasmids were transformed into Endura electrocompetent bacteria by electroporation. 2 µl DNA were carefully mixed with 25 µl of Endura bacteria. Bacteria-DNA suspension was transferred to a pre-chilled electroporation cuvette and electroporated (settings: 1.8 kV, 600 Ohm, 10 µF). Bacteria were immediately resuspended with 975 µl Recovery medium, transferred to a fresh tube and incubated (1 h, 37 °C, shaking). Bacteria suspension was plated onto 245 mm square agar dishes containing LB Agar supplemented with Ampicillin for pCDH backbone or LB Agar supplemented with Kanamycin for Topo plasmid backbone and incubated overnight at 37 °C. On the next day, all bacterial colonies were floated off using LB medium and cell suspension was collected for isolation of plasmid DNA (see 3.5.8).

3.5 Molecular biology methods

3.5.1 Annealing of oligonucleotides

For cloning of individual sgRNAs into lentiviral backbone, single-strand oligonucleotides (oligos) covering sgRNA and adjacent nucleotides to enable cloning were ordered from Eurofins Genomics (Ebersberg, Germany) or Sigma-Aldrich (St. Louis, USA). Complementary oligo strands were annealed with the following setup:

1 µl	Forward Oligo
1 µl	Reverse Oligo
18 µl	Annealing buffer

Reaction was incubated at 95 °C for 5 min and cooled to 25 °C (ramp down 0.1 °C per s). Annealing created double-stranded oligos including 5' and 3' overhangs compatible for ligation with overhangs created by BpiI restriction digestion. Annealed oligos were diluted 1:100 for subsequent ligation.

3.5.2 Restriction digestion

Expression constructs of hSpCas9 and sgRNAs were created by restriction cloning. Plasmids were digested at 37 °C for 1 h using either one or two different restriction enzymes.

2 µg	Plasmid
2 – 10 U	Enzyme
2 µl	10x digestion buffer
ad 20 µl	H_2O

Digested DNA fragments were either separated by agarose gel electrophoresis (see 3.5.6) or directly purified using NucleoSpin Gel and PCR Clean-up kit (Macherey-Nagel, Düren, Germany) according to the manufacturer's instruction.

3.5.3 Ligation

Annealed oligonucleotides or digested DNA fragments were ligated into digested lentiviral backbones containing complementary overhangs. 50 ng of vector backbone was ligated with vector insert in 1:3 molar ratio. Amount of vector insert was calculated as follows:

$$mass_{\,vector\ inser}\ [ng] = \frac{size_{\,vector\ insert}\ [kb]}{size_{\,vector\ backbone}\ [kb]} \times mass_{\,vector\ backbone}\ [ng] \times molar\ ratio$$

Diluted oligos were ligated using 1 µl oligos and 50 ng vector backbone. Ligation was performed as indicated (22 °C, 2 h).

50 ng	Plasmid backbone
X ng	Plasmid insert
1 µl	T4 DNA ligase
1 µl	10x ligase buffer
ad 10 µl	H_2O

3.5.4 Cloning of sgRNA library

Cloning of sgRNA library was performed as previously described (Becker et al., 2020). In brief, five sgRNA sequences per target and control gene were chosen based on well-established genome-wide libraries (Doench et al., 2016, Sanson et al., 2018, Kim et al., 2018). Adapter

sequences compatible for amplification and cloning were added *in silico* and a lyophilized pool of double-stranded DNA oligonucleotides containing all library sequences and additional libraries was ordered from Twist Bioscience (South San Francisco, USA). In a first amplification step, the reconstituted pool was amplified by PCR as recommended by the manufacturer's instructions using universal primers amplifying all libraries (see 3.5.11). Cloning into a TOPO vector enabled unlimited amplification (see 3.5.5). Library composition of the TOPO library plasmid was verified by NGS (see 3.5.12, 3.6.2).

Next, library-specific primers were used for targeted PCR amplification of the desired sequences (see 3.5.11). Resulting PCR products were purified and subjected to a second PCR to generate fragments ready for cloning into lentiviral sgRNA expression backbone. For both steps, several PCR reactions were run in parallel and pooled to ensure a sufficient amplification of all 1,196 oligos of the library without generating bias by overrepresentation of individual sgRNAs. In parallel, lentiviral backbone plasmid was digested using BpiI as described above (see 3.5.2). Digested fragment and library insert were cloned with Gibson assembly (see 3.5.6), transformed into bacteria by electroporation (see 3.4.3) and re-isolated by Maxi prep (see 3.5.8). sgRNA distribution within the library was analyzed by NGS (see 3.5.12, 3.6.2).

3.5.5 TOPO cloning

Amplified oligonucleotide DNA from library cloning was subjected to TOPO cloning using Zero Blunt TOPO PCR Cloning Kit (Invitrogen, Carlsbad, USA) with the following setup:

2 µl	PCR product
1 µl	Topo plasmid
1 µl	Salt Solution
2 µl	H_2O

To ensure sufficient coverage of each oligonucleotide, two independent reactions were performed in parallel. Reactions were incubated (30 min, RT), pooled and DNA was precipitated (see 3.5.10) and subjected to electroporation (see 3.4.3). After Maxi prep of plasmid DNA (see 3.5.8), a control PCR reaction was performed according to the manufacturer's instructions with the following setup:

PCR reaction	
5 µl	5x reaction buffer
50 ng	Plasmid
0.5 µl	M13 forward primer (375 nM)
0.5 µl	M13 reverse primer (375 nM)
2 µl	dNTPs
0.15 µl	GoTaq Polymerase
ad 25 µl	H_2O

Cycler conditions		
Temperature	Time	Cycles
95 °C	2 min	1
95 °C	30 s	25
45 °C	30 s	
72 °C	20 s	
72 °C	5 min	1

3.5.6 Gibson assembly

Library oligonucleotides amplified by PCR were cloned into digested lentiviral backbone using Gibson assembly. Reaction was prepared as follows and incubated at 50 °C for 1 h.

5 µl	2x Gibson MasterMix
1 µl	Plasmid backbone
1 µl	Insert
ad 10 µl	H_2O

3.5.7 Agarose gel electrophoresis

To determine and separate DNA fragment sizes, agarose gel electrophoresis was performed. Agarose gels were prepared by heating TAE buffer containing 1-2% agarose. 0.01% Midori Green was added and the gel was polymerized in a gel chamber. DNA Samples were mixed with loading dye and loaded onto the gel together with a 1 kb DNA ladder to determine fragment sizes. Gel electrophoresis was performed in TAE buffer (30 - 40 min, 100 V) and DNA fragment sizes were analyzed using a gel documentation station. For restriction cloning purposes, DNA fragments were cut from the gel and DNA was purified using NucleoSpin Gel and PCR Clean-up kit (Macherey-Nagel, Düren, Germany) according to the manufacturer's instruction.

3.5.8 Isolation of plasmid DNA

Depending on the amount of bacterial suspension, plasmid DNA was isolated using NucleoSpin Plasmid Easy Pure, NucleoBond Xtra Midi or NucleoBond Xtra Maxi Kit (all Macherey-Nagel, Düren, Germany) according to the manufacturer's instructions.

3.5.9 Isolation of genomic DNA

Genomic DNA from up to 1 x 10^7 fresh or thawed PDX cells was isolated using the QIAamp DNA Mini Kit (Qiagen, Hilden, Germany) according to manufacturer's instructions. DNA concentration and quality was analyzed using a NanoDrop (Thermo Fisher Scientific, Waltham, USA).

3.5.10 DNA precipitation

During library cloning, plasmid and PCR fragment DNA was precipitated for purification. DNA was mixed 1:1 (v/v) with 2-Propanol, supplemented with 1% 5 M NaCl and 0.5% Glycoblue. Mix was incubated (15 min, RT) and centrifuged (full speed, 15 min, RT). Supernatant was discarded, DNA pellet was washed twice using 1 ml 80% Ethanol (full speed, 5 min, RT). Supernatant was removed and DNA was re-suspended in H_2O.

3.5.11 Amplification of DNA for cloning

Oligonucleotide pools were amplified by PCR to enable library cloning into lentiviral backbones (see 3.5.4). Optimal annealing temperature for each primer pair was determined by gradient PCR. PCR was set-up using KAPA HiFi Kit (Roche, Basel, Switzerland) with the following protocol:

PCR reaction	
5 µl	5x KAPA HiFi buffer
50 pg – 800 ng	Template DNA
0.75 µl	Forward primer (10 µM)
0.75 µl	Reverse primer (10 µM)
0.75 µl	KAPA dNTP Mix
0.5 µl	KAPA HiFi Polymerase
ad 25 µl	H_2O

Cycler conditions		
Temperature	Time	Cycles
98 °C	30 s - 3 min	1
98 °C	5-30 s	15-30
62 °C	15 s	
72 °C	1-20 s	
72 °C	1-2 min	1

Correct PCR product size was verified by analysis of an aliquot by agarose gel electrophoresis (see 3.5.7). Remaining PCR product was purified using NucleoSpin Gel and PCR Clean-up kit (Macherey-Nagel, Düren, Germany) according to the manufacturer's instructions. DNA quantity was measured using a NanoDrop (Thermo Fisher Scientific, Waltham, USA).

3.5.12 Amplification of plasmid DNA for NGS

Library composition of the cloned library plasmid pool was analyzed by NGS as previously described (Becker et al., 2020). For analysis of the plasmid pool from both TOPO plasmid and lentiviral backbone, a single PCR was run to amplify the sgRNA sequence. PCR was set up with primers containing Illumina adapters and barcodes to facilitate sequencing and the following protocol:

PCR reaction	
10 µl	5x KAPA HiFi buffer
50 pg	Plasmid DNA
1.5 µl	P5-H1_f primer (10 µM)
1.5 µl	P7-EF1a_r primer (10 µM)
1.5 µl	KAPA dNTP Mix
1.5 µl	KAPA HiFi Polymerase
ad 50 µl	H_2O

Cycler conditions		
Temperature	Time	Cycles
98 °C	3 min	1
98 °C	30 s	30
62 °C	15 s	
72 °C	20 s	
72 °C	2 min	1

PCR products were purified using NucleoSpin Gel and PCR Clean-up kit (Macherey-Nagel, Düren, Germany) according to the manufacturer's instructions and subjected to NGS (see 3.6.2).

3.5.13 Amplification of genomic DNA for NGS

For analysis of *in vivo* screens by NGS, genomic DNA (gDNA) was isolated from PDX cells (see 3.5.9) and amplified using a nested PCR approach to efficiently amplify the integrated sgRNA sequence from gDNA. The necessary amount of gDNA input was calculated as follows:

$$mass\ (template\ DNA) = library\ size\ \times coverage\ (cells/sgRNA) \times mass\ (gDNA/cell)$$

$$mass\ (template\ DNA) = 1196\ \times 500\ \times 6.6\,pg = 3.95\ \mu g$$

The first PCR was run with the following setup and two reactions per sample to ensure sufficient coverage of individual sgRNA sequences:

PCR reaction	
5 µl	10x reaction buffer
up to 2 µg	Template DNA
2.5 µl	Forward primer (10 µM)
2.5 µl	Reverse primer (10 µM)
4 µl	dNTPs
0.5 µl	ExTaq Polymerase
ad 50 µl	H_2O

Cycler conditions		
Temperature	Time	Cycles
95 °C	5 min	1
95 °C	30 s	28
62 °C	30 s	
72 °C	20 s	
72 °C	10 min	1

After the first PCR, PCR products from identical samples were pooled and purified using MinElute PCR purification kit (Qiagen, Hilden, Germany) according to the manufacturer's instruction. The second PCR was set up using the identical protocol with 100 ng of PCR product from the first PCR and primers containing sample-specific Illumina sequencing barcodes to facilitate multiplexed NGS. Product size was analyzed by agarose gel electrophoresis (see 3.5.7), PCR products were purified as described above and submitted for sequencing (see 3.6.2).

3.5.14 Identification of PDX samples by analysis of mitochondrial DNA

To verify PDX sample identity across several passages *in vivo*, sample-specific single nucleotide variants (SNV) were analyzed as previously described (Hutter et al., 2004). Hypervariable Region 1 of mitochondrial DNA was amplified from gDNA (see 3.5.9) of PDX cells.

PCR reaction	
10 µl	5x reaction buffer
300 ng	gDNA
5 µl	Forward primer (10 pmol/µl)
5 µl	Reverse primer (10 pmol/µl)
1 µl	dNTPs
0.25 µl	GoTaq Polymerase
ad 50 µl	H_2O

Cycler conditions		
Temperature	Time	Cycles
95 °C	2 min	1
94 °C	30 s	35
60 °C	30 s	
72 °C	30 s	
72 °C	5 min	1

PCR products were purified using NucleoSpin Gel and PCR Clean-up kit (Macherey-Nagel, Düren, Germany) according to the manufacturer's instructions, analyzed by Sanger sequencing (see 3.6.1) and sequences were compared to established reference sequences from each PDX sample.

3.6 Sequencing Methods

3.6.1 Sanger sequencing

Plasmid DNA and PCR products were sequenced by GATC Biotech (Konstanz, Germany) or Microsynth (Balgach, Switzerland). 30-100 ng/µl DNA or purified PCR product were analyzed using 10 pmol/µl primer. Resulting sequences were analyzed using Geneious 11.1.5.

3.6.2 Next generation sequencing

sgRNA library composition of plasmid pools and library-transduced PDX samples was analyzed by NGS. PCR products (see 3.5.12, 3.5.13) containing sample-specific Illumina Sequencing barcodes were sequenced at the Laboratory for Functional Genome Analysis (LaFuGA, LMU, Munich). Sequencing was performed with Illumina HiSeq 2000 (Illumina, San Diego, USA) with 50 bp single-end reads, aiming for at least 500 reads per sgRNA. Demultiplexing of several samples from the same sequencing run was performed on Galaxy server using an established tool provided by LaFuGa.

Read counts per individual sgRNA were counted using customized Python scripts as previously described (Becker et al., 2020). In brief, scripts extracted reads from fastq files, identified sgRNA sequences within the reads and counted reads per individual sgRNA. Read count files were used for analysis of cloning efficiency and dropouts from *in vivo* screens (see 3.8.2).

3.6.3 Whole Exome Sequencing and data analysis

DNA isolation and exome sequencing was performed at LaFuGa. Murine BM containing PDX ALL cells was thawed and human cells were enriched (see 3.3.9). gDNA and library preparation was performed by Sylvia Mallok (LaFuGa) using QIAmp DNA Blood Mini Kit (Qiagen, Düren, Germany) and quantification by Nanodrop and Qubit dsDNA HS Assay Kit. Exome libraries were prepared and multiplexed using SureSelect Human All Exon V6 kit. Sequencing was performed with Illumina HiSeq 1500 with 100 bp or 150 bp paired-end reads.

Mapping, quality assessment and primary analyses of sequencing data was performed by Sebastian Vosberg (Klinikum der Universität München KUM, Munich). Sequencing reads with original length of 150 bp were trimmed to a length of 100 bp at the 5' end to ensure consistent mapping. All sequences were trimmed based on base calling quality (min 13) at both ends. Sequence reads containing "N" bases and reads with length smaller than 50 nucleotides after trimming were discarded. Reads were mapped to the hg19 reference genome using BWA-aln

0.7.10 with default parameters. Mapped reads were filtered based on mapping quality (min 13) and reads not mapping to annotated protein coding regions were discarded. Reads likely arising from PCR duplicates were removed using samtools rmdup. On average, app. 43 million high quality reads per sample were used in the analysis (range 32,427,883 - 58,527,169), resulting in an average target coverage of 86.5. Sequencing reads were realigned around insertions and deletions using GATK IndelRealigner. Sequence variants in individual samples were detected using samtools mpileup and VarScan 2.3.7 using a minimum variant allele frequency (VAF) of 20% with a minimum coverage of 10x and the number of variant supporting reads ≥3, and a base calling quality of 20. Low evidence variants found in donor sample were subtracted to call variants gained in all other samples. Low evidence variants in donor sample were called using reduced cutoffs: VAF ≥5%, coverage ≥1x, number of variant supporting reads ≥1, base calling quality ≥6. The translational effect of sequence variants was annotated using SnpEff 4.3 and the Ensembl GRCh37.75 annotation. CNAs were detected using GATK DepthOfCoverage and OptimalCaptureSegmentation as previously described (Vosberg et al., 2016). The following cutoffs were applied: mean exon coverage ≥10x, number of exons per segment ≥2, size of segments ≥100kb, and number of segments per chromosome ≤10.

Three samples were excluded from further analyses due to poor sequencing quality. Variant allele frequencies were filtered based on their genomic position and frequency. Mutations in regions of copy number loss were extracted by filtering for the respective genomic regions. Protein-coding genes assigned to these genomic regions were extracted using Ensembl Biomart with genome assembly GRCh37.p13 (Yates et al., 2020).

3.6.4 Transcriptome sequencing with prime-seq

RNA sequencing was performed using prime-seq, a bulk version of the single cell RNA-seq method mcSCRB-seq (Bagnoli et al., 2018). cDNA isolation, library preparation and quality controls were performed by Lucas Wange (AG Enard, LMU, Munich). Samples were analyzed in two different batches according to the same protocol with minor modifications. The first batch was carried out using individual amplification of cDNAs, the second batch using pooled amplification for less bias and improved quality.

In brief, murine BM containing PDX ALL was thawed and 2,000 human cells were enriched by FACS based on eGFP expression. Cells were sorted into 100 µL RLT Plus Buffer (Qiagen, Düren, Germany) supplemented with 1 % β-Mercaptoethanol. Samples were flash frozen and stored at -80 °C until further processing, which was performed by Lucas Wange.

Following digestion with Proteinase K, nucleic acids were isolated using SPRI Beads and DNAseI digestion was performed on beads. Reverse transcription of the isolated RNA was done using barcoded oligo-dT primers and a template switching oligo. Exonuclease I digestion was performed to remove excess primers. cDNA was amplified using Kapa HiFi HotStart

polymerase and quality was assessed using capillary gel electrophoresis. Library preparation was carried out in triplicates with 0.8 ng cDNA input each using the Nextera XT Kit (Illumina, San Diego, USA). Fragments of 300-900 bp size were selected by agarose gel electrophoresis and library sequencing was performed at LaFuGA (LMU, Munich) with Illumina HiSeq1500 (Illumina, San Diego, USA) with paired-end reads. Sequencing was designed to cover barcode and UMI sequences with 28 bp in the first read and cDNA fragments with 50 bp in the second read and aiming for at least 1 x 10^7 reads per sample. Raw fastq files were processed using the zUMIs pipeline (Parekh et al., 2018). Reads were mapped to a concatenated genome of human and mouse (hg38, mm10) and Ensembl gene models (GRCh38 v.84,GRCm38.85) were used for quantification of gene expression levels.

3.6.5 Targeted sequencing of recurrently mutated genes

To obtain a high sequencing depth of identified *TP53* mutations, an established sequencing panel of 68 recurrently mutated genes was utilized. Experimental procedure and data analysis was performed by Maja Rothenberg-Thurley (KUM, Munich) as previously described (Metzeler et al., 2016).

3.7 Expression analyses

3.7.1 Differential gene expression analysis

To correct the batch effect resulting from the use of different prime-seq sequencing time points, an empirical Bayesian method or the methodologies implemented in the limma package of R were applied as described previously (Johnson et al., 2007, Ritchie et al., 2015). Initial data analysis was performed by Tobias Herold (KUM, Munich). Normalization of read counts was performed using the voom function (Love et al., 2014). Differential gene expression was calculated using the DESeq2 and limma packages in R following recommended workflows (Love et al., 2014, Ritchie et al., 2015). Differential gene expression was calculated between resistant and untreated samples and significantly upregulated transcripts in resistant samples were defined with the following cut-offs: $p < 0.001$ and $\log_2$ fold-change >1.

3.7.2 Protein expression analysis

Proteome analysis was performed by Ashok Kumar Jayavelu (AG Mann, MPI, Planegg) as described previously (Kulak et al., 2014). Murine BM containing PDX ALL was thawed and human cells were enriched by FACS based on eGFP expression and washed thoroughly in PBS twice. Cells were lysed in 1% SDC buffer, incubated (15 min, on ice), boiled (5 min, 95 °C), sonicated for 20 cycles and boiled (5 min, 95 °C). Proteins were digested with LysC (1:100 ratio) and Trypsin (1:100 ratio) for 16 hours at 37 °C and reaction was stopped using 5:1 2-propanol/1% TFA. Resulting peptides were de-salted on equilibrated styrenedivinylbenzene-

reversed phase sulfonated (SDB-RPS) StageTips, washed once in isopropanol/1% TFA and twice with 0.2% TFA, eluted with 60 µl elution buffer (80% ACN, 1.25% NH_4OH) and dried under vacuum. The dried peptides were resuspended in loading buffer (3%ACN, 0.3% TFA) and subjected to mass spectrometry (MS).

MS analysis was performed using Q Exactive HF-X Hybrid Quadrupole-Orbitrap Mass Spectrometer (Thermo Fisher Scientific, Waltham, USA) coupled to a nanoflow EASY-nLC1000 HPLC (Thermo Fisher Scientific, Waltham, USA). App. 500 ng peptide was loaded onto a 50 cm column with 75 µM diameter, packed in house with 1.9 µM C18 ReproSil particles (Dr. Maisch, Ammerbuch, Germany), and column temperature was maintained at 50 °C. Peptides were separated using a gradient of a two-buffer system of 0.1% formic acid and 60% ACN plus 0.1% formic acid for 140 min at a flow rate of 300 nl/min. The survey scans were acquired at a resolution of 60,000 FWHM at a AGC target of 3×10^6 ions (300-1650 m/z, 200 m/z, maximum filling time 20 ms), followed by HCD (high energy collisional dissociation) fragmentation of Top15 dynamically chosen ions. The MS/MS scans were detected in the Orbitrap at a resolution of 15,000 FWHM.

Data analysis was performed using Maxquant version 1.5.5.2 (Cox and Mann, 2008). The MS/MS spectra were searched for tryptic peptides using a target-decoy approach with a reverse database from the reference Uniprot Human (version 2016) proteome and list of potential contaminants by the build in Andromeda search engine. Settings were adjusted as follows: max. of two missed cleavages allowed, minimum peptide length of seven amino acids, Carbamidomethyl of cysteine (C) as fixed modification, oxidized methionine (M), acetylation (protein N-term) as variable modification, false discovery rate of less than 1% at the levels of peptide and protein identification. The proteins were assigned to the same protein groups if two proteins could not be discriminated by unique peptides. The label-free quantification was performed with the MaxLFQ algorithum (Cox et al., 2014) requiring a minimum ratio count of two. Match between run feature was enabled for identification of peptide across runs based on mass accuracy and normalized retention times. After filtering of artefacts, such as reverse hits and contaminants, Perseus software was used to analyze Maxquant output tables (Tyanova et al., 2016).

3.8 Statistics

All statistical analyses were performed using GraphPad Prism 7.05 or R 3.6.1. Statistical information for each experiment is provided in the figure legends.

3.8.1 Statistical analysis of *in vivo* proliferation and therapy response

Statistical testing between two groups was performed using unpaired t-test. Comparison between more than two groups was calculated with one-way ANOVA followed by Tukey´s

multiple comparison test. Levels of significance were defined as follows: $p > 0.05$: n.s., $p \leq 0.05$: *, $p \leq 0.01$: **, $p \leq 0.001$: ***.

Correlation of flow cytometry and BLI signal intensity was calculated using non-linear regression.

In vivo doubling time was calculated by non-linear fitting of an exponential growth curve to data points of repetitive BLI using GraphPad Prism. Doubling time was based on two different time points ($(x_1|y_1)$ and $(x_2|y_2)$) and calculated as follows:

$$doubling\ time = \frac{ln(2)}{k} \qquad \text{with} \qquad k = \frac{ln(y_2) - ln(y_1)}{x_2 - x_1}$$

3.8.2 Statistical analysis of CRISPR/Cas9 *in vivo* screens

Significant dropouts of *in vivo* CRISPR/Cas9 screen were identified using the model-based analysis of genome-wide CRISPR/Cas9 knockout (MAGeCK) as previously described (Li et al., 2014). The MAGeCK pipeline based on the Galaxy server was used (Afgan et al., 2018). To analyze the evenness of sgRNA read counts in the library plasmid pool, fraction of sgRNAs was plotted against fraction of total read counts and GINI Index was calculated using the following formula (Wang et al., 2019):

$$GINI\ Index = \frac{area\ under\ the\ curve\ (measured)}{area\ under\ the\ curve\ (perfect\ distribution)}$$

4 Results

Therapy resistance remains a major obstacle in the treatment of leukemia patients. Better understanding of the mechanisms underlying resistance development is crucial to improve outcome of patients, but appropriate model systems remain scarce.

Development of resistance is usually studied using either patient samples or cell lines *in vitro*. Studies with patient material allow important insight into determinants of resistance without bias by additional mutations. These studies, however, mostly retrospectively analyze therapy resistant cells and can hardly provide insight into transition states during development of resistance. Additionally, material is limited and genetic engineering is not possible. Cell line models, on the other hand, allow longitudinal studies of resistance development from initially responding cells and provide unlimited material for further characterization and genetic engineering, but lack the context of an *in vivo* model including systemic and microenvironmental effects. Furthermore, most cell line models harbor additional mutations due to immortalization procedures and results are often not transferrable to the clinical context (Milan et al., 2019, Holohan et al., 2013). So far, a model which on the one hand only considers patient-relevant mutations and on the other hand allows longitudinal modelling of resistance development while still providing enough material for further characterization is lacking.

The aim of this work was a better understanding of underlying mechanisms of resistance development. To this end, I generated a preclinical *in vivo* model of resistance development during conventional chemotherapy treatment. This model was used to characterize resistant cells regarding their genomic and functional behavior and their expression profiles. Ultimately, resistant cells were genetically modified to identify genes which regulate the resistance phenotype.

4.1 Modelling resistance development *in vivo*

In a first step, a pre-clinical model of resistance development was established. To this end, a PDX ALL model was used in combination with chemotherapy treatment *in vivo*. The PDX model provided a large amount of material for comprehensive analyses, while at the same time did not rely on artificial mutations. Therefore, this model reflected the clinical situation much better than *in vitro* cell line models.

4.1.1 Combination chemotherapy generated strong treatment response *in vivo*

Within the last years, several targeted treatment strategies were developed (Carroll and Hunger, 2016, Terwilliger and Abdul-Hay, 2017). However, chemotherapeutic regimens continue to be a crucial pillar in treatment of ALL patients (Brown et al., 2020). A basic principle remains the use of several cytotoxic drugs with different modes of action in

combination (Vasan et al., 2019). To mimic treatment of patients in the PDX model, combination chemotherapy was adapted for application in NSG mice.

Treatment was adapted for use in three established, pediatric BCP-ALL PDX samples (Table 17). Selected samples covered disease stages from primary diagnosis to second relapse. While ALL-50 presented an initial diagnosis sample of t(1;19) TCF3-PBX1 subtype, classified as a subtype with good prognosis, ALL-265 presented a first relapse sample of a high-hyperdiploid ALL. Third, ALL-199 originated from a second relapse of a high-risk Philadelphia-like subtype the patient ultimately succumbed to. Thus, the three PDX samples covered distinct ALL subtypes from different disease stages. All three PDX samples had previously been lentivirally transduced with luciferase and a fluorochrome, allowing BLI, quantification of leukemic cells in murine BM by flow cytometry and enrichment of leukemic cells by FACS (Vick et al., 2015, Ebinger et al., 2016). Furthermore, strategies to mimic treatment of patients in the PDX ALL model had already been established in our group. Previous results had shown that VCR and Cyclo, which are part of routine ALL treatment, (i) were well tolerated by NSG mice, thus allowing prolonged treatment periods, (ii) induced a dose-dependent treatment response of PDX ALL *in vivo*, and (iii) showed synergistic effects when applied in combination (work by Erbey Özdemir, published in Ebinger et al., 2016).

Table 17: Clinical characteristics of PDX samples

Sample number	Disease stage	Age [years]	Gender	Molecular subgroup	Clinical outcome
ALL-50	primary diagnosis	7	f	t(1;19) TCF3-PBX1	unknown
ALL-199	second relapse	8	f	Philadelphia-like (P2RY8-CRLF2 fusion)	†
ALL-265	first relapse	5	f	High hyperdiploidy	unknown

To establish a model for treatment response and development of resistance, cells were injected into groups of NSG mice and mice were treated with the standard chemotherapeutic drugs VCR and Cyclo. Treatment was initiated at the stage of advanced leukemia, i.e. two weeks before animals would succumb to leukemia, at a mean BLI signal of 1×10^9 - 1×10^{10} photons per second (p/s), corresponding to 1-10% of leukemic cells in BM. Mice were treated with VCR, Cyclo, a combination of both or left untreated and repetitive BLI was performed to monitor response over time (Fig. 6A). Drugs were applied once per week. In pre-experiments, dosages had been slightly adapted for individual PDX samples in order to achieve comparable response rates (see 3.2.4, data not shown). In all three PDX ALL samples, increasing BLI signals indicated a high rate of proliferation of leukemia cells before start of treatment (Fig. 6B). At the selected dosages, VCR or Cyclo treatment individually resulted in a stable tumor burden, but did not constantly reduce tumor burden in any of the samples. In contrast, combination

chemotherapy led to a strong tumor reduction in all samples. Five weeks of therapy consistently reduced tumor burden by at least 100-fold, indicating that > 99 % of leukemic cells were eradicated. Thus, combination therapy provided an efficient tool for tumor reduction in PDX ALL in vivo, independent from genetic subtype and disease stage.

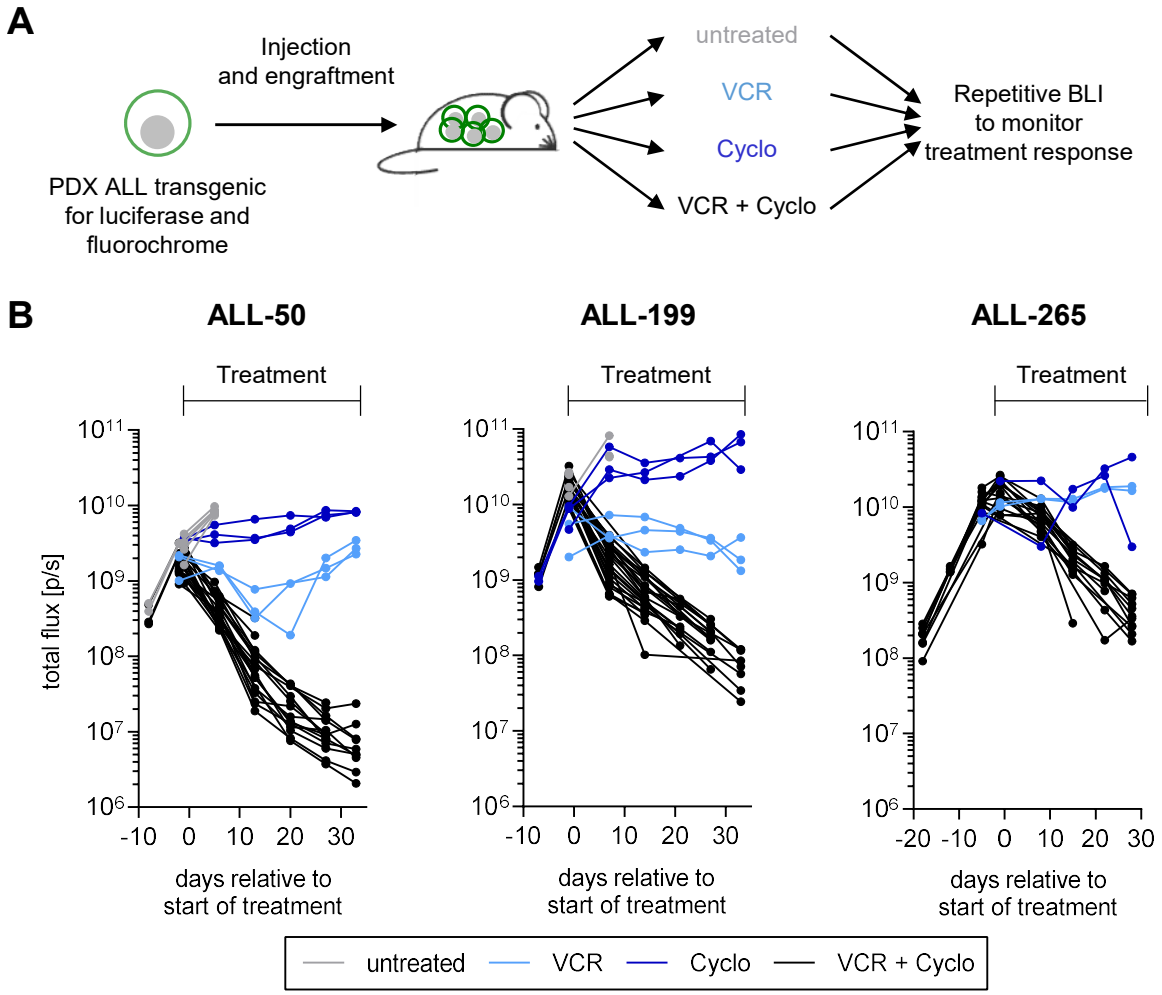

Figure 6: *In vivo* treatment response of PDX ALL cells

A) Experimental setup: NSG mice were engrafted with PDX ALL cells transgenic for luciferase and a fluorochrome. At high leukemic burden, mice were treated with Vincristine (VCR), Cyclophosphamide (Cyclo), a combination of both or left untreated. Treatment response was monitored by repetitive bioluminescence *in vivo* imaging (BLI). B) Quantification of BLI signal shows therapy response of three independent PDX ALL samples. One line represents one mouse (n=2 in ALL-265 single-treatment groups, n≥3 for all other groups). See methods section for drug dosages of individual samples (3.2.4).

4.1.2 Long-term treatment of ALL-199 led to development of resistance

Next, this model was adapted to longitudinally study effects of long-term chemotherapy treatment (Fig. 7A). PDX ALL were engrafted into NSG mice and treated with combination chemotherapy as long as treatment toxicity permitted or for up to 18 weeks. Effects of therapy were monitored by repetitive BLI and groups of mice were sacrificed at defined time points to re-isolate PDX cells from BM for further analyses. This approach allowed to specifically compare characteristics of leukemic cells extracted at different treatment stages, facilitating the follow-up of molecular changes and minimizing background effects.

As seen in Fig. 6, untreated ALL-199 cells showed a high rate of proliferation, but combination chemotherapy decreased tumor burden drastically, showing initial treatment sensitivity (Fig. 7B). On average, BLI signal intensity decreased by 100-fold from app. 1×10^{10} p/s to 1×10^{8} p/s within 35 days, indicating that less than 1% of leukemic cells survived the first seven weeks of treatment. Interestingly, within the following 30 days of on-going treatment, tumor burden did not reduce any further, resembling a plateau phase at a mean BLI signal of 4×10^{7} p/s. Subsequently, commencing app. ten weeks after start of treatment, BLI intensity increased despite on-going treatment, indicating treatment resistance. Tumor burden ultimately reached a mean of 2.2×10^{9} p/s in week 16 after start of treatment. Mean values were only depicted for time points, in which $n \geq 3$ mice remained in the experiment. Of note, two individual mice were treated for 18 weeks in total. Importantly, all mice which received treatment for at least 15 weeks developed resistance (n=8). Thus, constant, long-term chemotherapy treatment of ALL-199 resembled a tool to model development of resistance *in vivo*.

In chronological order, resistance acquisition was characterized by four distinct stages: (i) growth of untreated cells, (ii) treatment response of therapy sensitive cells, (iii) constant tumor load due to cells in a transition plateau; and (iv) increasing tumor load due to proliferation of therapy resistant cells. Groups of mice were sacrificed in each of the four stages for further characterization. Analysis of the PDX population in murine BM by flow cytometry confirmed that PDX cells were eradicated during treatment in the therapy sensitive stage, with only minute numbers remaining at the transition plateau stage, and tumor cell numbers increased at the therapy resistant stage (Fig. 7C). BLI pictures from the respective time points further supported this observation, with hardly any BLI signal at transition plateau stage, while the signal was clearly stronger at the therapy resistant stage (Fig. 7D). Taken together, continuous long-term chemotherapy treatment led to acquisition of resistance over time.

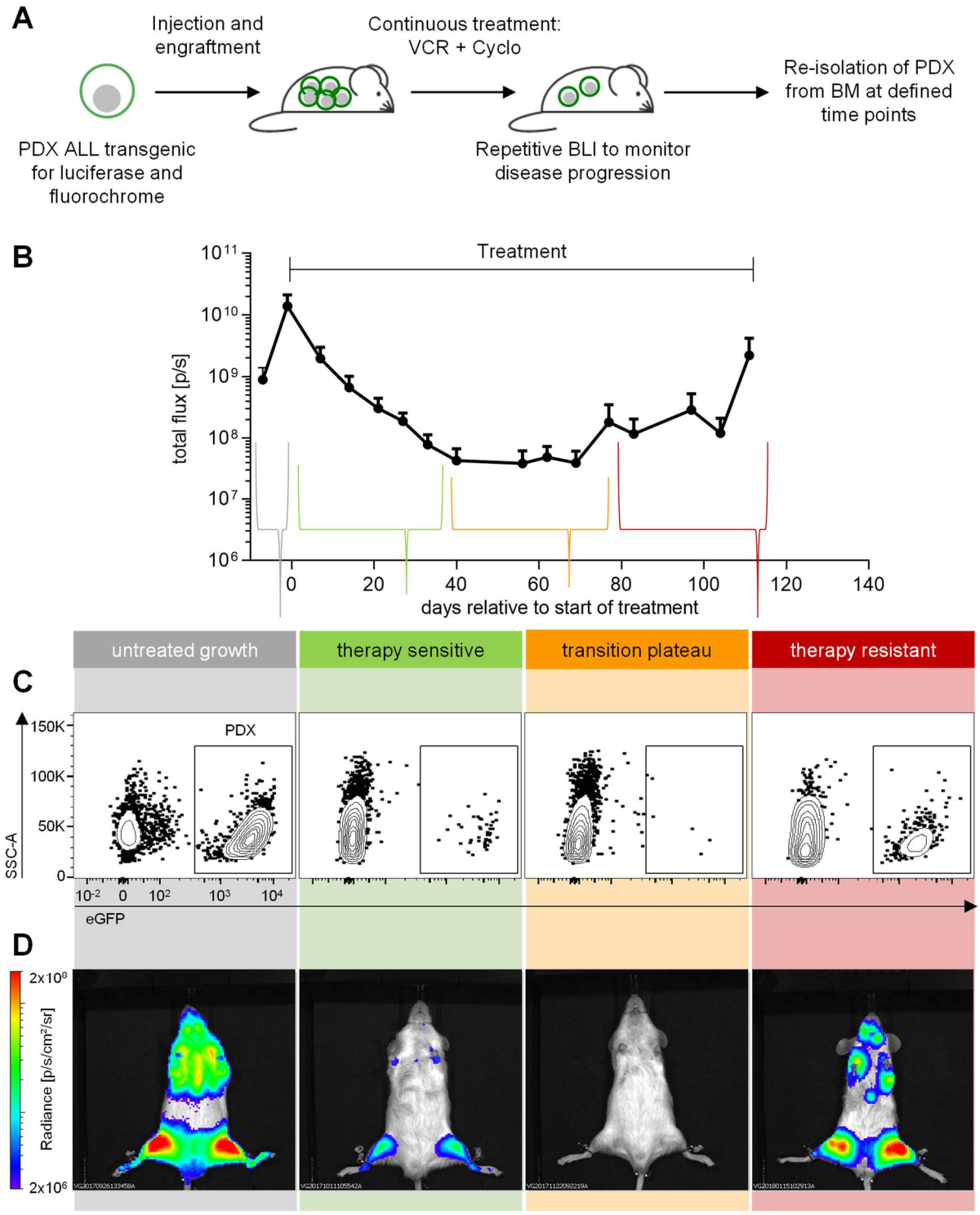

Figure 7: Long-term *in vivo* treatment of ALL-199 caused development of resistance

A) Experimental setup: NSG mice were engrafted with PDX ALL cells transgenic for luciferase and a fluorochrome. At high leukemic burden, all mice were treated with VCR and Cyclo and treatment response was monitored by repetitive BLI. At defined time points, groups of mice were sacrificed and leukemic cells were re-isolated from murine bone marrow (BM) for further analyses. B) Analysis of treatment response. Shown is mean BLI signal plus standard deviation (SD) of all mice monitored at the respective time points (n≥3, initial group size n=35). Resistance acquisition was characterized by four distinct stages as indicated. C) Groups of mice were sacrificed within each of the four indicated stages (first three stages: all on the same day, resistant stage: each mouse was treated as long as therapy was tolerated) and PDX population in murine BM was analyzed by flow cytometry (see Fig. 5 for all gating steps). eGFP+ gate represents the PDX population. One representative replicate of n ≥ 6 analyzed animals at the respective time point is shown. D) BLI pictures of one exemplary mouse measured in any of the four distinct stages. See 3.2.4 for drug dosages of individual samples.

4.1.3 Development of resistance was reproducible in PDX ALL

The observation that long-term treatment induced resistance development might be sample-specific for ALL-199 or indicate a broader phenotype of resistance development in ALL. To address these options, the experiment was repeated using two different PDX ALL samples.

The primary diagnosis sample ALL-50 initially presented a high sensitivity to combination chemotherapy (Fig. 8A). Three weeks of treatment reduced BLI signal from a mean of 1.9 x 10^9 p/s to 1.8 x10^7 p/s, thus eradicating > 99% of leukemic cells. This was followed by a short transition plateau phase, in which three weeks of treatment did not reduce tumor burden further. Importantly, six weeks after treatment start, an increasing BLI signal despite of on-going treatment was detected. This effect continued up to a mean of 1.4 x 10^8 p/s after ten weeks of treatment, indicating that ALL-50 cells acquired resistance. Thus, development of resistance is reproducible with ALL-50, albeit with a faster kinetics compared to ALL-199.

In line with the other two PDX samples, the hyperdiploid sample ALL-265 initially showed a strong response towards combination chemotherapy (Fig. 8B). This resulted in decrease of tumor burden from, on average, 1.5 x 10^{10} p/s at start of treatment to a mean of 1.6 x 10^8 p/s six weeks after treatment. For the following three weeks of treatment, tumor burden remained stable, indicating again a transition plateau stage. Of note, ALL-265 received the highest dosage of VCR due to reduced sensitivity towards VCR compared to the other PDX samples (0.3 mg/kg vs. 0.15 mg/kg in ALL-199). In consequence, treatment toxicity was increased, thus limiting therapy duration to nine weeks and preventing that development of resistance could be detected. However, the phenotype during the first week of treatment in ALL-265 resembled the other two samples, indicating that it was likely that cells would have ultimately developed resistance.

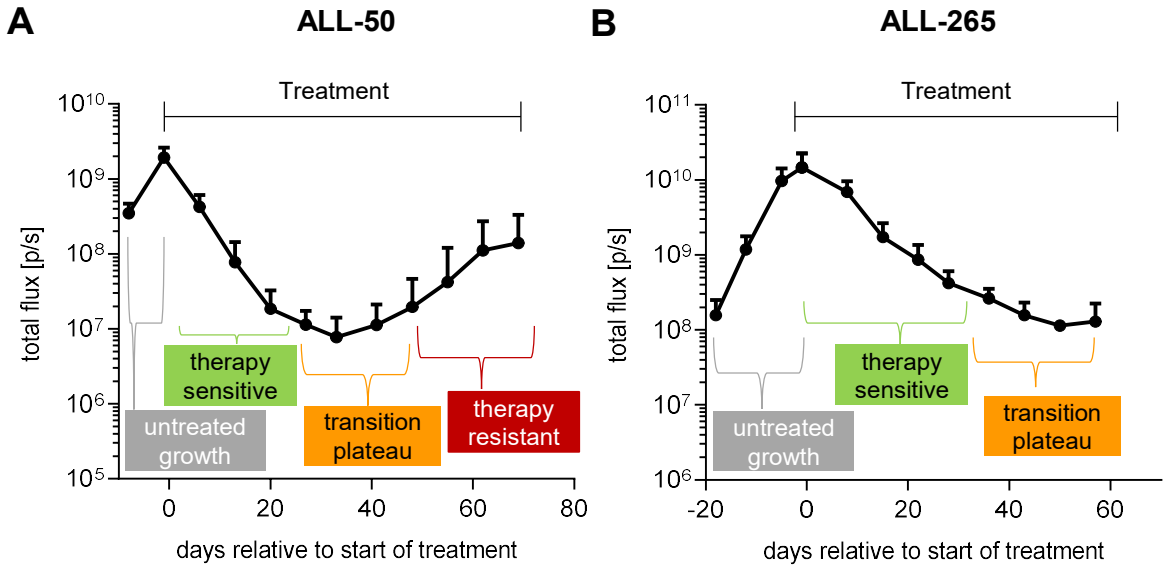

Figure 8: Long-term *in vivo* treatment of PDX ALL cells caused development of resistance

Experimental setup as described in Fig. 7A. Mean BLI signal plus SD is shown for ALL-50 (initial group size n=26) (A) or ALL-265 (initial group size n=24) (B) of all mice monitored at the respective time points (n≥3).

Taken together, three PDX ALL samples showed similar treatment response to combination chemotherapy with therapy sensitivity followed by a constant transition plateau stage. Treatment toxicity prevented that resistant cells could be obtained from ALL-265. Consequently, this sample was not included in further experiments. In conclusion, the resistant phenotype of ALL-199 was reproducible, indicating that conventional chemotherapy, applied for prolonged periods, induced acquired resistance of PDX ALL *in vivo*.

4.1.4 Initial stages of treatment diminished leukemic cells

In patients, quantification of leukemic blasts in bone marrow remains the gold standard to assess the efficacy of treatment (van Dongen et al., 2015). This readout can be easily adapted in the PDX ALL model due to fluorochrome marking of PDX cells, which allows quantification of leukemic cells in murine BM by flow cytometry (Ebinger et al., 2016). This approach was used to quantify the extent of treatment and resistance development further.

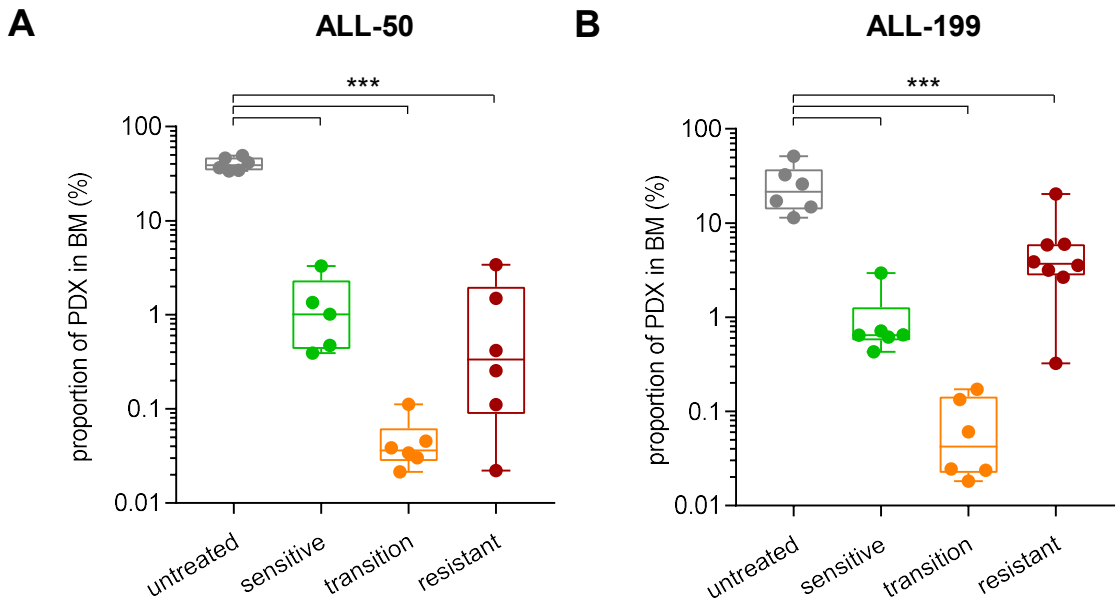

Figure 9: Initial stages of *in vivo* treatment diminished percentage of PDX ALL cells in murine BM

During long-term treatment of ALL-50 (A) and ALL-199 (B), groups of mice were sacrificed at indicated stages and murine BM was analyzed by flow cytometry as depicted in Fig. 7C. Shown is proportion of PDX cells within murine BM. One dot represents one mouse (n≥5 per time point). Statistical significance was calculated using one-way ANOVA followed by Tukey´s multiple comparisons test. ***: $p < 0.001$.

At each of the four distinct disease stages, groups of at least five mice from ALL-50 and ALL-199 were sacrificed for further analyses (Fig. 7, Fig. 8A). Fluorochrome expression of the PDX population was analyzed for each mouse to discriminate human leukemia from murine BM cells and percentage of leukemic cells in murine BM was calculated. At start of treatment, ALL-50 contained on average 40% leukemic cells in murine BM (Fig. 9A). Therapy significantly reduced these numbers to a mean of 0.05% in BM, while subsequent development of resistance led to app. 20-fold increase in leukemic cell numbers. ALL-199 harbored on average 25.6% leukemic cells in BM at start of treatment, which was significantly reduced to 0.07% at MRD plateau, representing an 355-fold reduction (Fig. 9B). BM collected at the

therapy resistant time-point contained 5.73% leukemic cells on average, showing a clear increase relative to MRD. Taken together, flow cytometric analysis supported the findings of BLI and clearly showed that therapy initially eradicated the majority of blasts, while resistance developed from a small population, which started proliferating again.

4.1.5 Flow cytometry and BLI were highly correlative measures of tumor burden

Both repetitive BLI and flow cytometry showed significant depletion of leukemia cells during treatment and regrowth during development of resistance. However, the extent of correlation between the two readouts was not clear. Previous analysis of ALL-199 had indicated a correlation of BLI and flow cytometry, albeit with a small sample size (work by Erbey Özdemir). To validate this observation and expand it to ALL-50, a correlative analysis was performed.

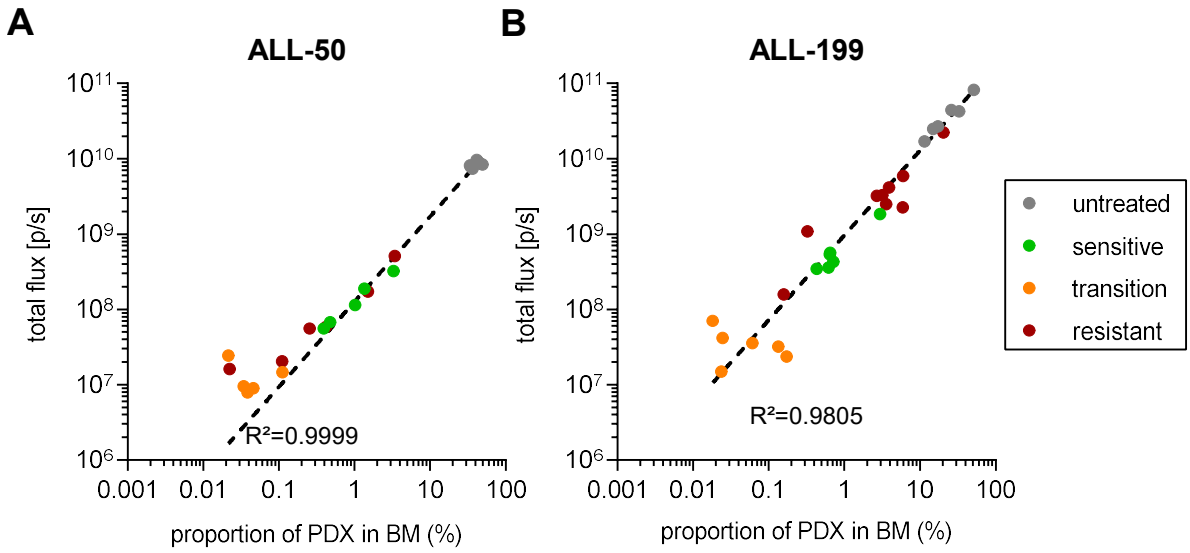

Figure 10: *In vivo* imaging and flow cytometric analyses were highly correlative measures to determine leukemic burden

Correlation of BLI signals and flow cytometric analysis of ALL-50 (A) and ALL-199 cells (B) in murine BM. One dot represents one mouse. Correlation curve and R^2 was calculated with non-linear regression.

Proportion of PDX in murine BM was quantified (Fig. 9) and correlated with the last BLI value from the respective mouse, which was usually obtained 1-2 days prior to sacrifice. Both ALL-199 and ALL-50 showed a very high rate of correlation between BLI and flow cytometry. In ALL-50, BLI of 8×10^9 p/s correlated with app. 40% of PDX in BM, while 1×10^7 p/s referred to app. 1 % of PDX (Fig. 10A). In ALL-199, BLI of 1×10^{10} p/s correlated with app. 10% of PDX in BM, while 1×10^8 p/s referred to app. 0.1% of PDX (Fig. 10B). In both PDX ALL, samples obtained from time points with low leukemic burden showed the weakest correlation. This was most likely due to technical reasons, as only a small fraction of the BM was analyzed, which might not be representative at this stage. Non-linear regression analysis generated a correlation coefficient of 0.9999 for ALL-50 and 0.9805 for ALL-199, respectively. Thus, BLI and flow cytometry were highly correlative and BLI allowed quantification of tumor load with a convincing reliability, albeit with limitations at very low tumor burden.

4.2 Contribution of tumor-intrinsic factors to resistance

The established model showed that long-term chemotherapy treatment led to development of resistance *in vivo*. A major advantage of the PDX model compared to cell line studies *in vitro* presents the ability to not only study cell-intrinsic mechanisms but also microenvironmental and systemic effects.

In theory, resistance could be mediated by intrinsic mechanisms of the leukemic cells as well as by a protective niche of the bone marrow microenvironment. In addition, systemic effects such as pharmacokinetics might influence resistance (Holohan et al., 2013, Vasan et al., 2019). Thus, experiments were designed and performed to decipher whether resistance was caused intrinsic or extrinsic factors.

4.2.1 Resistant ALL-199 showed decreased proliferation

Chemotherapy usually targets highly proliferative cells and treatment resistance might be associated with dormancy (Kreso and Dick, 2014, Ebinger et al., 2016, Tremblay et al., 2018, De Angelis et al., 2019, Shen et al., 2020). To understand whether proliferation was altered in treatment resistant cells, tumor growth of resistant ALL-199 was compared to treatment-naïve ALL-199.

Resistant ALL-199 cells isolated after long-term treatment (Fig. 7) were re-transplanted into new recipient NSG mice. In parallel, the same number of treatment-naïve ALL-199 cells from the first time-point of long-term treatment was re-transplanted (Fig. 11A). In this experiment, cells referred to as treatment-naïve originated from the untreated time point of long-term treatment. Tumor growth was analyzed by repetitive BLI. Interestingly, resistant ALL-199 cells showed a decelerated proliferation compared to the treatment-naïve counterparts (Fig. 11B). While mice injected with treatment-naïve ALL-199 cells reached a BLI signal of at least 1 x 10^9 p/s within 35 days, mice injected with resistant ALL-199 cells only reached this BLI signal after app. 55 days. Calculation of doubling times of the two populations from BLI curves showed a significant increase in doubling time from 1.78 to 2.94 days on average in treatment-naïve compared to resistant cells, respectively (Fig. 11C). Of note, variability in doubling times was larger in the resistant group. Thus, resistance development was accompanied by a heterogeneous decrease in proliferation.

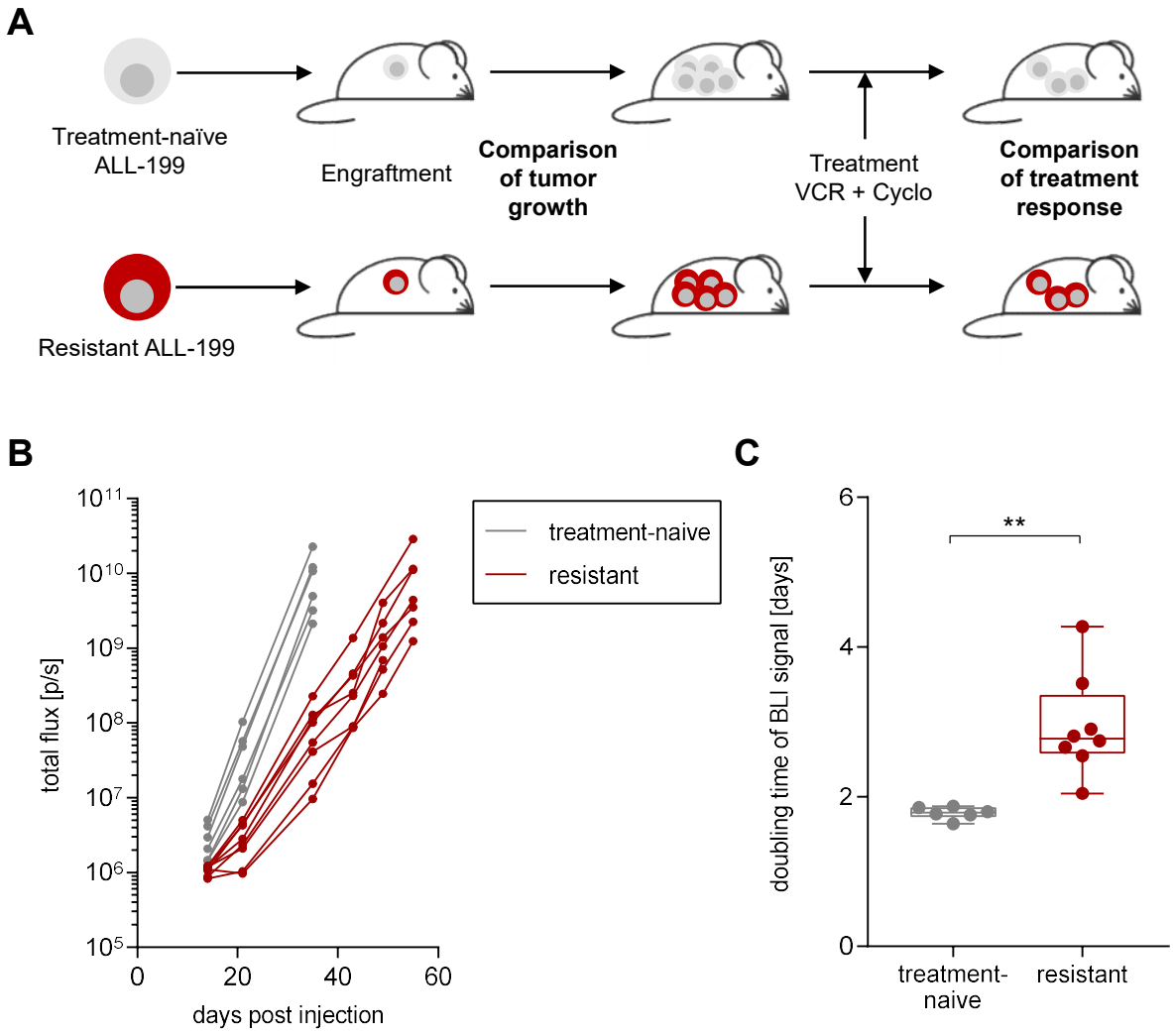

Figure 11: Resistant ALL-199 cells proliferated slower than treatment-naïve ALL-199 cells

A) Experimental setup: Resistant ALL-199 were obtained after long-term *in vivo* treatment, treatment-naïve ALL-199 were obtained from the first time point of the respective experiment (Fig. 7). Identical cell numbers of resistant and treatment-naïve ALL-199 cells were injected into groups of mice. Tumor growth was analyzed by repetitive BLI. At high leukemic burden, all mice were treated with VCR and Cyclo and treatment response was monitored by repetitive BLI. B) Quantification of BLI signal after injection. One line represents one mouse (n=6 for treatment-naïve cells, n=8 for resistant cells). C) Doubling time of BLI signal was calculated. One dot represents one mouse. Statistical significance was calculated by unpaired t-test. **: $p < 0.01$.

4.2.2 Resistant PDX ALL did not respond to treatment after re-transplantation

Next, the influence of the murine BM microenviroment on resistance of PDX ALL cells was analyzed. If a protective niche was relevant for maintenance of resistance, the resistant phenotype would not persist after re-transplantation of leukemic cells into a treatment-naïve bone marrow microenvironment. To investigate this, resistant PDX ALL cells obtained from long-term treatment were engrafted into NSG mice. Treatment response after re-transplantation was analyzed as a continuation of the experiment described above (Fig. 11A). In line with the experimental setup described in Fig. 7A, all mice injected with treatment-naïve or resistant ALL-199 cells were treated with established combination chemotherapy.

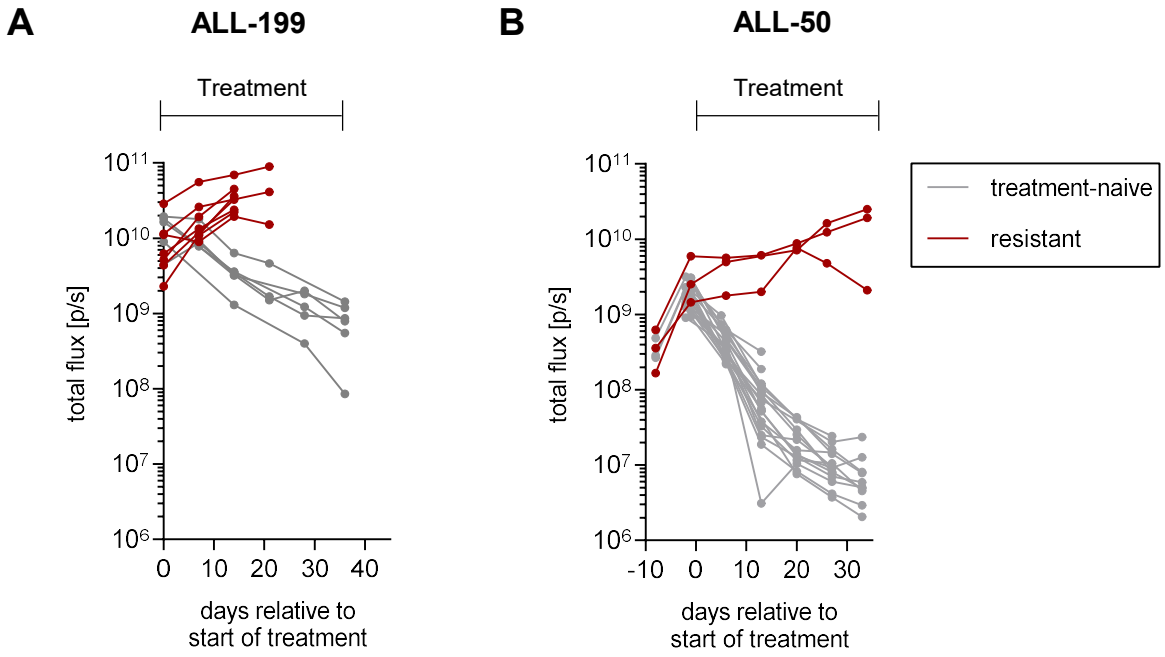

Figure 12: Resistant phenotype of PDX ALL cells persisted after re-transplantation

Experimental setup as described in Fig. 11A. Resistant or treatment-naïve cells were engrafted in NSG mice and treated with VCR and Cyclo. Treatment response was monitored by repetitive BLI. One line represents one mouse. A) ALL-199 (n=6 for treatment-naïve group, n=8 for resistant group). B) ALL-50 (n=3 for resistant group, BLI of treatment-naïve group was derived from Fig. 8A).

As expected, combination chemotherapy resulted in a decrease of tumor burden of mice engrafted with treatment-naïve ALL-199 cells (Fig. 12A). In contrast, resistant ALL-199 continued to proliferate despite therapy pressure. Resistant ALL-50 showed a similar response, as shown by an increasing BLI signal despite therapy pressure (Fig. 12B). Here, a control group was not implemented into the experiment and the control depicted the original data from the first treatment for more convenient visualization (Fig.8A).

Taken together, both ALL-199 and ALL-50 clearly showed that the resistant phenotype persists even after re-transplantation into new recipient mice. This indicated a mechanism of resistance maintenance intrinsic to leukemic cells.

4.2.3 Pre-treatment of the niche did not affect proliferation and treatment response

Even if an existing, resistant phenotype was maintained upon re-transplantation, the bone marrow niche might still contribute to resistance development. To address this hypothesis, NSG mice were pre-treated with combination chemotherapy prior to engraftment of treatment-naïve ALL-199 cells. This setup allowed to investigate if pre-treatment of the BM niche influenced engraftment and treatment response of PDX ALL cells.

Non-engrafted NSG mice were pre-treated with combination chemotherapy or PBS control for six weeks (Fig. 13A). This represented the period needed to reach the transition phase between therapy sensitive and resistant stages. After pre-treatment of recipient mice, treatment-naïve ALL-199 cells were injected and tumor growth was monitored by BLI. At high tumor burden, all mice were treated with combination therapy to analyze differences in treatment response following pre-treatment. In both groups, ALL-199 cells showed a fast and comparable proliferation rate, reaching BLI signals > 1 x 10^{10} p/s within 25 - 35 days (Fig. 13B). In line, both groups displayed comparable treatment sensitivity with a reduction of BLI signal from 1 x 10^{10} p/s to 2 x 10^{8} p/s within 40 days (Fig. 13C). In conclusion, in the experimental setting chosen, pre-treatment of recipient mice did not affect tumor growth and treatment response of ALL-199 cells.

Taken together, this set of experiments clearly indicated that intrinsic mechanisms of leukemic cells mediated the resistant phenotype, in contrast to a potential influence of the microenvironment. Thus, all further experiments focused on characterizing cell intrinsic mechanisms of resistance development.

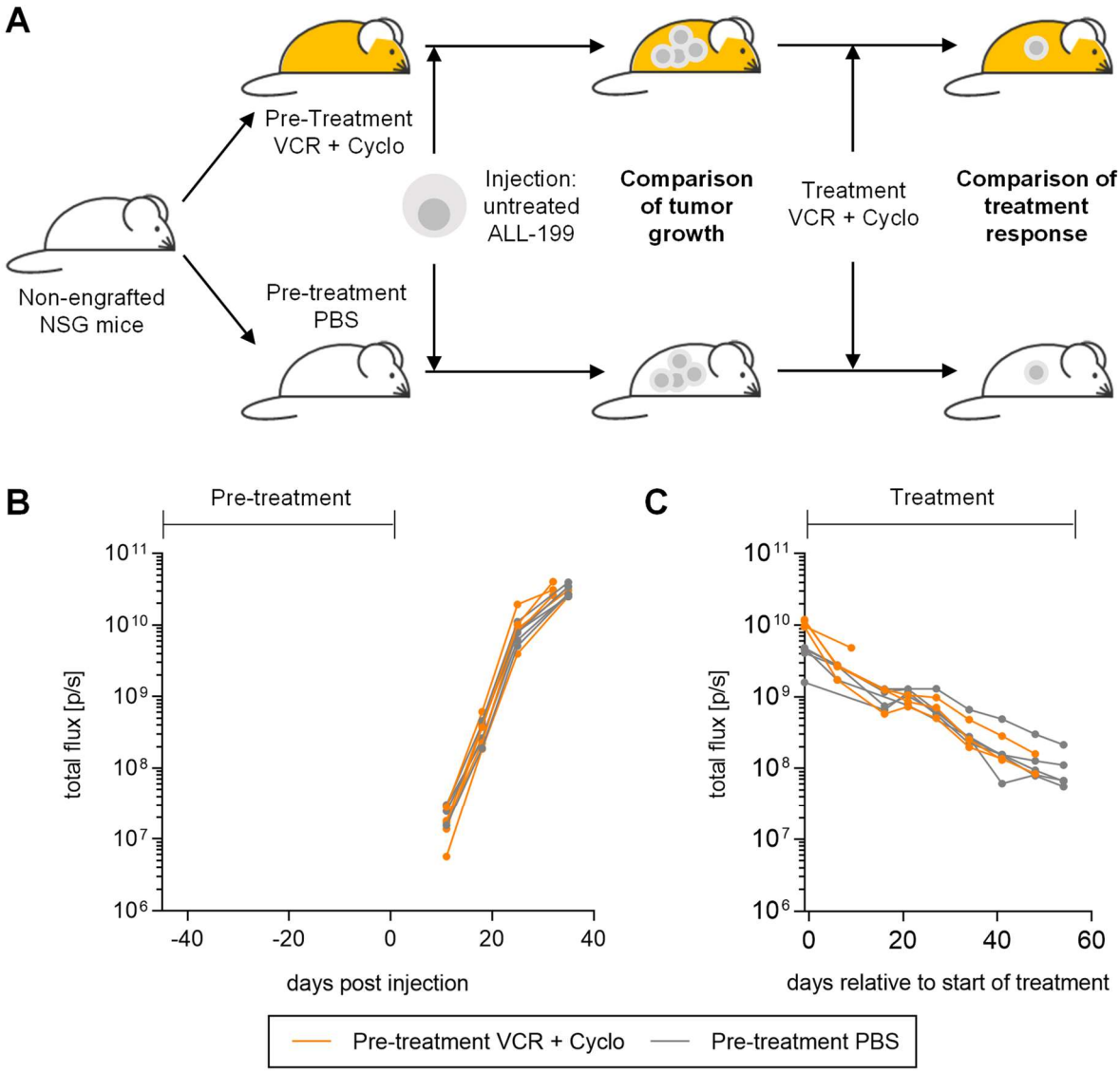

Figure 13: Chemotherapy pre-treatment of NSG mice did not affect proliferation and therapy response of treatment-naïve ALL-199 cells

A) Experimental Setup: NSG mice were treated with VCR and Cyclo or PBS for six weeks, followed by injection of treatment-naïve ALL-199 cells. Tumor growth was monitored by repetitive BLI. At high leukemia burden, both groups were treated with VCR and Cyclo for seven weeks and treatment response was monitored by repetitive BLI. Quantification of BLI signal after injection (B) and upon treatment (C). One line represents one mouse, n=5 per group

4.3 Genomic characterization of resistant ALL-199

The previous set of experiments indicated that resistance was mediated by intrinsic mechanisms of the leukemic cells rather than by a protective niche. Consequently, resistant ALL-199 cells were further characterized by genomic analyses to investigate whether resistance was determined by a characteristic genotype.

4.3.1 Resistant derivatives of ALL-199 generated by long-term treatment

As described above, ALL-199 cells developed resistance *in vivo* upon long-term chemotherapy treatment (Fig. 7). In this experiment, groups of mice were engrafted with the same donor cells originating from ALL-199 cells of the identical passage, defining them as biological replicates. All mice engrafted with ALL-199 cells received treatment until a defined time point or as long as treatment toxicity permitted (Fig. 7A). Importantly, all mice which received treatment for at least 15 weeks ultimately developed resistance. In total, eight of the mice shown in Fig. 7 were monitored until the last time point and all showed a similar pattern of resistance acquisition (Fig. 14). Cells were isolated individually from each replicate and biological replicates were subsequently named as resistant derivatives D1 - D8 of ALL-199. Notably, kinetics of resistance development was slightly different in D4 and D5 compared to the other derivatives. While all other derivatives reach a BLI signal of > 1 x 10^9 p/s within max. 16 weeks of treatment, D4 and D5 only reached > 1 x 10^9 p/s after 18 weeks of treatment, indicating a slower outgrowth. For subsequent genetic analyses, resistant derivatives were characterized individually.

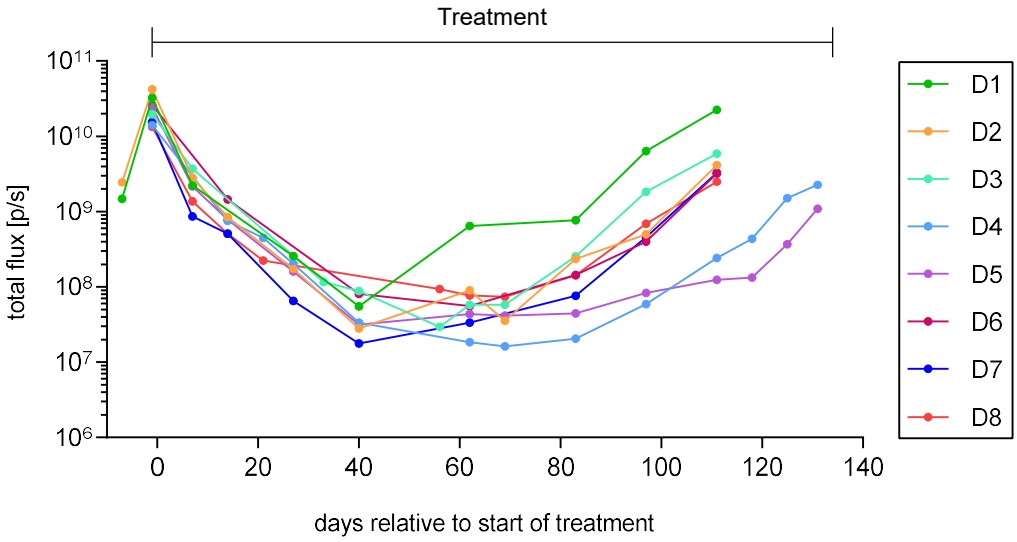

Figure 14: Generation of resistant derivatives of ALL-199

Quantification of BLI signal of eight biological replicates of ALL-199, which developed treatment resistance. Data depicts individual mice originating from the experiment described in Fig. 7, in which the mean of all mice is depicted. One line represents one mouse. Replicates are subsequently named and color-coded as derivatives D1-D8.

4.3.2 Treatment-naïve ALL-199 cells harbored various genetic alterations

Genomic analysis of resistant ALL-199 derivatives was performed in two steps. First, somatic alterations of ALL-199 cells before *in vivo* treatment were analyzed to establish a reference. Second, specific alterations occurring during development of resistance were determined by comparison of resistant ALL-199 cells to this reference. To this end, whole exome sequencing (WES) was performed using samples from different time points, i.e. both from the patient and from ALL-199 PDX cells (Fig. 15). Samples included (i) BM material of the patient in clinical remission after the first relapse serving as a healthy germline control, (ii) ALL-199 PDX cells which served as donor cells for the long-term therapy experiment, (iii) untreated ALL-199 cells from the first time-point of long-term treatment, and (iv) resistant derivatives generated after long-term therapy and amplification in next recipient mice. Comparative analysis of PDX donor cells vs. remission deciphered somatic alterations of the leukemia independent from any *in vivo* treatment. Comparative analysis of donor cells to untreated control cells deciphered alterations occurring during *in vivo* engraftment without treatment pressure. Consistently, comparative analysis of resistant derivatives to donor cells deciphered therapy-related alterations.

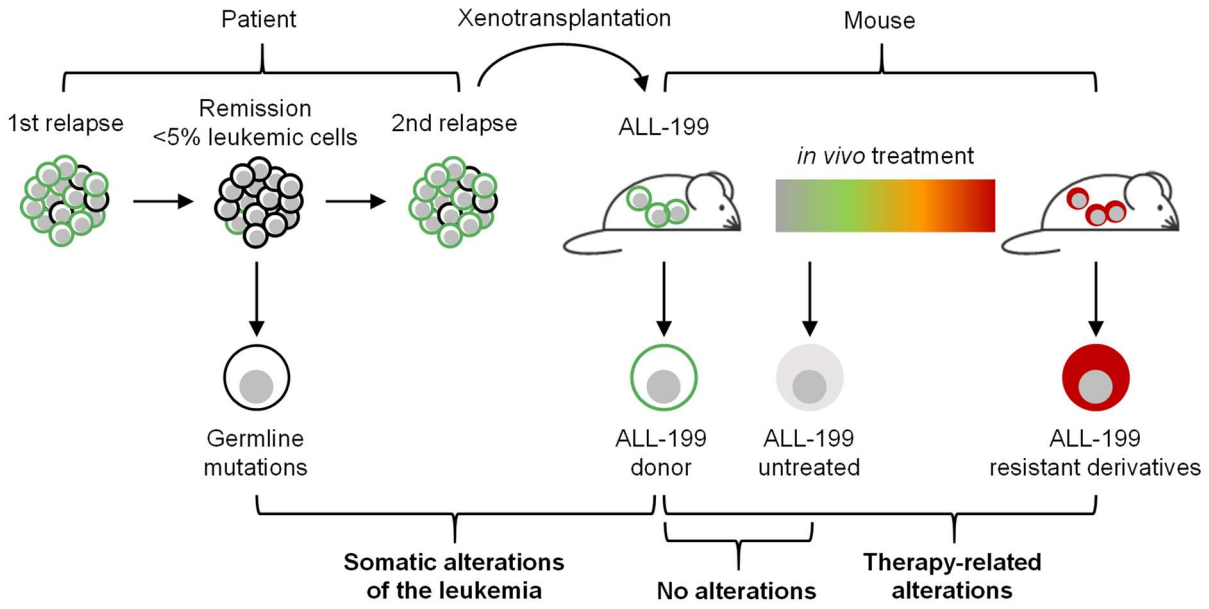

Figure 15: Origin of samples for whole exome sequencing

Samples for whole exome sequencing were derived both from the patient and from ALL-199 before and after resistance development. Sequencing was performed on bone marrow patient material from remission between 1st and 2nd relapse, which harbored max. 5% of leukemic cells, on ALL-199 PDX donor cells, which served as input for the long-term treatment experiment (Fig. 7), ALL-199 cells from untreated time point of the respective experiment and on the eight resistant derivatives of ALL-199 after long-term treatment. Comparison between ALL-199 donor and remission of the patient indicates somatic alterations of the leukemia compared to germline. Comparison between ALL-199 untreated and donor serves as control, in which no genetic alterations are expected. Comparison between ALL-199 donor and resistant derivatives indicates therapy-related alterations.

In a first step, germline and somatic alterations of the leukemia were determined. Information was collected from clinical data of the patient, i.e. cytogenetic analyses, and from independent readouts of PDX ALL-199 cells from other projects of the group, i.e. Nanopore sequencing and RNA sequencing (Table 18). The patient presented with trisomy 21 and cytogenetic analysis of the leukemia in the patient had identified a homozygous *CDKN2A* deletion on Chr. 9p. RNA sequencing of PDX ALL-199 cells had identified a P2RY8-CRLF2 fusion transcript, classifying the leukemia as Ph-like subtype. Furthermore, Nanopore sequencing detected a t(1;6) translocation in the ALL-199 PDX sample.

Additionally, WES data of the ALL-199 donor sample compared to the remission sample of the patient was implemented to detect further somatic alterations of the PDX sample already present before development of resistance. These might comprise both somatic alterations of the leukemic cells as well as artefacts occurring during establishment of the xenograft sample. Sebastian Vosberg (KUM, Munich) performed quality control, mapping of reads, calculations of CNAs and annotation of SNVs of all following WES data. Subsequent visualization and analysis steps were performed by me. Only variants with > 5% VAF were considered for further analyses to exclude mutations from residual leukemic cells in the remission sample. Mapping was performed using hg19 as a reference genome (technical details provided in 3.6.3). CNAs were calculated between PDX donor sample and remission sample of the patient, revealing specific differences between the PDX donor sample compared to germline (Fig. 16A). Several genomic regions presented heterozygous losses or gains (Table 18, Fig. 16A). Heterozygous loss of regions on Chr. 1q and 7p were detected, as well as homozygous loss of a region on Chr. 9p covering the *CDKN2A* deletion, thus confirming previous results. Furthermore, heterozygous gains of regions on Chr. 6q, 13q and 17q were identified.

In summary, ALL-199 donor cells already showed a high number of genomic alterations before *in vivo* development of resistance, which needed to be considered to identify treatment-related genomic changes.

Table 18: Genomic alterations of treatment-naïve ALL-199

Origin	Description	Source	Sample	Genomic regions affected
Germline	Trisomy 21	Clinical data of the patient	Patient sample	Chr. 21
Somatic	*P2RY8-CRLF2* fusion	RNAseq	PDX cells	Chr. X
Somatic	t(1;6)	Nanopore	PDX cells	Chr. 1 + Chr. 6
Somatic	*CDKN2A* deletion	Cytogenetics + Exome	Patient sample + PDX cells	Chr. 9
Somatic	Heterozygous gain	Exome	PDX cells	Chr. 6, 13, 17
Somatic	Heterozygous loss	Exome	PDX cells	Chr. 1, 7

4.3.3 Resistant derivatives of ALL-199 acquired various genomic alterations during treatment

In a second step, specific alterations occurring during development of resistance were determined by comparison of resistant ALL-199 cells to the donor sample (Fig. 15). To control for technical artefacts during transplantation and engraftment of PDX cells, untreated ALL-199 cells were compared to the donor sample. In total, WES was performed for one donor sample, three biological replicates of untreated ALL-199 cells and eight resistant derivatives of ALL-199. CNAs were calculated for untreated and resistant ALL-199 cells using the donor sample as a reference, facilitating specific detection of CNAs occurring during engraftment and *in vivo* treatment. Data of two untreated control samples and of resistant derivative D3 were excluded due to poor sequencing quality. As expected, the control sample from the untreated time point did not acquire large CNAs, indicating that transplantation and engraftment of PDX ALL cells does not affect the genotype. Of note, the only exception presented a small region of less than 1 Mb on Chr. 10p, which showed copy number gain with unknown relevance.

Surprisingly, CNA calculation of the resistant derivatives revealed that all derivatives acquired at least one CNA (Fig. 16B, Appendix Table A1). D1, D5, and D7 acquired heterozygous gains in Chr. 1q and Chr. 6q regions, which occurred concomitantly. Derivatives D1 and D2 showed copy number loss of Chr. 17, while D4 – D8 lost regions of Chr. 1p. Importantly, there was no common CNA identified within all resistant derivatives. This suggested that either genomic alterations were not indicative of the resistant phenotype and were only passenger alterations, or that more than one genomic hit would lead to development of resistance. Since all derivatives showed heterozygous loss on either Chr. 17 or on Chr. 1, this suggested that these two regions might be indicative of resistance. Consequently, these regions were analyzed in more detail.

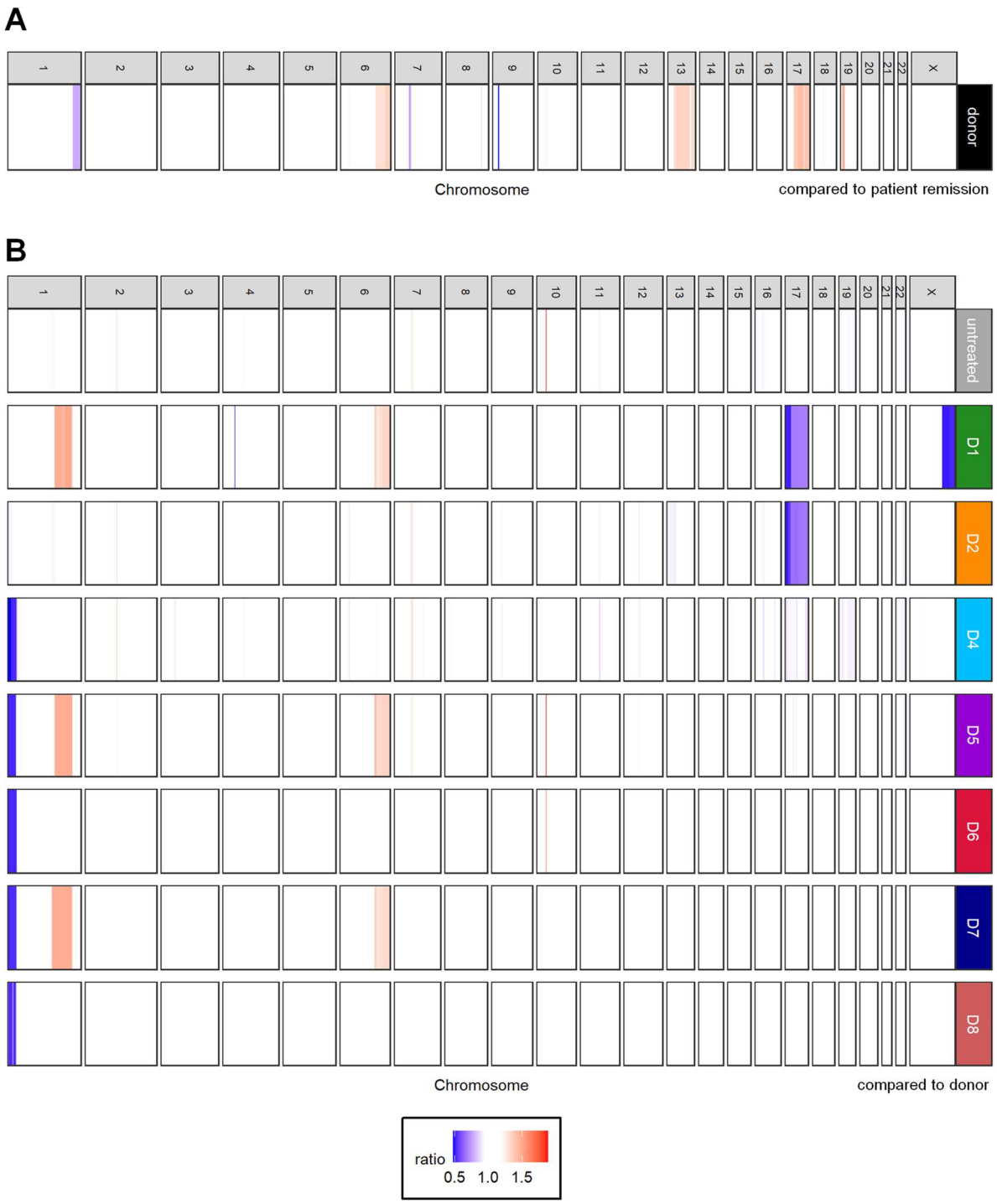

Figure 16: ALL-199 cells acquired genomic copy number alterations both during leukemia development and during development of resistance

A) Copy number alterations of ALL-199 donor cells related to non-leukemogenic germline control of the patient during remission. One column represents one chromosome. Blue bars (ratio <1) indicate loss of copy number, red bars (ratio >1) indicate gain of copy number in the respective genomic regions. B) Copy number alterations of resistant derivatives of ALL-199 and one untreated control sample of ALL-199 related to donor sample of ALL-199. Visualization as described in A).

4.3.4 Heterogeneous mutation patterns in derivatives with Chr. 1p deletion

Having identified loss of Chr. 1p as a potential factor for resistance development, CNAs and SNVs within this chromosome were analyzed in detail. Visualization of Chr. 1 CNAs of all resistant derivatives and the untreated control vs. the donor sample showed a common deleted region on Chr. 1p36 (chr1:69085-28477537) in D4 – D8 (Fig. 17A). Furthermore, D1, D5 and D7 gained one allele on Chr. 1q (chr1:159141551-218614709).

Next, VAFs of SNVs on Chr. 1 were analyzed (mapping and calculation performed by Sebastian Vosberg, visualization and further analyses performed by me). The pattern of VAFs was used to verify the identified CNAs and to give additional information on the deleted alleles (Fig. 17B). Furthermore, resistance could be developed due to a loss of heterozygosity (LOH), leading to loss of function of a gene essential for treatment sensitivity. Thus, analysis of mutations in the deleted region would help to identify a second hit for development of resistance. In theory, LOH is displayed by a hemizygous SNV, i.e. VAF app. 100%, in a region with only one remaining allele due to copy number loss. This SNV could either be already present at a heterozygous level before copy number loss or be acquired during treatment. Consequently, homozygous variants which are already present before copy number loss were not relevant in this scenario.

In a targeted approach to identify LOH, homozygous variants in the donor sample were excluded from the analysis, since mutations already present before start of treatment should not be indicative of resistance. Furthermore, variants with < 20% VAF were excluded from visualization. Since VAFs were not normalized within the experiment, the donor sample was included as an individual sample. The donor sample showed 1309 SNVs on Chr. 1 with VAF > 0.2 and < 0.8 compared to hg19 (Fig. 17B). Importantly, the untreated control sample did not show any obvious changes in the general VAF pattern compared to donor.

In contrast, all CNAs of resistant derivatives were be confirmed by the mutational pattern. The gain on Chr. 1q, generating three alleles in D1, D5 and D7, was clearly reflected by VAFs of app. 33% and 66% in the respective region. Furthermore, loss of the respective region of Chr. 1p36 in D6 - D8 was clearly accompanied by a high number of variants at app. 100% VAF, indicating that only one allele was left. Interestingly, D4 showed allele frequencies of app. 40% and 60% in the region with one remaining allele and D5 showed VAFs at 25% and 75%, indicating that both derivatives might harbor subclonal structures. When SNVs in the region of CNA were analyzed for genes which might play a role in development of resistance, no obvious genes described by literature in the context of treatment resistance were detected (data not shown). Taken together, CNA and VAF data indicated that D6 - D8 showed a similar genotype except for an additional gain of Chr. 1q in D7, while D4 and D5 lost the same region on Chr. 1p36 but most likely harbored subclonal structures.

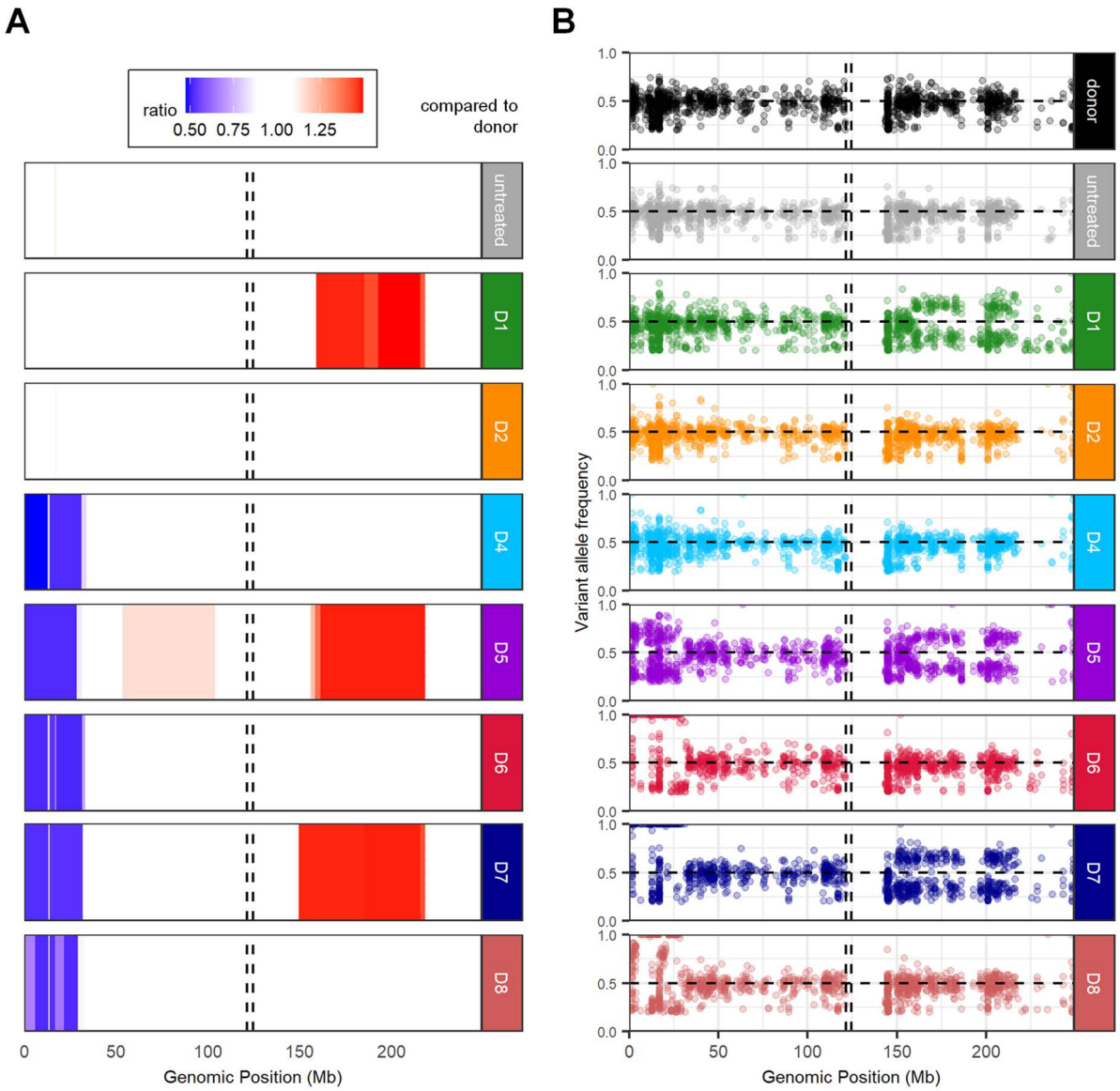

Figure 17: Resistant derivatives harbored different genomic alterations on Chr. 1

Analysis of WES for CNAs and mutations on Chr.1. A) CNAs on Chr. 1 of resistant derivatives and one untreated control sample related to ALL-199 donor sample. Dashed lines represent centromere position. Blue bars (ratio <1) indicate loss of copy number, red bars (ratio >1) indicate gain of copy number in the indicated genomic region. B) Variant allele frequencies (VAF) on Chr. 1 of donor sample, untreated control and resistant derivatives of ALL-199. One dot represents one single nucleotide variant (SNV) as detected with hg19 as reference; high color intensity indicates several mutations in the same area; homozygous SNVs present before therapy (VAF >0.8) and mutations with VAF < 0.2 were excluded. Horizontal dashed line represents VAF = 0.5 and vertical dashed lines represent centromere positions.

4.3.5 Derivatives with Chr. 17p deletion acquired additional *TP53* mutations

D1 and D2 showed chromosomal loss of Chr. 17, which might be a complementary hit to loss of the Chr. 1p36 region. Thus, CNA and SNV analysis were performed identical as described for Chr. 1. Importantly, the donor sample already presented chromosomal alterations in this region. Comparison of donor sample to germline control as well as mutational analysis of the donor sample showed a chromosomal gain of Chr. 17q (Fig. 16A, Fig. 18B). Thus, one allele had previously been amplified, resulting in SNV VAFs of 33% and 66% within this region in the donor sample. D1 and D2 showed varying copy number ratios related to the donor sample depending on the location on either Chr. 17p or Chr. 17q (Fig. 18A). Chr. 17p showed a copy number ratio of 0.5, indicating that from initially two alleles, one allele was remaining. Chr. 17q showed a copy number ratio of app. 0.66, indicating that from initially three alleles two alleles were remaining. This showed that both derivatives lost one whole Chr. 17, while the part which had been amplified before treatment still remained. In conclusion, Chr. 17q harbored two alleles after treatment in D1 and D2, while Chr. 17p only contained one allele.

This observation was reflected by the mutational pattern of Chr. 17 (Fig. 18B). D4 - D8 showed the same VAF pattern as the donor sample and untreated control, and the CNA analysis did not reveal any significant changes, indicating that the gain of Chr. 17q was preserved upon treatment in those derivatives. In contrast, the chromosomal loss of 17p in D1 and D2 was clearly reflected by the VAF pattern, as a high number of mutations with app. 100% VAF was detected, indicating homozygous mutations.

Interestingly, VAFs in Chr. 17q showed striking differences between D1 and D2, although both contained two alleles. D1 again mostly harbored mutations with app. 100% VAF, while D2 showed a high number of heterozygous mutations. Furthermore, while 1042 mutations with VAF < 0.8 and > 0.2 were detected in the donor sample, 898 SNVs were detected in D2 and only 635 SNVs were detected in D1 within this range of VAF. This suggests that both derivatives lost complementary alleles of Chr. 17. While D1 lost the allele, which had only been present in one copy before treatment, ending up with two identical alleles, D2 lost the allele, which had initially been amplified, ending up with two different alleles and reflecting a normal genotype of Chr. 17q. Regarding a resistance mechanism, these findings suggested that most likely no driver mutation of resistance existed on Chr. 17q since any of the two alleles could be lost. Thus, Chr. 17p appeared as the more interesting region putatively harboring mutations responsible for acquired resistance. Consequently, this genomic region was analyzed for a second hit in the remaining allele, which might explain the resistant phenotype.

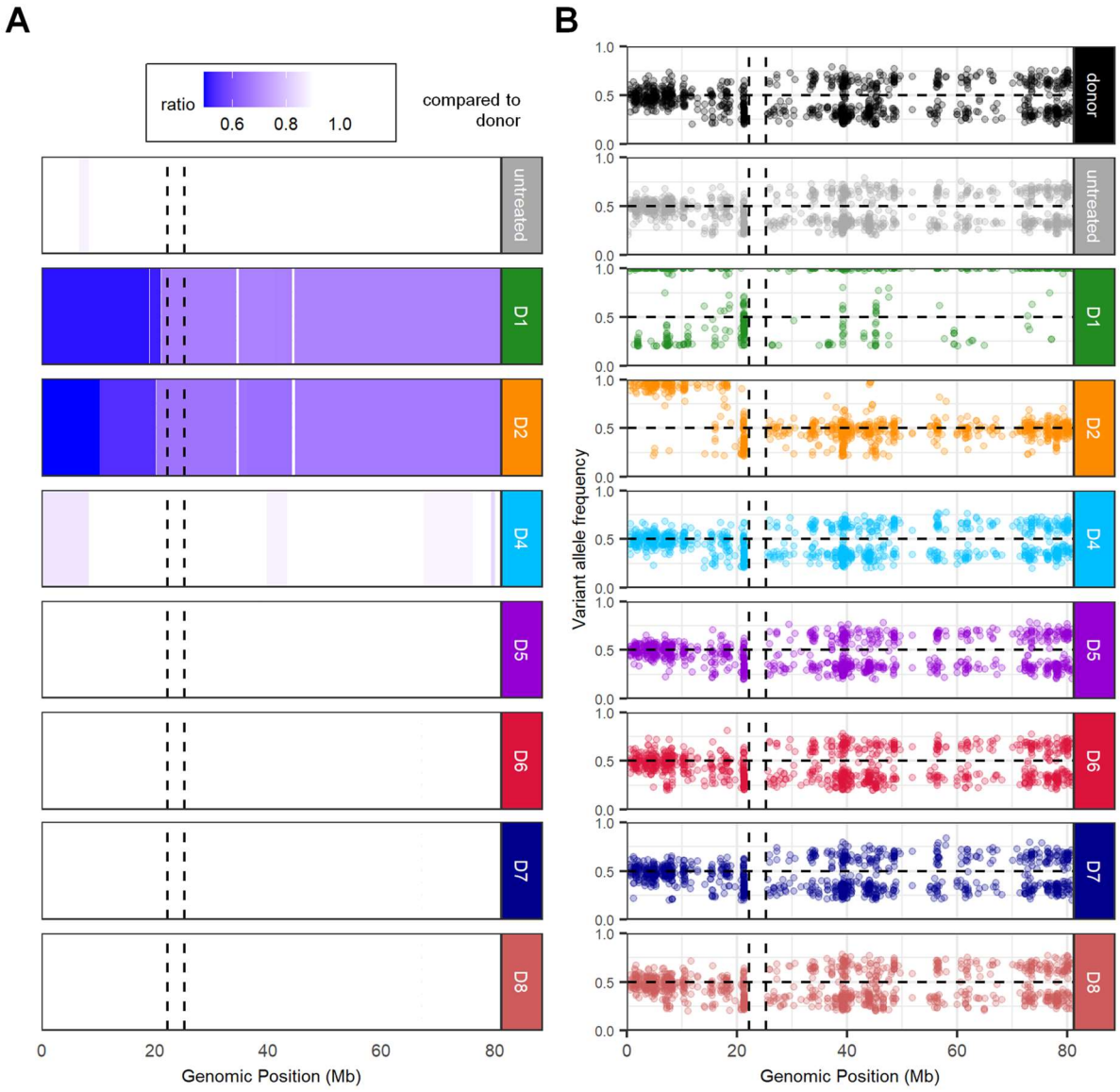

Figure 18: Resistant derivatives harbored different genomic alterations on Chr. 17

Analysis of WES for CNAs and mutations on Chr.17. A) CNAs on Chr. 17 of resistant derivatives and one untreated control sample related to ALL-199 donor sample. Dashed lines represent centromere position. Blue bars (ratio <1) indicate loss of copy number, red bars (ratio >1) indicate gain of copy number in the indicated genomic region. B) Variant allele frequencies (VAF) on Chr. 17 of donor sample, untreated control and resistant derivatives of ALL-199. One dot represents one single nucleotide variant (SNV) as detected with hg19 as reference; homozygous SNVs present before therapy (VAF > 0.8) and mutations with VAF < 0.2 were excluded. Horizontal dashed line represents VAF = 0.5 and vertical dashed lines represent centromere positions.

Annotation of SNVs to genomic loci revealed that not only VAFs of pre-existing mutations from the patient or the donor sample changed due to CNAs, but that also new mutations were acquired during treatment. Strikingly, both D1 and D2 acquired different point mutations in the *TP53* gene, a well-described tumor suppressor gene encoding the protein p53 (Fig. 19). Mutations were further analyzed for VAF, presence in the donor sample and in other derivatives and location within the *TP53* gene.

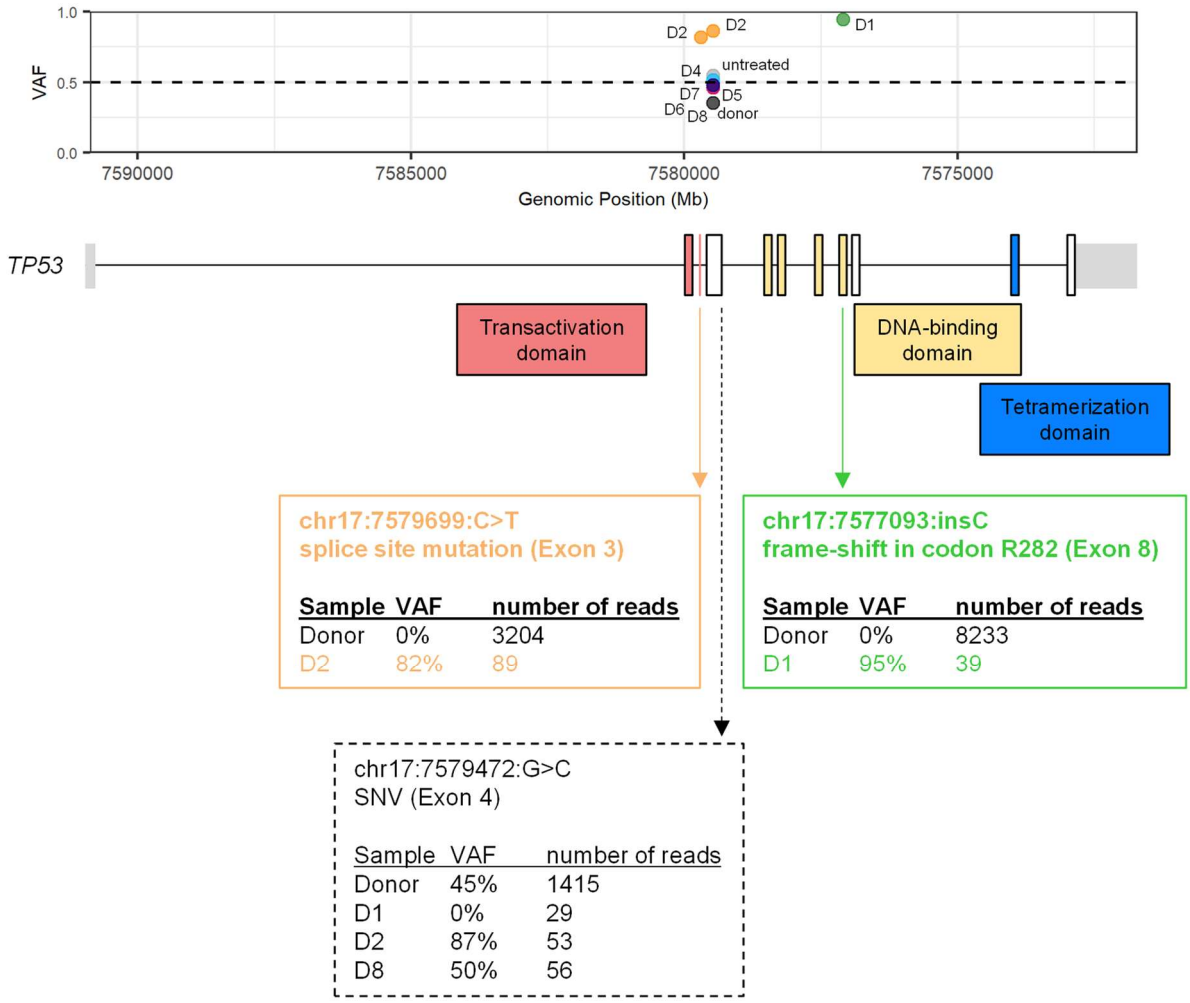

Figure 19: D1 and D2 acquired *TP53* mutations during development of resistance

Analysis of mutations in *TP53* locus detected by WES. Upper plot shows mutations in *TP53* gene present at the indicated genomic position (one dot represents one mutation in one sample). Lower plot represents genomic locus of *TP53* on Chr.17p with its exon structure; coloring indicates the encoded protein domains. Three different mutations were detected within *TP53* locus, of which two are newly acquired during *in vivo* development of resistance (defined within green and orange box) and one was present before therapy (defined in grey dashed box). Boxes indicate the exact mutation and the detected VAF and number of sequencing reads in targeted NGS of the donor sample and in WES of the individual derivatives.

D2 acquired a splice site mutation in Exon 3, encoding the transactivation domain of p53, with a VAF of 82%. This mutation was not detected in the donor sample. To analyze whether the mutation had already been present in the donor sample at a lower frequency, which could not be detected by limited coverage of WES, the respective locus was sequenced with a higher sequencing depth using targeted NGS. Sequencing and analysis of raw data was performed by Maja Rothenberg-Thurley (KUM, Munich). When I analyzed the respective locus of *TP53*, the mutation was detected in 0/3204 reads, indicating that it could have only been present before treatment with max. 0.03% frequency.

D1 acquired a frame-shift mutation in codon R282 of Exon 8, encoding the DNA-binding domain of p53 and representing a well-described mutational hotspot of p53 (Boettcher et al., 2019). This mutation was detected with 95% VAF in D1, but neither in any of the other

derivatives nor in the donor sample. Again, targeted NGS did not detect this mutation within 8233 reads at the respective position in the donor cells, indicating that the mutation could have only been present with max. 0.01% frequency. Additionally, mutational analysis detected a pre-existing heterozygous SNV in Exon 4 of *TP53*, which remained heterozygous in all derivatives not affected by CNA in this region (D8 is shown as representative sample). D1 lost this variant while D2 showed the variant with 87% VAF, again indicating that both derivatives lost complementary alleles. However, since this variant was already present in the donor sample and was lost in the resistant derivative D1, it was most likely not relevant for the resistant phenotype.

Taken together, both D1 and D2 showed heterozygous loss of different alleles of Chr. 17, resulting in only one remaining allele of Chr. 17p. Additionally, both derivatives acquired distinct and unique mutations in *TP53* on the remaining allele.

4.4 Functional characterization of resistant ALL-199

Unexpectedly, resistant derivatives of ALL-199 showed numerous genomic changes occurring exclusively during long-term treatment and resistance development. Importantly, we could not identify one common genotype of all resistant derivatives.

In consequence, more than one genomic alteration might be able to drive resistance, with several routes leading to resistance. Alternatively, genomic alterations might not relevant for the resistant phenotype. To evaluate these options, resistant derivatives were functionally characterized by *in vivo* experiments.

4.4.1 Resistant derivatives showed heterogeneous treatment response following drug holiday

In order to identify drivers of a resistant phenotype, it is crucial to understand whether resistance only persists in case of on-going therapy pressure or whether it is acquired irreversibly. An on-off-switch mechanism would indicate e.g. epigenetic regulations of resistance, while an irreversible resistance acquisition would indicate e.g. genetic drivers. Thus, analysis of these options gives valuable information for the resistance mechanism.

To this end, resistant derivatives of ALL-199 cells were grown without selection pressure for a total period of app. six months, followed by re-challenge with chemotherapy. Since PDX ALL cells did not proliferate *in vitro*, derivatives were repetitively transplanted into NSG mice (Fig. 20A). Each derivative was transplanted into one recipient mouse, proliferation was monitored by BLI, and PDX cells were re-isolated from murine bone marrow at BLI signals > 1×10^{10} p/s and re-transplanted to next recipient mice. This procedure was repeated twice. At the fourth re-transplantation, cells of each derivative were distributed to two recipient mice each, of which one received combination chemotherapy as previously established and one was left untreated.

Since the resistant phenotype was accompanied by an increase in doubling time (Fig. 11), proliferation of resistant derivatives in the absence of selection pressure was analyzed (Fig. 20B). BLI signals were used to calculate doubling times of each derivative in each recipient mouse (passage 1 – 4). On average, doubling time did not change over passages, ranging from a mean of 3.03 days in p2 to 3.44 days in p1. Notably, doubling times were similar to the ones calculated earlier (Fig. 11C). Yet, individual derivatives displayed variability in doubling times between the passages. This was most likely due to technical reasons, since doubling times were calculated from only two individual BLI data points. Thus, proliferation did not accelerate in the absence of treatment pressure.

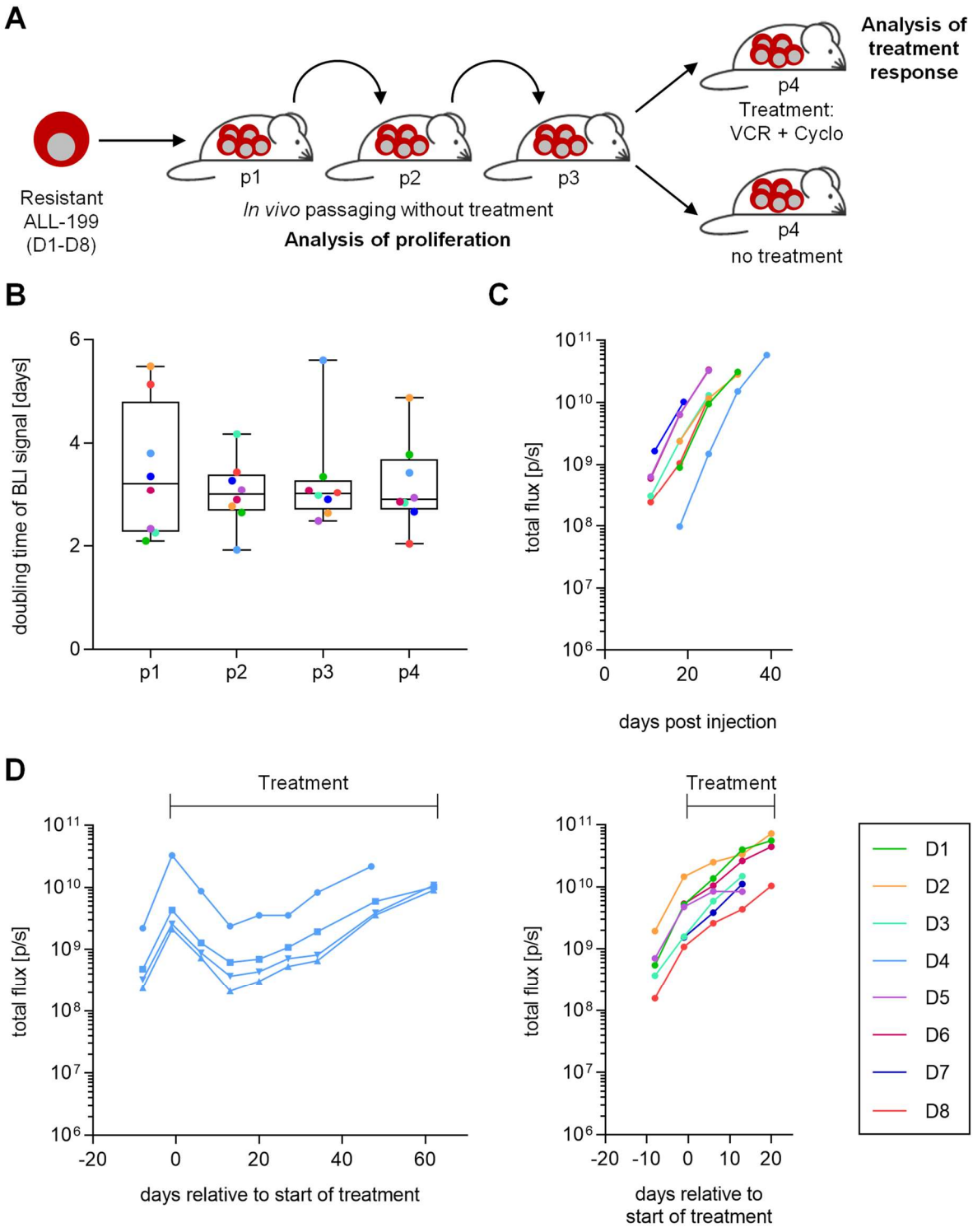

Figure 20: Heterogeneous treatment response of resistant derivatives following drug holiday

A) Experimental setup: Resistant derivatives D1 - D8 of ALL-199 were injected into NSG mice (one mouse per derivative). Tumor growth was monitored by regular BLI and cells were re-transplanted into the next recipient mouse at high leukemic burden (total flux > 1 x 10^{10} p/s). In the fourth re-transplantation step, cells were distributed to two recipient mice per derivative, of which one mouse was treated with VCR and Cyclo as established and the other mouse left untreated. Therapy response was monitored by BLI. B) Doubling time of BLI signals of individual derivatives was calculated from repetitive BLI signals of each re-transplantation. One dot represents one mouse. Colors indicate the individual derivatives. Statistical testing with one-way ANOVA followed by Tukey´s multiple comparisons test did not show any statistical significance. C) Quantification of BLI signals showed similar proliferation between each derivative in p4 without treatment. D) Quantification of BLI signals showed treatment response of each derivative in p4 after drug holiday. Data is distributed to two plots for more convenient visualization. One line represents one mouse (n=4 for D4, n=1 for all other derivatives).

At the fourth re-transplantation step, each derivative was distributed to two recipient mice. In the untreated control group, engraftment and proliferation did not differ between the individual derivatives (Fig. 20C). However, response towards combination chemotherapy varied between the derivatives: Upon re-challenge of the individual derivatives with combination chemotherapy, six out of eight derivatives clearly showed persistent resistance as indicated by increasing BLI signal despite therapy pressure (Fig. 20D, right panel). Strikingly, D5 responded partially, resulting in a stable tumor burden, and D4 presented a restored sensitivity towards treatment with a reduction in BLI signal (Fig. 20D, left panel). Tumor burden was reduced by more than 10-fold within two weeks of treatment. Thus, treatment was prolonged, leading to a re-gain of resistance after a short intermediate phase with stable disease burden. To rule out technical problems during the experiment, the treatment passage was repeated for D4 with three additional mice (included in Fig. 20D, left panel). All mice displayed identical treatment response with a very similar kinetic, arguing against technical problems of the experimental procedure.

Taken together, a drug holiday neither affected proliferation of the derivatives without treatment pressure nor affected treatment response in six out of eight derivatives. Surprisingly, D4 displayed a different phenotype and partially responded towards treatment, but quickly re-gained resistance. This suggests that resistant derivatives are not only genomically but also functionally heterogeneous.

4.4.2 Resistant derivatives undergoing high-dose treatment showed heterogeneous treatment response

Resistance acquisition by long-term treatment was achieved using relatively low concentrations of drugs, compared to other treatment strategies established in the PDX model, to minimize treatment toxicity (Liem et al., 2004, Samuels et al., 2014, Ebinger et al., 2016). However, it remained unclear whether treatment-naïve PDX ALL could be cured with the same combination chemotherapy by applying a higher dose. If treatment-naïve ALL-199 already harbored resistant subclones at a very low frequency, it would be likely that they also mediate resistance towards a higher dose. In this case, mice bearing treatment-naïve ALL-199 cells would not get cured with the established combination chemotherapy, independent from the applied dose, but eventually the resistant clone would grow out. On the other hand, it is possible that a higher dose of the same drugs would still result in treatment sensitivity of the previously generated, resistant derivatives.

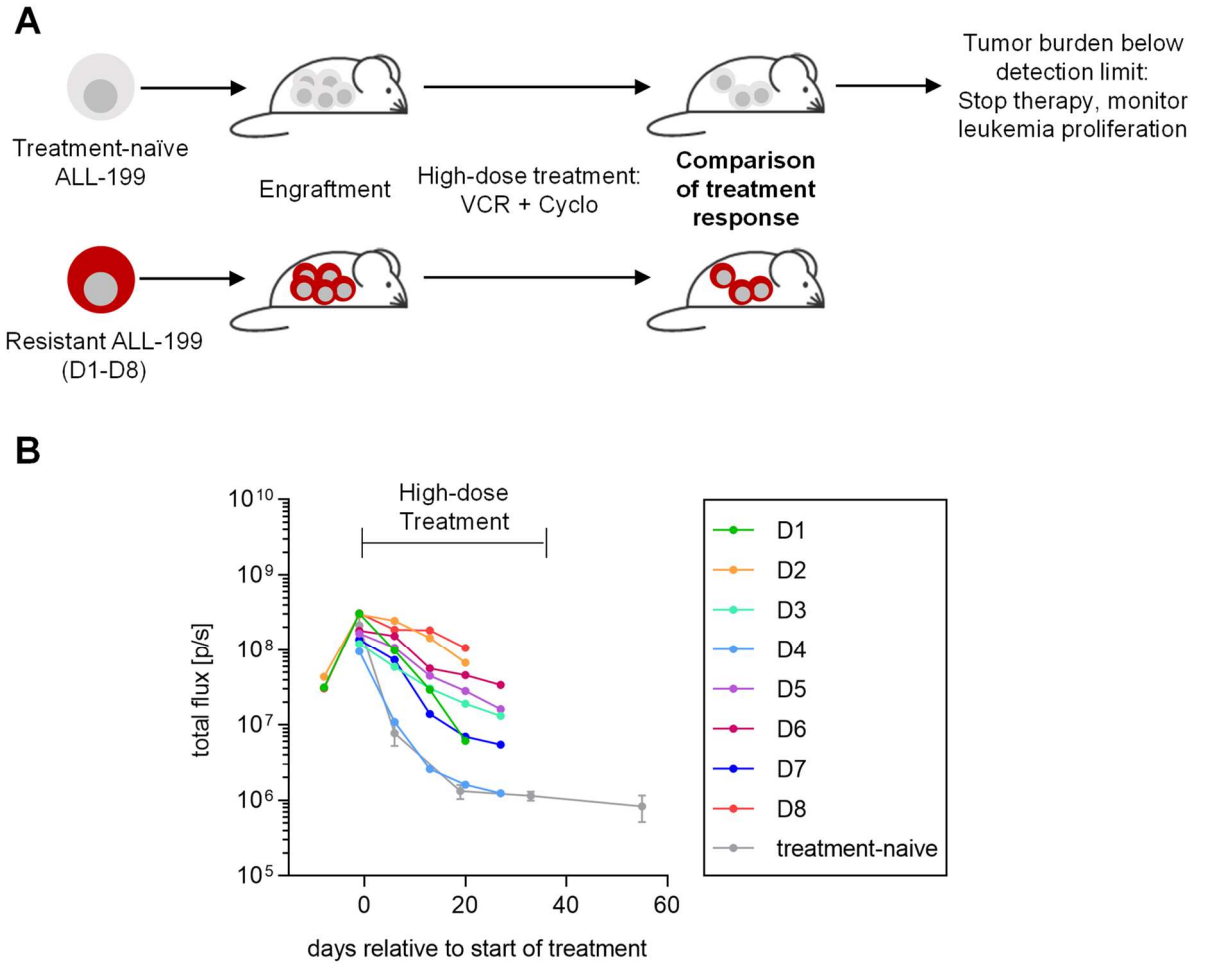

Figure 21: High-dose treatment did not eliminate resistant ALL-199

A) Experimental setup: Resistant derivatives D1-D8 of ALL-199 or treatment-naïve control cells were injected into NSG mice. After confirmed engraftment, mice were treated with the highest tolerated dose of combination chemotherapy (VCR 0.6 mg/kg, Cyclo 100 mg/kg). Treatment response was monitored by repetitive BLI. When tumor burden was below detection limit, therapy was stopped and mice were regularly monitored by BLI to assess leukemia re-growth or cure. B) Quantification of BLI signals showed treatment response in resistant and treatment-naïve ALL-199 cells (n=1 per derivative, n=5 for treatment-naïve control).

Thus, treatment-naïve ALL-199 and resistant derivatives were analyzed regarding their response to the same drugs applied at a higher dose. Treatment-naïve cells and cells from each derivative were re-transplanted into NSG mice (Fig. 21A). After successful engraftment (BLI signal > 10^8 p/s), all mice were treated with a combination chemotherapy of VCR and Cyclo in the highest tolerated dose (0.6 mg/kg and 100 mg/kg, respectively). Treatment was applied for 4-5 weeks and response was analyzed by BLI. Treatment-naïve ALL-199 showed a strong response to high-dose treatment and reached detection limit below 1 x 10^6 p/s in BLI, resembling < 0.001% blasts in BM, within three weeks (Fig. 21B). Consequently, treatment was stopped and mice were further monitored by BLI to analyze if residual cells had survived treatment and would grow out. Three weeks after stop of treatment, no increase in tumor burden was detected, suggesting that mice were cured from their disease.

Resistant derivatives displayed a heterogeneous treatment response to high-dose treatment. Upon treatment, BLI signal was reduced in all resistant derivatives, indicating that none of the

derivatives showed absolute treatment resistance independent from the applied dose. Interestingly, D4 showed a similar sensitivity as treatment-naïve ALL-199. In contrast, treatment hardly reduced tumor load in D2 and D8. In all other derivatives, five weeks of treatment reduced tumor burden by app. 10-fold, thus showing a certain degree of treatment response, but suggesting that a complete cure with a high dosage is unlikely.

Taken together, treatment-naïve ALL-199 most likely were cured with high-dose combination chemotherapy. Resistant derivatives showed heterogeneity in response to high-dose treatment, with D4 responding similar to treatment-naïve ALL-199, while D2 and D8 only showed stable tumor burden. Thus, the obtained data strongly indicated functional heterogeneity of the derivatives.

4.5 Expression profiles of resistant ALL-199

As mentioned above, development of resistance might not only be mediated by genetic alterations, but also by epigenetic and post-transcriptional regulation (Chatterjee and Bivona, 2019). Furthermore, mutations and CNAs would most likely only be relevant for the resistant phenotype, if downstream effects were detected. To this end, gene and protein expression profiles of resistant ALL-199 were established. To determine differentially expressed genes or proteins between resistant and untreated ALL-199 reliably across all derivatives and to ensure sufficient numbers of replicates, resistant samples were analyzed as one group, independently from the individual derivatives. Furthermore, this approach allowed to determine shared expression profiles of all resistant ALL-199 cells, which might enable novel treatment options of more general relevance.

4.5.1 Differential gene expression analysis revealed common profiles

Transcriptome profiling of ALL-199 was performed using samples from the four individual time points during resistance development (Fig. 7) as well as resistant samples both with and without treatment pressure from the subsequent experiments (Fig. 11, Fig. 12, Fig. 20) to increase group size and control for potential bias by the presence of treatment. cDNA isolation, library preparation and quality controls were performed by Lucas Wange (AG Enard, LMU, Munich). Tobias Herold (KUM, Munich) performed initial data processing. Details on analysis procedure is provided in methods section (see 3.6.4). Differential gene expression analysis and subsequent steps were performed by me. Differential gene expression analysis between resistant ALL-199 with and without presence of therapy pressure did not reveal significant differences, indicating that this does not bias the analysis (data not shown). Subsequently, all resistant samples were pooled into one group for analysis. Next, differential gene expression analysis between resistant and untreated ALL-199 was performed. This comparison demonstrated a high number of significantly differentially expressed genes (Fig. 22A and Appendix Table A2). 273 transcripts showed significant upregulation in resistant samples, while 252 showed significant downregulation in resistant samples ($p < 0.01$). Notably, resistant samples overall showed clear differences compared to untreated samples, while the heterogeneity within the resistant sample group was rather small, indicating that the individual derivatives only accounted for minor variability in gene expression profiles.

If differential gene expression was linked to resistance development, intermediate levels of resistance development (i.e. sensitive and transition time points) should potentially show intermediate expression levels. When sensitive and transition samples were analyzed for the expression of the 525 top differentially expressed genes, sensitive samples showed similar expression levels as untreated, while transition samples mostly showed intermediate levels between the two groups (Fig. 22A).

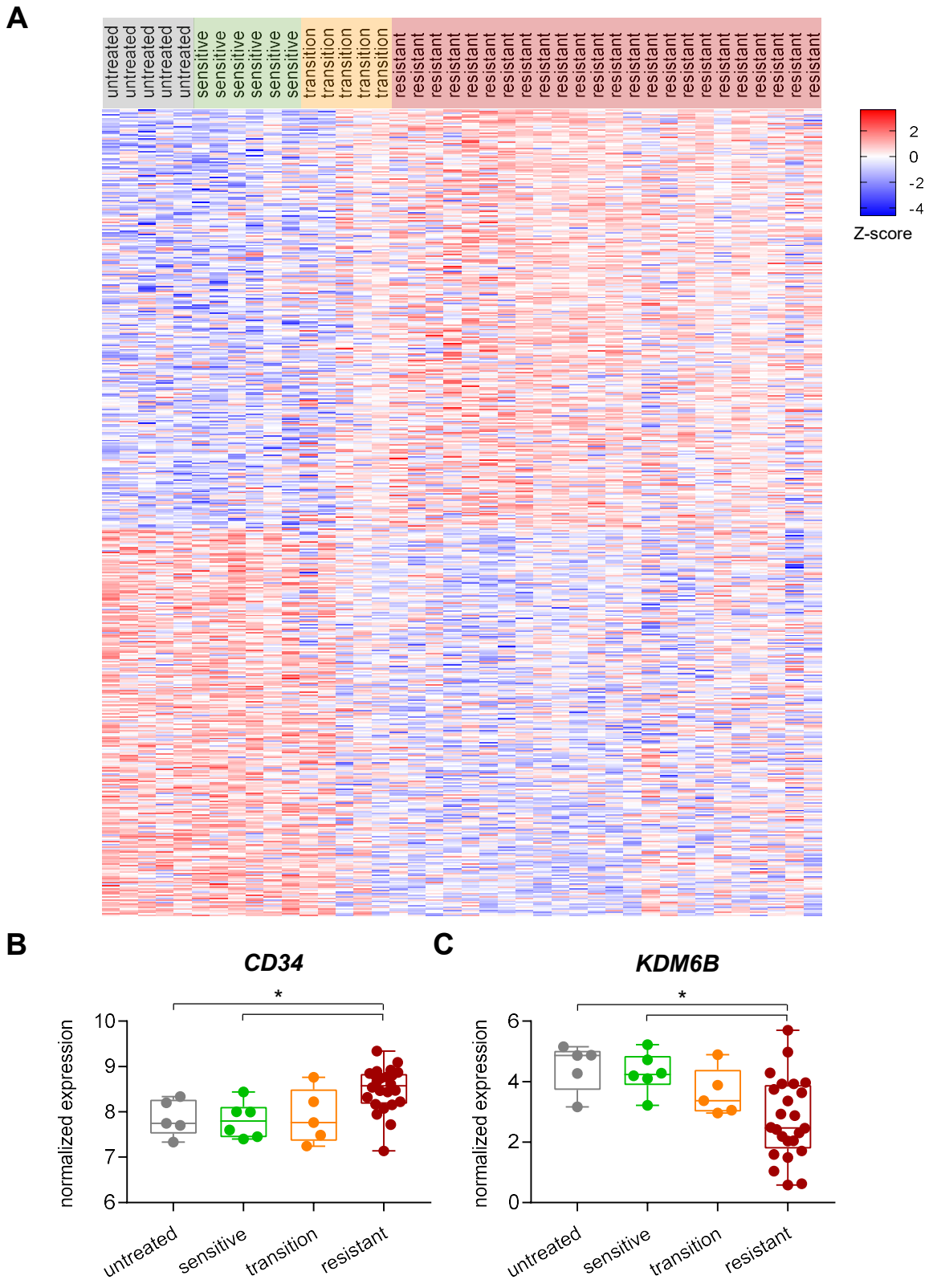

Figure 22: Transcriptome profiles showed differential gene expression during development of resistance

Transcriptome profiles of ALL-199 cells from four stages of long-term treatment (Fig. 7) and subsequent experiments (Fig. 11, Fig. 20) were analyzed using bulk primeSeq (n=5 untreated, n=6 sensitive, n=5 transition, n=24 resistant, n=6 were excluded from analysis due to technical reasons). A) Heatmap of differentially expressed genes between resistant and untreated cells shows transcripts which are consistently up- or downregulated in resistant samples. One row represents one transcript, all transcripts with $p < 0.01$ are shown (n=525, Appendix Table A2). B+C) Normalized read counts for expression of *CD34* (B) and *KDM6B* (C) mRNA. One dot represents one mouse. Statistical analysis was performed using one-way ANOVA followed by Tukey´s multiple comparisons test. *: $p < 0.05$.

Normalized transcript expression analysis of two exemplary transcripts further strengthened this observation (Fig. 22B, C). *CD34* was found to be one of the most upregulated candidates in resistant cells compared to untreated as assessed by p-value. Normalized transcript expression of the four individual groups showed a significant upregulation not only between untreated and resistant, but also between sensitive and resistant samples, while transition samples showed intermediate expression levels (Fig. 22B). Vice versa, normalized transcript expression of *KDM6B*, which was one of the most significantly downregulated candidates between resistant and untreated, not only confirmed this finding but again showed significant downregulation between sensitive and resistant samples and intermediate expression in transition samples (Fig. 22C).

Taken together, resistant ALL-199 show common, differentially expressed genes compared to untreated ALL-199, indicating that genes are differentially regulated during resistance development. These transcripts might help to identify the resistance mechanism.

4.5.2 Differential protein expression analysis revealed common profiles

To complement transcriptome profiling and to account for post-transcriptional regulation, which might differ between resistant and untreated ALL-199, proteome analysis was performed. Sample preparation and initial data analysis was performed by Ashok Kumar Jayavelu (AG Mann, MPI, Planegg). I performed subsequent data analysis. Four samples from untreated time points were analyzed together with four different resistant derivatives and their corresponding four samples from following experiments without treatment pressure, which were pooled together in one resistant group to obtain a larger group size (Fig. 7, Fig. 20).

Principal component analysis revealed a separation between untreated and resistant samples (Fig. 23A). Notably, one resistant sample clustered separately. For analysis of differentially expressed proteins, resistant samples were pooled into one group, resulting in eight resistant samples. Analysis of differentially expressed proteins revealed significantly up- and downregulated proteins in resistant cells (Fig. 23B). The top 22 differentially expressed proteins contained eight proteins consistently downregulated and 14 upregulated proteins. Of note, four of these proteins were not upregulated in the absence of treatment pressure, while the other proteins were consistently upregulated, with a tendency to higher expression in the original resistant derivatives. Importantly, protein expression analysis did not reveal differences in expression between the individual derivatives. Taken together, proteome profiling revealed differentially expressed proteins between resistant and untreated ALL-199 cells.

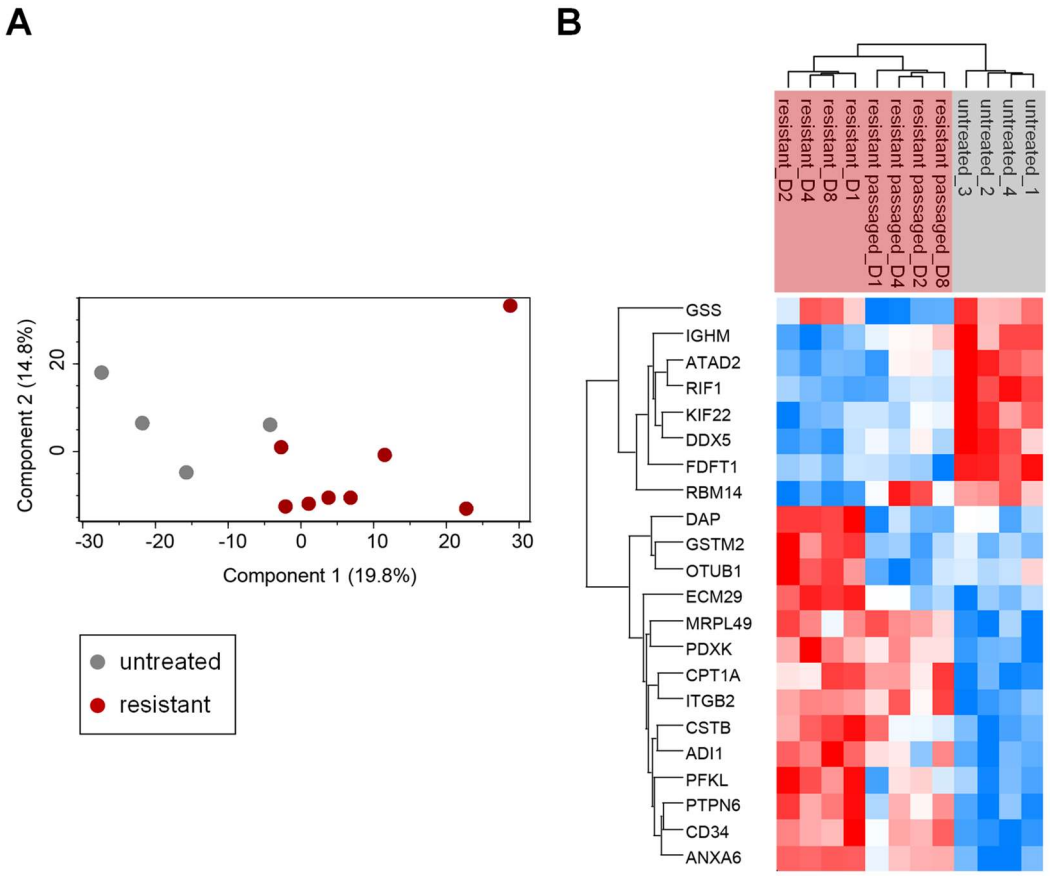

Figure 23: Resistant cells showed differential protein expression

Proteome profiling of untreated and resistant ALL-199 from long-term treatment (Fig. 7) and resistant ALL-199 after serial transplantation (Fig. 20, n = 4 for each group). A) Principal component analysis of proteome data shows that resistant and untreated samples cluster separately regarding protein expression. One dot represents one mouse, resistant ALL-199 from long-term treatment and after serial transplantation were classified as one group. B) Heatmap of top 22 differentially expressed proteins between untreated and resistant ALL-199.

4.5.3 Selection of candidate genes for further evaluation

Despite genomic and functional heterogeneity, resistant derivatives of ALL-199 showed common profiles of differentially expressed genes and proteins compared to untreated ALL-199 cells. This suggested that even if genomic hits leading to resistance were unique for each derivative, downstream effects might be similar. In consequence, they presented common targets of all derivatives to tackle treatment resistance.

In theory, development of resistance could be accompanied by upregulation of genes which drive the resistant phenotype (Fig. 24). These candidates might represent putative therapeutic targets and their inhibition could lead to re-sensitization of resistant leukemia cells. I therefore extracted upregulated genes from transcriptome and proteome profiling to target them by CRISPR/Cas9-mediated knockout (Doudna and Charpentier, 2014). If a candidate was essential for maintenance of resistance, a knockout of the respective candidate in resistant cells would lead to restored treatment sensitivity *in vivo*. The CRISPR/Cas9 system allowed parallel screening of many candidate genes using a sgRNA library (Shalem et al., 2014, Wang et al., 2014). My group had recently established CRISPR/Cas9 *in vivo* screens in PDX models of acute

leukemia (unpublished results). Here, it became obvious that library screening *in vivo* was limited by the maximum number of leukemic cells that can be injected and engraft into NSG mice, requiring a customized selection candidate genes (data provided by Ehsan Bahrami). Based on the established setup, I adapted this innovative technique to study upregulated genes for their relevance in maintenance of resistance, aiming for app. 200 genes to be tested.

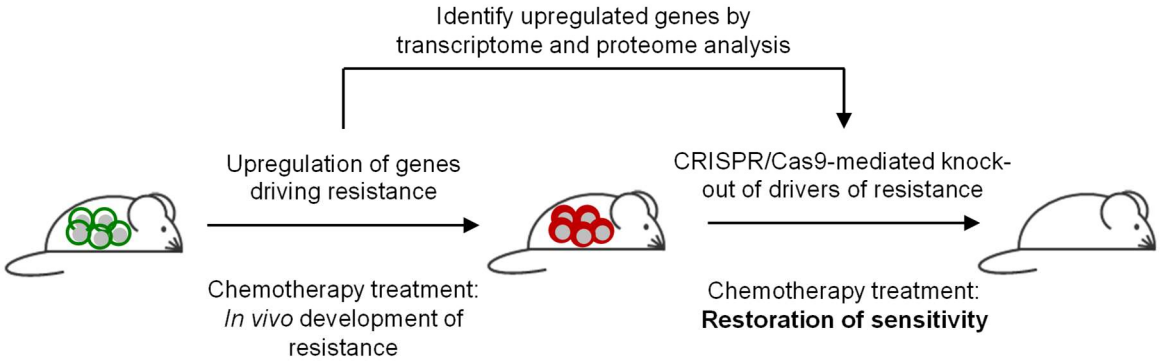

Figure 24: Hypothesis for development of resistance and experimental approach

During long-term *in vivo* treatment, PDX ALL cells develop resistance, possibly by upregulating genes driving resistance. Upregulated genes are identified by analysis of differentially expressed transcripts and proteins. CRISPR/Cas9-mediated knockout of identified candidates in resistant cells might inhibit the resistance mechanism, thus restoring treatment sensitivity.

In a first step, transcriptome and proteome profiles were filtered for significantly upregulated targets in resistant ALL-199 cells in order to define a list of candidates. Candidates from transcriptome analysis were chosen based on p-value and $\log_2$-fold change between resistant and untreated ALL-199 (Fig. 25A, left panel). Out of 15210 transcripts identified in total, only transcripts with p-value < 0.005 and $\log_2$-fold change > 0, i.e. significantly upregulated in resistant compared to untreated ALL-199 cells, were considered for further evaluation, resulting in 240 candidates (Fig. 25A, right panel, Appendix Table A2). Further selection criteria were applied to reduce the number of candidates. Pseudogenes, non-coding RNAs and unknown transcripts were excluded, since validation of these targets is technically challenging. All remaining candidates were evaluated by database research for function and expression, resulting in 135 candidates for further validation (Appendix Table A4).

Proteome data was evaluated in a similar way to identify significantly upregulated proteins in resistant vs. untreated ALL-199 cells (Fig. 25B, left panel). From a total of 3457 detected proteins, candidates were selected based on p < 0.01 between resistant and untreated, resulting in 85 candidates (Fig. 25B, right panel, Appendix Table A3). Identified peptides which could not clearly be annotated to one gene were excluded. Additionally, overlaps between proteome and transcriptome were included into the candidate list even if p-values exceeded the defined threshold. Notably, the overlap only included 7 genes. In total, 223 candidates from proteome and transcriptome analysis were chosen for further characterization (Appendix Table A4).

In summary, both transcriptome and proteome profiling revealed substantial differences in expression profiles of resistant and untreated ALL-199 cells. In addition, differentially expressed candidates showed similar expression levels across the resistant derivatives. Upregulated candidates might represent putative therapeutic targets, since their inhibition could lead to restoration of treatment sensitivity in resistant leukemia cells. Accordingly, a list of target genes was designed for subsequent investigation using CRISPR/Cas9 library screening.

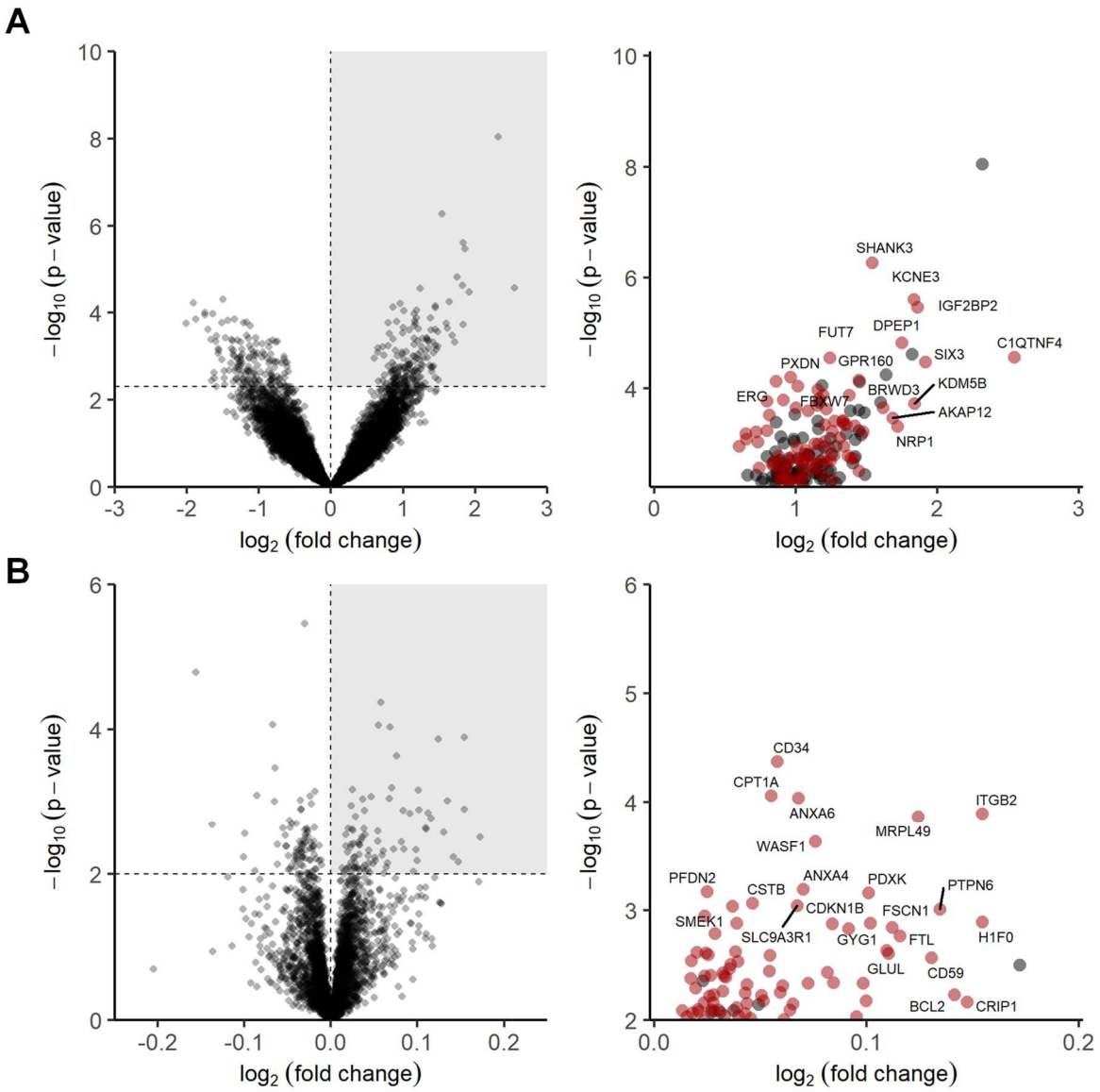

Figure 25: Selection of significantly upregulated genes from transcriptome and proteome analysis

A) Left panel: Volcano plot of differential gene expression between resistant and untreated ALL-199 identified by primeSeq analysis. One dot represents one transcript. Dashed lines indicate cut-offs for significant up- or downregulation ($p < 0.005$ and log_2 fold-change > 0 or < 0). Grey area indicates significantly upregulated transcripts specified in the right panel. Right panel: Significantly upregulated genes of left panel. Red dots indicate candidates which were chosen for further analyses. Labels indicate top-ranked protein-coding transcripts. B) Left panel: Volcano plot of differential protein expression between resistant and untreated ALL-199 identified by mass spectrometry analysis. One dot represents one protein. Dashed lines indicate cut-offs for significant up- or downregulation ($p < 0.01$ and log_2 fold-change > 0 or < 0). Grey area indicates significantly upregulated proteins specified in the right panel. Right panel: Significantly upregulated proteins of left panel. Red dots indicate candidates which were chosen for further analyses. Labels indicate top-ranked proteins.

4.6 CRISPR/Cas9 *in vivo* screen to identify drivers of resistance

Transcriptome and proteome profiling identified candidates, which were consistently upregulated in resistant ALL-199 cells compared to untreated cells. This suggested that these candidates might be essential for maintenance of the resistant phenotype. To enable targeted, parallel analysis of all candidates, a CRISPR/Cas9 *in vivo* library dropout screen was performed. This was facilitated with a customized sgRNA library consisting of many plasmids, of which each one contained a specific sgRNA sequence targeting one of the candidate genes.

While the CIRSPR/Cas9 system and its use for dropout screens in PDX leukemia models *in vivo* was generally established in the lab, I adapted it here to functionally validate upregulated targets. First, the CRISPR/Cas9 system was established in resistant ALL-199 cells and functionality and gene editing efficiency was analyzed. Following this, library cloning was performed to ultimately perform a CRISPR/Cas9 *in vivo* screen in resistant ALL-199 cells. PCR amplification of the sgRNA locus followed by NGS allowed individual analysis of each gene with MAGeCK (Li et al., 2014). With this approach, the list of candidates was narrowed to a few genes, which were then individually validated for their role in maintaining resistance.

4.6.1 CRISPR/Cas9 is functional in resistant ALL-199

To facilitate targeted knockout using the CRISPR/Cas9 system, Cas9 endonuclease and a sgRNA targeting a specific genomic locus needed to be delivered into target cells. In resistant ALL-199 cells, this was enabled using a two-step lentiviral transduction to enable stable expression of Cas9, followed by additional stable expression of the sgRNA.

To this end, human codon-optimized Streptococcus pyogenes Cas9 (hSpCas9, abbreviated with Cas9) was cloned into a lentiviral backbone under control of the SFFV promoter (cloning performed by Wen-Hsin Liu). I modified the existing vector to express the fluorochrome marker mCherry in addition (Fig. 26A). Both sequences were linked by a T2A self-cleaving peptide, enabling equimolar expression of Cas9 and mCherry. mCherry expression was used as a surrogate of Cas9 expression and to enrich transduced cells by FACS (Fig. 26B). Due to the large size of the Cas9 gene of app. 4.3 kb, initial transduction in resistant ALL-199 D7 cells achieved a low efficiency of 8.13%, as expected. mCherry-positive cells were sorted and amplified in NSG mice, achieving enrichment to 54.2% positive cells. A second sorting and amplification step resulted in a purity of 89.3% mCherry-positive cells. This population was used for subsequent transduction with the lentivirus harboring the sgRNA sequence.

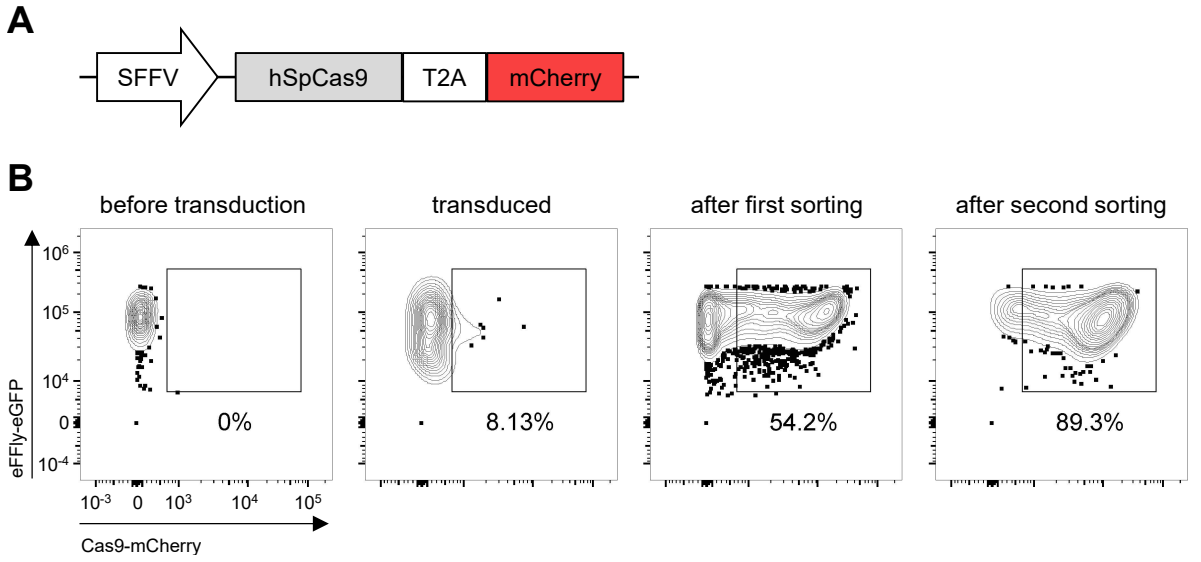

Figure 26: Constitutive expression of Cas9 in resistant ALL-199

A) Scheme of lentiviral construct: humanized S. pyogenes Cas9 (Cas9) and mCherry as fluorochrome marker are expressed under the control of spleen focus-forming virus (SFFV)-promoter. B) Flow cytometric analysis of Cas9 expression in resistant ALL-199 D7 on day 7 after transduction and after two enrichment steps by FACS.

To assess functionality of Cas9 and editing efficiency of the CRISPR/Cas9 system in resistant ALL-199, Cas9-expressing cells were transduced with a sgRNA targeting *CD19*, which encodes a well-described surface marker of B-cells. This enabled easy readout of gene editing efficiency by surface antibody staining of CD19 and flow cytometry analysis. Two different sgRNAs targeting *CD19* were individually cloned into a lentiviral backbone (cloning performed by Martin Becker), resulting in expression of the sgRNA and its scaffold under control of the human H1 promoter (Fig. 27A). Additionally, the plasmid encoded the fluorochrome marker mtagBFP under control of the human EF1α promoter, allowing analysis of transduced cells by flow cytometry. I transduced Cas9-positive ALL-199 with either of the two sgRNA constructs and analyzed CD19 expression 14 days later by flow cytometry (Fig. 27B). Gating was performed based on viable lymphocytes and expression of the pre-existing eFFly-eGFP and Cas9-mCherry constructs. Double-positive cells were analyzed for sgRNA expression using the mtagBFP marker and mtagBFP-negative cells served as internal control of CD19 expression. Staining of CD19 revealed a high expression of CD19 in the control population, while expression was strongly reduced in mtagBFP-positive cells. Thus, gene editing of the CD19 locus was successful, indicating that Cas9 is functional in resistant ALL-199 D7 cells.

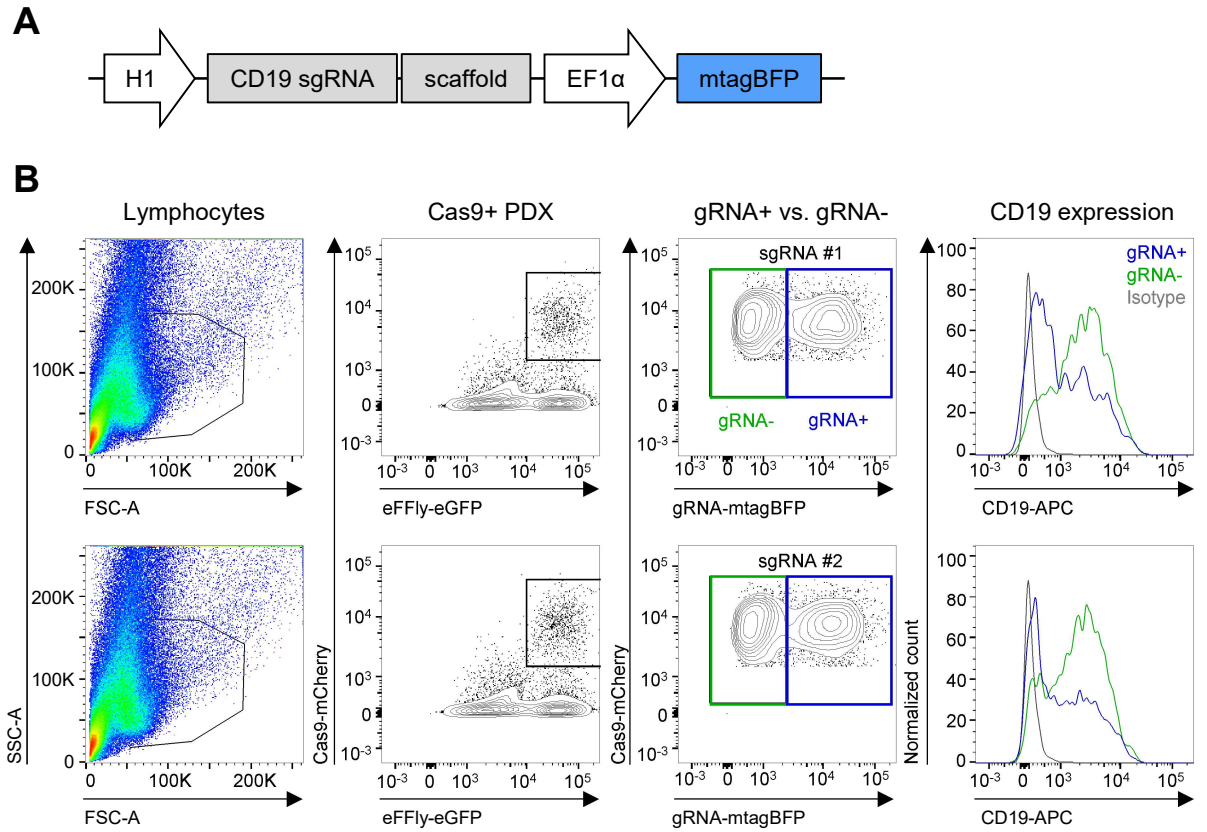

Figure 27: Functionality of the CRISPR/Cas9 system in resistant ALL-199

A) Scheme of lentiviral construct: *CD19* single guide RNA (sgRNA) and scaffold are expressed under control of the human H1 promoter, followed by mtagBFP as fluorochrome marker under the control of the human EF1α-promoter. B) Flow cytometric analysis CD19 after gRNA transduction. Two different sgRNA targeting *CD19* (upper and lower panels, respectively) were transduced into Cas9-expressing ALL-199. Gating was performed based on viability ("Lymphocytes"), Cas9-mCherry expression ("Cas9+ PDX") and gRNA-mtagBFP expression ("gRNA+ vs. gRNA-"). Efficiency of gene editing was compared between gRNA-positive and gRNA-negative cells based on CD19 surface staining ("CD19 expression") on day 14 after transduction.

4.6.2 Cloning of sgRNA library

After functionality of CRISPR/Cas9 gene editing in ALL-199 cells had been verified, I designed and cloned a sgRNA library for testing of the defined candidates. The library was designed to target all 223 previously defined candidates from proteome and transcriptome analysis, together with eleven pan-essential genes extracted from Project Achilles as positive controls (Fig. 28A). Five sgRNAs per target were selected based on well-established algorithms and supplemented with 26 non-targeting sgRNAs as negative controls (Doench et al., 2016, Sanson et al., 2018, Kim et al., 2018). In total, the library contained 1,196 different sgRNA sequences. This library was cloned into the sgRNA cloning site of a lentiviral backbone, which allowed expression of sgRNA and its scaffold under control of the human H1 promoter (Fig. 28B). Furthermore, expression of a H2Kk-mtagBFP fusion construct under control of the human EF1α promoter enabled enrichment of transduced cells using both MACS of the resulting surface protein as well as FACS based on mtagBFP expression. Library design and cloning was

performed as previously established by our group (Becker et al., 2020). Details on cloning procedure are listed in the methods section (see 3.5.4).

Cloning efficiency and library composition of the plasmid pool were analyzed by PCR amplification and NGS of the sgRNA locus. Analysis of read counts per individual sgRNA showed a narrow distribution of individual sgRNAs (Fig. 28C). Only three sgRNAs received less than 10 reads in sequencing, indicating that they were lost during cloning. This resembles a cloning efficiency of 99.7%. The evenness of read count distributions in comparison to a perfect distribution, in which, e.g., 10% of sgRNA sequences would also be covered with 10% of sequencing reads, was analyzed using the GINI Index (Wang et al., 2019) (Fig. 28D). Read count distribution of the cloned library resembled a GINI Index of 0.3182, indicating a high quality and homogeneous distribution of sgRNAs in the library pool. In conclusion, library cloning was highly efficient and individual sgRNAs were distributed homogeneously within the library.

A

Group	Number of genes	Number of sgRNAs
Upregulated in Proteome	81	405
Upregulated in Transcriptome	135	675
Upregulated in Proteome AND Transcriptome	7	35
Positive control	11	55
Non-targeting control	NA	26
Total	**234**	**1196**

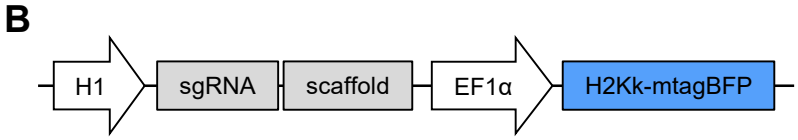

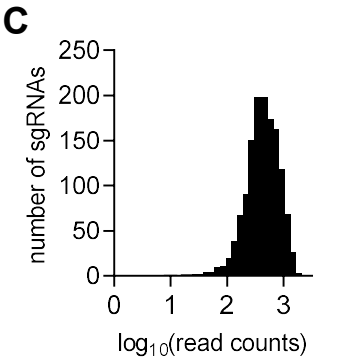

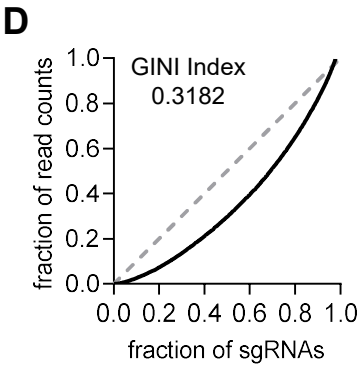

Figure 28: Composition and quality control of sgRNA library

A) The sgRNA library contained 5 sgRNAs per candidate gene upregulated in resistant cells in differential analysis of either proteome, transcriptome or both (Fig. 25), complemented by positive and negative controls (supplementary table A4). B) Scheme of lentiviral construct: individual sgRNAs of the library together with scaffold are expressed under control of human H1 promoter, followed by mtagBFP-H2Kk fusion marker enabling MACS and FACS enrichment under control of the human EF1α-promoter. C) Read count distribution of sgRNA library plasmid after cloning as determined by NGS and counting of reads per individual sgRNA (log_{10} read counts per sgRNA). D) Cumulative read count distribution of sgRNA plasmid. Dotted line represents perfect distribution, solid line represents cloned sgRNA library plasmid. GINI Index was calculated as area under the curve $(AUC)_{plasmid}$ / $AUC_{perfect\ distribution}$.

4.6.3 Technical setup of CRISPR/Cas9 *in vivo* screen

The established library was subsequently used to evaluate the relevance of the identified candidates for maintenance of the resistant phenotype. To this end, a CRISPR/Cas9 *in vivo* screen of resistant ALL-199 D7 was performed (Fig. 29). Notably, due to limited resources, *in vivo* screening and subsequent validation was limited to D7, because it represents the major group of derivatives with loss of Chr. 1p36 and an irreversible resistant phenotype.

Cas9-expressing, resistant ALL-199 D7 cells were transduced with the sgRNA library pool and engrafted into groups of mice, while one fraction of cells was reserved as input control. Importantly, cells were kept *in vitro* for three days to enable H2Kk marker expression for enrichment of sgRNA-positive cells. However, within this period, gene editing most likely had not taken place yet and the input sample should harbor a complete representation of the sgRNA library pool. Following successful engraftment, mice were randomly distributed to three groups: One group served as start of treatment control, one group received three weeks of combination chemotherapy as previously established and one group received three weeks of PBS.

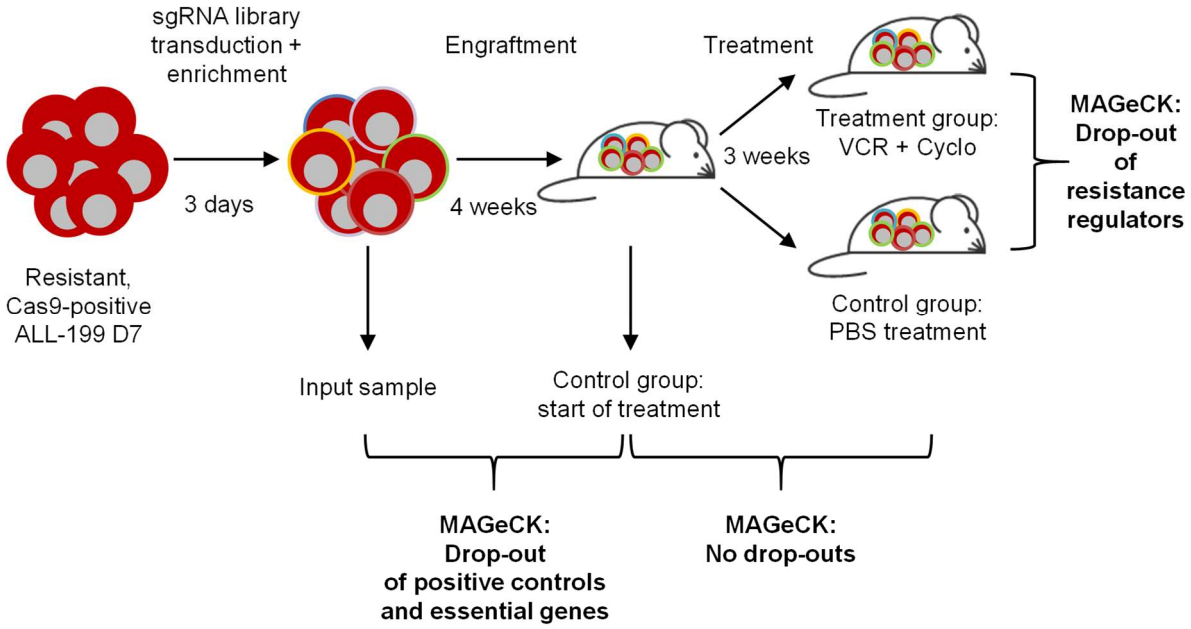

Figure 29: Experimental setup of CRISPR/Cas9 *in vivo* screen

Resistant ALL-199 D7, which had been transduced with Cas9-mCherry (Fig. 26) were transduced with sgRNA library, enriched for H2Kk-mtagBFP expression, and injected into groups of NSG mice, restoring one fraction of cells as input sample. After successful engraftment, a control group of mice was sacrificed for NGS analysis of the sgRNA loci. Remaining mice received VCR and Cyclo treatment as previously established or PBS control treatment. After three weeks of treatment, leukemic cells were re-isolated and library composition was analyzed by NGS. Comparison of different experimental groups with MAGeCK allowed to identify main regulators of resistance and to control quality of the screen.

Comparative NGS analysis of the library compositions between the individual groups using MAGeCK was expected to show various results: During the engraftment period, gene editing should take place and subsequently cells with knockout of a gene essential for cell survival should be depleted. Thus, when sgRNA composition of input and start of treatment groups were compared, a depletion of positive control sgRNAs was supposed be detected in the start of treatment group. PBS treatment should not lead to further depletion of cells, thus MAGeCK analysis of PBS treated vs. start of treatment would not identify any depletions but might only increase differences due to three more weeks of growth. In contrast, knockout of a gene which is essential for treatment resistance would cause restoration of treatment sensitivity. In a library screen setup, cells with a knockout of such a gene would be diminished upon treatment compared to cells with knockout of genes not relevant for resistance. In consequence, sgRNAs targeting the respective gene would not be identified anymore after treatment in comparison of chemotherapy treated vs. PBS treated cells.

With this rationale, the experimental setup of the CRISPR/Cas9 *in vivo* screen was performed as previously established in the lab (unpublished data provided by Ehsan Bahrami). Cas9-expressing, resistant ALL-199 D7 cells, which had been generated previously (Fig. 26), were transduced with the sgRNA library aiming for a low transduction efficiency of app. 30% to ensure single integration of only one sgRNA per cell (Fig. 30). Three days after transduction, H2Kk-positive cells were enriched by MACS to a purity of 92.4% sgRNA-positive cells. One fraction of cells was restored as input sample to analyze library composition within the transduced cell pool. Based on previous results of the group, it was assumed that 5% of injected cells engraft in murine bone marrow (unpublished data provided by Ehsan Bahrami). Aiming for a coverage of 200 cells per sgRNA with a library size of 1,193 sgRNAs, at least 4.8 Mio transduced cells were injected per mouse.

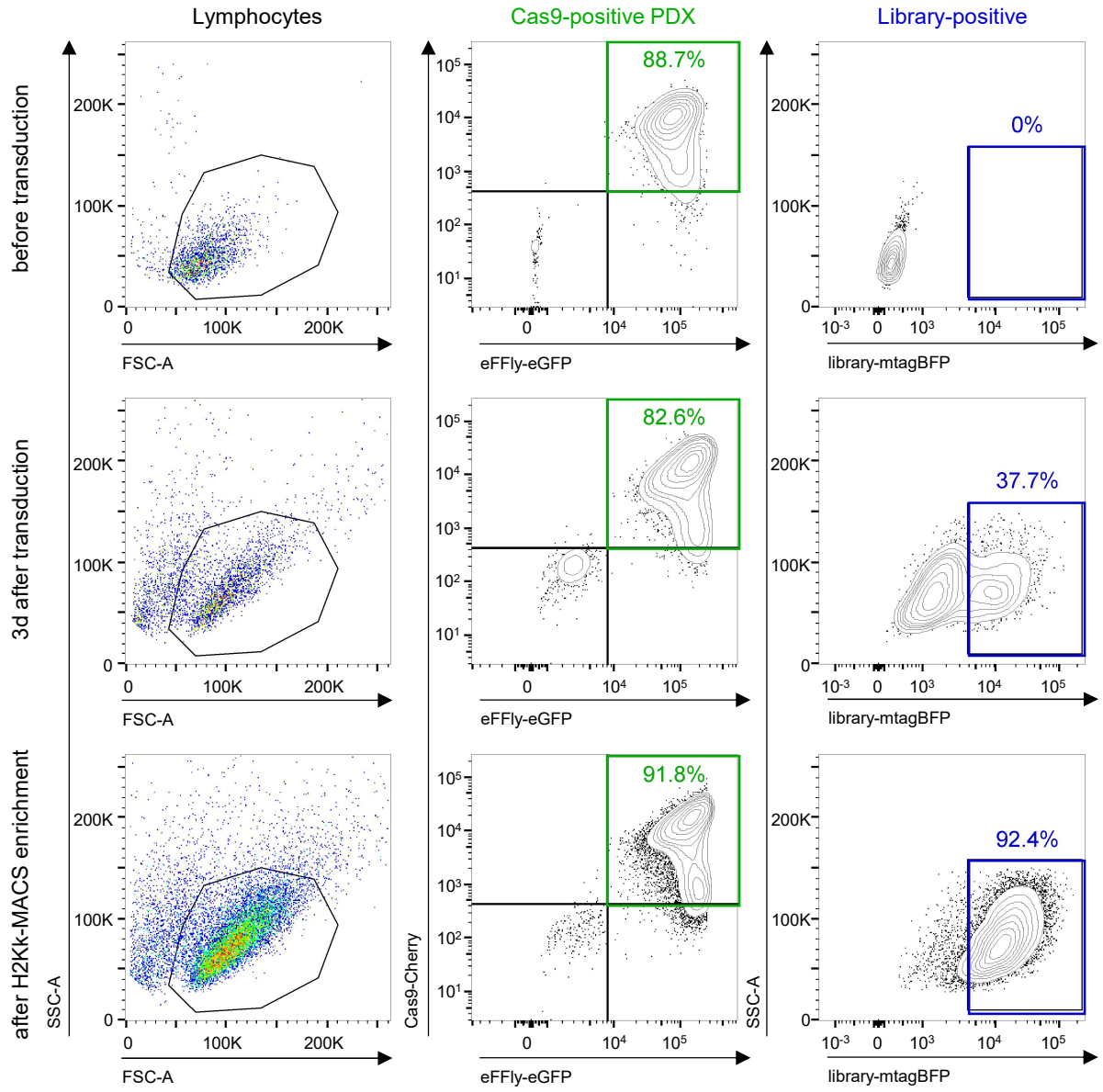

Figure 30: Transduction and enrichment of sgRNA library in ALL-199 D7

Flow cytometric analysis of ALL-199 D7 before library transduction (upper panel), three days after transduction (middle panel) and after H2Kk-MACS enrichment prior to injection (lower panel). Gating strategy included gating on viable cells ("Lymphocytes"), followed by analysis of Cas9-mCherry and library-mtagBFP expression. Cas9-positive PDX cells were analyzed for expression of library-mtagBFP, verifying successful transduction and enrichment.

The enriched cell pool was transplanted into groups of NSG mice and engraftment was monitored by repetitive BLI (Fig. 31). At a mean BLI signal of 1 x 10^9 p/s, mice were randomly distributed to the three defined groups. Importantly, BLI showed that all mice engrafted and that they did not display differences between the individual groups. Upon treatment, mice receiving combination chemotherapy showed a slightly reduced signal, i.e. mean BLI of 8.15 x 10^{10} p/s in chemotherapy treated vs. 1.57 x 10^{11} p/s in PBS treated group at day 20 after start of treatment. After three weeks of treatment, mice were sacrificed and PDX cells were re-isolated from murine BM to analyze library composition by NGS. Taken together, the established experimental workflow of CRISPR/Cas9 *in vivo* screening was successfully adapted for use in resistant ALL-199 cells.

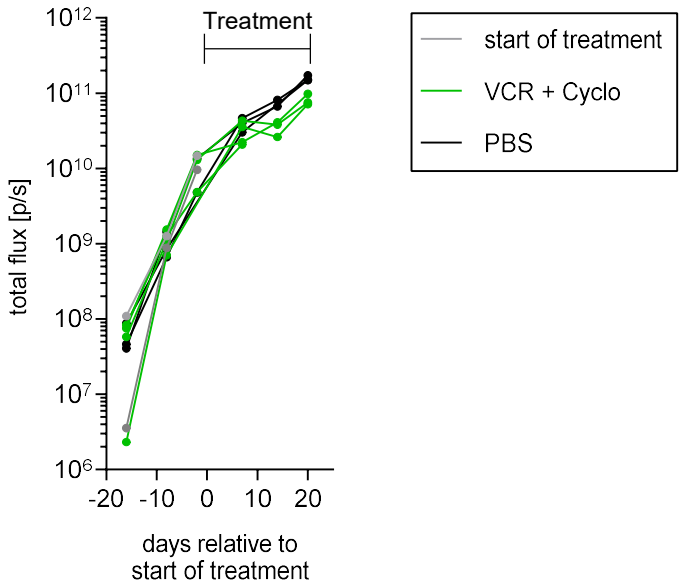

Figure 31: BLI of CRISPR/Cas9 *in vivo* library screen

Experimental setup as described in Fig. 29. Tumor growth and treatment response was monitored by regular BLI. Quantification of BLI signals, one lines represents one mouse (n=2 start of treatment, n=3 PBS treated, n=4 VCR and Cyclo).

4.6.4 Read count distribution of CRISPR/Cas9 screening groups

Next, the library compositions of the individual screening groups were analyzed and compared in order to identify essential candidates of the resistance phenotype and to evaluate screening quality. To this end, gDNA was isolated from BM of each mouse and the sgRNA locus was amplified by PCR for subsequent NGS based on established protocols (Becker et al., 2020). Read counts of the individual time points were counted and drop-outs were calculated using MAGeCK (Li et al., 2014). Technical details on NGS procedure are provided in the methods section (see 3.5.12, 3.6.2, 3.8.2).

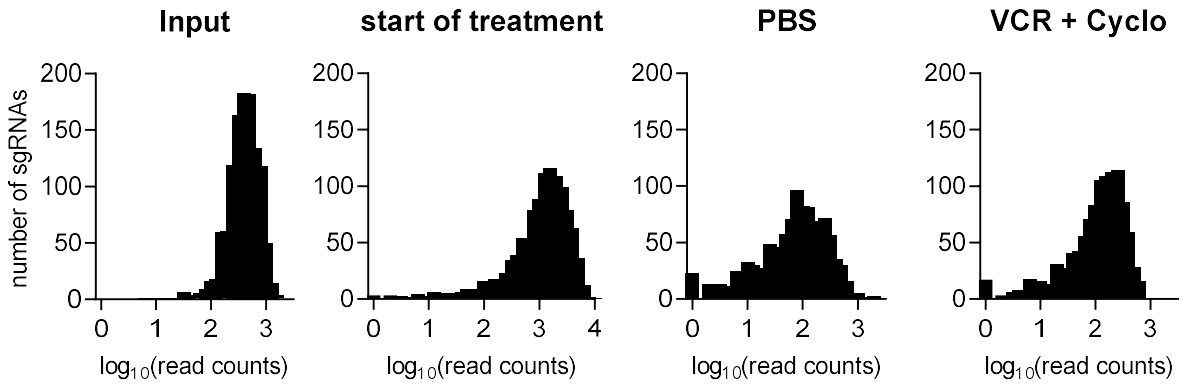

Figure 32: Read count distribution in CRISPR/Cas9 *in vivo* library screen

Experimental setup as described in Fig. 29. sgRNA locus was amplified from purified PDX gDNA and analyzed by NGS. Depicted are $\log_{10}$-transformed read counts of one representative mouse per group or of input sample, respectively.

gDNA isolation and initial PCR were performed aiming for a coverage of 500 cells per sgRNA. Sample-specific identifiers were added by a second PCR and NGS was performed, aiming for 2×10^6 reads per sample. Read counts for each individual sgRNA were counted and distribution was analyzed (Fig. 32). The input sample was analyzed to assess library representation within the PDX population after transduction. Ideally, this should be identical to the plasmid pool (Fig. 28C), indicating that transduction did not bias library distribution and that all sgRNAs were successfully transduced. Read count distribution of the input sample showed a narrow distribution (Fig. 32). Out of 1,193 cloned sgRNAs, 1,191 were covered with at least 10 reads. This showed that library transduction was successful and library representation was preserved. The start of treatment group indicated whether gene editing was successful. During four weeks of engraftment *in vivo*, each cell should acquire a knockout of the respective target. Thus, positive controls targeting genes which are essential for cellular function should be depleted and the respective sgRNAs not be identified anymore. Read counts showed skewing and more sgRNAs with few read counts compared to the input sample, indicating effective gene editing. This effect was increased in PBS and treated samples, indicating more gene editing over time. In summary, the read count distributions indicated a successful screening approach.

4.6.5 Analysis of CRISPR/Cas9 screen using MAGeCK

Read count distributions of individual screening groups indicated a successful screening approach. To verify depletion of positive controls and to determine interesting candidates essential for maintenance of resistance, pairwise MAGeCK was performed as previously described (Li et al., 2014) (Fig. 33). MAGeCK summarized all biological replicates from a certain group and summarizes the five individual sgRNAs into an overall analysis of each gene, resulting in p-value, false discovery rate (FDR) and $\log_2$-fold change between two distinct groups for each gene. Significantly depleted genes (dropouts) were defined by p-value < 0.05 and FDR < 0.3.

Quality controls included comparison of treatment start group vs. input to analyze whether gene editing was efficient and positive controls were depleted. MAGeCK analysis of the two groups revealed that all eleven positive controls were significantly depleted in the start of treatment group compared to input (Fig. 33A). This clearly showed that gene editing was successful. Further dropouts in this comparison indicated genes, which might be essential for engraftment or proliferation of resistant ALL-199. Next, PBS-treated samples were compared with start of treatment samples. Here, MAGeCK did not reveal any significantly depleted gene (Fig. 33B). This confirmed the anticipated result, since no changes were expected within three weeks of PBS treatment following the initial engraftment, in which all essential genes had already been depleted. Both results clearly showed that screening setup worked as predicted.

Finally, chemotherapy treated samples were compared with PBS treated samples to identify genes, which were essential for resistance maintenance. MAGeCK revealed six genes which were significantly depleted (Fig. 33C). Notably, this again included two positive controls, *SARS* and *RPL37*, which had already been significantly depleted before treatment (Fig. 33A). Furthermore, the candidate genes *TBX21*, *BCL2*, *SCN1B* and *CSNK2A1* were identified as significantly depleted upon treatment. Analysis of the log_2-fold change of the four genes showed a strong reduction between treated and PBS group, while levels were comparable between all other groups (Fig. 33D). In contrast, the positive control *SARS* showed strong reduction mainly in the comparison of start of treatment vs. input, indicated as negative log_2-fold change, while a negative control remained unchanged in all comparisons. T-Box Transcription Factor 21 (*TBX21*), a transcription factor involved in the regulation of developmental processes, and B-cell lymphoma 2 (*BCL2*), a protein that blocks apoptotic cell death, showed the highest depletion under therapy, indicating that these targets might be the most relevant drivers of acquired resistance.

Taken together, quality controls of the CRISPR/Cas9 *in vivo* screen in resistant ALL-199 showed the predicted outcome, indicating that dropouts provide reliably candidates. The four genes *TBX21*, *BCL2*, *SCN1B* and *CSNK2A1* were specifically depleted upon treatment of resistant ALL-199 cells. This indicated that these genes were relevant for maintenance of resistance and an individual validation of these candidates should be performed to further define their role in maintenance of resistance.

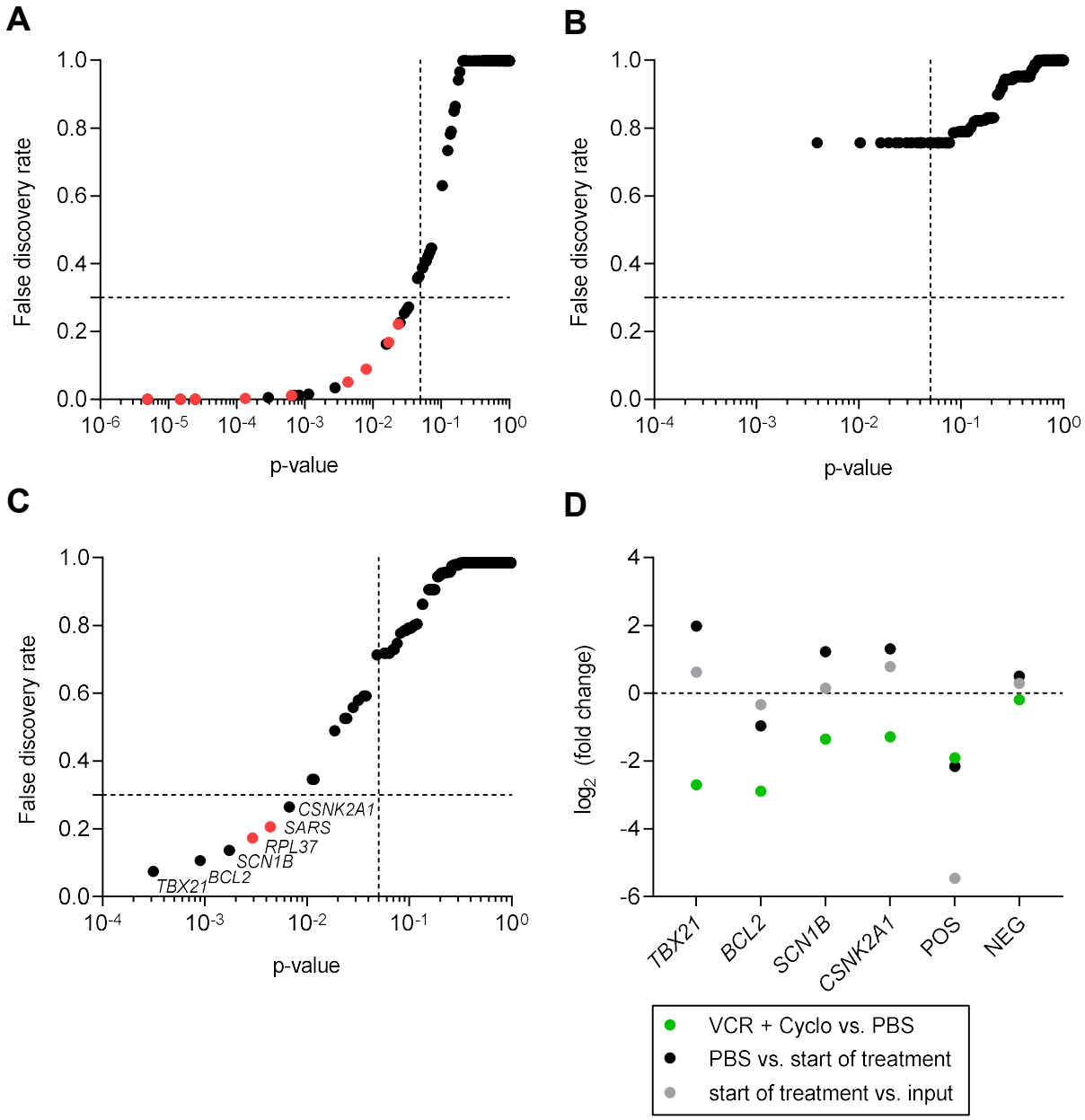

Figure 33: MAGeCK analysis of CRISPR/Cas9 *in vivo* library screen

A)-C) Visualization of MAGeCK comparison. Plotted is p-value vs. false discovery rate (FDR) for each individual comparison. One dot represents one gene (pooled analysis of 5 sgRNAs per gene). Red dots indicate positive controls with $p < 0.05$. Dashed lines indicate cut-off of $p = 0.05$ and FDR = 0.3. MAGeCK comparisons of (A) start of treatment vs. input, (B) PBS vs. start of treatment and (C) VCR and Cyclo vs. PBS. D) Combined analysis of p-values depicted in A)-C) for top candidates, including one positive (POS) and negative (NEG) control. Top candidates are defined by $p < 0.05$ and FDR < 0.3 in C).

4.6.6 Molecular and pharmacological validation of Bcl-2 as potential target

In a final step and as a proof-of-principle, the relevance of Bcl-2 for drug resistance was validated. Bcl-2 was a top hit obtained from CRISPR/Cas9 *in vivo* screen and upregulated in proteome analysis of resistant ALL-199. Since resistant ALL-199 cells with knockout of *BCL2* were only depleted upon treatment with combination chemotherapy, this was implemented into the experimental setup. Validation was performed with two different experimental approaches: On the one hand, effect of individual knockout of *BCL2* upon therapy pressure was assessed using CRISPR/Cas9 (Fig. 34A). On the other hand, treatment with the Bcl-2 inhibitor Venetoclax was used as a surrogate for knockout of *BCL2* and applied together with combination chemotherapy (Fig. 35A).

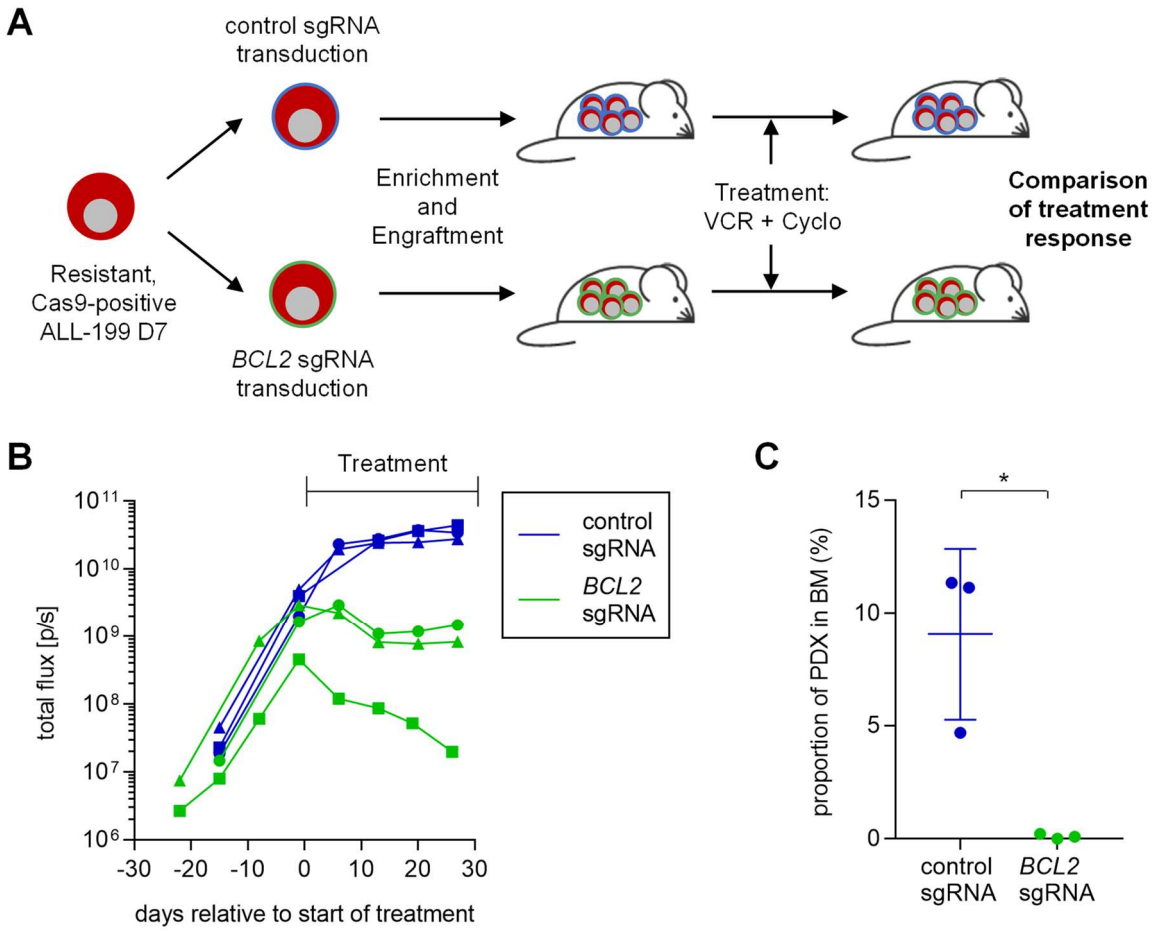

Figure 34: Molecular validation of Bcl-2

A) Experimental setup: Resistant ALL-199 D7 cells were either transduced with a non-targeting control sgRNA or with one of three different sgRNAs targeting *BCL2*. Three days later, transduced cells were enriched by FACS and engrafted into NSG mice. At high leukemic burden, all mice were treated with VCR and Cyclo and treatment response was monitored by repetitive BLI. B) Analysis of treatment response by repetitive BLI. One line represents one mouse (n=3 control sgRNA, n=3 *BCL2* sgRNA). C) At the end of the experiment, PDX population in murine BM was analyzed by flow cytometry. One dot represents one mouse. Statistical significance was calculated by unpaired t-test. *: $p < 0.05$.

The three sgRNAs with the highest depletion efficiency within the CRISPR/Cas9 *in vivo* screen and one non-targeting control sgRNA were individually cloned into a lentiviral backbone and resistant ALL-199 D7 cells were transduced with one of the respective constructs. Three days after transduction, sgRNA-expressing cells were enriched by FACS based on mtagBFP expression and subsequently transplanted into individual NSG mice. Here, cells harboring a sgRNA targeting *BCL2* were transplanted into one mouse per sgRNA sequence, while cells harboring the control sgRNA were transplanted into three mice. Engraftment was monitored by repetitive BLI and combination chemotherapy was initiated at a BLI signal of 1 x 10^9 p/s. Treatment response was monitored by repetitive BLI (Fig. 34B). Importantly, BLI showed that all mice engrafted similarly and did not display growth differences between control and *BCL2* knockout. This verified that *BCL2* knockout was not essential for survival of resistant ALL-199 without therapy pressure, in line with observation from the screen (Fig. 33D). Upon treatment, mice harboring cells with the control sgRNA displayed continued increase in BLI signal (Fig. 34B). In contrast, mice harboring cells with knockout of *BCL2* consistently showed a reduction in BLI signal. Notably, the effect was comparable in all mice despite different sgRNA sequences targeting *BCL2*, leading to a mean BLI signal of 6.7 x 10^8 p/s in the *BCL2* knockout group vs. 2.6 x 10^{10} p/s in the control group after two weeks of treatment. After four weeks of treatment, mice were sacrificed and proportion of PDX cells in murine BM was analyzed by flow cytometry (Fig. 34C). In line with the observation from BLI, mice engrafted with ALL-199 harboring *BCL2* knockout showed significantly less leukemic cells in BM than the control group, i.e. < 1 % vs. 9.1 %, respectively. These data indicated that eliminating Bcl-2 sensitized resistant cells for treatment and proved that upregulation of Bcl-2 served as mechanism for acquired treatment resistance.

To approximate the clinical situation and translate the findings into a putatively translatable context, the Bcl-2 inhibitor Venetoclax was applied as surrogate for *BCL2* knockout in combination with VCR and Cyclo *in vivo*. Venetoclax treatment was performed as previously published and was applied either as monotherapy or in combination with the established schedule of VCR and Cyclo (Khaw et al., 2016) (details in methods section 3.2.4). Control groups of VCR and Cyclo or PBS treatment were obtained from previous experiments (Fig. 31). Groups of mice were engrafted with resistant ALL-199 D7 cells and engraftment was monitored by BLI. Treatment was initiated at a BLI signal of 1 x 10^{10} p/s and treatment response was monitored by repetitive BLI (Fig. 35B). Single treatment with Venetoclax did not reduce tumor burden compared to combination chemotherapy or PBS control, again verifying that Bcl-2 is not essential for survival of resistant ALL-199 in the absence of treatment pressure. However, triple treatment induced a decrease in BLI signal starting in the second week of treatment. Within this period of treatment, triple therapy reduced tumor burden to a mean of 3.0 x 10^9 p/s, while Venetoclax treatment alone resulted in a BLI signal of 3.3 x 10^{10} p/s on average. Mice were sacrificed and proportion of PDX cells in BM was analyzed by flow cytometry (Fig. 35C).

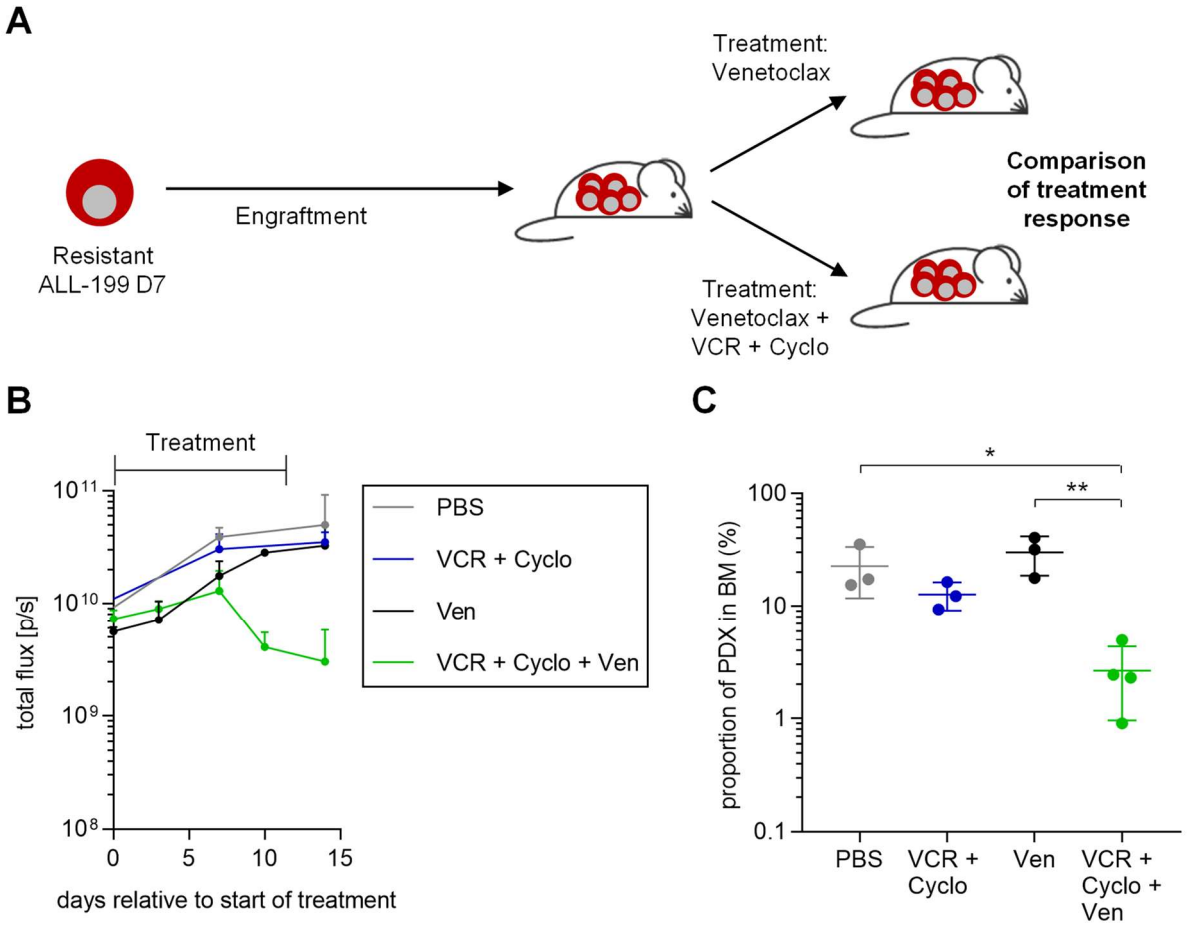

Figure 35: Pharmacological validation of Bcl-2

A) Experimental setup: Resistant ALL-199 D7 cells were engrafted into groups of NSG mice. At high leukemic burden, mice were treated either with combination of VCR, Cyclo and Venetoclax (Ven) or with Ven only. See methods section for drug dosages and schedules. Treatment response was monitored by repetitive BLI. B) Analysis of treatment response by repetitive BLI. Shown is mean and SD of each group (n=4 VCR, Cyclo and Ven, n=4 Ven only). Mean BLI of PBS and VCR + Cyclo groups were derived from Fig. 31. C) At the end of the experiment, PDX population in murine BM was analyzed by flow cytometry. One dot represents one mouse. Statistical significance was calculated using one-way ANOVA followed by Tukey´s multiple comparisons test. *: $p < 0.05$, **: $p < 0.01$.

In line with the observation from BLI, mice that had received triple therapy had significantly less leukemic cells in BM compared to mice that had received Venetoclax only, i.e. 2.7% vs. 30.2%, respectively.

Taken together, Bcl-2 was successfully validated as putative target *in vivo* using both a molecular approach by CRISPR/Cas9 guided knockout as well as pharmacological inhibition by Venetoclax. In both approaches, Bcl-2 inhibition sensitized resistant ALL-199 cells towards combination chemotherapy, indicating that Bcl-2 is essential for maintenance of the resistant phenotype.

In summary, I was able to establish a novel, preclinical model of resistance development using long-term chemotherapy for treatment of PDX ALL *in vivo*. This approach not only allowed to follow resistance acquisition over time, but also to re-isolate and characterize resistant cells. Sequential development of resistance was reproducible in two PDX ALL samples and both

displayed leukemia cell-intrinsic maintenance of resistance, which was preserved upon re-transplantation into secondary recipient mice. Using replicate mice inoculated with the same PDX ALL sample resulted in generation of 8 individual, resistant derivatives. Strikingly, upon characterization of the individual derivatives, genomic and functional heterogeneity became apparent. When expression profiles were determined by transcriptome and proteome analyses, resistant derivatives clearly separated from untreated counterparts and revealed common expression profiles across the derivatives. The relevance of upregulated genes and proteins for maintenance of resistance was analyzed in an innovative CRISPR/Cas9 *in vivo* library dropout screen. Here, I adapted previously established workflows from the lab to specifically study genes essential for treatment resistance. *In vivo* screening identified, among others, *BCL2* as essential for maintenance of resistance. This result was subsequently confirmed in individual knockout experiments and with pharmacological inhibition using Venetoclax treatment *in vivo*. Thus, Bcl-2 represents an attractive therapeutic target for leukemia with acquired treatment resistance.

5 Discussion

Therapy resistance remains a major challenge in treatment of ALL and other tumor entities. Despite numerous studies on patient samples and cell lines, conclusions on mechanisms of resistance remain scarce and adequate model systems are lacking.

In this project, I generated a model of resistance acquisition *in vivo* using the PDX ALL mouse model and long-term treatment with combination of conventional chemotherapy. Functional and genomic characterization of individual resistant derivatives from the same patient sample revealed substantial heterogeneity between the replicates. However, proteome and transcriptome analysis revealed common expression patterns across the derivatives, facilitating the identification of shared upregulated genes in resistant cells, which represent promising candidates to overcome resistance. CRISPR/Cas9 *in vivo* screening of these targets identified, among others, the known regulator of apoptosis, Bcl-2, as essential for maintenance of resistance.

5.1 Long-term combination chemotherapy of PDX ALL *in vivo* models development of resistance during therapy

Improved outcome of ALL patients, especially in a relapse situation, relies on a better understanding of mechanisms leading to development of resistance. To achieve this knowledge, adequate model systems are needed. PDX models accurately recapitulate the human disease and at the same time allow genetic engineering, *in vivo* drug treatment, studies on cancer stem cells and evolutionary processes, and generation of potentially unlimited material (Byrne et al., 2017, Goto, 2020). Thus, they have been applied to study various aspects of relapse and therapy resistance.

In earlier studies, combination chemotherapy regimens were successfully modeled in PDX ALL by application of distinct combinations of up to four different drugs *in vivo*, resulting in substantial response rates across a variety of ALL samples (Ebinger et al., 2016, Szymanska et al., 2012, Samuels et al., 2014). These models were used to characterize residual cells after blocks of treatment by comparing those remaining cells to treatment-naïve cells (Samuels et al., 2014, Ebinger et al., 2016, Yadav et al., 2016). Treatment of T-ALL PDX cells with a combination of four chemotherapeutic drugs and subsequent comparison of residual cells to treatment-naïve cells was used to analyze mechanisms of resistance. However, as cells were treated for only four weeks and did not gain resistance under therapy pressure, the potential drug to overcome resistance, Simvastatin, failed to delay leukemia progression in this model. Furthermore, cells were not resistant in re-challenging experiments (Samuels et al., 2014). Therefore, duration of therapy has to be prolonged to establish a sustainable model for resistance acquisition and cells should gain resistance under therapy pressure.

In a different approach, studies in the PDX model focused on relationship between *in vivo* treatment response and the clinical outcome of patients. Results in various PDX models confirmed a strong correlation between the two, allowing to use treatment response in the PDX model as a predictive tool (Lock et al., 2002, Liem et al., 2004, Hidalgo et al., 2014, Pompili et al., 2016). For example, *in vivo* treatment response of various PDX ALL samples to combination chemotherapy was correlated with the clinical outcome of the respective patients to predict occurrence of relapse (Alruwetei et al., 2020). While this approach might help to improve prognostic tools, conclusions on mechanisms of treatment resistance are biased by inter-patient heterogeneity (Milan et al., 2019). Longitudinal studies comparing serial samples from the same patient would reduce heterogeneity and enable a more reliable identification of markers associated with resistance.

I aimed at generating a reliable *in vivo* model for treatment-induced development of resistance in order to investigate underlying molecular mechanisms. To this end, I successfully adapted the PDX ALL model for treatment with long-term *in vivo* combination chemotherapy. PDX ALL cells from the same patient were injected into groups of mice and VCR and Cyclo were applied once per week in a continuous schedule, which had been established before (Fig. 7) (Ebinger et al., 2016). VCR and Cyclo can be both applied in the PDX mouse model and are well tolerated. Furthermore, resistance mechanisms to other routine chemotherapeutic agents, such as nucleoside analogues, have already been well defined (Tzoneva et al., 2013). Notably, application of combination chemotherapy is essential to understand multidrug resistance mechanisms, which are often not associated with changes in the direct targets of the individual drugs (Pritchard et al., 2012). While combination of more drugs would mimic treatment of patients closer, treatment toxicity impedes long-term *in vivo* treatment protocols in mice due to ethical reasons.

In line, doses were titrated in a way that, on the one hand, PDX ALL cells initially showed treatment sensitivity, but on the other hand, continuous treatment was tolerated well over a long period, enabling a follow-up for up to 18 weeks of continuous therapy. This setup accounts for the long periods of maintenance therapy in ALL, which usually takes 2-3 years and in which combination chemotherapy is applied constantly (Brown et al., 2020). Since relapse frequently happens under chemotherapeutic pressure, this is an important factor for a model of resistance acquisition (Gokbuget et al., 2012a). Furthermore, doses were chosen equivalently to clinically relevant doses for patients and are in line with previously published approaches (Lock et al., 2002, Szymanska et al., 2012, Ebinger et al., 2016, Nair and Jacob, 2016). Additionally, transgenic expression of luciferase in PDX ALL cells allowed monitoring tumor burden by repetitive BLI, while previous studies relied on flow cytometric analysis of human leukemic cells in peripheral blood (Lock et al., 2002, Samuels et al., 2014, Alruwetei et al., 2020). While analysis of tumor cells in the blood does not facilitate detection of residual cells in the bone

marrow, BLI enables sensitive quantification of minute cell numbers in the whole organism (Terziyska et al., 2012, Ebinger et al., 2016). This is especially important for studies on treatment resistance, which usually arises from rare residual cells persisting during treatment.

ALL-199 cells rapidly engrafted into murine BM, as observed by fast increase in BLI signal before start of treatment (Fig. 7). Importantly and in contrast to previously established models, treatment was only started at high leukemic burden, app. two weeks before mice would succumb to leukemia. First weeks of combination chemotherapy decreased tumor burden of mice substantially and BLI signal decreased by more than 99%. After 40 days of treatment, tumor burden did not decrease any further, as shown by stable BLI signal despite on-going treatment, resembling a transition stage en route to treatment resistance. Beginning ten weeks after initiation of treatment, BLI signal even started to increase despite continued therapy, indicating that cells had developed treatment resistance. Notably, PDX cells developed resistance in all replicate mice that received treatment for at least 15 weeks and, interestingly, did so with very similar kinetics (Fig. 14). Groups of mice were sacrificed in these four distinct stages of disease, enabling longitudinal analysis of tumor cells during development of resistance while at the same time minimizing inter-patient heterogeneity. Importantly, cells remained resistant upon re-transplantation into secondary recipient mice and subsequent identical treatment, cells remained resistant, indicating a sustained acquisition of treatment resistance due to cell-intrinsic mechanisms (Fig. 12). To my knowledge, this is the first *in vivo* model of acquired resistance to combination chemotherapy treatment in B-ALL.

Interestingly, the response pattern observed in this approach closely matches the typical disease course of patients (Fig. 1, Fig. 7). Initial treatment sensitivity reflects the typical response in patients, which frequently achieve complete remission. However, both in the PDX ALL model as well as in a fraction of patients, residual cells survive treatment and persist, thus preventing a complete cure of patients. Ultimately, these cells cause relapse due to treatment resistance (Rafei et al., 2019). Since the course of the disease in relapse patients and the PDX model is very similar, this again supports the applicability of the established model.

Of note, similar models have been established in PDX models of other tumor entities. Continuous *in vivo* treatment of melanoma PDX cells with the targeted inhibitor Vemurafenib or with combination of Dabrafenib and Trametinib caused development of resistance to the respective drugs (Das Thakur et al., 2013, Rambow et al., 2018). Furthermore, resistant PDX models of breast cancer were developed by continuous treatment with doxorubicin and Cyclo (Echeverria et al., 2019). In line with my results, development of resistance was characterized by a distinct sequence of treatment sensitivity, transition phase and outgrowth of resistant cells. These studies successfully utilized the mouse model to characterize transition from treatment sensitive to resistant cells and identified specific changes during this transition,

which can be targeted to prevent or delay development of resistance (Rambow et al., 2018, Echeverria et al., 2019).

Taken together, I generated an *in vivo* model for resistance acquisition of patient-derived ALL cells, by combining long-term combination chemotherapy treatment, real-time disease monitoring and longitudinal sampling. This model represents a promising approach to identify molecular mechanisms of treatment resistance in acute leukemia, which has already been applied successfully in other tumor entities.

5.2 Development of resistance is reproducible with PDX ALL of different disease stages

Next, the established approach was extended to two further PDX ALL samples of different stages of disease and molecular subtype. While ALL-199 presents a second relapse of high-risk, Philadelphia-like subtype, ALL-50 originates from initial diagnosis of a low-risk, t(1;19) TCF3-PBX1 subtype, and ALL-265 originates from a first relapse of a high-risk, high-hyperdiploid ALL (Table 3). By using samples from different subtypes and stages of disease, the applicability of the model and the reproducibility of the resistant phenotype were assessed. Doses were adjusted individually for each sample in order to achieve a comparable treatment response and to eradicate at least 99% of leukemic cells within the first weeks of treatment (Fig. 6). Notably, dose ranges remained small despite the diverse sample origin, i.e. within 0.15 – 0.3 mg/kg VCR and 70 mg/kg Cyclo for all samples (see 3.2.4). Interestingly, variations in the VCR dose did not correlate with the stage of the disease, as second relapse ALL-199 even received the lowest dose of VCR.

Although none of the PDX ALL samples have received treatment in mice before, cells from relapse samples had received chemotherapy in the patient. Since VCR and Cyclo are part of routine combination chemotherapy protocols, it is likely that ALL-265 and ALL-199 cells had been treated with these drugs before in the patient (Brown et al., 2020). However, both samples showed sensitivity towards combination chemotherapy in clinically relevant concentrations *in vivo*. It remains unclear whether disease relapse in the patient was caused by resistance towards VCR and/or Cyclo, which was consequently lost during establishment of the PDX sample, or whether relapse was caused by independent mechanisms. In this context, it was proposed that absence of drug treatment during the establishment of PDX models could render a resistant disease sensitive towards treatment (Byrne et al., 2017). In a recent study on resistance development in melanoma PDX models, one out of three different PDX samples had already received treatment in the patient. Notably, *in vivo* results between the three samples remained comparable (Rambow et al., 2018). This suggests that pretreatment of cells in the patient does not hamper results obtained from the PDX model.

In line with this assumption, all three PDX ALL samples showed comparable response to chemotherapy *in vivo*. Single treatments induced stable tumor burden in all samples, with VCR being consistently more effective than Cyclo at the applied doses (Fig. 6). Upon injection into NSG mice, all samples engrafted fast and the first weeks of combination chemotherapy consistently reduced tumor burden by at least 99% in all mice of all PDX ALL samples (Fig. 7, Fig. 8). Commencing between 20 and 40 days after start of treatment, tumor burden was not reduced any further despite on-going treatment. This shows a transition stage on the way to treatment resistance, which was consistently observed in all PDX ALL samples analyzed. Similar to ALL-199, ALL-50 cells ultimately developed resistance and tumor load increased under therapy pressure. However, ALL-50 showed a faster kinetics of resistance development compared to ALL-199, with start of resistance observed after 50 days of continuous treatment in contrast to 80 days in ALL-199. This implies that, although the phenotype is clearly reproducible, different mechanism might account for this. Nevertheless, both samples showed persistent resistance upon re-transplantation into secondary recipient mice. This suggests that in both samples, cell-intrinsic mechanisms account for this phenotype.

Due to technical challenges, development of resistance could not be modeled in ALL-265. Achieving an initial decrease in tumor burden of at least 99% required a VCR dose of 0.3 mg/kg in this sample, as opposed to 0.15 mg/kg for ALL-199. In consequence, treatment toxicity was increased and treatment had to be stopped after nine weeks due to ethical reasons. However, also in ALL-265, initial treatment sensitivity was followed by a transition stage where tumor burden was not decreased despite on-going treatment (Fig. 8). This strongly indicates that ALL-265 would have developed resistance if treatment could have been prolonged further.

This model was established to investigate mechanisms of resistance development. To assess whether the results would be clinically relevant, correlation with the clinical outcome of the patient would be important. While it is known that the patient, of which ALL-199 cells originate, died of the second relapse which remained untreated, the clinical outcome of patients from ALL-50 and ALL-265 is unknown. This information should be obtained in order to conclude whether the model would correlate with the clinical outcome.

Taken together, *in vivo* long-term combination chemotherapy leads to development of resistance in two PDX ALL samples of different molecular subtype and disease stage. Importantly, similar phenotypes were obtained in PDX models of different tumor entities using different therapeutic approaches (Rambow et al., 2018, Echeverria et al., 2019). In conclusion, long-term combination chemotherapy in the PDX model represents a broadly applicable model for generation and analysis of treatment resistance. However, due to restraints in time and resources, only resistant ALL-199 cells were characterized in depth in this project.

5.3 Genomic and functional heterogeneity suggests parallel evolution of different resistant clones

Several studies have analyzed mechanisms of ALL relapse and resistance by comparison of matched relapse and diagnosis samples of patients (Mullighan et al., 2008, Yang et al., 2008, Kawamata et al., 2009, Oshima et al., 2016, Waanders et al., 2020). While they have provided important insight, e.g. by identifying recurrently mutated genes, which can in turn be used as prognostic markers, they also face several limitations. When CNA patterns of 40 matched diagnosis and relapse samples were subjected to unsupervised hierarchical clustering, samples from the same patient always clustered together (Yang et al., 2008). This indicates that common relapse patterns are difficult to decipher from these analyses due to substantial inter-patient heterogeneity (Milan et al., 2019). In contrast, the established PDX model bears the advantage that development of resistance can be assessed by longitudinal comparison of different time points from the same PDX sample. This reduces inter-patient heterogeneity and enables targeted identification of alterations, which are specific for acquisition of resistance. Furthermore, analysis of biological replicates, which all developed resistance in parallel, increases reliability of the detected alterations.

Importantly, all resistant derivatives of ALL-199 developed resistance in an identical sequence of different disease stages and with very similar kinetics, e.g. all initially responded to treatment for the same timeframe and to the same extent, all underwent a transition phase and all gained therapy resistance (Fig. 7, Fig. 14). Of note, two resistant derivatives D4 and D5 showed a slightly reduced rate of tumor growth upon development of resistance as opposed to all other derivatives (Fig. 14). To elucidate genomic changes occurring specifically during chemotherapy treatment, WES of resistant derivatives and untreated controls was compared to the ALL-199 donor sample (Fig. 15). Strikingly, this analysis revealed unexpected findings regarding CNA patterns: First, development of resistance was accompanied by acquisition of CNAs, and second, there was no shared CNA pattern between all resistant derivatives (Fig. 16).

All resistant derivatives acquired at least one large as well as several minor CNAs under chemotherapy pressure (Fig. 16). Occurrence of CNAs between relapse and diagnosis has been well described in studies on patient cohorts of ALL (Mullighan et al., 2008, Yang et al., 2008, Forero-Castro et al., 2020). In comparison of diagnosis and relapse samples of B-ALL, relapse showed significantly more CNAs, of which the majority were deletions (Mullighan et al., 2008, Yang et al., 2008). However, considering the short timeframe of max. 18 weeks of resistance acquisition in the PDX model compared to several months or even years in the patient, the finding of substantial CNAs in the PDX model was rather surprising. To my knowledge, only one study previously analyzed acquisition of CNAs in response to single agent treatments in PDX ALL cells (Nowak et al., 2015). In line with my results, CNAs increased upon treatment,

e.g. with VCR, but missing germ-line controls did not allow conclusions on whether these alterations were definitely gained during treatment or were already present in the patient. Thus, results from the current study present a major improvement, since they allow a conclusion on which CNAs were specifically gained during treatment. In addition, implementation of an untreated control sample showed that transplantation of PDX cells per se did not induce CNAs, thus arguing against technical artefacts and providing reliability of the CNAs in resistant derivatives.

Strikingly, resistant derivatives did not share a common CNA (Fig. 16). This is particularly surprising, since they all are biological replicates from the same donor PDX sample, received identical treatment and showed a similar kinetic in acquisition of resistance. Instead, they can be classified into at least two different groups, with D1 and D2 showing a heterozygous loss of Chr. 17p and all other derivatives showing a heterozygous loss of Chr. 1p36. While additional CNAs are present in each derivative, this classification is the only one that includes two mutually exclusive CNAs, which define all resistant derivatives. For this reason, derivatives were classified based on this pattern and Chr. 17p and Chr. 1p36 were characterized further (Fig. 36). Notably, VAF patterns of D4 and D5 in the hemizygous region of Chr. 1p36 revealed substantial differences to the other derivatives. While D6, D7 and D8 showed VAFs close to 100%, matching the hemizygosity due to copy number loss detected in this region, D4 and D5 showed VAFs of 40 – 60% and 25% vs. 75%, respectively (Fig. 17). This indicates presence of subclones in these derivatives (Fig. 36).

Considering the strong similarity in development of resistance between the derivatives, it might be possible that chromosomal heterogeneity is not relevant for the resistant phenotype. Consequently, functional *in vivo* assays were performed to assess if genomic heterogeneity leads to functional heterogeneity. While most derivatives developed an irreversible resistant phenotype, which persisted even after six months of absence from therapeutic pressure, D4 showed partial response to treatment in this experiment, but quickly regained resistance upon prolonged treatment (Fig. 20). In this setup, treatment of D5 resulted in a constant tumor burden. Furthermore, treatment of resistant derivatives with the highest tolerated doses of VCR and Cyclo resulted in substantial decrease of tumor burden in D4, comparable to sensitive ALL-199 cells (Fig. 21). To exclude technical artefacts as a reason for those heterogeneous results, D4 cells obtained after drug holiday were transplanted into three more mice and challenged with combination chemotherapy. Importantly, this resulted in identical treatment response (Fig. 20). This not only excludes technical artefacts as reason for this surprising observation, but also confirms the reliability of n=1 studies in PDX models (Gao et al., 2015, Townsend et al., 2016). Consequently, results obtained from functional characterization of resistant derivatives provide reliable results, even though they are not derived from experimental replicates.

Although functional heterogeneity was a surprising finding in itself, the patterns closely matched the chromosomal heterogeneity (Fig. 36). This indicates that CNA patterns as well as subclonal structures of D4 and D5 are relevant for the resistant phenotype. Subclones would most likely represent individual populations with varying degrees of resistance and even different mechanisms of resistance. In order to investigate this further, mutational patterns need to be derived from exome data and assigned to individual clones. This approach would also allow deciphering patterns of clonal evolution in the other derivatives. In theory, resistance can develop from pre-existing, minor or major resistant clones or evolve by acquisition of additional lesions (Dagogo-Jack and Shaw, 2018, Turajlic et al., 2019, Marusyk et al., 2020). In light of the heterogeneity between the derivatives, a pure selective process seems very unlikely. Since at least 1 x 10^6 ALL-199 donor cells were injected into every mouse, a pre-existing, resistant subclone would probably have occurred in several resistant derivatives. If more than one resistant subclone was already present before treatment, it would imply that one derivative shows a mix of these clones. Instead, considering genomic and functional heterogeneity, it suggest that resistant clones evolved during treatment. However, this needs to be analyzed in detail to draw definite conclusions.

Regarding the development of resistance, the absence of a common chromosomal lesion implies that several mechanisms of resistance are present. Owing to inter-patient heterogeneity, different mechanisms of resistance have been described in different ALL patients (Mullighan et al., 2008, Kawamata et al., 2009, Waanders et al., 2020). However, only a few studies have shown different mechanisms of resistance within the same tumor. Heterogeneous mechanisms of resistance were suggested in a PDX model of induction chemotherapy (Yadav et al., 2016). In this study, two independent experiments using the same PDX sample with the same induction regimen resulted in substantially different kinetics of treatment response, implying heterogeneous underlying mechanisms. In primary patient samples, heterogeneous mechanisms of resistance were observed across metastases of the same primary tumor. Analysis of one primary melanoma sample together with resulting metastases revealed the presence of several different mechanisms conferring resistance to Vemurafenib, not only across metastases but even within the same metastasis (Kemper et al., 2015). Continuous treatment of lung cancer cell lines revealed that not only one, but several different mechanisms of resistance can emerge in parallel (Hata et al., 2016, Ramirez et al., 2016). This is particularly interesting since cell lines comprise rather homogeneous populations as opposed to PDX models. Here, exome sequencing identified hits in different genes of the same pathway downstream of EGFR, which in turn led to resistance. Interestingly, this was reflected in substantially heterogeneous responses upon re-challenge of resistant cell lines after a drug holiday (Ramirez et al., 2016). Furthermore, both selection of a resistant clone as well as evolution of resistance can arise in parallel, but with very different kinetics (Hata et al., 2016). In this model, acquisition of drug resistance was described as a multi-step

process, in which drug-tolerant persister cells survive treatment and evolve into resistant clones upon continued treatment (Sharma et al., 2010, Hata et al., 2016, Ramirez et al., 2016). Similarly, evolving resistance to targeted therapy in a melanoma PDX model was accompanied by heterogeneity of transcriptome profiles in drug-tolerant persister cells, indicating that the hypothesis of various resistance mechanisms evolving in parallel is applicable to a wider range of tumor entities (Rambow et al., 2018). Interestingly, all aforementioned studies used the same approach of long-term, continuous treatment that was also used in the present study, both *in vitro* and *in vivo* (Hata et al., 2016, Ramirez et al., 2016, Rambow et al., 2018). Since both phenotype of evolution of resistance and heterogeneous properties match with the results from the present study, this indicates that indeed heterogeneous mechanisms of resistance evolve in parallel.

Taken together, resistant derivatives from ALL-199 cells displayed surprising, substantial chromosomal heterogeneity. Functional heterogeneity *in vivo* mirrored this observation, indicating that genomic changes are relevant for the resistance mechanism. This indicates that different resistant clones evolved in parallel during treatment.

5.4 Acquisition of mutations in *TP53* is not a prerequisite for development of resistance

WES of resistant derivatives of ALL-199 revealed not only substantial heterogeneity between the derivatives, but also acquisition of specific mutations upon development of resistance. Most prominently, resistant derivatives D1 and D2 not only showed a heterozygous loss of Chr. 17p, comprising a number of different genes, but also specific point mutations on the remaining allele of Chr. 17p in the location of the *TP53* gene, leading to a loss of heterozygosity (Fig. 18, Fig. 19). Both mutations were neither detected in any of the other resistant derivatives nor in the ALL-199 donor sample after sequencing with a high coverage of at least 3,000 reads. Thus, it is very likely that those mutations were acquired during treatment.

TP53 encodes the transcription factor cellular tumor antigen p53 (p53), which is a well-established tumor suppressor and is often referred to as the guardian of the genome. As such, it induces repair or elimination of cells upon DNA damage, which is e.g. caused by chemotherapy (Kastenhuber and Lowe, 2017). p53 is involved in a broad range of cellular processes, with cell cycle arrest, DNA repair and apoptosis being the most important in the context of response to chemotherapy. Due to its high relevance for genome stability, *TP53* represents the gene most frequently mutated in cancer (Kastenhuber and Lowe, 2017). In pediatric ALL, alterations in *TP53*, both due to copy number variations and mutations, are associated with chemoresistance and poor overall survival rates. Furthermore, the majority of alterations in *TP53* is gained at relapse (Hof et al., 2011, Forero-Castro et al., 2020).

Additionally, mutations in *TP53* are a hallmark of hypodiploid ALL and this subtype is associated with a poor prognosis (Holmfeldt et al., 2013, Roberts and Mullighan, 2015).

The specific point mutations identified in D1 and D2 have not been described in detail before. However, the frame-shift mutation in codon R282 detected in D1 is located in a hotspot mutational region encoding the DNA-binding domain of p53, in which 80% of *TP53* mutations are located (Kastenhuber and Lowe, 2017). A recent study in AML cell lines showed that a missense mutation in codon R282 prevents activation of downstream targets of p53 upon DNA damage by chemotherapy treatment (Boettcher et al., 2019). Since the mutation in D2 is located at the splice-site of Exon 3, this suggests that it results in an altered or non-functional protein. Strikingly, both mutations in the resistant derivatives of ALL-199 were detected with VAF of 82% and 95%, respectively (Fig. 19). This implies that almost every cell of the resistant population possesses this mutation. As it is rather unlikely, that several cells in parallel acquired the exact same mutation, one can conclude that the whole population arose from one ancestor cell, which gained a substantial selection advantage by acquisition of this mutation.

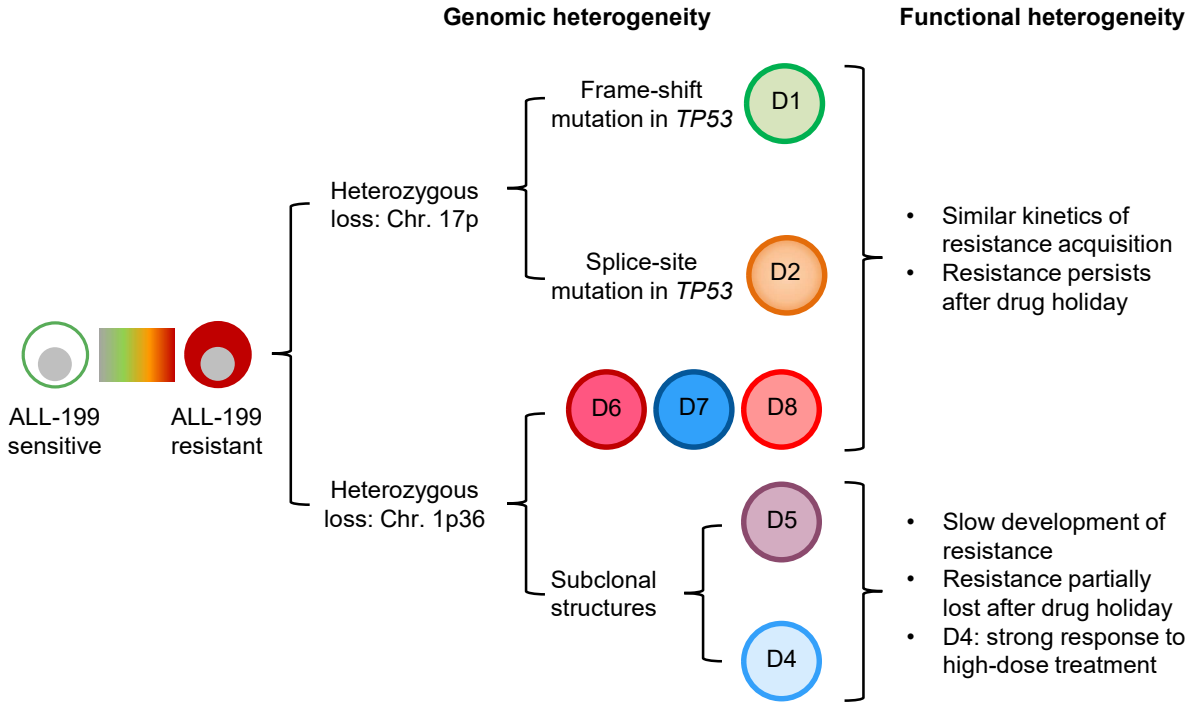

Figure 36: Genomic and functional heterogeneity of resistant derivatives

Resistant derivatives of ALL-199 arise from the identical ALL-199 sample during long-term treatment, but display substantial heterogeneity. On a genomic level, derivatives present heterozygous loss either on Chr. 17p or on Chr. 1p36. Loss of Chr. 17p is accompanied by a frame-shift mutation of *TP53* in D1 and a splice-site mutation of *TP53* in D2. D6, D7 and D8 are similar in their genotype, while D4 and D5 present subclonal structures on the remaining allele of Chr. 1p36. Genomic heterogeneity is mirrored in functional differences. D1, D2, D6, D7 and D8 show a similar kinetics of resistance acquisition and an irreversible resistant phenotype persisting also after drug holiday. In contrast, D4 and D5 show a similar, but slower development of resistance compared to the other derivatives. Both show partial response to treatment after drug holiday and D4 shows strong response to high-dose treatment, indicating further differences between the two derivatives.

Although loss of function of p53 is presumably one effect of Chr. 17p deletion, the affected region includes more than 340 protein-coding genes and is frequently deleted across a variety of tumor entities (Kastenhuber and Lowe, 2017). This implies that the biological relevance of Chr. 17p loss is not restricted to loss of function of p53. In fact, heterozygous deletion of Chr. 17p shows stronger effects on cancer development than deletion of *TP53* alone (Liu et al., 2016). Therefore, heterozygous loss of Chr. 17p in resistant derivatives D1 and D2 might impose more consequences than impairment of p53, which have not been investigated yet.

Importantly, loss of function in p53 was only detected in two out of seven derivatives and the other derivatives did not acquire changes in the *TP53* locus, neither by loss of Chr. 17p nor by point mutations. Instead, they consistently acquired a heterozygous loss of Chr. 1p36 (Fig. 17). This implies that a knockout of *TP53* might be one route to develop resistance, but it is not the only one (Fig. 36). The common deleted region of resistant derivatives D4 – D8 contains more than 400 protein-coding genes on Chr. 1p36. This region is frequently deleted across a variety of cancer types and is therefore believed to encode at least one tumor suppressor gene, but has not been described in ALL so far (Bagchi and Mills, 2008, Henrich et al., 2012). Furthermore, the identity of the respective tumor suppressor remains controversial, indicating that there might be several important genes encoded in this region. It is likely that resistant derivatives D4 - D8 acquired loss of function in a tumor suppressor on Chr. 1p36 as a mechanism of resistance. Importantly, according to the two-hit hypothesis, a pure gene dosage effect by loss of one allele would not be sufficient to abolish function of a tumor suppressor gene (Knudson, 1971). Furthermore, it does not explain the functional heterogeneity between the resistant derivatives D4 compared to D6 – D8 (Fig. 20, Fig. 21, Fig. 36). In conclusion, a second hit in this region needs to be present at least in D6 – D8 in order to explain different levels of resistance. However, no obvious second hit in a known tumor suppressor could be identified by WES. Thus, it is likely that resistance would be mediated by other mechanisms, such as epigenetic regulations of tumor suppressors or dysregulation of micro RNAs (miRNAs), which can be encoded in intronic regions and are frequently involved in cancer development and progression (Bhat et al., 2020). Notably, a well-described downstream regulator of p53 signaling, miR-34a, is encoded on Chr. 1p36 (Hermeking, 2007, Welch et al., 2007, Hermeking, 2010). As such, miR-34a targets many genes of the p53 network and supports function of p53, e.g. by induction of apoptosis via inhibition of the pro-apoptotic protein Bcl-2 (Welch et al., 2007, Rokavec et al., 2014, Navarro and Lieberman, 2015). Consequently, miR-34a levels are frequently reduced in various tumor types and its loss is associated with resistance to chemotherapy, e.g. in leukemia (Zenz et al., 2009, Asslaber et al., 2010, Hermeking, 2010, Rokavec et al., 2014, Li et al., 2019, Naghizadeh et al., 2020). miR-34a levels are not only regulated via transcriptional activation by p53, but also by epigenetic mechanisms, such as promoter hypermethylation (Ali Syeda et al., 2020). It is intriguing to speculate that miR-34a function is abolished in resistant derivatives of ALL-199 with loss of Chr. 1p36, thus

leading to the same downstream effects as loss of p53 in D1 and D2. However, this needs to be validated, e.g. by sequencing of the miR-34a locus, analysis of its expression levels and assessment of its promoter methylation status.

Taken together, mutations in *TP53* are acquired in ALL-199 during development of resistance, but only in a minor fraction of resistant derivatives (Fig. 36). The other derivatives develop a heterozygous loss of Chr. 1p36, but no second genetic hit in a tumor suppressor of this region could be identified so far. In conclusion, loss of function in p53 is most likely one, but definitely not the only, mechanisms of development of resistance.

5.5 Bcl-2 is essential for maintenance of resistance

Development of treatment resistance is often accompanied by diverse changes in transcriptional programs (Cottu et al., 2014, Rambow et al., 2018, Echeverria et al., 2019). Identification and specific targeting of these adaptations, e.g. using pharmacological inhibitors, allows preventing development of resistance and restoring sensitivity. With this rationale, transcriptome and proteome of resistant derivatives and donor cells were analyzed and a candidate list was established based on differentially expressed genes and proteins in resistant ALL-199. Subsequently, relevance of the candidates for the resistant phenotype was assessed using a CRISPR/Cas9 *in vivo* dropout screen. This approach has been successfully applied for identification of genes involved in treatment resistance across a variety of tumor entities (Shalem et al., 2014, Wang et al., 2014, Krall et al., 2017, Lian et al., 2020, Schleicher et al., 2020).

CRISPR/Cas9 *in vivo* screens in the PDX model impose several technical challenges and so far have only been reported once in PDX ALL (Hulton et al., 2020). In contrast to *in vitro* studies, the number of genes to be analyzed is limited by the number of cells that can be injected and engraft into one mouse, requiring a careful selection of candidates. Considering the genetic and functional heterogeneity across the individual derivatives of resistant ALL-199 cells, candidates could be selected in a variety of ways. In this study, combined selection of candidates from transcriptome and proteome accounts for different regulatory options on transcriptional and post-transcriptional levels. Here, candidates were derived from a pooled analysis of all resistant derivatives compared to all untreated samples (Fig. 25). Thus, selected candidates are most likely consistently deregulated across all derivatives, independent from the genotype. This approach bears the advantage to identify common targets, which restore treatment sensitivity independent from the causative genetic hit. Considering applicability for treatment of patients, specific inhibitors can target upregulated candidates, while targeting of downregulated genes is technically more challenging. Thus, the analysis was restricted to genes, which are upregulated in resistant cells (Fig. 25).

Upon *in vivo* screening, all essential genes, which were included into the library as positive controls, were depleted within the first four weeks of engraftment before start of treatment, while all non-targeting controls remained unchanged during the course of the experiment (Fig. 33D). This represents an important quality control for the screen and shows that the technical setup worked as predicted. Consequently, genes that were significantly depleted upon treatment present reliable candidates. Resistant ALL-199 D7 cells with knockout of *TBX21*, *BCL2*, *SCN1B* or *CSNK2A1* were significantly depleted upon treatment, indicating that these genes are essential for the resistant phenotype (Fig. 33C, D). Since all sgRNA sequences targeting these genes were not depleted before start of treatment, they should not be essential for survival of resistant ALL-199 cells without therapy pressure (Fig. 33D). Limitations in resources did not allow to perform screening for all resistant derivatives. Screening was limited to D7, because it represents the group of derivatives with loss of Chr. 1p36 and an irreversible resistant phenotype. Candidates from screening should be validated individually in D7 and also in other derivatives.

As a proof of principle, effect of Bcl-2 inhibition on treatment sensitivity of resistant ALL-199 cells was analyzed. Bcl-2 is a well-described, pro-survival regulator of intrinsic apoptosis and as such inhibits programmed cell death (Czabotar et al., 2014). Expression of Bcl-2 allows cell survival independent from cellular stress and consequently confers resistance to various apoptotic stimuli, such as chemotherapy (Iacovelli et al., 2015). Pharmacological inhibition of Bcl-2 using Venetoclax has shown promising results in patients suffering from chronic lymphocytic leukemia (CLL) (Montero and Letai, 2018). Thus, identification of Bcl-2 as an essential regulator of resistance in PDX ALL seems obvious. As such, it proves the reliability of the established *in vivo* model for development of resistance.

In vivo validation of the role of Bcl-2 for treatment resistance was performed by establishment of a *BCL2* knockout in resistant ALL-199 cells and by treatment of resistant ALL-199 cells with the Bcl-2 inhibitor Venetoclax (Fig. 34, Fig. 35). In both approaches, the effect of Bcl-2 inhibition on treatment response of resistant ALL-199 D7 cells to combination chemotherapy was analyzed. Neither knockout of *BCL2* nor Venetoclax treatment alone had an effect on tumor growth, validating that ALL-199 cells are not dependent on Bcl-2 expression for survival. Together with combination chemotherapy, however, tumor burden could be reduced, leading to significantly less leukemic cells in murine BM after treatment compared to control groups. In conclusion, inhibition of Bcl-2 restores sensitivity of resistant ALL-199 cells to combination chemotherapy.

Considering that both Venetoclax treatment and validation using sgRNAs targeting *BCL2* were performed without further experimental optimization, effects might even be increased by optimizing the experimental procedure. For example, titration of Venetoclax and adjustment of the treatment schedule might increase the effect on tumor burden. In line, presumably not

all sgRNA-transduced cells achieved a complete knockout of *BCL2*. In conclusion, both approaches underestimate the effect of Bcl-2 inhibition on treatment sensitivity.

Bcl-2 is highly expressed in various types of hematological malignancies, such as CLL, follicular lymphoma and mantle-cell lymphoma (Perini et al., 2018). In ALL, the relevance of high Bcl-2 expression levels remains a matter of debate. While high levels of Bcl-2 are frequent and dependency on Bcl-2 was shown for some, but not all, cell lines and primary samples, other studies did not identify a prognostic relevance (Coustan-Smith et al., 1996, Salomons et al., 1999, Del Gaizo Moore et al., 2008, Alford et al., 2015, Benito et al., 2015, Seyfried et al., 2019). Overall, this indicates a heterogeneous role of Bcl-2 in ALL.

Bcl-2 is subject to various regulatory mechanisms and posttranslational modifications, but their consequences remain controversial (Czabotar et al., 2014, Perini et al., 2018). In this context, it is interesting to note that Bcl-2 was specifically upregulated in proteome analysis of resistant ALL-199, but not in transcriptome, indicating posttranslational regulation (Fig. 25). Importantly, upon activation of p53 by DNA damage, pro-apoptotic Bcl-2 family members are activated, in turn inhibit anti-apoptotic proteins, such as Bcl-2, and initiate apoptosis (Roberts and Huang, 2017, Valentin et al., 2018). Since loss of function of p53 occurred in two resistant derivatives of ALL-199, it is likely that this pathway is involved in development of resistance. Hypothetically, loss of function of p53 leads to inhibition of apoptosis by upregulation of Bcl-2 and inhibition of Bcl-2 would restore treatment sensitivity in these derivatives. So far, time constraints did not allow investigating effects of Venetoclax treatment on resistant ALL-199 D1 and D2. However, in light of the initial approval of Venetoclax for CLL with deletion of Chr. 17p and the described negative regulation of Bcl-2 by p53, sensitivity of these derivatives to combination of Venetoclax, VCR and Cyclo is probable.

Given the abundance of high Bcl-2 expression levels in cancer, specific Bcl-2 inhibitors were developed. The most successful inhibitor, Venetoclax, acts as BH3-mimetics and as such blocks activity of Bcl-2 (Montero and Letai, 2018). Initial approval of Venetoclax was granted for CLL with deletion of Chr. 17p in 2016 (Roberts and Huang, 2017). Additionally, several on-going clinical trials investigate efficiency of Venetoclax as single treatment or in combination with chemotherapy and targeted agents for a variety of hematological malignancies (Perini et al., 2018, Valentin et al., 2018). Preclinical evaluation in PDX ALL showed heterogeneous results depending on ALL subtype. In two different studies, PDX ALL samples with *KMT2A* rearrangement were shown to be sensitive to Venetoclax treatment alone or in combination with chemotherapy (Benito et al., 2015, Khaw et al., 2016). In line with results from this project, previous studies applying single treatment with Venetoclax in PDX ALL without *KMT2A* rearrangement only yielded effects in some samples, mostly with short duration and minimal efficacy (Khaw et al., 2016, Jones et al., 2017). This indicates that in ALL, inhibition of Bcl-2 is only effective in combination with chemotherapy.

Clinical trials of Venetoclax in combination with chemotherapy for relapsed pediatric ALL are currently on-going (NCT03236857). Since it has been approved for treatment of other hematological malignancies, a fast implementation into ALL treatment protocols is possible. First results from the present study confirm that treatment of relapsed ALL patients with combination of Venetoclax and chemotherapy provides a promising approach in order to reverse treatment resistance and improve the outcome of ALL patients.

5.6 Conclusion and outlook

The present study revealed that several genomic mechanisms of resistance co-occur in response to the same combination treatment within the same PDX ALL sample. This poses a very challenging situation for treatment of patients, implying that several evasion mechanisms need to be tackled in parallel to prevent manifestation of relapse.

However, the model also showed shared expression profiles independent from genomic hits. Bcl-2 was validated as an essential regulator of the resistant phenotype in one derivative using two different experimental approaches. This supplements existing data on the relevance of Bcl-2 in other hematological malignancies and provides a rationale to expand the clinical application of Venetoclax to relapsed ALL.

It will be important to investigate, whether *TP53* mutated derivatives can also be sensitized to chemotherapy by pharmacological inhibition of Bcl-2. Since p53 is a negative regulator of Bcl-2 signaling, this seems very probable. In this case, several different, genomic hits would lead into the same pathway, thus conferring the resistant phenotype. While the evolution of different mechanisms of resistance would nevertheless be scientifically interesting, it would be of smaller importance from the clinical perspective since it would allow tackling relapse with a generalized strategy.

Furthermore, the longitudinal sampling established in this model allows to follow resistance development over time. So far, data analysis has been focused on identifying and validating alterations in the resistant samples. Next, exact timing of the acquisition of these alterations can be analyzed to identify vulnerable time points in development of resistance. Potentially, by targeting of these time points, development of resistance could even be prevented.

While Bcl-2 has already been associated with disease relapse before, the CRISPR/Cas9 screen also identified the novel candidates *TBX21*, *SCN1B* and *CSNK2A1* as essential for resistance, which should be investigated further. These genes might present additional, previously unknown vulnerabilities to tackle resistant disease.

Bibliography

Afgan, E, Baker, D, Batut, B, Van Den Beek, M, Bouvier, D, Cech, M, . . . Blankenberg, D 2018. The Galaxy platform for accessible, reproducible and collaborative biomedical analyses: 2018 update. *Nucleic Acids Res,* 46**,** W537-W544.

Alford, SE, Kothari, A, Loeff, FC, Eichhorn, JM, Sakurikar, N, Goselink, HM, . . . Chambers, TC 2015. BH3 Inhibitor Sensitivity and Bcl-2 Dependence in Primary Acute Lymphoblastic Leukemia Cells. *Cancer Res,* 75**,** 1366-75.

Ali Syeda, Z, Langden, SSS, Munkhzul, C, Lee, M & Song, SJ 2020. Regulatory Mechanism of MicroRNA Expression in Cancer. *Int J Mol Sci,* 21.

Alruwetei, AM, Bendak, K, Yadav, BD, Carol, H, Evans, K, Mayoh, C, . . . Lock, RB 2020. Examining treatment responses of diagnostic marrow in murine xenografts to predict relapse in children with acute lymphoblastic leukaemia. *Br J Cancer,* 123**,** 742-751.

Anderson, K, Lutz, C, Van Delft, FW, Bateman, CM, Guo, Y, Colman, SM, . . . Greaves, M 2011. Genetic variegation of clonal architecture and propagating cells in leukaemia. *Nature,* 469**,** 356-61.

Andersson, BS, Sadeghi, T, Siciliano, MJ, Legerski, R & Murray, D 1996. Nucleotide excision repair genes as determinants of cellular sensitivity to cyclophosphamide analogs. *Cancer Chemother Pharmacol,* 38**,** 406-16.

Asslaber, D, Pinon, JD, Seyfried, I, Desch, P, Stocher, M, Tinhofer, I, . . . Greil, R 2010. microRNA-34a expression correlates with MDM2 SNP309 polymorphism and treatment-free survival in chronic lymphocytic leukemia. *Blood,* 115**,** 4191-7.

Baersch, G, Mollers, T, Hotte, A, Dockhorn-Dworniczak, B, Rube, C, Ritter, J, . . . Vormoor, J 1997. Good engraftment of B-cell precursor ALL in NOD-SCID mice. *Klin Padiatr,* 209**,** 178-85.

Bagchi, A & Mills, AA 2008. The quest for the 1p36 tumor suppressor. *Cancer Res,* 68**,** 2551-6.

Bagnoli, JW, Ziegenhain, C, Janjic, A, Wange, LE, Vieth, B, Parekh, S, . . . Enard, W 2018. Sensitive and powerful single-cell RNA sequencing using mcSCRB-seq. *Nat Commun,* 9**,** 2937.

Bakker, E, Qattan, M, Mutti, L, Demonacos, C & Krstic-Demonacos, M 2016. The role of microenvironment and immunity in drug response in leukemia. *Biochim Biophys Acta,* 1863**,** 414-426.

Barrett, DM, Seif, AE, Carpenito, C, Teachey, DT, Fish, JD, June, CH, . . . Reid, GS 2011. Noninvasive bioluminescent imaging of primary patient acute lymphoblastic leukemia: a strategy for preclinical modeling. *Blood,* 118**,** e112-7.

Becker, M, Noll-Puchta, H, Amend, D, Nolte, F, Fuchs, C, Jeremias, I & Braun, CJ 2020. CLUE: a bioinformatic and wet-lab pipeline for multiplexed cloning of custom sgRNA libraries. *Nucleic Acids Res,* 48**,** e78.

Ben-David, U, Siranosian, B, Ha, G, Tang, H, Oren, Y, Hinohara, K, . . . Golub, TR 2018. Genetic and transcriptional evolution alters cancer cell line drug response. *Nature,* 560**,** 325-330.

Benito, JM, Godfrey, L, Kojima, K, Hogdal, L, Wunderlich, M, Geng, H, . . . Konopleva, M 2015. MLL-Rearranged Acute Lymphoblastic Leukemias Activate BCL-2 through H3K79 Methylation and Are Sensitive to the BCL-2-Specific Antagonist ABT-199. *Cell Rep,* 13**,** 2715-27.

Berry, DA, Zhou, S, Higley, H, Mukundan, L, Fu, S, Reaman, GH, . . . Radich, JP 2017. Association of Minimal Residual Disease With Clinical Outcome in Pediatric and Adult Acute Lymphoblastic Leukemia: A Meta-analysis. *JAMA Oncol,* 3**,** e170580.

Bhat, AA, Younes, SN, Raza, SS, Zarif, L, Nisar, S, Ahmed, I, . . . Uddin, S 2020. Role of non-coding RNA networks in leukemia progression, metastasis and drug resistance. *Mol Cancer,* 19**,** 57.

Boettcher, S, Miller, PG, Sharma, R, Mcconkey, M, Leventhal, M, Krivtsov, AV, . . . Ebert, BL 2019. A dominant-negative effect drives selection of TP53 missense mutations in myeloid malignancies. *Science,* 365**,** 599-604.

Bomken, S, Buechler, L, Rehe, K, Ponthan, F, Elder, A, Blair, H, . . . Heidenreich, O 2013. Lentiviral marking of patient-derived acute lymphoblastic leukaemic cells allows in vivo tracking of disease progression. *Leukemia,* 27**,** 718-21.

Borgmann, A, Baldy, C, Von Stackelberg, A, Beyermann, B, Fichtner, I, Nurnberg, P & Henze, G 2000. Childhood all blasts retain phenotypic and genotypic characteristics upon long-term serial passage in NOD/SCID mice. *Pediatr Hematol Oncol,* 17**,** 635-50.

Bouwman, P & Jonkers, J 2012. The effects of deregulated DNA damage signalling on cancer chemotherapy response and resistance. *Nat Rev Cancer,* 12**,** 587-98.

Braun, TP, Eide, CA & Druker, BJ 2020. Response and Resistance to BCR-ABL1-Targeted Therapies. *Cancer Cell,* 37**,** 530-542.

Brown, P, Inaba, H, Annesley, C, Beck, J, Colace, S, Dallas, M, . . . Ogba, N 2020. Pediatric Acute Lymphoblastic Leukemia, Version 2.2020, NCCN Clinical Practice Guidelines in Oncology. *J Natl Compr Canc Netw,* 18**,** 81-112.

Bukowski, K, Kciuk, M & Kontek, R 2020. Mechanisms of Multidrug Resistance in Cancer Chemotherapy. *Int J Mol Sci,* 21.

Burrell, RA & Swanton, C 2014. Tumour heterogeneity and the evolution of polyclonal drug resistance. *Mol Oncol,* 8**,** 1095-111.

Byrne, AT, Alferez, DG, Amant, F, Annibali, D, Arribas, J, Biankin, AV, . . . Trusolino, L 2017. Interrogating open issues in cancer precision medicine with patient-derived xenografts. *Nat Rev Cancer,* 17**,** 254-268.

Cahu, X, Calvo, J, Poglio, S, Prade, N, Colsch, B, Arcangeli, ML, . . . Pflumio, F 2017. Bone marrow sites differently imprint dormancy and chemoresistance to T-cell acute lymphoblastic leukemia. *Blood Adv,* 1**,** 1760-1772.

Carroll, WL & Hunger, SP 2016. Therapies on the horizon for childhood acute lymphoblastic leukemia. *Curr Opin Pediatr,* 28**,** 12-8.

Cassidy, JW, Caldas, C & Bruna, A 2015. Maintaining Tumor Heterogeneity in Patient-Derived Tumor Xenografts. *Cancer Res,* 75**,** 2963-8.

Castro Alves, C, Terziyska, N, Grunert, M, Gundisch, S, Graubner, U, Quintanilla-Martinez, L & Jeremias, I 2012. Leukemia-initiating cells of patient-derived acute lymphoblastic leukemia xenografts are sensitive toward TRAIL. *Blood,* 119**,** 4224-7.

Chatterjee, N & Bivona, TG 2019. Polytherapy and Targeted Cancer Drug Resistance. *Trends Cancer,* 5**,** 170-182.

Choi, S, Henderson, MJ, Kwan, E, Beesley, AH, Sutton, R, Bahar, AY, . . . Norris, MD 2007. Relapse in children with acute lymphoblastic leukemia involving selection of a preexisting drug-resistant subclone. *Blood,* 110**,** 632-9.

Chow, RD & Chen, S 2018. Cancer CRISPR Screens In Vivo. *Trends Cancer,* 4**,** 349-358.

Clappier, E, Gerby, B, Sigaux, F, Delord, M, Touzri, F, Hernandez, L, . . . Soulier, J 2011. Clonal selection in xenografted human T cell acute lymphoblastic leukemia recapitulates gain of malignancy at relapse. *J Exp Med,* 208**,** 653-61.

Clevers, H 2011. The cancer stem cell: premises, promises and challenges. *Nat Med,* 17**,** 313-9.

Cottu, P, Bieche, I, Assayag, F, El Botty, R, Chateau-Joubert, S, Thuleau, A, . . . Marangoni, E 2014. Acquired resistance to endocrine treatments is associated with tumor-specific molecular changes in patient-derived luminal breast cancer xenografts. *Clin Cancer Res,* 20**,** 4314-25.

Coustan-Smith, E, Kitanaka, A, Pui, CH, Mcninch, L, Evans, WE, Raimondi, SC, . . . Campana, D 1996. Clinical relevance of BCL-2 overexpression in childhood acute lymphoblastic leukemia. *Blood,* 87**,** 1140-6.

Cox, J, Hein, MY, Luber, CA, Paron, I, Nagaraj, N & Mann, M 2014. Accurate proteome-wide label-free quantification by delayed normalization and maximal peptide ratio extraction, termed MaxLFQ. *Mol Cell Proteomics,* 13**,** 2513-26.

Cox, J & Mann, M 2008. MaxQuant enables high peptide identification rates, individualized p.p.b.-range mass accuracies and proteome-wide protein quantification. *Nat Biotechnol,* 26**,** 1367-72.

Czabotar, PE, Lessene, G, Strasser, A & Adams, JM 2014. Control of apoptosis by the BCL-2 protein family: implications for physiology and therapy. *Nat Rev Mol Cell Biol,* 15**,** 49-63.

Dagogo-Jack, I & Shaw, AT 2018. Tumour heterogeneity and resistance to cancer therapies. *Nat Rev Clin Oncol,* 15**,** 81-94.

Das Thakur, M, Salangsang, F, Landman, AS, Sellers, WR, Pryer, NK, Levesque, MP, . . . Stuart, DD 2013. Modelling vemurafenib resistance in melanoma reveals a strategy to forestall drug resistance. *Nature,* 494**,** 251-5.

De Angelis, ML, Francescangeli, F, La Torre, F & Zeuner, A 2019. Stem Cell Plasticity and Dormancy in the Development of Cancer Therapy Resistance. *Front Oncol,* 9**,** 626.

Del Gaizo Moore, V, Schlis, KD, Sallan, SE, Armstrong, SA & Letai, A 2008. BCL-2 dependence and ABT-737 sensitivity in acute lymphoblastic leukemia. *Blood,* 111**,** 2300-9.

Dobson, SM, Garcia-Prat, L, Vanner, RJ, Wintersinger, J, Waanders, E, Gu, Z, . . . Dick, JE 2020. Relapse-Fated Latent Diagnosis Subclones in Acute B Lineage Leukemia Are Drug Tolerant and Possess Distinct Metabolic Programs. *Cancer Discov,* 10**,** 568-587.

Doench, JG, Fusi, N, Sullender, M, Hegde, M, Vaimberg, EW, Donovan, KF, . . . Root, DE 2016. Optimized sgRNA design to maximize activity and minimize off-target effects of CRISPR-Cas9. *Nat Biotechnol,* 34**,** 184-191.

Doudna, JA & Charpentier, E 2014. Genome editing. The new frontier of genome engineering with CRISPR-Cas9. *Science,* 346**,** 1258096.

Downing, JR, Wilson, RK, Zhang, J, Mardis, ER, Pui, CH, Ding, L, . . . Evans, WE 2012. The Pediatric Cancer Genome Project. *Nat Genet,* 44**,** 619-22.

Druker, BJ, Sawyers, CL, Kantarjian, H, Resta, DJ, Reese, SF, Ford, JM, . . . Talpaz, M 2001. Activity of a specific inhibitor of the BCR-ABL tyrosine kinase in the blast crisis of chronic myeloid

leukemia and acute lymphoblastic leukemia with the Philadelphia chromosome. *N Engl J Med,* 344**,** 1038-42.
Druker, BJ, Tamura, S, Buchdunger, E, Ohno, S, Segal, GM, Fanning, S, . . . Lydon, NB 1996. Effects of a selective inhibitor of the Abl tyrosine kinase on the growth of Bcr-Abl positive cells. *Nat Med,* 2**,** 561-6.
Duan, CW, Shi, J, Chen, J, Wang, B, Yu, YH, Qin, X, . . . Hong, DL 2014. Leukemia propagating cells rebuild an evolving niche in response to therapy. *Cancer Cell,* 25**,** 778-93.
Ebinger, S, Ozdemir, EZ, Ziegenhain, C, Tiedt, S, Castro Alves, C, Grunert, M, . . . Jeremias, I 2016. Characterization of Rare, Dormant, and Therapy-Resistant Cells in Acute Lymphoblastic Leukemia. *Cancer Cell,* 30**,** 849-862.
Echeverria, GV, Ge, Z, Seth, S, Zhang, X, Jeter-Jones, S, Zhou, X, . . . Piwnica-Worms, H 2019. Resistance to neoadjuvant chemotherapy in triple-negative breast cancer mediated by a reversible drug-tolerant state. *Sci Transl Med,* 11.
Elder, A, Bomken, S, Wilson, I, Blair, HJ, Cockell, S, Ponthan, F, . . . Vormoor, J 2017. Abundant and equipotent founder cells establish and maintain acute lymphoblastic leukaemia. *Leukemia,* 31**,** 2577-2586.
Emadi, A, Jones, RJ & Brodsky, RA 2009. Cyclophosphamide and cancer: golden anniversary. *Nat Rev Clin Oncol,* 6**,** 638-47.
Esparza, SD & Sakamoto, KM 2005. Topics in pediatric leukemia--acute lymphoblastic leukemia. *MedGenMed,* 7**,** 23.
Ferrando, AA & Lopez-Otin, C 2017. Clonal evolution in leukemia. *Nat Med,* 23**,** 1135-1145.
Forero-Castro, M, Montano, A, Robledo, C, Garcia De Coca, A, Fuster, JL, De Las Heras, N, . . . Hernandez-Rivas, JM 2020. Integrated Genomic Analysis of Chromosomal Alterations and Mutations in B-Cell Acute Lymphoblastic Leukemia Reveals Distinct Genetic Profiles at Relapse. *Diagnostics (Basel),* 10.
Freireich, EJ, Wiernik, PH & Steensma, DP 2014. The leukemias: a half-century of discovery. *J Clin Oncol,* 32**,** 3463-9.
Gan, PP & Kavallaris, M 2008. Tubulin-targeted drug action: functional significance of class ii and class IVb beta-tubulin in vinca alkaloid sensitivity. *Cancer Res,* 68**,** 9817-24.
Gao, H, Korn, JM, Ferretti, S, Monahan, JE, Wang, Y, Singh, M, . . . Sellers, WR 2015. High-throughput screening using patient-derived tumor xenografts to predict clinical trial drug response. *Nat Med,* 21**,** 1318-25.
Gerhards, NM & Rottenberg, S 2018. New tools for old drugs: Functional genetic screens to optimize current chemotherapy. *Drug Resist Updat,* 36**,** 30-46.
Gilbert, LA & Hemann, MT 2010. DNA damage-mediated induction of a chemoresistant niche. *Cell,* 143**,** 355-66.
Gillet, JP, Calcagno, AM, Varma, S, Marino, M, Green, LJ, Vora, MI, . . . Gottesman, MM 2011. Redefining the relevance of established cancer cell lines to the study of mechanisms of clinical anti-cancer drug resistance. *Proc Natl Acad Sci U S A,* 108**,** 18708-13.
Gokbuget, N, Kneba, M, Raff, T, Trautmann, H, Bartram, CR, Arnold, R, . . . German Multicenter Study Group for Adult Acute Lymphoblastic, L 2012a. Adult patients with acute lymphoblastic leukemia and molecular failure display a poor prognosis and are candidates for stem cell transplantation and targeted therapies. *Blood,* 120**,** 1868-76.
Gokbuget, N, Stanze, D, Beck, J, Diedrich, H, Horst, HA, Huttmann, A, . . . German Multicenter Study Group for Adult Acute Lymphoblastic, L 2012b. Outcome of relapsed adult lymphoblastic leukemia depends on response to salvage chemotherapy, prognostic factors, and performance of stem cell transplantation. *Blood,* 120**,** 2032-41.
Golay, J, Di Gaetano, N, Amico, D, Cittera, E, Barbui, AM, Giavazzi, R, . . . Introna, M 2005. Gemtuzumab ozogamicin (Mylotarg) has therapeutic activity against CD33 acute lymphoblastic leukaemias in vitro and in vivo. *Br J Haematol,* 128**,** 310-7.
Gorre, ME, Mohammed, M, Ellwood, K, Hsu, N, Paquette, R, Rao, PN & Sawyers, CL 2001. Clinical resistance to STI-571 cancer therapy caused by BCR-ABL gene mutation or amplification. *Science,* 293**,** 876-80.
Goto, T 2020. Patient-Derived Tumor Xenograft Models: Toward the Establishment of Precision Cancer Medicine. *J Pers Med,* 10.
Greaves, M & Maley, CC 2012. Clonal evolution in cancer. *Nature,* 481**,** 306-13.
Groenendijk, FH & Bernards, R 2014. Drug resistance to targeted therapies: deja vu all over again. *Mol Oncol,* 8**,** 1067-83.
Habringer, S, Lapa, C, Herhaus, P, Schottelius, M, Istvanffy, R, Steiger, K, . . . Keller, U 2018. Dual Targeting of Acute Leukemia and Supporting Niche by CXCR4-Directed Theranostics. *Theranostics,* 8**,** 369-383.

Hall, AG & Tilby, MJ 1992. Mechanisms of action of, and modes of resistance to, alkylating agents used in the treatment of haematological malignancies. *Blood Rev,* 6**,** 163-73.

Hata, AN, Niederst, MJ, Archibald, HL, Gomez-Caraballo, M, Siddiqui, FM, Mulvey, HE, . . . Engelman, JA 2016. Tumor cells can follow distinct evolutionary paths to become resistant to epidermal growth factor receptor inhibition. *Nat Med,* 22**,** 262-9.

Hawkins, ED, Duarte, D, Akinduro, O, Khorshed, RA, Passaro, D, Nowicka, M, . . . Lo Celso, C 2016. T-cell acute leukaemia exhibits dynamic interactions with bone marrow microenvironments. *Nature,* 538**,** 518-522.

Henrich, KO, Schwab, M & Westermann, F 2012. 1p36 tumor suppression--a matter of dosage? *Cancer Res,* 72**,** 6079-88.

Hermeking, H 2007. p53 enters the microRNA world. *Cancer Cell,* 12**,** 414-8.

Hermeking, H 2010. The miR-34 family in cancer and apoptosis. *Cell Death Differ,* 17**,** 193-9.

Hidalgo, M, Amant, F, Biankin, AV, Budinska, E, Byrne, AT, Caldas, C, . . . Villanueva, A 2014. Patient-derived xenograft models: an emerging platform for translational cancer research. *Cancer Discov,* 4**,** 998-1013.

Hof, J, Krentz, S, Van Schewick, C, Korner, G, Shalapour, S, Rhein, P, . . . Kirschner-Schwabe, R 2011. Mutations and deletions of the TP53 gene predict nonresponse to treatment and poor outcome in first relapse of childhood acute lymphoblastic leukemia. *J Clin Oncol,* 29**,** 3185-93.

Holmfeldt, L, Wei, L, Diaz-Flores, E, Walsh, M, Zhang, J, Ding, L, . . . Mullighan, CG 2013. The genomic landscape of hypodiploid acute lymphoblastic leukemia. *Nat Genet,* 45**,** 242-52.

Holohan, C, Van Schaeybroeck, S, Longley, DB & Johnston, PG 2013. Cancer drug resistance: an evolving paradigm. *Nat Rev Cancer,* 13**,** 714-26.

Hulton, CH, Costa, EA, Shah, NS, Quintanal-Villalonga, A, Heller, G, De Stanchina, E, . . . Poirier, JT 2020. Direct genome editing of patient-derived xenografts using CRISPR-Cas9 enables rapid in vivo functional genomics. *Nature Cancer,* 1**,** 359-369.

Hunger, SP & Raetz, EA 2020. How I treat relapsed acute lymphoblastic leukemia in the pediatric population. *Blood,* 136**,** 1803-1812.

Hutter, G, Nickenig, C, Garritsen, H, Hellenkamp, F, Hoerning, A, Hiddemann, W & Dreyling, M 2004. Use of polymorphisms in the noncoding region of the human mitochondrial genome to identify potential contamination of human leukemia-lymphoma cell lines. *Hematol J,* 5**,** 61-8.

Iacobucci, I & Mullighan, CG 2017. Genetic Basis of Acute Lymphoblastic Leukemia. *J Clin Oncol,* 35**,** 975-983.

Iacovelli, S, Ricciardi, MR, Allegretti, M, Mirabilii, S, Licchetta, R, Bergamo, P, . . . Tafuri, A 2015. Co-targeting of Bcl-2 and mTOR pathway triggers synergistic apoptosis in BH3 mimetics resistant acute lymphoblastic leukemia. *Oncotarget,* 6**,** 32089-103.

Inaba, H & Mullighan, CG 2020. Pediatric acute lymphoblastic leukemia. *Haematologica,* Online ahead of print.

Irving, JA, Bloodworth, L, Bown, NP, Case, MC, Hogarth, LA & Hall, AG 2005. Loss of heterozygosity in childhood acute lymphoblastic leukemia detected by genome-wide microarray single nucleotide polymorphism analysis. *Cancer Res,* 65**,** 3053-8.

Johnson, WE, Li, C & Rabinovic, A 2007. Adjusting batch effects in microarray expression data using empirical Bayes methods. *Biostatistics,* 8**,** 118-27.

Jones, L, Richmond, J, Evans, K, Carol, H, Jing, D, Kurmasheva, RT, . . . Lock, RB 2017. Bioluminescence Imaging Enhances Analysis of Drug Responses in a Patient-Derived Xenograft Model of Pediatric ALL. *Clin Cancer Res,* 23**,** 3744-3755.

Kamel-Reid, S, Letarte, M, Doedens, M, Greaves, A, Murdoch, B, Grunberger, T, . . . Et Al. 1991. Bone marrow from children in relapse with pre-B acute lymphoblastic leukemia proliferates and disseminates rapidly in scid mice. *Blood,* 78**,** 2973-81.

Kamel-Reid, S, Letarte, M, Sirard, C, Doedens, M, Grunberger, T, Fulop, G, . . . Dick, JE 1989. A model of human acute lymphoblastic leukemia in immune-deficient SCID mice. *Science,* 246**,** 1597-600.

Kantarjian, HM, Keating, MJ & Freireich, EJ 2018. Toward the potential cure of leukemias in the next decade. *Cancer,* 124**,** 4301-4313.

Kastenhuber, ER & Lowe, SW 2017. Putting p53 in Context. *Cell,* 170**,** 1062-1078.

Kawamata, N, Ogawa, S, Seeger, K, Kirschner-Schwabe, R, Huynh, T, Chen, J, . . . Koeffler, HP 2009. Molecular allelokaryotyping of relapsed pediatric acute lymphoblastic leukemia. *Int J Oncol,* 34**,** 1603-12.

Kemper, K, Krijgsman, O, Cornelissen-Steijger, P, Shahrabi, A, Weeber, F, Song, JY, . . . Peeper, DS 2015. Intra- and inter-tumor heterogeneity in a vemurafenib-resistant melanoma patient and derived xenografts. *EMBO Mol Med,* 7**,** 1104-18.

Khaw, SL, Suryani, S, Evans, K, Richmond, J, Robbins, A, Kurmasheva, RT, . . . Lock, RB 2016. Venetoclax responses of pediatric ALL xenografts reveal sensitivity of MLL-rearranged leukemia. *Blood,* 128**,** 1382-95.

Kim, HK, Min, S, Song, M, Jung, S, Choi, JW, Kim, Y, . . . Kim, HH 2018. Deep learning improves prediction of CRISPR-Cpf1 guide RNA activity. *Nat Biotechnol,* 36**,** 239-241.

Klumper, E, Pieters, R, Veerman, AJ, Huismans, DR, Loonen, AH, Hahlen, K, . . . Henze, G 1995. In vitro cellular drug resistance in children with relapsed/refractory acute lymphoblastic leukemia. *Blood,* 86**,** 3861-8.

Knudson, AG, Jr. 1971. Mutation and cancer: statistical study of retinoblastoma. *Proc Natl Acad Sci U S A,* 68**,** 820-3.

Koelling, TM, Yeager, AM, Hilton, J, Haynie, DT & Wiley, JM 1990. Development and characterization of a cyclophosphamide-resistant subline of acute myeloid leukemia in the Lewis x Brown Norway hybrid rat. *Blood,* 76**,** 1209-13.

Krall, EB, Wang, B, Munoz, DM, Ilic, N, Raghavan, S, Niederst, MJ, . . . Hahn, WC 2017. KEAP1 loss modulates sensitivity to kinase targeted therapy in lung cancer. *Elife,* 6.

Kreso, A & Dick, JE 2014. Evolution of the cancer stem cell model. *Cell Stem Cell,* 14**,** 275-91.

Kulak, NA, Pichler, G, Paron, I, Nagaraj, N & Mann, M 2014. Minimal, encapsulated proteomic-sample processing applied to copy-number estimation in eukaryotic cells. *Nat Methods,* 11**,** 319-24.

Lahaye, T, Riehm, B, Berger, U, Paschka, P, Muller, MC, Kreil, S, . . . Hochhaus, A 2005. Response and resistance in 300 patients with BCR-ABL-positive leukemias treated with imatinib in a single center: a 4.5-year follow-up. *Cancer,* 103**,** 1659-69.

Le Sage, C, Lawo, S, Panicker, P, Scales, TME, Rahman, SA, Little, AS, . . . Cross, BCS 2017. Dual direction CRISPR transcriptional regulation screening uncovers gene networks driving drug resistance. *Sci Rep,* 7**,** 17693.

Lee, EM, Bachmann, PS & Lock, RB 2007. Xenograft models for the preclinical evaluation of new therapies in acute leukemia. *Leuk Lymphoma,* 48**,** 659-68.

Li, Q, Song, W & Wang, J 2019. TUG1 confers Adriamycin resistance in acute myeloid leukemia by epigenetically suppressing miR-34a expression via EZH2. *Biomed Pharmacother,* 109**,** 1793-1801.

Li, W, Xu, H, Xiao, T, Cong, L, Love, MI, Zhang, F, . . . Liu, XS 2014. MAGeCK enables robust identification of essential genes from genome-scale CRISPR/Cas9 knockout screens. *Genome Biol,* 15**,** 554.

Lian, B, Pei, YC, Jiang, YZ, Xue, MZ, Li, DQ, Li, XG, . . . Shao, ZM 2020. Truncated HDAC9 identified by integrated genome-wide screen as the key modulator for paclitaxel resistance in triple-negative breast cancer. *Theranostics,* 10**,** 11092-11109.

Liem, NL, Papa, RA, Milross, CG, Schmid, MA, Tajbakhsh, M, Choi, S, . . . Lock, RB 2004. Characterization of childhood acute lymphoblastic leukemia xenograft models for the preclinical evaluation of new therapies. *Blood,* 103**,** 3905-14.

Liu, WH, Mrozek-Gorska, P, Wirth, AK, Herold, T, Schwarzkopf, L, Pich, D, . . . Jeremias, I 2020. Inducible transgene expression in PDX models in vivo identifies KLF4 as a therapeutic target for B-ALL. *Biomark Res,* 8**,** 46.

Liu, Y, Chen, C, Xu, Z, Scuoppo, C, Rillahan, CD, Gao, J, . . . Lowe, SW 2016. Deletions linked to TP53 loss drive cancer through p53-independent mechanisms. *Nature,* 531**,** 471-475.

Liu, Y, Mi, Y, Mueller, T, Kreibich, S, Williams, EG, Van Drogen, A, . . . Aebersold, R 2019. Multi-omic measurements of heterogeneity in HeLa cells across laboratories. *Nat Biotechnol,* 37**,** 314-322.

Lock, RB, Liem, N, Farnsworth, ML, Milross, CG, Xue, C, Tajbakhsh, M, . . . Rice, AM 2002. The nonobese diabetic/severe combined immunodeficient (NOD/SCID) mouse model of childhood acute lymphoblastic leukemia reveals intrinsic differences in biologic characteristics at diagnosis and relapse. *Blood,* 99**,** 4100-8.

Love, MI, Huber, W & Anders, S 2014. Moderated estimation of fold change and dispersion for RNA-seq data with DESeq2. *Genome Biol,* 15**,** 550.

Ma, X, Edmonson, M, Yergeau, D, Muzny, DM, Hampton, OA, Rusch, M, . . . Zhang, J 2015. Rise and fall of subclones from diagnosis to relapse in pediatric B-acute lymphoblastic leukaemia. *Nat Commun,* 6**,** 6604.

Ma, X, Liu, Y, Liu, Y, Alexandrov, LB, Edmonson, MN, Gawad, C, . . . Zhang, J 2018. Pan-cancer genome and transcriptome analyses of 1,699 paediatric leukaemias and solid tumours. *Nature,* 555**,** 371-376.

Malard, F & Mohty, M 2020. Acute lymphoblastic leukaemia. *Lancet,* 395**,** 1146-1162.

Maloney, KW, Mcgavran, L, Odom, LF & Hunger, SP 1999. Acquisition of p16(INK4A) and p15(INK4B) gene abnormalities between initial diagnosis and relapse in children with acute lymphoblastic leukemia. *Blood,* 93**,** 2380-5.

Marusyk, A, Janiszewska, M & Polyak, K 2020. Intratumor Heterogeneity: The Rosetta Stone of Therapy Resistance. *Cancer Cell,* 37**,** 471-484.
Metzeler, KH, Herold, T, Rothenberg-Thurley, M, Amler, S, Sauerland, MC, Gorlich, D, . . . Group, AS 2016. Spectrum and prognostic relevance of driver gene mutations in acute myeloid leukemia. *Blood,* 128**,** 686-98.
Meyer, LH & Debatin, KM 2011. Diversity of human leukemia xenograft mouse models: implications for disease biology. *Cancer Res,* 71**,** 7141-4.
Milan, T, Canaj, H, Villeneuve, C, Ghosh, A, Barabe, F, Cellot, S & Wilhelm, BT 2019. Pediatric leukemia: Moving toward more accurate models. *Exp Hematol,* 74**,** 1-12.
Montero, J & Letai, A 2018. Why do BCL-2 inhibitors work and where should we use them in the clinic? *Cell Death Differ,* 25**,** 56-64.
Morisot, S, Wayne, AS, Bohana-Kashtan, O, Kaplan, IM, Gocke, CD, Hildreth, R, . . . Civin, CI 2010. High frequencies of leukemia stem cells in poor-outcome childhood precursor-B acute lymphoblastic leukemias. *Leukemia,* 24**,** 1859-66.
Mullighan, CG, Phillips, LA, Su, X, Ma, J, Miller, CB, Shurtleff, SA & Downing, JR 2008. Genomic analysis of the clonal origins of relapsed acute lymphoblastic leukemia. *Science,* 322**,** 1377-80.
Naghizadeh, S, Mohammadi, A, Duijf, PHG, Baradaran, B, Safarzadeh, E, Cho, WC & Mansoori, B 2020. The role of miR-34 in cancer drug resistance. *J Cell Physiol,* 235**,** 6424-6440.
Nair, AB & Jacob, S 2016. A simple practice guide for dose conversion between animals and human. *J Basic Clin Pharm,* 7**,** 27-31.
Navarro, F & Lieberman, J 2015. miR-34 and p53: New Insights into a Complex Functional Relationship. *PLoS One,* 10**,** e0132767.
Nijmeijer, BA, Mollevanger, P, Van Zelderen-Bhola, SL, Kluin-Nelemans, HC, Willemze, R & Falkenburg, JH 2001. Monitoring of engraftment and progression of acute lymphoblastic leukemia in individual NOD/SCID mice. *Exp Hematol,* 29**,** 322-9.
Nowak, D, Liem, NL, Mossner, M, Klaumunzer, M, Papa, RA, Nowak, V, . . . Koeffler, HP 2015. Variegated clonality and rapid emergence of new molecular lesions in xenografts of acute lymphoblastic leukemia are associated with drug resistance. *Exp Hematol,* 43**,** 32-43 e1-35.
Olivieri, M, Cho, T, Alvarez-Quilon, A, Li, K, Schellenberg, MJ, Zimmermann, M, . . . Durocher, D 2020. A Genetic Map of the Response to DNA Damage in Human Cells. *Cell,* 182**,** 481-496 e21.
Oshima, K, Khiabanian, H, Da Silva-Almeida, AC, Tzoneva, G, Abate, F, Ambesi-Impiombato, A, . . . Ferrando, AA 2016. Mutational landscape, clonal evolution patterns, and role of RAS mutations in relapsed acute lymphoblastic leukemia. *Proc Natl Acad Sci U S A,* 113**,** 11306-11311.
Parekh, S, Ziegenhain, C, Vieth, B, Enard, W & Hellmann, I 2018. zUMIs - A fast and flexible pipeline to process RNA sequencing data with UMIs. *Gigascience,* 7.
Perini, GF, Ribeiro, GN, Pinto Neto, JV, Campos, LT & Hamerschlak, N 2018. BCL-2 as therapeutic target for hematological malignancies. *J Hematol Oncol,* 11**,** 65.
Pompili, L, Porru, M, Caruso, C, Biroccio, A & Leonetti, C 2016. Patient-derived xenografts: a relevant preclinical model for drug development. *J Exp Clin Cancer Res,* 35**,** 189.
Pritchard, JR, Bruno, PM, Gilbert, LA, Capron, KL, Lauffenburger, DA & Hemann, MT 2013. Defining principles of combination drug mechanisms of action. *Proc Natl Acad Sci U S A,* 110**,** E170-9.
Pritchard, JR, Lauffenburger, DA & Hemann, MT 2012. Understanding resistance to combination chemotherapy. *Drug Resist Updat,* 15**,** 249-57.
Rabinovich, BA, Ye, Y, Etto, T, Chen, JQ, Levitsky, HI, Overwijk, WW, . . . Hwu, P 2008. Visualizing fewer than 10 mouse T cells with an enhanced firefly luciferase in immunocompetent mouse models of cancer. *Proc Natl Acad Sci U S A,* 105**,** 14342-6.
Rafei, H, Kantarjian, HM & Jabbour, EJ 2019. Recent advances in the treatment of acute lymphoblastic leukemia. *Leuk Lymphoma,* 60**,** 2606-2621.
Rambow, F, Rogiers, A, Marin-Bejar, O, Aibar, S, Femel, J, Dewaele, M, . . . Marine, JC 2018. Toward Minimal Residual Disease-Directed Therapy in Melanoma. *Cell,* 174**,** 843-855 e19.
Ramirez, M, Rajaram, S, Steininger, RJ, Osipchuk, D, Roth, MA, Morinishi, LS, . . . Altschuler, SJ 2016. Diverse drug-resistance mechanisms can emerge from drug-tolerant cancer persister cells. *Nat Commun,* 7**,** 10690.
Ritchie, ME, Phipson, B, Wu, D, Hu, Y, Law, CW, Shi, W & Smyth, GK 2015. limma powers differential expression analyses for RNA-sequencing and microarray studies. *Nucleic Acids Res,* 43**,** e47.
Roberts, AW & Huang, D 2017. Targeting BCL2 With BH3 Mimetics: Basic Science and Clinical Application of Venetoclax in Chronic Lymphocytic Leukemia and Related B Cell Malignancies. *Clin Pharmacol Ther,* 101**,** 89-98.
Roberts, KG, Morin, RD, Zhang, J, Hirst, M, Zhao, Y, Su, X, . . . Mullighan, CG 2012. Genetic alterations activating kinase and cytokine receptor signaling in high-risk acute lymphoblastic leukemia. *Cancer Cell,* 22**,** 153-66.

Roberts, KG & Mullighan, CG 2015. Genomics in acute lymphoblastic leukaemia: insights and treatment implications. *Nat Rev Clin Oncol,* 12**,** 344-57.

Rokavec, M, Li, H, Jiang, L & Hermeking, H 2014. The p53/miR-34 axis in development and disease. *J Mol Cell Biol,* 6**,** 214-30.

Ruiz, S, Mayor-Ruiz, C, Lafarga, V, Murga, M, Vega-Sendino, M, Ortega, S & Fernandez-Capetillo, O 2016. A Genome-wide CRISPR Screen Identifies CDC25A as a Determinant of Sensitivity to ATR Inhibitors. *Mol Cell,* 62**,** 307-313.

Sabnis, AJ & Bivona, TG 2019. Principles of Resistance to Targeted Cancer Therapy: Lessons from Basic and Translational Cancer Biology. *Trends Mol Med,* 25**,** 185-197.

Salomons, GS, Smets, LA, Verwijs-Janssen, M, Hart, AA, Haarman, EG, Kaspers, GJ, . . . Kamps, WA 1999. Bcl-2 family members in childhood acute lymphoblastic leukemia: relationships with features at presentation, in vitro and in vivo drug response and long-term clinical outcome. *Leukemia,* 13**,** 1574-80.

Samuels, AL, Beesley, AH, Yadav, BD, Papa, RA, Sutton, R, Anderson, D, . . . Lock, RB 2014. A pre-clinical model of resistance to induction therapy in pediatric acute lymphoblastic leukemia. *Blood Cancer J,* 4**,** e232.

Sanson, KR, Hanna, RE, Hegde, M, Donovan, KF, Strand, C, Sullender, ME, . . . Doench, JG 2018. Optimized libraries for CRISPR-Cas9 genetic screens with multiple modalities. *Nat Commun,* 9**,** 5416.

Schleicher, EM, Dhoonmoon, A, Jackson, LM, Clements, KE, Stump, CL, Nicolae, CM & Moldovan, GL 2020. Dual genome-wide CRISPR knockout and CRISPR activation screens identify mechanisms that regulate the resistance to multiple ATR inhibitors. *PLoS Genet,* 16**,** e1009176.

Senthebane, DA, Rowe, A, Thomford, NE, Shipanga, H, Munro, D, Mazeedi, M, . . . Dzobo, K 2017. The Role of Tumor Microenvironment in Chemoresistance: To Survive, Keep Your Enemies Closer. *Int J Mol Sci,* 18.

Seyfried, F, Demir, S, Horl, RL, Stirnweiss, FU, Ryan, J, Scheffold, A, . . . Meyer, LH 2019. Prediction of venetoclax activity in precursor B-ALL by functional assessment of apoptosis signaling. *Cell Death Dis,* 10**,** 571.

Shalem, O, Sanjana, NE, Hartenian, E, Shi, X, Scott, DA, Mikkelson, T, . . . Zhang, F 2014. Genome-scale CRISPR-Cas9 knockout screening in human cells. *Science,* 343**,** 84-87.

Shalem, O, Sanjana, NE & Zhang, F 2015. High-throughput functional genomics using CRISPR-Cas9. *Nat Rev Genet,* 16**,** 299-311.

Sharma, SV, Lee, DY, Li, B, Quinlan, MP, Takahashi, F, Maheswaran, S, . . . Settleman, J 2010. A chromatin-mediated reversible drug-tolerant state in cancer cell subpopulations. *Cell,* 141**,** 69-80.

Sharma, V & Mcneill, JH 2009. To scale or not to scale: the principles of dose extrapolation. *Br J Pharmacol,* 157**,** 907-21.

Shen, S, Vagner, S & Robert, C 2020. Persistent Cancer Cells: The Deadly Survivors. *Cell,* 183**,** 860-874.

Shultz, LD, Lyons, BL, Burzenski, LM, Gott, B, Chen, X, Chaleff, S, . . . Handgretinger, R 2005. Human lymphoid and myeloid cell development in NOD/LtSz-scid IL2R gamma null mice engrafted with mobilized human hemopoietic stem cells. *J Immunol,* 174**,** 6477-89.

Siegel, RL, Miller, KD & Jemal, A 2020. Cancer statistics, 2020. *CA Cancer J Clin,* 70**,** 7-30.

Szczepanek, J, Styczynski, J, Haus, O, Tretyn, A & Wysocki, M 2011. Relapse of acute lymphoblastic leukemia in children in the context of microarray analyses. *Arch Immunol Ther Exp (Warsz),* 59**,** 61-8.

Szymanska, B, Wilczynska-Kalak, U, Kang, MH, Liem, NL, Carol, H, Boehm, I, . . . Lock, RB 2012. Pharmacokinetic modeling of an induction regimen for in vivo combined testing of novel drugs against pediatric acute lymphoblastic leukemia xenografts. *PLoS One,* 7**,** e33894.

Teicher, BA, Herman, TS, Holden, SA, Wang, YY, Pfeffer, MR, Crawford, JW & Frei, E, 3rd 1990. Tumor resistance to alkylating agents conferred by mechanisms operative only in vivo. *Science,* 247**,** 1457-61.

Terwilliger, T & Abdul-Hay, M 2017. Acute lymphoblastic leukemia: a comprehensive review and 2017 update. *Blood Cancer J,* 7**,** e577.

Terziyska, N, Castro Alves, C, Groiss, V, Schneider, K, Farkasova, K, Ogris, M, . . . Jeremias, I 2012. In vivo imaging enables high resolution preclinical trials on patients' leukemia cells growing in mice. *PLoS One,* 7**,** e52798.

Townsend, EC, Murakami, MA, Christodoulou, A, Christie, AL, Koster, J, Desouza, TA, . . . Weinstock, DM 2016. The Public Repository of Xenografts Enables Discovery and Randomized Phase II-like Trials in Mice. *Cancer Cell,* 29**,** 574-586.

Tremblay, CS, Saw, J, Chiu, SK, Wong, NC, Tsyganov, K, Ghotb, S, . . . Curtis, DJ 2018. Restricted cell cycle is essential for clonal evolution and therapeutic resistance of pre-leukemic stem cells. *Nat Commun,* 9**,** 3535.

Turajlic, S, Sottoriva, A, Graham, T & Swanton, C 2019. Resolving genetic heterogeneity in cancer. *Nat Rev Genet,* 20**,** 404-416.

Tyanova, S, Temu, T, Sinitcyn, P, Carlson, A, Hein, MY, Geiger, T, . . . Cox, J 2016. The Perseus computational platform for comprehensive analysis of (prote)omics data. *Nat Methods,* 13**,** 731-40.

Tzoneva, G, Perez-Garcia, A, Carpenter, Z, Khiabanian, H, Tosello, V, Allegretta, M, . . . Ferrando, A 2013. Activating mutations in the NT5C2 nucleotidase gene drive chemotherapy resistance in relapsed ALL. *Nat Med,* 19**,** 368-71.

Valentin, R, Grabow, S & Davids, MS 2018. The rise of apoptosis: targeting apoptosis in hematologic malignancies. *Blood,* 132**,** 1248-1264.

Van Dongen, JJ, Van Der Velden, VH, Bruggemann, M & Orfao, A 2015. Minimal residual disease diagnostics in acute lymphoblastic leukemia: need for sensitive, fast, and standardized technologies. *Blood,* 125**,** 3996-4009.

Vasan, N, Baselga, J & Hyman, DM 2019. A view on drug resistance in cancer. *Nature,* 575**,** 299-309.

Verrills, NM, Po'uha, ST, Liu, ML, Liaw, TY, Larsen, MR, Ivery, MT, . . . Kavallaris, M 2006. Alterations in gamma-actin and tubulin-targeted drug resistance in childhood leukemia. *J Natl Cancer Inst,* 98**,** 1363-74.

Verrills, NM, Walsh, BJ, Cobon, GS, Hains, PG & Kavallaris, M 2003. Proteome analysis of vinca alkaloid response and resistance in acute lymphoblastic leukemia reveals novel cytoskeletal alterations. *J Biol Chem,* 278**,** 45082-93.

Vick, B, Rothenberg, M, Sandhofer, N, Carlet, M, Finkenzeller, C, Krupka, C, . . . Jeremias, I 2015. An advanced preclinical mouse model for acute myeloid leukemia using patients' cells of various genetic subgroups and in vivo bioluminescence imaging. *PLoS One,* 10**,** e0120925.

Vosberg, S, Herold, T, Hartmann, L, Neumann, M, Opatz, S, Metzeler, KH, . . . Greif, PA 2016. Close correlation of copy number aberrations detected by next-generation sequencing with results from routine cytogenetics in acute myeloid leukemia. *Genes Chromosomes Cancer,* 55**,** 553-67.

Waanders, E, Gu, Z, Dobson, SM, Antic, Z, Crawford, JC, Ma, X, . . . Mullighan, CG 2020. Mutational landscape and patterns of clonal evolution in relapsed pediatric acute lymphoblastic leukemia. *Blood Cancer Discov,* 1**,** 96-111.

Wang, B, Wang, M, Zhang, W, Xiao, T, Chen, CH, Wu, A, . . . Liu, XS 2019. Integrative analysis of pooled CRISPR genetic screens using MAGeCKFlute. *Nat Protoc,* 14**,** 756-780.

Wang, T, Wei, JJ, Sabatini, DM & Lander, ES 2014. Genetic screens in human cells using the CRISPR-Cas9 system. *Science,* 343**,** 80-4.

Welch, C, Chen, Y & Stallings, RL 2007. MicroRNA-34a functions as a potential tumor suppressor by inducing apoptosis in neuroblastoma cells. *Oncogene,* 26**,** 5017-22.

Witkowski, MT, Dolgalev, I, Evensen, NA, Ma, C, Chambers, T, Roberts, KG, . . . Aifantis, I 2020. Extensive Remodeling of the Immune Microenvironment in B Cell Acute Lymphoblastic Leukemia. *Cancer Cell,* 37**,** 867-882 e12.

Woiterski, J, Ebinger, M, Witte, KE, Goecke, B, Heininger, V, Philippek, M, . . . Andre, MC 2013. Engraftment of low numbers of pediatric acute lymphoid and myeloid leukemias into NOD/SCID/IL2Rcgammanull mice reflects individual leukemogenecity and highly correlates with clinical outcome. *Int J Cancer,* 133**,** 1547-56.

Wong, NC, Bhadri, VA, Maksimovic, J, Parkinson-Bates, M, Ng, J, Craig, JM, . . . Lock, RB 2014. Stability of gene expression and epigenetic profiles highlights the utility of patient-derived paediatric acute lymphoblastic leukaemia xenografts for investigating molecular mechanisms of drug resistance. *BMC Genomics,* 15**,** 416.

Yadav, BD, Samuels, AL, Wells, JE, Sutton, R, Venn, NC, Bendak, K, . . . Lock, RB 2016. Heterogeneity in mechanisms of emergent resistance in pediatric T-cell acute lymphoblastic leukemia. *Oncotarget,* 7**,** 58728-42.

Yang, JJ, Bhojwani, D, Yang, W, Cai, X, Stocco, G, Crews, K, . . . Carroll, WL 2008. Genome-wide copy number profiling reveals molecular evolution from diagnosis to relapse in childhood acute lymphoblastic leukemia. *Blood,* 112**,** 4178-83.

Yates, AD, Achuthan, P, Akanni, W, Allen, J, Allen, J, Alvarez-Jarreta, J, . . . Flicek, P 2020. Ensembl 2020. *Nucleic Acids Res,* 48**,** D682-D688.

Zenz, T, Mohr, J, Eldering, E, Kater, AP, Buhler, A, Kienle, D, . . . Stilgenbauer, S 2009. miR-34a as part of the resistance network in chronic lymphocytic leukemia. *Blood,* 113**,** 3801-8.

Zhang, J, Tian, Q, Chan, SY, Duan, W & Zhou, S 2005. Insights into oxazaphosphorine resistance and possible approaches to its circumvention. *Drug Resist Updat,* 8**,** 271-97.

Zheng, HC 2017. The molecular mechanisms of chemoresistance in cancers. *Oncotarget,* 8**,** 59950-59964.

Appendix

A1. CNA data from whole exome sequencing

Table 19: CNA of donor sample of ALL-199 related to complete remission of patient as germline control.

Start and end position of hg19 reference genome. Ratio was calculated as donor sample/complete remission. Only ratio >1.1 or <0.9 are listed.

Sample	Chr	Start position	End position	Ratio
donor	1	219352484	249212567	0.50
donor	2	25376576	27852314	1.12
donor	3	361455	9506361	0.87
donor	6	25921229	33385092	1.25
donor	6	117639346	150266713	1.39
donor	6	150267503	167796366	1.49
donor	6	168227808	170893674	1.37
donor	7	48685008	55606355	0.48
donor	7	55620341	76866351	1.10
donor	7	76871003	96637148	0.90
donor	7	151970785	158937468	0.84
donor	8	7218627	11710968	1.11
donor	8	122626344	124096585	0.63
donor	9	21007031	24545652	0.00
donor	9	71114138	90584269	0.90
donor	10	29169062	31139301	1.32
donor	10	55719487	70191733	0.87
donor	11	3660867	6953908	1.18
donor	11	62284211	67048259	1.10
donor	12	58191660	66620622	0.90
donor	13	41556114	47224485	1.39
donor	13	47243160	95725563	1.47
donor	13	95726463	98660401	1.20
donor	13	98662130	111287128	1.41
donor	13	111287810	115091761	1.40
donor	14	19377589	25076958	1.11
donor	14	25077466	33836479	0.88
donor	16	28735638	31505262	1.15
donor	16	66885361	70531963	1.15
donor	16	70534856	71954730	0.87
donor	16	71955241	74447061	1.15
donor	17	26091002	39767487	1.53
donor	17	39767592	57058397	1.62
donor	17	57060274	61996141	1.41
donor	17	62006581	81052325	1.55
donor	18	33751005	34753049	0.75
donor	19	6833190	9026320	1.56
donor	19	9027211	15383915	1.69
donor	19	51914348	55354378	1.24
donor	20	44469082	46262944	1.13
donor	21	10906900	14987896	2.39
donor	21	46931020	48084291	0.86
donor	22	21075581	31904367	1.10
donor	X	37985836	71363429	1.20
donor	X	99891600	134856800	1.17
donor	X	134869959	151870260	1.15
donor	X	152969409	155240079	1.16
donor	Y	150850	21154600	1.14
donor	Y	21867876	59343085	1.14

Table 20: CNA of resistant derivatives and untreated control related to donor sample of ALL-199.

Start and end position of hg19 reference genome. Ratio was calculated as donor sample/complete remission. Only ratio >1.1 or <0.9 are listed.

Sample	Chr	Start position	End position	Ratio
untreated	1	16894469	17084157	1.16
untreated	2	97788619	98173600	1.40
untreated	2	106774509	109378656	1.27
untreated	4	69334592	71021799	1.21
untreated	7	57187542	64853819	1.25
untreated	7	76991895	94156523	1.11
untreated	8	62538827	75929353	1.10
untreated	8	88365859	91946590	1.15
untreated	9	14802	175789	1.14
untreated	9	38016003	67938663	1.11
untreated	10	32745174	33143422	1.88
untreated	11	132016171	134257558	1.13
untreated	12	81025966	88519151	1.16
untreated	13	96553056	96684230	1.60

Continued Table 20:

Sample	Chr	Start position	End position	Ratio
untreated	14	19377589	19573149	1.35
untreated	15	102192469	102463267	1.18
untreated	16	28606683	28836728	1.11
untreated	17	6662976	8408229	0.88
untreated	18	14524907	14799299	1.19
untreated	19	19770702	30018307	1.15
untreated	21	14992474	15525010	1.74
untreated	22	48885400	49042563	1.61
D1	1	159141551	185240526	1.48
D1	1	185245731	193020952	1.44
D1	1	193028310	215747187	1.50
D1	1	215747411	218614709	1.41
D1	2	97851170	98173600	1.16
D1	4	42119530	43032562	0.49
D1	5	10618440	11236940	0.49
D1	6	117586922	123600232	1.34
D1	6	123637597	132796806	1.26
D1	6	132824580	143789307	1.30
D1	6	143792093	167417304	1.33
D1	6	167417747	170893674	1.33
D1	8	39550114	39695709	1.74
D1	17	6006	18996944	0.51
D1	17	19186428	21117470	0.52
D1	17	21146621	34432710	0.68
D1	17	34842539	41332839	0.68
D1	17	41338262	44249514	0.68
D1	17	44625673	81052325	0.68
D1	X	109693841	120009529	0.50
D1	X	120181534	134967501	0.50
D1	X	134978397	153847474	0.52
D1	X	153880398	154528463	0.49
D1	X	154563675	154774942	0.73
D2	1	16894469	17085086	1.12
D2	2	97783796	98173600	1.29
D2	2	106774509	109378656	1.28
D2	3	134369662	134977967	1.25
D2	4	53378	338224	1.46
D2	4	69334592	71021799	1.18
D2	6	29913006	33290696	0.90
D2	6	167417747	170893674	1.10
D2	7	56149318	64853819	1.26
D2	9	14802	175789	1.14
D2	11	130749514	134257558	1.17
D2	12	56915803	64480811	1.15
D2	12	82872706	89745821	1.18
D2	14	19377589	19573149	1.57
D2	15	102194780	102463267	1.14
D2	16	28606683	28734649	1.15
D2	17	6006	10322123	0.49
D2	17	10322199	20217383	0.54
D2	17	20353281	34432710	0.66

Sample	Chr	Start position	End position	Ratio
D2	17	34522680	34842634	0.89
D2	17	34842774	36342637	0.66
D2	17	36343881	44249514	0.65
D2	17	44771836	81052325	0.67
D2	18	14524907	14843100	1.22
D2	19	19774075	30018307	1.18
D2	19	43228129	43772306	1.14
D2	19	52785359	53995345	1.15
D2	21	10906900	15002226	1.11
D2	21	15003257	15525010	1.30
D2	22	16258181	16449809	1.39
D2	22	17071762	18166092	0.90
D2	22	39498512	42459033	0.89
D2	22	48885400	49042563	1.81
D4	1	69085	12943220	0.48
D4	1	13802309	31210551	0.52
D4	1	31211782	33999512	0.81
D4	2	41603	25049000	1.14
D4	2	97788619	98197036	1.44
D4	2	106774509	109378656	1.31
D4	4	69327534	71021799	1.26
D4	4	190864352	191013439	1.46
D4	6	29910326	33608336	0.89
D4	6	121577225	123600232	1.22
D4	7	57187542	64441803	1.28
D4	7	76991895	94156523	1.12
D4	7	99686609	101962102	0.90
D4	8	62538827	75929353	1.12
D4	8	144413389	146279548	0.86
D4	9	14802	156532	1.18
D4	9	37955875	67938663	1.12
D4	9	139326271	140356077	0.82
D4	11	193095	1093938	0.86
D4	11	63520536	67816469	0.85
D4	12	6344390	7360681	0.87
D4	12	58335480	93258768	1.11
D4	14	19377589	19573149	1.44
D4	16	277236	3543992	0.83
D4	16	28855052	31505262	0.86
D4	16	66948114	69969894	0.90
D4	16	88071574	90142323	0.89
D4	17	6006	8395832	0.86
D4	17	39725673	43364735	0.88
D4	17	67124755	67501992	1.16
D4	17	67512991	76230061	0.88
D4	17	79405389	80059747	0.83
D4	18	14524907	14799299	1.27
D4	19	9875607	11688137	0.87
D4	19	12719967	14675104	0.84
D4	19	19779768	30019374	1.17
D4	20	58514082	62904958	0.90

Continued Table 20:

Sample	Chr	Start position	End position	Ratio
D4	21	10906900	14990781	1.19
D4	21	14992474	15525010	1.80
D4	22	46739154	50566941	0.88
D4	22	50572431	51220727	0.83
D4	X	152818488	155240079	0.89
D5	1	69085	28477537	0.52
D5	1	28527754	31188161	0.84
D5	1	53393064	104166848	1.16
D5	1	156127856	158299443	1.23
D5	1	158299637	161483727	1.38
D5	1	161487760	218614709	1.48
D5	2	97788619	98173600	1.23
D5	2	106729097	109378656	1.22
D5	3	134369662	134920536	1.25
D5	4	190864352	191013439	1.41
D5	6	117586922	123600232	1.42
D5	6	123637597	143789307	1.32
D5	6	143792093	167417304	1.34
D5	6	167417747	170893674	1.41
D5	7	56147216	64853819	1.23
D5	9	37948627	67938663	1.12
D5	10	32742267	33137651	1.89
D5	11	130288943	134257558	1.10
D5	15	28566503	28957474	1.49
D5	16	97425	1261810	1.13
D5	16	53265554	69995992	1.11
D5	16	69996874	70165327	1.34
D5	16	70166049	74452201	1.14
D5	16	74454394	90142323	1.14
D5	17	37873568	38923910	0.90
D5	18	14524907	14799299	1.21
D5	19	19770702	30199335	1.15
D5	19	43233270	43702432	1.11
D5	21	10906900	15002226	1.13
D5	21	15003257	15525010	1.31
D5	22	16258181	16449809	1.37
D5	X	70329073	70817893	0.88
D6	1	69085	12908147	0.51
D6	1	13802309	16913761	0.53
D6	1	16914215	17298147	0.69
D6	1	17298850	31468072	0.51
D6	1	31478695	33066025	0.72
D6	2	97788619	98197036	1.30
D6	10	32745174	33137651	1.67
D6	17	30325672	30520268	1.15
D6	19	110674	4037878	1.31
D6	19	4047745	6833969	1.27
D6	19	6836438	8118011	1.18
D6	21	38460491	38563730	1.15
D7	1	69085	13183877	0.52
D7	1	13802309	32044873	0.53
D7	1	149762788	185240526	1.48
D7	1	185245731	215747187	1.48
D7	1	215747411	218614709	1.43
D7	2	97788619	98173600	1.21
D7	6	117252489	123600232	1.34
D7	6	123637597	132796806	1.27
D7	6	132824580	143789307	1.30
D7	6	143792093	167417304	1.32
D7	6	167417747	170893674	1.33
D7	15	49776502	49903470	1.67
D7	17	67161100	67293505	1.11
D8	1	69085	6132863	0.66
D8	1	6133788	13183877	0.52
D8	1	13802309	16913761	0.52
D8	1	16914215	21771717	0.65
D8	1	21795176	29139127	0.52
D8	1	29185461	32692136	0.87
D8	2	97845470	98173600	1.23
D8	4	70803513	71021799	1.11
D8	14	19377589	19573149	1.11

A2. Differentially expressed transcripts from prime-Seq

Table 21: Significantly upregulated transcripts of resistant vs. untreated ALL-199 cells.

All transcripts with $p < 0.01$ are listed and ranked by log_2 fold change (log_2 fc) between resistant and untreated ALL-199 cells.

#	Gene name	log_2 fc	p-value	#	Gene name	log_2 fc	p-value
1	C1QTNF4	2.5432	2.69E-05	49	RAB5A	1.2565	5.94E-04
2	FP325335.1	2.3193	8.96E-09	50	COPS2	1.2548	4.49E-03
3	SIX3	1.9138	3.33E-05	51	AL359076.1	1.2541	1.54E-03
4	IGF2BP2	1.8610	3.38E-06	52	ZCCHC7	1.2482	7.10E-03
5	KDM5B	1.8367	1.86E-04	53	APC	1.2459	1.99E-03
6	KCNE3	1.8322	2.47E-06	54	MCM3AP-AS1	1.2458	4.74E-03
7	LINC02273	1.8223	2.38E-05	55	KLHL23	1.2457	5.37E-03
8	DPEP1	1.7503	1.51E-05	56	TMEM92	1.2450	7.94E-04
9	NRP1	1.7190	4.76E-04	57	MBIP	1.2429	3.02E-03
10	AKAP12	1.6857	3.36E-04	58	TPO	1.2429	7.99E-03
11	P2RY14	1.6371	5.57E-05	59	FUT7	1.2394	2.81E-05
12	BRWD3	1.6158	2.24E-04	60	CD163L1	1.2335	1.17E-03
13	AC008060.4	1.5996	1.78E-04	61	UBE2E2	1.2277	9.39E-03
14	SHANK3	1.5391	5.42E-07	62	COL23A1	1.2249	3.11E-03
15	AC245060.5	1.4881	3.53E-03	63	RHOXF2	1.2161	2.31E-04
16	SV2C	1.4845	2.71E-04	64	NEXN	1.2125	2.14E-03
17	TSPAN5	1.4769	5.97E-04	65	BLNK	1.2074	9.04E-04
18	ASPM	1.4650	5.97E-03	66	MPP6	1.2049	6.49E-03
19	AC008060.1	1.4638	6.82E-04	67	CD9	1.2033	4.48E-04
20	SRP9	1.4509	6.64E-03	68	GSPT2	1.2024	4.55E-03
21	AC078883.2	1.4491	7.61E-05	69	PSMG2	1.1991	2.34E-03
22	CYP46A1	1.4448	5.70E-04	70	CREB3L4	1.1951	1.13E-03
23	GPR160	1.4445	6.98E-05	71	FSCN1	1.1939	1.84E-03
24	ERGIC2	1.4444	2.44E-04	72	FNDC3B	1.1920	5.02E-03
25	SLC25A36	1.4434	3.04E-03	73	RFX8	1.1919	6.09E-03
26	CREG2	1.4204	1.68E-03	74	FXYD5	1.1916	1.30E-04
27	ZNF644	1.4193	8.25E-04	75	GGH	1.1879	7.12E-03
28	F11R	1.4155	4.74E-04	76	PTPN12	1.1852	3.57E-03
29	SYNE2	1.4096	1.80E-03	77	EEF1A1P38	1.1838	8.71E-05
30	FXYD6-FXYD2	1.4007	2.21E-03	78	SERPINE2	1.1745	3.78E-03
31	ATF6	1.3889	1.81E-03	79	LARGE2	1.1739	2.08E-03
32	INAFM2	1.3855	2.50E-04	80	IFITM3	1.1728	4.23E-03
33	H1FX	1.3766	1.30E-04	81	LAX1	1.1727	6.03E-03
34	MYLK	1.3710	5.60E-03	82	SORBS1	1.1690	1.78E-04
35	STK38	1.3682	1.63E-03	83	GSE1	1.1654	7.03E-03
36	AC135983.2	1.3571	6.52E-04	84	MSANTD3	1.1610	1.54E-04
37	RIPOR1	1.3569	4.48E-04	85	SDK2	1.1596	9.98E-04
38	MME	1.3397	4.38E-04	86	LARP1B	1.1571	5.29E-04
39	EVI2B	1.3382	1.09E-03	87	PRCD	1.1553	3.88E-04
40	C9	1.3320	3.73E-04	88	TBX21	1.1543	1.06E-04
41	ZNF793	1.3311	3.96E-04	89	RPS29P5	1.1535	1.31E-03
42	MPST	1.3100	7.67E-04	90	CSNK2A1	1.1504	1.98E-04
43	PLCH1	1.3080	4.04E-03	91	AC127502.1	1.1484	2.28E-03
44	SNHG14	1.2847	1.09E-03	92	RUFY2	1.1465	5.89E-03
45	TSHZ1	1.2815	4.99E-03	93	C9orf139	1.1455	2.88E-03
46	TCF7	1.2781	5.48E-03	94	OLFML2A	1.1402	3.30E-03
47	DHRS7	1.2744	3.88E-04	95	CBR4	1.1380	5.12E-03
48	FRZB	1.2703	1.61E-03	96	TMEM225	1.1350	3.41E-03

Continued Table 21:

#	Gene name	log_2 fc	p-value
97	BRIP1	1.1348	2.75E-03
98	PDCD6IP	1.1338	9.90E-04
99	AC012254.2	1.1292	7.38E-03
100	SCN1B	1.1280	2.26E-03
101	FXYD2	1.1263	7.15E-03
102	NA	1.1239	6.76E-03
103	TTK	1.1209	9.67E-03
104	BABAM2	1.1128	1.95E-03
105	LIG4	1.1072	8.16E-03
106	ZBED3	1.0919	9.01E-03
107	AL590226.1	1.0908	1.60E-03
108	WHAMMP3	1.0883	1.55E-03
109	CTHRC1	1.0840	2.49E-04
110	ARL17A	1.0838	6.65E-03
111	NSD3	1.0836	1.53E-03
112	DSTN	1.0781	3.37E-03
113	ZNF467	1.0754	6.53E-03
114	SLC25A43	1.0752	5.24E-03
115	UPF3AP2	1.0738	4.54E-03
116	NEK1	1.0719	6.51E-03
117	CNOT10	1.0684	1.32E-03
118	ANKRD28	1.0650	1.52E-03
119	KDSR	1.0637	7.96E-03
120	DMAC2	1.0633	2.88E-03
121	UBXN7	1.0616	4.11E-03
122	BCL9	1.0598	1.82E-03
123	AC015961.1	1.0588	6.88E-03
124	LRRC37A17P	1.0519	6.13E-03
125	LMBRD2	1.0503	6.52E-03
126	C2orf68	1.0502	5.38E-03
127	PRKRA	1.0473	8.72E-03
128	SCCPDH	1.0469	7.82E-04
129	BICD1	1.0469	2.17E-03
130	FYN	1.0469	2.32E-03
131	RF00019	1.0466	4.90E-03
132	DIP2B	1.0465	2.92E-03
133	GBP4	1.0425	7.77E-03
134	CCDC69	1.0389	5.11E-03
135	DYSF	1.0353	4.37E-03
136	H6PD	1.0305	7.52E-03
137	NA	1.0289	6.81E-03
138	RPL32P3	1.0281	6.00E-03
139	BIN1	1.0241	3.68E-03
140	BCL6B	1.0210	4.75E-03
141	ZNF45	1.0177	3.75E-03
142	SLC35E3	1.0165	4.17E-03
143	NA	1.0161	1.85E-03
144	ZNF544	1.0159	3.05E-03
145	ZNF260	1.0147	8.53E-03
146	AC023794.5	1.0130	3.13E-03
147	ELP3	1.0118	9.10E-03
148	B4GALT6	1.0115	1.79E-03
149	FBXW7	1.0115	9.11E-05
150	FGF16	1.0104	7.02E-03
151	ADGRG1	1.0053	1.09E-03
152	RAP1GAP2	1.0009	2.22E-04
153	AC005324.3	1.0002	6.56E-03
154	APBB2	0.9958	7.69E-03
155	LINC00189	0.9956	6.69E-03
156	CD164	0.9954	8.22E-03
157	TMX4	0.9918	2.94E-04
158	SETD8P1	0.9896	9.03E-04
159	EIF1B	0.9827	8.10E-04
160	ADGRE2	0.9799	5.71E-03
161	JKAMP	0.9777	4.16E-03
162	MIR155HG	0.9771	3.47E-03
163	FGD5-AS1	0.9736	7.13E-03
164	FERMT2	0.9705	1.74E-03
165	NFE2	0.9679	9.30E-03
166	AC100788.2	0.9675	3.22E-03
167	THAP2	0.9662	9.55E-03
168	PIK3C2A	0.9654	9.67E-03
169	PXDN	0.9635	6.14E-05
170	OSBPL10	0.9605	6.35E-03
171	PLXND1	0.9576	1.95E-03
172	PRRT3	0.9571	8.55E-03
173	MELK	0.9508	4.57E-03
174	RASGEF1A	0.9495	4.89E-03
175	AC125257.1	0.9481	4.96E-03
176	DERA	0.9480	1.81E-03
177	SFXN5	0.9409	4.39E-03
178	SPINT1	0.9346	2.30E-03
179	PARG	0.9318	2.95E-03
180	PLAGL2	0.9312	5.98E-03
181	RF00012	0.9305	9.94E-03
182	KLHL12	0.9268	2.69E-03
183	AC093014.1	0.9217	2.57E-03
184	C1RL	0.9211	6.37E-03
185	FBXO34	0.9173	4.11E-03
186	NDC1	0.9168	9.70E-04
187	MDK	0.9126	1.59E-04
188	RALGPS2	0.9108	8.58E-03
189	SMIM24	0.9064	9.84E-03
190	SLC25A40	0.9061	3.63E-03
191	FBXL5	0.9038	4.52E-03
192	NOA1	0.9026	6.61E-03
193	PEMT	0.8979	2.97E-03
194	ST3GAL6	0.8965	9.31E-03
195	SLC15A4	0.8962	5.09E-03
196	GRIK5	0.8942	7.45E-04
197	WFS1	0.8927	3.06E-03
198	PDE8B	0.8906	6.11E-03
199	KMT2A	0.8892	5.03E-03
200	ZNF100	0.8858	1.97E-03

Continued Table 21:

#	Gene name	log_2 fc	p-value
201	XBP1	0.8851	3.23E-03
202	DUSP14	0.8849	4.24E-03
203	HHAT	0.8845	8.00E-03
204	AC087633.2	0.8835	6.83E-03
205	MDM2	0.8810	9.53E-03
206	RGP1	0.8807	9.65E-03
207	SNAPC3	0.8805	8.37E-03
208	RCAN1	0.8788	4.27E-03
209	EFNA1	0.8782	2.07E-03
210	CD99	0.8769	1.63E-03
211	AF201337.1	0.8757	4.08E-03
212	ZDHHC2	0.8728	6.75E-03
213	LIN9	0.8727	3.34E-03
214	PALM	0.8716	7.15E-03
215	CCNB1	0.8714	2.09E-03
216	CALML4	0.8671	5.31E-03
217	AMH	0.8649	3.20E-03
218	AC025048.6	0.8601	7.47E-03
219	ERG	0.8599	7.37E-05
220	AC245297.3	0.8598	7.65E-03
221	AC117386.2	0.8592	4.04E-04
222	LRRC37A	0.8584	9.15E-03
223	NA	0.8557	5.96E-03
224	GAPDHP73	0.8538	1.39E-03
225	PDPK2P	0.8532	4.77E-03
226	CHRFAM7A	0.8508	7.14E-03
227	ARL1	0.8477	7.97E-03
228	MARCH8	0.8439	9.04E-03
229	MPO	0.8438	2.32E-03
230	AC008124.1	0.8422	7.87E-03
231	GAPDHP44	0.8406	2.11E-03
232	PRAM1	0.8355	9.80E-03
233	PPIP5K2	0.8345	3.84E-03
234	AIG1	0.8345	9.05E-03
235	AC139256.2	0.8337	4.73E-03
236	FGFR1	0.8289	2.35E-03
237	SH3GLB1	0.8249	6.61E-03
238	RNF38	0.8247	5.97E-03
239	NSMCE1	0.8234	9.83E-03
240	FAM72C	0.8194	7.80E-03
241	TXLNG	0.8162	9.78E-03
242	B3GLCT	0.8151	7.00E-03
243	CD34	0.8125	3.01E-04
244	CPT1A	0.8102	6.06E-03
245	PPP1R11	0.8065	5.17E-03
246	NA	0.8020	6.09E-03
247	WARS2	0.7997	6.21E-03
248	TNFRSF1A	0.7969	1.68E-04
249	LIMD1	0.7969	5.70E-04
250	LAPTM4A	0.7940	1.66E-03
251	ST13P19	0.7861	7.16E-03
252	GSKIP	0.7824	5.56E-03
253	C14orf132	0.7795	7.66E-03
254	ZNF395	0.7680	4.26E-03
255	GNAI3	0.7670	8.83E-03
256	NGLY1	0.7582	6.31E-03
257	YTHDF1	0.7566	4.84E-03
258	CDK9	0.7412	2.72E-03
259	CSF3R	0.7326	9.33E-04
260	NUP43	0.7287	5.26E-03
261	AC008969.1	0.7199	3.64E-03
262	COL5A1	0.7165	6.09E-04
263	NPIPB3	0.7151	8.90E-03
264	SBF2	0.6976	5.89E-03
265	ALKBH3	0.6969	8.44E-03
266	RPF1	0.6968	6.22E-03
267	NPIPB12	0.6603	3.67E-03
268	TVP23C-CDRT4	0.6547	6.51E-03
269	ECM1	0.6515	8.14E-04
270	GYPC	0.6469	6.44E-04
271	AC020917.1	0.5996	8.13E-03
272	PRKD2	0.5990	1.10E-03
273	AC026403.1	0.5568	6.31E-03

Table 22: Significantly downregulated transcripts of resistant vs. untreated ALL-199 cells.

All transcripts with $p < 0.01$ are listed and ranked by log_2 fold change (log_2 fc) between resistant and untreated ALL-199 cells.

#	Gene name	log_2 fc	p-value
1	FAM129C	-0.4873	5.78E-03
2	ACLY	-0.5106	6.63E-03
3	HSPA5	-0.5271	7.13E-03
4	NARF	-0.5396	5.89E-03
5	ARHGAP45	-0.5598	5.01E-03
6	ATP5MC1	-0.5640	6.44E-03
7	TPI1	-0.5839	7.05E-03
8	COLGALT1	-0.5913	2.24E-03
9	MAP4K1	-0.5914	4.89E-03
10	SLC27A4	-0.5963	9.23E-03
11	CORO1A	-0.5968	5.80E-03
12	TPP1	-0.6030	8.90E-03
13	TRABD	-0.6079	1.40E-03
14	CCNL2	-0.6088	7.14E-03
15	VIRMA	-0.6091	7.17E-03
16	SEPT9	-0.6103	1.72E-03
17	SLC44A2	-0.6151	4.93E-03
18	NUDC	-0.6271	8.15E-03
19	H3F3C	-0.6298	5.26E-03
20	HLA-DQA1	-0.6331	1.37E-03
21	MRPL27	-0.6340	6.21E-03
22	PHF12	-0.6381	4.80E-03
23	IER2	-0.6398	2.46E-03
24	NXF1	-0.6423	3.08E-03
25	MAD2L2	-0.6440	7.72E-03
26	GAB3	-0.6495	1.13E-03
27	PRKCE	-0.6525	1.01E-03
28	PKIG	-0.6598	4.04E-03
29	EIF4A3	-0.6786	1.45E-03
30	RPA2	-0.6864	8.65E-03
31	ATP6V1G2-DDX39B	-0.6896	9.44E-03
32	DGKD	-0.6988	4.58E-03
33	KCNA5	-0.7038	9.86E-03
34	PYCARD	-0.7055	4.44E-03
35	POLR2G	-0.7079	3.22E-03
36	RABEP2	-0.7129	5.82E-03
37	VASP	-0.7222	3.39E-03
38	MKNK2	-0.7263	7.34E-03
39	RPS6KA1	-0.7372	4.60E-04
40	MIDN	-0.7374	1.33E-03
41	E2F2	-0.7394	2.84E-03
42	APEH	-0.7423	9.69E-03
43	NDUFA13	-0.7453	4.74E-03
44	KIAA2013	-0.7519	3.77E-03
45	PRMT1	-0.7621	4.68E-04
46	DBI	-0.7638	8.50E-03
47	FAM96B	-0.7639	8.86E-03
48	OSTF1	-0.7674	7.74E-03
49	SCPEP1	-0.7714	1.35E-03
50	FMNL1	-0.7812	3.75E-03
51	HIST2H2BE	-0.7822	1.77E-03
52	MSRA	-0.7856	6.24E-03
53	WASH3P	-0.7864	5.75E-03
54	COTL1	-0.7945	7.03E-03
55	RCC2	-0.7981	5.69E-03
56	PIK3C2B	-0.7981	1.25E-03
57	RBM38	-0.8066	4.23E-04
58	KDM4C	-0.8082	9.90E-03
59	ATAD3B	-0.8092	3.13E-03
60	RALGDS	-0.8095	9.73E-03
61	AC020915.1	-0.8139	9.68E-03
62	TMEM268	-0.8161	2.80E-03
63	METTL13	-0.8182	7.14E-03
64	AL391069.3	-0.8198	7.71E-03
65	SEC23A	-0.8213	9.25E-03
66	GRIPAP1	-0.8230	3.53E-03
67	WDR54	-0.8236	4.48E-03
68	FTLP17	-0.8262	2.44E-03
69	CHEK2	-0.8269	3.41E-03
70	IMP3	-0.8269	2.79E-03
71	TPI1P1	-0.8298	4.72E-03
72	CDK11A	-0.8322	3.49E-03
73	MGAT5	-0.8336	8.77E-04
74	SNRPG	-0.8366	9.70E-03
75	IRF8	-0.8406	1.27E-03
76	BICD2	-0.8435	9.53E-03
77	CDK16	-0.8482	4.45E-03
78	ITGAE	-0.8554	7.44E-03
79	TCL1A	-0.8560	1.43E-03
80	CDKN1A	-0.8576	2.10E-03
81	HIST1H2BB	-0.8583	4.72E-04
82	ZCCHC14	-0.8593	6.54E-03
83	DNAAF5	-0.8598	8.07E-03
84	RPL22P2	-0.8604	6.13E-04
85	CLCN5	-0.8626	8.51E-03
86	SPINDOC	-0.8639	3.80E-03
87	DLST	-0.8774	5.44E-03
88	DCANP1	-0.8804	1.11E-03
89	HARS	-0.8812	8.68E-03
90	DNAJC30	-0.8854	8.22E-03
91	DCAF4	-0.8884	7.92E-03
92	EMC9	-0.8958	9.32E-03
93	RAB11FIP3	-0.8959	8.21E-03
94	TNFRSF13C	-0.9010	6.81E-03
95	EFHD2	-0.9061	2.61E-03
96	AC022217.1	-0.9093	6.30E-03

Continued Table 22:

#	Gene name	log_2 fc	p-value
97	PMS2P4	-0.9172	7.12E-03
98	LY9	-0.9229	9.19E-04
99	RPS7P14	-0.9295	8.01E-03
100	REC8	-0.9320	6.01E-03
101	AC092017.1	-0.9325	6.85E-03
102	TNFAIP1	-0.9375	6.25E-03
103	C12orf49	-0.9402	8.21E-04
104	AC009117.1	-0.9415	4.76E-03
105	AGTRAP	-0.9416	5.21E-03
106	MINOS1P2	-0.9489	5.75E-03
107	DAPK3	-0.9497	5.14E-04
108	RFX1	-0.9518	8.37E-03
109	CCDC116	-0.9568	6.26E-03
110	ALOX5AP	-0.9628	1.04E-03
111	RHOB	-0.9671	8.69E-03
112	DAPP1	-0.9755	2.33E-03
113	SPRYD3	-0.9808	3.60E-03
114	IFRD1	-0.9814	9.09E-03
115	LINC01102	-0.9912	8.10E-03
116	GBP1P1	-0.9931	7.18E-03
117	AP000253.1	-0.9953	6.61E-03
118	TGDS	-0.9971	7.10E-03
119	FAM86C1	-0.9977	9.63E-03
120	PCED1B-AS1	-1.0038	3.62E-03
121	HBEGF	-1.0074	8.93E-03
122	SRRM1P3	-1.0127	4.49E-03
123	LINC02367	-1.0177	1.61E-03
124	MBP	-1.0184	5.31E-03
125	KCNAB2	-1.0236	8.29E-04
126	AC009803.1	-1.0239	5.77E-03
127	JUN	-1.0301	2.75E-03
128	PRDM15	-1.0356	5.23E-04
129	AC079905.1	-1.0401	9.61E-04
130	GDPD5	-1.0409	9.55E-03
131	SNHG12	-1.0433	3.74E-04
132	RPL35P5	-1.0454	4.10E-03
133	HELQ	-1.0534	3.66E-03
134	ITGB2	-1.0566	3.51E-03
135	ADAM19	-1.0569	6.02E-03
136	HIST1H4B	-1.0655	6.42E-03
137	SLC12A7	-1.0661	1.21E-03
138	KLC2	-1.0662	8.79E-03
139	ARHGEF1	-1.0674	2.13E-03
140	CDK11B	-1.0688	2.49E-03
141	GADD45B	-1.0693	9.51E-04
142	RPL21P18	-1.0721	7.96E-04
143	WDR25	-1.0753	8.72E-03
144	MBNL1-AS1	-1.0803	9.62E-03
145	HCK	-1.0827	5.12E-03
146	CYTH4	-1.0864	2.90E-03
147	AC005229.1	-1.0883	8.50E-03
148	GLYCTK	-1.0888	4.38E-03
149	NPL	-1.0907	4.35E-03
150	LAMP5	-1.0918	6.39E-03
151	AC005837.2	-1.1010	8.51E-03
152	KLF2	-1.1028	6.83E-04
153	CDH1	-1.1046	6.46E-03
154	AL031777.1	-1.1051	6.17E-03
155	GYS1	-1.1164	1.99E-04
156	FCER1G	-1.1217	6.87E-03
157	KCNN1	-1.1232	2.15E-03
158	FTLP2	-1.1236	5.73E-04
159	RTEL1	-1.1264	5.60E-03
160	ZNF624	-1.1329	8.75E-03
161	EIF4A1P2	-1.1331	1.04E-03
162	ZNF350	-1.1351	3.42E-03
163	FAM43A	-1.1380	1.11E-03
164	ID1	-1.1404	5.02E-03
165	SNX32	-1.1407	8.03E-03
166	COMMD5	-1.1421	6.81E-03
167	MRPL41	-1.1426	1.72E-03
168	RPL35P4	-1.1427	2.24E-03
169	VPS26C	-1.1434	3.88E-04
170	AAGAB	-1.1478	2.04E-03
171	FAM19A1	-1.1525	6.91E-03
172	AC025627.3	-1.1545	3.85E-03
173	LYVE1	-1.1588	2.23E-03
174	AL031729.1	-1.1597	3.51E-03
175	DAP3P2	-1.1639	8.99E-03
176	SLC7A3	-1.1644	4.54E-03
177	AC113367.1	-1.1648	3.33E-04
178	AC006122.1	-1.1653	1.64E-04
179	PYDC1	-1.1717	9.90E-03
180	NCF1	-1.1736	2.63E-03
181	SERPINB8	-1.1968	8.21E-03
182	RAB26	-1.2007	3.90E-03
183	PIK3CD-AS1	-1.2064	6.06E-03
184	MYLIP	-1.2096	1.70E-04
185	AC022217.2	-1.2135	4.93E-03
186	GRAP2	-1.2181	3.41E-03
187	APCDD1	-1.2219	3.39E-03
188	FARS2	-1.2235	1.45E-03
189	EXO1	-1.2245	8.37E-03
190	HSPA12B	-1.2286	2.10E-03
191	RPL36AP13	-1.2291	8.92E-04
192	PDCD2L	-1.2301	4.85E-03
193	WDFY4	-1.2333	6.81E-04
194	NCF1C	-1.2376	7.53E-03
195	ACSL5	-1.2414	1.20E-03
196	RF00003	-1.2485	1.01E-03
197	HIST1H1E	-1.2488	1.55E-03
198	TRAF7	-1.2517	4.70E-04
199	AL079342.1	-1.2520	5.68E-03
200	ART4	-1.2548	2.65E-03

Continued Table 22:

#	Gene name	log_2 fc	p-value
201	TLCD1	-1.2573	1.37E-03
202	AL021807.1	-1.2584	1.07E-03
203	WT1	-1.2713	8.19E-03
204	RNVU1-19	-1.2757	3.88E-03
205	CBX8	-1.2797	2.05E-03
206	LINC01374	-1.2877	6.77E-03
207	ATF3	-1.2887	1.55E-03
208	DDIT3	-1.2898	1.74E-03
209	TSPEAR-AS2	-1.2913	1.14E-03
210	ACOT7	-1.2914	1.11E-03
211	DDIT4	-1.2923	4.24E-04
212	IQCN	-1.3086	3.35E-03
213	PLK2	-1.3094	3.19E-03
214	NOC2LP1	-1.3167	1.88E-03
215	LINC00926	-1.3279	9.05E-03
216	AC087239.1	-1.3283	2.20E-03
217	FOS	-1.3387	1.41E-04
218	TEX14	-1.3459	9.78E-04
219	AC022535.1	-1.3510	3.85E-03
220	ZFP36	-1.3550	9.03E-04
221	CD48	-1.3561	7.40E-04
222	TFAP4	-1.3581	4.47E-04
223	DFFB	-1.3754	4.12E-04
224	RGS1	-1.3786	6.65E-04
225	TMSB4Y	-1.3874	8.26E-03
226	AL356750.1	-1.3875	1.42E-03
227	SEL1L3	-1.4130	2.12E-03
228	RPL21P39	-1.4249	1.47E-04
229	TMEM221	-1.4626	3.72E-04
230	SIK1B	-1.4708	4.45E-03
231	SHC1	-1.4795	3.15E-03
232	NCF1B	-1.4817	2.15E-03
233	RN7SL827P	-1.4964	4.89E-05
234	TLE1	-1.5090	1.18E-03
235	ALDH3A2	-1.5125	1.69E-04
236	JUNB	-1.5512	7.29E-04
237	AC245014.3	-1.5610	8.74E-04
238	KCNN2	-1.5623	6.67E-04
239	DDN	-1.5856	4.93E-03
240	RNVU1-15	-1.5891	3.45E-04
241	STAMBPL1	-1.5998	4.53E-04
242	TCTN1	-1.6139	3.17E-03
243	SETBP1	-1.6240	2.37E-03
244	AC113189.2	-1.6404	1.05E-04
245	NR4A1	-1.6538	3.63E-03
246	MATN1-AS1	-1.6629	4.18E-04
247	CR1	-1.7090	2.39E-04
248	RPL31P47	-1.7458	1.00E-04
249	KDM6B	-1.7490	1.11E-04
250	EGR1	-1.8724	1.39E-04
251	LINC01977	-1.9099	6.01E-05
252	AL590385.2	-2.0103	1.77E-04

A3. Differentially expressed proteins

Table 23: Significantly upregulated proteins of resistant vs. untreated ALL-199 cells.

All upregulated proteins with $p < 0.01$ are listed and ranked by log2 fold change (log2 fc) between resistant and untreated ALL-199 cells.

#	Name	log_2 fc	p-value
1	TSNAX;DISC1	0.1721	3.14E-03
2	ITGB2	0.1544	1.28E-04
3	H1F0	0.1544	1.27E-03
4	CRIP1	0.1474	6.77E-03
5	BCL2	0.1414	5.86E-03
6	PTPN6	0.1344	9.72E-04
7	CD59	0.1306	2.68E-03
8	MRPL49	0.1244	1.37E-04
9	FTL	0.1157	1.70E-03
10	FSCN1	0.1120	1.42E-03
11	GLUL	0.1103	2.45E-03
12	GYG1	0.1095	2.32E-03
13	CDKN1B	0.1017	1.30E-03
14	PDXK	0.1008	6.91E-04
15	ZNF207	0.0996	6.62E-03
16	CD47	0.0983	4.61E-03
17	ALOX5	0.0951	9.19E-03
18	ADI1	0.0914	1.46E-03
19	ALDH1A1	0.0844	4.55E-03
20	FTH1	0.0838	1.33E-03
21	TMSB4X	0.0814	3.64E-03
22	WASF1	0.0757	2.33E-04
23	ALDH2	0.0724	4.57E-03
24	ANXA4	0.0701	6.38E-04
25	ANXA6	0.0679	9.19E-05
26	SLC9A3R1	0.0672	8.95E-04
27	GSN	0.0652	7.05E-03
28	TST	0.0639	8.03E-03
29	PNKP	0.0610	9.85E-03
30	SEC24D	0.0603	4.80E-03
31	MAPK8IP3	0.0592	5.52E-03
32	CD34	0.0579	4.24E-05
33	CPT1A	0.0550	8.77E-05
34	SNX27	0.0545	2.56E-03
35	SBF1	0.0542	3.57E-03
36	GBP1	0.0514	6.61E-03
37	MTMR14	0.0505	5.94E-03
38	WAPAL	0.0489	7.15E-03
39	CSTB	0.0463	8.55E-04
40	NME4	0.0453	9.59E-03
41	ATP6V1E1	0.0436	4.72E-03
42	PPP1R14B	0.0436	7.02E-03
43	REL	0.0429	5.59E-03
44	MRPS36	0.0427	8.70E-03
45	FNBP1	0.0397	9.09E-03
46	PIK3R4	0.0393	2.89E-03
47	RNASEH2C	0.0387	7.64E-03
48	ACTN1	0.0387	1.31E-03
49	PSMB9	0.0382	2.38E-03
50	PROSC	0.0373	8.17E-03
51	SMEK1	0.0367	9.11E-04
52	PLAA	0.0358	3.10E-03
53	CSRP1	0.0352	3.37E-03
54	CTSB	0.0336	4.03E-03
55	DBNL	0.0330	8.97E-03
56	SCAMP1	0.0326	3.96E-03
57	LZTFL1	0.0323	5.44E-03
58	TXLNA	0.0322	3.69E-03
59	C14orf159	0.0310	8.46E-03
60	SETD3	0.0303	8.06E-03
61	GOLGA3	0.0286	1.61E-03
62	IMPDH1	0.0280	5.84E-03
63	SCP2	0.0280	8.27E-03
64	TBCA	0.0276	6.93E-03
65	USP9X;USP9Y	0.0269	8.48E-03
66	YWHAG	0.0267	8.08E-03
67	TPM4	0.0264	3.88E-03
68	NAMPT	0.0260	6.01E-03
69	COPS2	0.0253	2.52E-03
70	PFDN2	0.0248	6.72E-04
71	PSMD9	0.0243	2.43E-03
72	SNX12	0.0237	1.12E-03
73	ZC3H13	0.0237	3.92E-03
74	PSMA3	0.0235	9.96E-03
75	DYNLL1	0.0233	6.91E-03
76	NDUFC2	0.0229	4.35E-03
77	CCDC86	0.0209	8.38E-03
78	LRRFIP1	0.0205	7.95E-03
79	EIF2S2	0.0199	2.40E-03
80	MSN	0.0193	5.06E-03
81	PSMD2	0.0180	8.59E-03
82	PRDX1	0.0173	2.87E-03
83	VARS	0.0171	4.15E-03
84	TARS	0.0154	9.26E-03
85	TLN1	0.0132	8.17E-03

A4. MAGeCK analysis of *in vivo* CRISPR/Cas9 screen

Table 24: MAGeCK analysis of CRISPR/Cas9 *in vivo* screen.

p-value, false discovery rate (FDR) and log_2 fold change (log_2 FC) were calculated by comparison of two groups as indicated, five sgRNAs per gene were pooled per gene.

	Start of treatment vs. Input			PBS vs. start of treatment			VCR + Cyclo vs. PBS		
Gene Name	**p-value**	**FDR**	**log_2 FC**	**p-value**	**FDR**	**log_2 FC**	**p-value**	**FDR**	**log_2 FC**
ACCS	0.9583	0.9979	0.2143	0.8404	0.9995	0.3100	0.7183	0.9842	-0.2625
ACTN1	0.7267	0.9979	0.1260	0.1012	0.7895	-0.2199	0.9802	0.9842	0.7748
ADARB1	0.7455	0.9979	0.0748	0.8442	0.9995	0.2686	0.2916	0.9782	-0.1470
ADGRE2	0.4127	0.9979	-0.2830	0.1147	0.7895	-0.8463	0.9469	0.9842	1.2862
ADGRE5	0.6892	0.9979	0.0046	0.8939	0.9995	0.0940	0.5903	0.9842	0.0457
ADGRG1	0.9054	0.9979	0.2539	0.5479	0.9897	-0.2358	0.7474	0.9842	0.2878
ADI1	0.5320	0.9979	0.4511	0.2490	0.9182	-1.0299	0.6553	0.9842	0.6399
AIG1	0.8277	0.9979	0.0520	0.7288	0.9995	-0.2978	0.1345	0.8626	-0.0330
AKAP12	0.7363	0.9979	-0.1333	0.4722	0.9525	0.5416	0.1765	0.9057	0.0270
ALDH1A1	0.5097	0.9979	-0.1690	0.1669	0.8233	-0.7656	0.9563	0.9842	1.0833
ALDH2	0.8517	0.9979	-0.2112	0.5536	0.9897	-0.0078	0.7483	0.9842	0.4913
ALOX5	0.9860	0.9979	0.4722	0.4382	0.9525	0.0030	0.5654	0.9842	-0.3780
ANXA4	0.5041	0.9979	-0.0581	0.8670	0.9995	0.3854	0.9091	0.9842	-0.3359
ANXA6	0.8139	0.9979	0.1915	0.6891	0.9995	0.3894	0.2993	0.9782	-0.1313
APC	0.3691	0.9979	-0.4342	0.6068	0.9995	-0.2365	0.0113	0.3457	-1.0758
ARV1	0.9193	0.9979	0.1063	0.9903	0.9995	0.4057	0.3598	0.9842	0.2446
ATF6	0.2670	0.9979	-0.4454	0.4515	0.9525	-0.6714	0.6770	0.9842	0.1431
ATP6V1E1	0.0250	0.2267	-0.9997	0.0484	0.7563	-1.6691	0.2603	0.9750	0.4495
ATP9B	0.9256	0.9979	0.5071	0.4020	0.9525	0.1371	0.1973	0.9477	0.1808
B4GALT6	0.9544	0.9979	0.3841	0.4040	0.9525	0.7975	0.2966	0.9782	0.0407
BABAM2	0.6692	0.9979	0.4561	0.3185	0.9438	-0.8851	0.8545	0.9842	0.6115
BCL2	0.3589	0.9979	-0.3419	0.0953	0.7895	-0.9639	0.0009	0.1065	-2.8857
BCL6B	0.5214	0.9979	0.0320	0.9841	0.9995	0.5097	0.4459	0.9842	-0.4888
BCL9	0.9155	0.9979	0.2380	0.1817	0.8302	-1.3340	0.9105	0.9842	1.8289
BICD1	0.9341	0.9979	0.2322	0.8701	0.9995	0.3026	0.2184	0.9547	0.5025
BIN1	0.5228	0.9979	-0.0949	0.7351	0.9995	0.6865	0.4957	0.9842	0.2200
BLNK	0.8874	0.9979	0.0711	0.5317	0.9875	-0.3514	0.7623	0.9842	-0.2212
BRIP1	0.7543	0.9979	-0.0360	0.1401	0.8220	-1.3694	0.0234	0.5250	-1.2371
BRWD3	0.9482	0.9979	0.4417	0.9010	0.9995	0.2573	0.7250	0.9842	0.3776
BTN3A3	0.6156	0.9979	0.1448	0.9070	0.9995	0.1652	0.8499	0.9842	-0.2128
C14orf159	0.8225	0.9979	0.3920	0.1901	0.8302	-0.9123	0.4082	0.9842	1.0098
C1QTNF4	0.6580	0.9979	0.2401	0.3801	0.9525	-0.0542	0.8555	0.9842	0.5234
C9	0.8705	0.9979	0.2646	0.6654	0.9995	-0.3200	0.9131	0.9842	0.4727
CCDC69	0.6489	0.9979	0.0210	0.7059	0.9995	0.3417	0.2847	0.9782	-0.4673
CCDC86	0.0008	0.0121	-1.2013	0.4466	0.9525	-0.8764	0.0245	0.5250	-1.5516
CD163L1	0.9042	0.9979	-0.0165	0.1171	0.7895	-0.1830	0.7690	0.9842	0.2447
CD34	0.6938	0.9979	0.1746	0.0596	0.7563	-1.8374	0.8337	0.9842	0.4063
CD47	0.0453	0.3560	-1.9431	0.1709	0.8233	-2.1964	0.9800	0.9842	0.6902
CD59	0.8098	0.9979	0.5321	0.9953	0.9995	0.3838	0.0187	0.4893	-1.5633
CD9	0.5716	0.9979	0.0712	0.9962	0.9995	0.7025	0.4993	0.9842	-0.3406
CD96	0.9578	0.9979	0.5487	0.1526	0.8220	-1.3414	0.6808	0.9842	0.6381
CD99	0.8983	0.9979	0.1826	0.9623	0.9995	0.9523	0.5247	0.9842	-0.5455
CDK7	0.0043	0.0509	-1.6006	0.0232	0.7563	-2.6259	0.0920	0.7842	0.7536
CDK9	0.0000	0.0002	-5.4015	0.7250	0.9995	-1.7445	0.2008	0.9477	0.6222
CDKN1B	0.4914	0.9979	-0.1076	0.1932	0.8302	-0.8110	0.8917	0.9842	1.4751
CNOT10	0.1041	0.6301	-0.7830	0.8861	0.9995	0.0245	0.0117	0.3457	-1.0439

Continued Table 24:

	Start of treatment vs. Input			PBS vs. start of treatment			VCR + Cyclo vs. PBS		
Gene Name	**p-value**	**FDR**	**log_2 FC**	**p-value**	**FDR**	**log_2 FC**	**p-value**	**FDR**	**log_2 FC**
COL5A1	0.6465	0.9979	0.1129	0.4531	0.9525	-0.6451	0.7909	0.9842	0.8361
COPS2	0.0159	0.1632	-1.1848	0.2613	0.9342	-1.2953	0.2445	0.9570	0.8580
CPT1A	0.6991	0.9979	0.7086	0.1602	0.8220	-0.9512	0.4501	0.9842	0.0445
CRIP1	0.5983	0.9979	0.0025	0.5169	0.9759	-0.3297	0.8711	0.9842	1.1353
CSF3R	0.9411	0.9979	0.4196	0.2529	0.9182	-0.1797	0.6253	0.9842	-0.0480
CSNK2A1	0.9777	0.9979	0.7818	0.9995	0.9995	1.2992	0.0067	0.2645	-1.2882
CSRP1	0.6858	0.9979	0.5307	0.1155	0.7895	-0.1839	0.9702	0.9842	0.1445
CSTB	0.5184	0.9979	0.0124	0.2687	0.9438	-0.7455	0.6847	0.9842	1.0543
CTHRC1	0.6348	0.9979	0.0019	0.6311	0.9995	0.1467	0.7139	0.9842	0.2674
CTSB	0.9048	0.9979	0.0242	0.7820	0.9995	-0.1023	0.7400	0.9842	0.1953
DBNL	0.9841	0.9979	0.4630	0.6466	0.9995	-0.1781	0.8993	0.9842	-0.0006
DDX59	0.0476	0.3624	-0.7670	0.2076	0.8302	-0.2546	0.8755	0.9842	-0.4460
DHRS7	0.8929	0.9979	0.1721	0.4614	0.9525	-0.4526	0.7381	0.9842	-0.1842
DPEP1	0.9103	0.9979	0.1378	0.0645	0.7563	-1.5223	0.9712	0.9842	0.7325
DSTN	0.5275	0.9979	0.0003	0.3200	0.9438	-0.7874	0.5515	0.9842	-0.4641
DUSP26	0.8416	0.9979	0.1819	0.7469	0.9995	-0.2071	0.5572	0.9842	-0.1795
DYNLL1	0.0542	0.3876	-0.7422	0.1155	0.7895	-1.0473	0.9692	0.9842	0.7722
DYSF	0.9806	0.9979	0.6117	0.6510	0.9995	0.4497	0.1619	0.9057	-0.9288
ECM1	0.6098	0.9979	0.2046	0.6823	0.9995	0.2567	0.4415	0.9842	-0.1943
EFNA1	0.7026	0.9979	0.5636	0.1991	0.8302	0.1076	0.4489	0.9842	-0.3476
EIF2S2	0.0007	0.0110	-1.1327	0.4684	0.9525	-0.3575	0.0981	0.7920	-1.0368
ENG	0.9791	0.9979	0.3409	0.6368	0.9995	0.1771	0.7086	0.9842	-0.4136
ERG	0.4265	0.9979	-0.1946	0.8536	0.9995	-0.1138	0.1352	0.8626	-0.3974
EVI2B	0.9085	0.9979	0.4834	0.4880	0.9677	-0.5451	0.4099	0.9842	0.2509
EXD3	0.8823	0.9979	0.5153	0.6107	0.9995	0.2990	0.7036	0.9842	-0.3207
F11R	0.5060	0.9979	0.0544	0.0764	0.7563	-1.3175	0.7095	0.9842	1.0626
FBXL5	0.0011	0.0154	-2.9582	0.8109	0.9995	0.6736	0.2835	0.9782	-0.1960
FBXW7	0.0681	0.4342	-0.4738	0.4193	0.9525	-0.5214	0.7764	0.9842	-0.3739
FERMT2	0.9590	0.9979	0.1782	0.0404	0.7563	-0.6178	0.8177	0.9842	0.3020
FGF16	0.5117	0.9979	-0.1539	0.2957	0.9438	0.0245	0.1120	0.8006	0.6963
FGFR1	0.4104	0.9979	0.4241	0.9414	0.9995	0.8796	0.1722	0.9057	-0.6845
FNBP1	0.8963	0.9979	0.4778	0.4176	0.9525	-0.5799	0.7307	0.9842	0.5235
FRZB	0.8193	0.9979	0.1941	0.7978	0.9995	0.0091	0.6368	0.9842	-0.0532
FSCN1	0.7904	0.9979	0.3467	0.3057	0.9438	0.4207	0.7928	0.9842	-0.3511
FTH1	0.0000	0.0002	-5.3127	0.4483	0.9525	-0.9123	0.0594	0.7177	-0.0768
FTL	0.3018	0.9979	-0.2923	0.5433	0.9897	0.5082	0.7017	0.9842	0.2441
FUT7	0.2461	0.9979	0.0520	0.6671	0.9995	0.4579	0.5620	0.9842	0.0222
FXYD5	0.8386	0.9979	0.4643	0.4483	0.9525	-0.0319	0.4142	0.9842	-0.0125
FYN	0.6974	0.9979	0.0677	0.6927	0.9995	0.6684	0.6202	0.9842	-0.1845
GBP1	0.6259	0.9979	-0.1246	0.8675	0.9995	0.9402	0.5584	0.9842	-0.3398
GLUL	0.5706	0.9979	-0.1252	0.0375	0.7563	-1.5243	0.5441	0.9842	1.1199
GOLGA3	0.9240	0.9979	1.1181	0.2006	0.8302	0.1879	0.2465	0.9570	0.2979
GPR160	0.8481	0.9979	-0.0254	0.5860	0.9995	0.3993	0.0574	0.7177	-1.4780
GPSM1	0.9556	0.9979	0.0722	0.1035	0.7895	-0.1116	0.1903	0.9441	0.6833
GPX4	0.6903	0.9979	0.1234	0.8133	0.9995	-0.0628	0.9620	0.9842	0.7675
GSE1	0.5483	0.9979	0.1868	0.9295	0.9995	0.4380	0.2849	0.9782	-0.2824
GSN	0.6406	0.9979	0.3938	0.5031	0.9731	0.4077	0.6178	0.9842	0.1069
GYG1	0.8943	0.9979	0.3640	0.9085	0.9995	0.5862	0.0319	0.5786	-0.9851
GYPC	0.4650	0.9979	0.3967	0.0739	0.7563	-0.1540	0.6627	0.9842	0.7507
H1F0	0.7117	0.9979	0.3251	0.6219	0.9995	0.3625	0.4975	0.9842	-0.5557
H1FX	0.1795	0.9415	-0.5574	0.9290	0.9995	0.8138	0.6351	0.9842	-0.1804

Continued Table 24:

	Start of treatment vs. Input			PBS vs. start of treatment			VCR + Cyclo vs. Input		
Gene Name	**p-value**	**FDR**	**log_2 FC**	**p-value**	**FDR**	**log_2 FC**	**p-value**	**FDR**	**log_2 FC**
HEATR6	0.9396	0.9979	0.5463	0.3424	0.9525	0.5153	0.2522	0.9598	-0.6312
HHAT	0.4970	0.9979	0.1621	0.8972	0.9995	0.4552	0.6708	0.9842	0.0766
HSPE1	0.0000	0.0006	-3.0213	0.2050	0.8302	-2.4808	0.2326	0.9570	0.5638
IGF2BP2	0.9953	0.9979	0.4790	0.3977	0.9525	0.6583	0.1707	0.9057	-0.9766
IGLL1	0.8248	0.9979	0.0173	0.5520	0.9897	0.1528	0.8206	0.9842	-0.2817
IMPDH1	0.7234	0.9979	0.1744	0.4256	0.9525	1.0463	0.6320	0.9842	-0.1701
ITGB2	0.8695	0.9979	0.2537	0.7166	0.9995	0.3256	0.9270	0.9842	0.1345
ITM2C	0.8697	0.9979	0.1500	0.7066	0.9995	-0.0190	0.7151	0.9842	0.3164
KANK2	0.8054	0.9979	-0.0056	0.7970	0.9995	0.7248	0.3363	0.9842	-0.5649
KCNE3	0.6869	0.9979	0.4882	0.2458	0.9182	-0.8621	0.6151	0.9842	-0.3036
KDM5B	0.8758	0.9979	0.4319	0.7751	0.9995	0.3808	0.1759	0.9057	-0.9240
KLHL12	0.7612	0.9979	0.4442	0.0619	0.7563	-1.6514	0.9687	0.9842	0.7688
KLHL23	0.9979	0.9979	0.7120	0.3548	0.9525	-0.6215	0.2725	0.9782	-0.3781
KMT2A	0.0720	0.4470	-0.9189	0.9964	0.9995	1.6827	0.0359	0.5916	-1.6677
LIMD1	0.7832	0.9979	0.2243	0.9773	0.9995	0.7331	0.1734	0.9057	-0.9261
LRRFIP1	0.8636	0.9979	0.0817	0.2324	0.8992	-0.6122	0.4269	0.9842	0.5816
LZTFL1	0.7443	0.9979	0.2722	0.0844	0.7865	0.3415	0.7269	0.9842	-0.0568
MAPK8IP3	0.1407	0.7906	-0.6142	0.3546	0.9525	-0.4031	0.9442	0.9842	0.4218
MDK	0.8298	0.9979	0.1341	0.3633	0.9525	-0.4482	0.5878	0.9842	1.3582
MELK	0.9623	0.9979	0.6106	0.2011	0.8302	-0.5298	0.9787	0.9842	1.0191
MLXIP	0.8880	0.9979	0.4232	0.0594	0.7563	-0.4524	0.9321	0.9842	0.0909
MME	0.7499	0.9979	0.6572	0.7290	0.9995	-0.1050	0.7259	0.9842	-0.2480
MPO	0.9211	0.9979	0.3239	0.6430	0.9995	-0.1145	0.7613	0.9842	-0.0949
MPP6	0.5302	0.9979	0.0869	0.6330	0.9995	-0.3167	0.9155	0.9842	0.7069
MPST	0.6797	0.9979	-0.0321	0.2899	0.9438	-0.4662	0.5827	0.9842	0.6077
MRPL49	0.0584	0.4051	-0.8958	0.0196	0.7563	-2.0579	0.6913	0.9842	1.7310
MRPS36	0.7409	0.9979	-0.0100	0.4606	0.9525	0.7262	0.3477	0.9842	-0.5526
MSANTD3	0.6032	0.9979	-0.1782	0.7739	0.9995	-0.1933	0.9124	0.9842	0.1848
MSN	0.1548	0.8495	-0.9878	0.0769	0.7563	0.9834	0.6168	0.9842	0.1783
MTMR14	0.6996	0.9979	0.0759	0.4444	0.9525	-0.1769	0.6588	0.9842	0.3792
MTRNR2L1	0.0604	0.4070	-0.4144	0.9517	0.9995	1.3143	0.1192	0.8040	-1.0611
MYLK	0.7255	0.9979	0.6135	0.9331	0.9995	0.3977	0.0759	0.7467	-1.3476
N4BP1	0.6536	0.9979	0.0315	0.4930	0.9695	-0.5544	0.7507	0.9842	0.3401
NAMPT	0.0000	0.0006	-4.7073	0.8033	0.9995	-0.3709	0.0571	0.7177	-0.4678
NDUFC2	0.1882	0.9655	-0.3932	0.4503	0.9525	0.0132	0.1662	0.9057	-0.6979
NEG	0.9861	0.9979	0.5705	0.7354	0.9995	0.1869	0.5233	0.9842	0.1950
NEG_	0.9977	0.9979	0.2907	0.9650	0.9995	0.4976	0.3895	0.9842	-0.1970
NEXN	0.9917	0.9979	0.5672	0.0294	0.7563	-0.7173	0.9842	0.9842	1.1561
NME4	0.4489	0.9979	0.0827	0.4146	0.9525	0.4730	0.1626	0.9057	-0.2157
NPRL2	0.2260	0.9979	-0.4037	0.1053	0.7895	-0.8321	0.2193	0.9547	-0.8544
NRP1	0.5852	0.9979	0.2380	0.4105	0.9525	-0.5259	0.8256	0.9842	0.9649
NSD3	0.5936	0.9979	0.2102	0.0328	0.7563	-1.2384	0.9709	0.9842	1.2430
PACSIN1	0.5782	0.9979	0.0738	0.5760	0.9995	0.5515	0.2395	0.9570	-0.7985
PARG	0.3248	0.9979	-0.3944	0.7172	0.9995	0.4470	0.1920	0.9441	0.7433
PCDH12	0.8334	0.9979	0.3494	0.0528	0.7563	0.2866	0.5548	0.9842	-0.5442
PDCD6IP	0.5817	0.9979	-0.1723	0.9846	0.9995	0.7103	0.3633	0.9842	-0.0798
PDXK	0.2081	0.9979	-0.4680	0.0103	0.7563	-1.0225	0.7315	0.9842	0.3408
PFDN2	0.0644	0.4219	-0.7140	0.0420	0.7563	-3.1876	0.7736	0.9842	1.1873
PGBD1	0.4557	0.9979	-0.3045	0.9220	0.9995	-0.1222	0.8912	0.9842	0.5723
PIK3R4	0.2290	0.9979	-0.5588	0.5738	0.9995	0.0811	0.0283	0.5574	-1.7775
PLAA	0.4988	0.9979	0.1800	0.8174	0.9995	0.7426	0.8881	0.9842	0.1745

Continued Table 24:

	Start of treatment vs. Input			PBS vs. start of treatment			VCR + Cyclo vs. PBS		
Gene Name	**p-value**	**FDR**	**log_2 FC**	**p-value**	**FDR**	**log_2 FC**	**p-value**	**FDR**	**log_2 FC**
PLPP3	0.7222	0.9979	-0.0390	0.6255	0.9995	-0.3352	0.6437	0.9842	0.3139
PLXND1	0.8425	0.9979	0.2728	0.1257	0.8018	0.2854	0.9634	0.9842	0.4846
PNKP	0.1359	0.7822	-0.6506	0.0866	0.7865	-1.0852	0.4595	0.9842	0.2978
POLR2L	0.0000	0.0002	-5.0269	0.3626	0.9525	-3.0806	0.2972	0.9782	-0.0427
PPP1R14B	0.8033	0.9979	0.6739	0.0589	0.7563	-1.0102	0.1080	0.7966	0.9089
PRDX1	0.8655	0.9979	0.3078	0.3056	0.9438	0.1588	0.5316	0.9842	0.2206
PRKD2	0.7788	0.9979	-0.2053	0.8546	0.9995	0.3899	0.7526	0.9842	-0.2749
PRSS36	0.5520	0.9979	-0.2231	0.5259	0.9850	-0.1928	0.8787	0.9842	-0.3017
PSMA3	0.0003	0.0058	-3.7268	0.8851	0.9995	-0.3337	0.2474	0.9570	0.5545
PSMB3	0.0000	0.0004	-3.8378	0.7889	0.9995	-0.4467	0.5990	0.9842	0.4158
PSMB9	0.9501	0.9979	0.4306	0.2759	0.9438	-0.6142	0.4941	0.9842	0.1869
PSMD2	0.2112	0.9979	-0.1381	0.1349	0.8187	-1.6420	0.8225	0.9842	0.2185
PSMD9	0.9938	0.9979	0.5473	0.1896	0.8302	-0.3901	0.7325	0.9842	0.4380
PTGDR	0.6053	0.9979	0.5242	0.3613	0.9525	-0.1156	0.8169	0.9842	0.5741
PTPN12	0.9874	0.9979	0.9404	0.0039	0.7563	-1.4187	0.9097	0.9842	0.9983
PTPN6	0.9648	0.9979	0.6217	0.8307	0.9995	0.0828	0.9292	0.9842	0.4947
PXDN	0.7105	0.9979	0.2162	0.2796	0.9438	-0.1080	0.2138	0.9547	-0.0142
RAB5A	0.8611	0.9979	0.5305	0.8268	0.9995	0.9238	0.1192	0.8040	-0.6323
RACK1	0.0000	0.0004	-3.4999	0.2284	0.8982	-2.3770	0.0892	0.7842	-0.6498
RAN	0.0000	0.0004	-4.9184	0.6714	0.9995	-0.9035	0.3354	0.9842	0.1240
RAP1GAP2	0.9145	0.9979	0.1144	0.8152	0.9995	0.5950	0.6016	0.9842	-0.5054
RASGEF1A	0.5561	0.9979	0.0531	0.9820	0.9995	0.3087	0.3731	0.9842	-0.0489
RBFOX2	0.9732	0.9979	0.3392	0.3107	0.9438	-0.4765	0.8102	0.9842	0.5016
RCAN1	0.6146	0.9979	0.0891	0.9410	0.9995	0.2401	0.3538	0.9842	-0.1744
REL	0.7532	0.9979	0.0963	0.9592	0.9995	0.0503	0.6700	0.9842	0.2627
RFX8	0.6822	0.9979	0.0018	0.3261	0.9502	-0.4486	0.9771	0.9842	1.0693
RGL4	0.7856	0.9979	-0.2801	0.9948	0.9995	1.2912	0.2368	0.9570	-0.8084
RHOXF2	0.5913	0.9979	0.4588	0.0708	0.7563	-1.1624	0.5419	0.9842	0.9480
RIPOR1	0.8012	0.9979	0.1766	0.3006	0.9438	-0.6992	0.9783	0.9842	0.9958
RNASEH2C	0.4341	0.9979	-0.0645	0.0398	0.7563	0.9871	0.0710	0.7287	-0.7249
RPL12	0.0080	0.0895	-1.8560	0.1242	0.8018	-2.0758	0.3765	0.9842	1.1918
RPL37	0.0171	0.1678	-1.0270	0.9805	0.9995	0.2523	0.0029	0.1732	-1.7521
RPLP0	0.0028	0.0345	-1.7157	0.4192	0.9525	-0.6816	0.3383	0.9842	-0.1783
RPS2	0.0007	0.0112	-3.9924	0.8041	0.9995	-1.4667	0.2225	0.9547	0.1510
RRM2	0.0000	0.0002	-5.4086	0.4060	0.9525	-1.8847	0.0693	0.7287	-0.0927
SARS	0.0001	0.0029	-5.4608	0.4648	0.9525	-2.1591	0.0044	0.2064	-1.9048
SBF1	0.6247	0.9979	0.5321	0.1749	0.8253	-0.4745	0.7210	0.9842	-0.0188
SBF2	0.8740	0.9979	0.6682	0.2960	0.9438	0.2016	0.6082	0.9842	-0.6190
SCAMP1	0.9308	0.9979	0.2872	0.0249	0.7563	-1.0928	0.6942	0.9842	0.6736
SCN1B	0.9429	0.9979	0.1447	0.9981	0.9995	1.2169	0.0017	0.1369	-1.3562
SCP2	0.7467	0.9979	0.4730	0.4794	0.9587	-0.3224	0.7174	0.9842	0.1104
SDC1	0.7198	0.9979	-0.0007	0.9065	0.9995	-0.1848	0.1032	0.7920	0.0670
SDK2	0.8677	0.9979	0.3822	0.1571	0.8220	-0.9410	0.9280	0.9842	0.5232
SEC24D	0.8472	0.9979	0.1080	0.9971	0.9995	0.8725	0.4301	0.9842	-0.4696
SELPLG	0.8836	0.9979	0.4593	0.4236	0.9525	-0.0482	0.8064	0.9842	0.0955
SETD3	0.8534	0.9979	-0.1064	0.7948	0.9995	0.3149	0.6133	0.9842	0.1285
SFXN5	0.9611	0.9979	0.7473	0.6884	0.9995	0.4077	0.0483	0.7127	-0.9236
SHANK3	0.4781	0.9979	-0.2862	0.1592	0.8220	0.1778	0.8677	0.9842	0.8865
SIX3	0.6135	0.9979	0.9802	0.7835	0.9995	0.0499	0.3026	0.9782	-0.3787
SLC16A2	0.6643	0.9979	0.5496	0.3641	0.9525	0.0259	0.9218	0.9842	0.1833
SLC25A36	0.0532	0.3876	-0.7430	0.8761	0.9995	0.2163	0.0635	0.7177	-1.0284

Continued Table 24:

	Start of treatment vs. Input			PBS vs. start of treatment			VCR + Cyclo vs. PBS		
Gene Name	**p-value**	**FDR**	**log_2 FC**	**p-value**	**FDR**	**log_2 FC**	**p-value**	**FDR**	**log_2 FC**
SLC45A3	0.8213	0.9979	0.3319	0.3404	0.9525	-0.1514	0.6725	0.9842	0.8733
SLC9A3R1	0.6774	0.9979	-0.0790	0.1353	0.8187	-0.0549	0.6334	0.9842	0.0833
SMAD5	0.8593	0.9979	0.6850	0.6992	0.9995	0.3255	0.5749	0.9842	-0.1438
SMEK1	0.1611	0.8638	-0.7272	0.4564	0.9525	-0.5445	0.1040	0.7920	0.6952
SNRNP200	0.0006	0.0110	-3.9620	0.9037	0.9995	0.2026	0.0376	0.5916	-1.0255
SNX12	0.8844	0.9979	0.4699	0.5356	0.9875	0.6092	0.4670	0.9842	-0.4439
SNX27	0.5501	0.9979	0.1375	0.5085	0.9757	-0.4384	0.9512	0.9842	0.6916
SORL1	0.8086	0.9979	-0.0766	0.6417	0.9995	0.1195	0.9197	0.9842	0.2528
SPON2	0.9972	0.9979	0.6739	0.5131	0.9759	0.2649	0.7585	0.9842	-0.2555
SS18L2	0.0235	0.2214	-1.5194	0.1541	0.8220	-2.0605	0.3293	0.9842	0.5384
SSBP2	0.4249	0.9979	0.0573	0.9415	0.9995	0.4055	0.0930	0.7842	-1.2993
STK38	0.4614	0.9979	0.8035	0.1111	0.7895	-1.0337	0.5250	0.9842	1.1860
SYNE2	0.9838	0.9979	0.4251	0.6976	0.9995	0.5748	0.6253	0.9842	-0.1891
TARS	0.0156	0.1632	-0.8852	0.0164	0.7563	-1.5714	0.9255	0.9842	1.7519
TBCA	0.0012	0.0154	-2.7190	0.1699	0.8233	-1.4127	0.0823	0.7771	0.3534
TBX21	0.9171	0.9979	0.6144	0.9958	0.9995	1.9806	0.0003	0.0741	-2.7033
TCF7	0.8544	0.9979	0.3989	0.7661	0.9995	-0.0979	0.3632	0.9842	-0.0030
TLN1	0.1243	0.7334	-0.6221	0.7960	0.9995	-0.3061	0.2784	0.9782	-0.6876
TMEM173	0.7510	0.9979	0.3153	0.2379	0.9057	-0.6260	0.1555	0.9057	-0.0840
TMSB4X	0.9731	0.9979	1.1609	0.8193	0.9995	0.3237	0.0639	0.7177	-1.2896
TNFRSF1A	0.9552	0.9979	0.2710	0.9504	0.9995	0.3711	0.7555	0.9842	-0.4342
TPM4	0.7975	0.9979	0.0165	0.4985	0.9723	-0.5305	0.7334	0.9842	0.0216
TPO	0.7522	0.9979	0.1947	0.6588	0.9995	-0.2020	0.5927	0.9842	-0.1181
TSNAX	0.7015	0.9979	-0.2464	0.8222	0.9995	-0.3259	0.8345	0.9842	0.6510
TSPAN5	0.9333	0.9979	0.5723	0.3008	0.9438	-0.6361	0.7681	0.9842	0.4478
TST	0.6019	0.9979	0.2241	0.6970	0.9995	-0.1726	0.4700	0.9842	0.3046
TXLNA	0.7385	0.9979	0.9124	0.3186	0.9438	-0.3631	0.4174	0.9842	-0.1948
USP9X	0.8868	0.9979	0.0444	0.1444	0.8220	-0.0511	0.3158	0.9842	-0.2519
VARS	0.0000	0.0002	-4.7071	0.7523	0.9995	-2.1072	0.2070	0.9547	-0.0142
WAPAL	0.0290	0.2532	-0.7741	0.9100	0.9995	-0.2088	0.8453	0.9842	0.3016
WASF1	0.7327	0.9979	-0.1374	0.9336	0.9995	0.8372	0.8507	0.9842	0.6357
XBP1	0.4197	0.9979	-0.0095	0.7380	0.9995	-0.0582	0.6098	0.9842	-0.0395
YWHAG	0.6928	0.9979	0.2028	0.0698	0.7563	-0.0782	0.5107	0.9842	1.4766
ZC3H13	0.0335	0.2724	-0.7211	0.3781	0.9525	-0.2070	0.3599	0.9842	-0.0704
ZNF207	0.0314	0.2649	-0.9047	0.3716	0.9525	-1.0974	0.5137	0.9842	-0.3611
ZNF467	0.9949	0.9979	0.6288	0.6810	0.9995	0.6128	0.5082	0.9842	-0.5497
ZNF793	0.6337	0.9979	0.1378	0.6773	0.9995	-0.0504	0.3868	0.9842	0.5775

Danksagung

Diese Arbeit wäre ohne die Unterstützung und Hilfe vieler Menschen nicht möglich gewesen.

Zunächst möchte ich Irmela Jeremias dafür danken, dass sie mir ermöglicht hat, Teil ihrer Arbeitsgruppe zu sein und besonders für das Vertrauen in mich, dieses spannende Projekt eigenständig zu bearbeiten.

Außerdem möchte ich Wolfgang Enard für die Betreuung als Doktorvater und die Ideen zu meinem Projekt danken. Vielen Dank auch an die zwei weiteren Mitglieder meines Thesis Advisory Committees, Tobias Herold und Klaus Metzeler, dass sie sich Zeit dafür genommen haben und für die wertvollen und ermutigenden Ratschläge.

Vielen Dank an alle Kooperations-Partner, vor allem Lucas Wange, Sebastian Vosberg und Ashok Jayavelu, für die unkomplizierte und produktive Zusammenarbeit und die zahlreichen Diskussionen, die das Projekt erheblich vorangebracht haben.

Außerdem möchte ich allen aktuellen und früheren Mitglieder der AHS Gruppe für ihre Unterstützung, ihre guten Ideen und auch ihre kritischen Fragen danken. Ich möchte mich vor allem bei Erbey Özdemir bedanken für die Einarbeitung in die Gruppe und für seine Unterstützung, damit ich das Projekt alleine weiterführen konnte. Vielen Dank auch an Binje Vick für die Korrektur der Dissertation.

Außerdem möchte ich allen TAs der Gruppe und den TierpflegerInnen für ihre Hilfe bei meinen Experimenten danken. Ganz besonders möchte ich mich bei Annette Frank für ihre endlose Unterstützung bei meinen Versuchen danken, ohne sie hätte ich viele Experimente nicht durchführen können!

Besonders dankbar bin ich allen Freunden aus dem 002 Doktorandenbüro für die super Gemeinschaft, produktive Diskussionen unserer Projekte, gemeinsame Feiern von guten Ergebnissen, Unterstützung in schwierigen Momenten, 4-Uhr Pausen und Stammtische. Ohne euch wäre das alles nicht so lustig gewesen!

Vielen Dank allen meinen Freunden für ihre Unterstützung, vor allem Lukas für seine stetige Ermutigung und die Korrektur meiner Dissertation.

Besonders möchte ich Nicolas dafür danken, dass er in den schwierigen Zeiten von Pandemie und Dissertation für mich da war und mich immer unterstützt.

Zuletzt möchte ich meiner ganzen Familie und besonders meinen Eltern dafür danken, dass sie immer an mich glauben und mir die Möglichkeit gegeben haben, meine eigenen Ziele zu verfolgen. Vielen Dank, dass ihr immer für mich da seid!